Cranfield Institute
of Technology

G. M. Oddie

The Characterisation of Multicomponent (Liquid) Flows Using Scattered Ultrasound

Department of Fluid Engineering
And Instrumentation

School of Mechanical Engineering

Ph.D. Thesis.

Cranfield Institute of Technology

Department of Fluid Engineering and Instrumentation

Ph.D. Thesis

Academic Year 1991/92

G.M.Oddie

The Characterisation of Multicomponent (Liquid) Flows Using Scattered Ultrasound

Supervisor: Dr. C.P. Lenn

1992

ABSTRACT

The aim of this work is to determine the applicability of ultrasonic techniques to developing a non invasive flow meter capable of characterising multicomponent (liquid) flows. The possibility of detecting flow parameters such as velocity distributions, droplet/particle size distributions, spatial distribution and void fraction of the discontinuous phase has been investigated

An early consideration of the likely applications of this meter, revealed that an ultrasonic technique would be the most versatile and suitable. Consequently, a theoretical study of the interaction of an ultrasonic wave and a disperse system has been carried out, as well as a study of the possible regimes where these principles may be applied.

The work begins from first principles, studying both experimentally and theoretically the interaction of an acoustic wave with a single particle. This is then extended to characterising a flowing multicomponent system on a larger scale.

The nature of complex flows was then investigated from the point of view of a chaotic dynamical system. Both theoretical and experimental methods show this to be a valid approach to understanding the flow of mixtures.

Acknowledgements

Primary thanks must go to my supervisor, Dr Chris Lenn, for his guidance, encouragement and patience throughout the course of this work.

Thanks must also go to the following for their willing guidance, support and useful discussions;

J. Hemp (DFEI, Cranfield)

A.R. Guilbert (DFEI, Cranfield)

C. Armistead (School of Management, Cranfield)

E.L. Dinham (BP Exploration)

J.S.S. Miller (BP Engineering)

P.K. Chown (BP Engineering)

P. Frances (BP Exploration)

I. Mackley (BP Exploration)

G.P. Lucas (Schlumberger Cambridge Research)

S. Fauve (Ecole Superieur Normale, Lyons, France)

For technical assistance, without whose skills the work would not have progressed, the following are heartily thanked;

D. Macleod

C. Evans

R. Dunn

D. I. Greenhalgh

As for the nameless many whose comments and encouragement helped clarify the ideas and complete the work, thankyou.

CONTENTS

Chapter 3: Ultrasonic Scattering from a Single Particle.

Chapter 4: Scattering Cross-Section of a Single Particle.

Chapter 5: Larger Scale Experiments.

Appendix C: Select Literature Review: Multiphase and Multicomponent Flows.

Appendix D: Chaos in Fluid Flows.

Figures.

Chapter 1

Chapter 2

Chapter 3

Chapter 4

Chapter 5

Chapter 6

Appendix A

Appendix B

Appendix C

C.2a Flow regimes for gas/liquid flow in a horizontal pipe.

C.2b Flow regimes for gas/liquid flow in a vertical pipe.

C.3a Baker flow pattern map.

C.3b Scott's modification to the Baker flow map.

C.3c Bell's modification to the Baker flow map.

C.3d Eaton's flow map.

C.3e Comparison between Mandhane's flow map and the work of Govier and Aziz.

C.3f Comparison between Mandhane's flow map and the experimental results of Taitel, showing variations with pipe diameter.

C.3g Comparison between Mandhane's flow map and the experimental results of Taitel.

C.3h Variation of transition boundaries with fluid properties.

C.3i Definition of some system parameters for gas/liquid flow in a pipe.

C.3j Theoretical flow map from Taitel and Dukler.

C.3k Comparison between Taitel and Dukler and Mandhane for a 2.5cm air/water flow.

C.3l As above but for a 5.1cm tube.

C.3m Comparison of experimental results (3.8cm, 165Cp glycerine/air) with theory for 165Cp and theory for 1.0Cp liquid.

C.3n Flow map comparisons between Baker, Hoogendoorn and Govier and Omer (revised by Govier and Aziz).

C.3o The revised Govier Omer map.

C.3p A superposition of experimental transitions by Choe, limited to 1" pipes, but good for most combinations of fluids.

C.3q Flow patterns observed at the end of a 1.2cm diameter tube by Weisman.

C.3r Comparison of transitions in 2.54cm and 12.7cm air water flows from Weisman.

C.3s Comparison of experiment and theory at the end of a 5.1cm air/water pipe from Weisman.

C.3t Flow regime map by Sakaguchi for 30mm air/water flows. Note the unusual orientation of the axes, and La is the pipe length required for fully developed annular flow.

C.3u Flow regime map by Spedding and Nguyen for 4.55cm air/water flows.

C.3v Flow regime map for oil/water flow in a horizontal pipe (Charles).

Appendix D

discrete points are taken. Again, the slope tends to a value of 2.3 and shows how insensitive the routine is to the spacing of the data points.

D.5g The unmodified logistic equation, with feedback factors (R) of 3.85 and 3.90. The slopes of 1/3 and 1 respectively represent the variation in the complexity of the behaviour as R is varied.

D.5h A pseudo-random number generator, given by the following equation; X(N)=100tan(N)-INT.100tan(N), has an embedding dimension of at least 5. A purely random number series would have an ∞ dimensionality, but would require an ∞ amount of data to be analysed.

D.5i A simple series given by the equation; X(N)=sin(N), has a slope of 1, as would be expected, since a plot of X(N) vs X(N+1) is a Lissajous figure, which is a one dimensional line.

D.5j A block diagram of the circuit used to to analyse experimental attractors.

D.5k Circuit designed to realise the above block diagram.

D.5l Sketch of image seen on storage scope for various values of embedding dimension.

D.6a Cylindrical Taylor-Couette cell and basic vortex patterns for (a) inner cylinder rotating, outer cylinder at rest and (a') counter rotating cylinders.

D.6b Flow pattern map for cylindrical Taylor-Couette flow in Reynolds' number space.

D.6c Radial velocity component at $(r_o+r_i)/2$, Re=129.47 with a fluid gap aspect ratio, Γ=4.278 as a function of time , and the reconstructed attractor.

D.6c' Radial velocity component at $(r_o+r_i)/2$, Re=129.47 with a fluid gap aspect ratio, Γ=4.272 as a function of time , and the reconstructed attractor.

D.6d The transition from Couette flow, comparing the Rayleigh criterion (theory - dashed line), the cylindrical system (theory - solid line) and the spherical system (experimental - points).

D.6e Streamlines of the vortices in spherical Couette flow for (a) inner sphere rotating, outer sphere at rest, (b) fast counter rotating spheres and (c) slightly counter rotating spheres.

D.6f Gortler vortices on a concave wall.

D.6g The motion of the earth's atmosphere according to Hadley and (g') a modern representation.

Nomenclature

A_i	Area of pipe covered by phase i
a	Droplet radius
a	Radius of ultrasonic transducer face
a	Air
C	Correlation
c	Correlation
c	Speed of sound
D	Pipe diameter
D	Fractal dimension
D180	Dielectric 180 spark erosion oil
d	Droplet diameter
d	Fractal dimension
F_b	Buoyancy force
f	Frequency
f(θ)	Angular scattering distribution function
G	Superficial mass flow rate
g	Acceleration due to gravity
g	Glass
h_m	Spherical Hankel function of order m
H	Height of convecting system
h	Mean liquid depth in pipe
I	Scattered intensity
i	$(-1)^{1/2}$
J_m	Bessel function of order m
j_m	Spherical Bessel function of order m
K	Thermal diffusivity
k	Gas compressibility
k	Wavenumber
k	Kerosene
M	Embedding dimension
m	Embedding dimension
m'	Mass flow rate
N	Number density of scatterers
N	Number of data points
n	Kinematic viscosity
P_m	Legendre polynomial of order m

P	Acoustic pressure
p	Acoustic pressure
Q	Mass flow rate
R	Radius of pipe
R	Radial coordinate
R	Reynolds number
Re	Reynolds Number
Rx	Receiver
r	Radial coordinate
S	Droplet separation
s	Sand
Tx	Transmitter
t	Time
U	Velocity
U_{is}	Superficial velocity of phase i
V	Particle velocity
We	Weber number
w	Water
w	Mass flow rate
y	radial coordinate in pipe
y_m	Spherical Neumann function of order m
α	Void fraction
α	Coefficient of attenuation
α	Thermal coefficient of expansion
β	Pipe inclination angle
Γ	Aspect ratio
γ	Ratio of specific heats
ε	Stick length or cube side for determining fractal dimension
ε	Pipe roughness
θ	Angle
λ	Wavelength
λ	Liapunov exponent
λ_o	Kolmogorov length
λ	Baker parameter (Appendix C)
μ	Dynamic Viscosity

ρ	Density
σ	Differential scattering cross-section
σ	Surface tension
τ	Time increment
φ	Angle
ψ	Bit resolution in data series
ψ	Baker parameter (Appendix C)
Ω	Angular velocity
ω	Angular frequency

Subscripts

angle	Scattering angle
c	Critical value
cl	Centreline
e	Material inside scatterer
g	Gas
i	Incident
l	Liquid
l	Material outside scatterer
n	Attenuation due to viscosity effects
o	Initial value
o	Attenuation due to continuous phase
s	Scattered
s	Superficial
s	Attenuation due to inertia effects
T	Attenuation due to thermal effects
T	Terminal (velocity)
1	Fluid 1
2	Fluid 2

Superscripts and Operators

'	First derivative with respect to argument or time as specified
'	Material inside droplet
*	Effective (mass)
< >	Mean value

Chapter 1: Introduction: Multiphase Flowmetering In The Oil Industry.

This thesis is concerned with the experimental and theoretical investigation of oil-water mixtures using ultrasonic methods. The emphasis lies with the analysis of ultrasonic waves scattered from the flowing mixture.

To this end it is necessary to define the extent of the problems encountered in this field and to describe the solutions that have been proposed to overcome these problems. A detailed study of the interaction of ultrasonic waves with systems of increasing complexity, starting with single discontinuities and ending with the characterisation of flowing emulsions is then be carried out. The use and application of concepts new to this field, such as chaos theory, are also investigated.

The monitoring and measurement of multiphase flows provides a very large class of problems within the process industries and especially the petrochemical industry. The latter area can be further divided into more specialist subsections, as follows;

1) General multiphase/multicomponent metering.
2) Water in crude oil, fiscal implications.
3) Oil in water, effluent from offshore installations.
4) Sand in oil or gas.

In order to understand the current state of thinking and practices in each of these areas, the following questions can be asked and investigated;

a) What is the nature of the physical problem? Under what circumstances are the flows encountered, including pipe size and geometry? What is the flow rate? What parameters of the flow are required, such as particle sizes, flow rates and flow quality? To what accuracy are these values required and how good are the current methods?

b) What practices and methods are in use at present? What physical principles are being utilised in currently available meters? How big are

the flowmeters as a whole package and can trade-offs be made between required accuracy and necessary cost? What is this cost in terms of money and manpower, including installation costs, running costs and the cost of decommissioning/change-over? In other words, what is the total value of the instrument? Can the reliability of the meters be quantified? What is the market size for each type of meter, who is using them and how many does each use?

c) Are there problems of introducing new technologies such as ultrasonic methods? How accurate or cheap must a new design be, for the markets, either old or new, to use the design? What is the extent of market inertia and how long would it take for a new meter to be accepted? How large could the total market be?

The following sections are the result of discussions with several specialists at BP Britannic House, London, on 27th November 1989 and elsewhere since that date.

1.1 General Multiphase Metering.

It is the aim of this section to outline the main areas of industry where multiphase flow metering is being considered. Also described are the techniques currently available or in development that might be of use in instrumenting these flows. Special reference will be made to the problems encountered in the oil industry, with its solid-liquid-liquid-gas flows, which pose some of the most complex flow problems.

Most areas of the chemical/process industries rely upon single phase measurements of the constituent parts of a multiphase flow before they are mixed, and use correlations thereafterwards. Problems arise when the initial conditions of a flow system are not known very accurately, for example; the output from a mixing device (cement), or when there is a relative slip velocity between the phases (food), or when the phases are reacting with each other and the pipework system (mass and heat transfer reactors).

The physical techniques available for measuring two phase flow parameters, such as quality and flow rates, are listed below along with brief details of the approaches taken by a selection of companies in that area. Further details can be found in the references cited and the trade literature from each company. (Lenn 1987, Furness 1989, Dinham 1989).

(a) Photometric, UV, IR, fibre optic (phase and fraction determination).

Anacon (Instuments) Ltd. IR Absorption methods in development.

Fluid Data (UK) Ltd. Produce single phase IR absorption meters that could be applied to two phase systems.

Photonetics. Near IR refractive index detector, point measurement, in production.

(b) Microwave (phase and fraction determination).

Lee Engineering (Agar Corp.). Absorption methods, and also a multi principle liquid-liquid-gas meter for subsea and land use, including a turbine meter, a separator, two nucleonic meters, temperature and pressure sensors. Accuracy is quoted as ±0.5-2% for the liquids and ±0.5-3% for the gas, depending on their relative concentrations, the errors referring to the whole flow.

Phase Dynamics Inc. An electronic loading method (Yang 1990), in which the amplifier load required to drive a resonant microwave cavity varies sensitively with water cut. With allowances for salinity, temperature and pressure effects, accuracies of better than ±0.035% in water cut have been obtained, when compared with the Dean-Stark distillation method, for water cuts less than 0.5% at a cost of £15k per unit.

Texaco Ltd. For some years, this group have been developing an oil/water/gas subsea meter and its progress is well documented (Dowty 1992 and Dean 1990). It incorporates a gas separator and a microwave water cut monitor and accuracies around 5% in each phase are quoted across the full range of flows and fractions.

SRI International. A design has been patented (Gaisford 1990) which uses the pipe and flow as a resonant waveguide whose resonant frequency is determined by the mean dielectric properties of the flowing mixture. After a measurement of the density, and

allowances for temperature and pressure, the three phases can be quantified.

(c) Capacitive (phase and fraction determination).

Endress & Hauser. In conjunction with BP have developed 'Aquasyst' which is accurate to ±0.05% of the total flow, though allowance must be made for the dielectric constant of the oil (see later). The flow must be homogeneous for this level of accuracy.

Fluenta, amongst several other types of multiphase meter, produce a high precision water in oil monitor with an accuracy of ±0.05% with 5% water, rising to ±0.5% at 80% water. The capacitive meter fails when there is any gas in the flow, though another model is produced that also incorporates a γ ray densitometer for characterising liquid/liquid/gas flows (Fluenta 1991).

(d) Nucleonic (phase, fraction and density determination)

ICI Physics and Radio-isotopes Services. This is a γ-ray bulk density meter, which is essentially a single phase meter, but the principles are being extended to two phase. 400 were sold in the period 1981-1987.

Lee Engineering. See (b) above.

Panatron Radiation Engineering. Here medical radiological methods are being applied to multiphase flows. Novel electret/acoustic technology is also being considered and both are still, at the design study stage

Ramsey Process Controls Ltd. These provide several types of single phase meters based on nucleonic densitometers which they are tentatively marketing in the North Sea.

Ronan Engineering. General nucleonic density metering.

Berthold (UK) Ltd. Single phase metering, but looking at two phase flows.

Norsk Hydro have developed a multi-principle oil/water/gas meter incorporating a static mixer, venturi meter and dual energy gamma densitometers. The mixer allows the meter to work to work to 10% errors in any combination of phases including the usually

difficult elongated bubble and slug flow regimes (Norsk Hydro 1991).

(e) Ultrasonic.

Kent Industrial Measurements. These market a purpose built multi-channel cross correlation multi-phase meter. The device is flow regime specific.

NEL are working with oil-water-gas flows using cross-correlation and attenuation methods, in association with Kent and others.

Panametrics. Single phase technology is being applied to oil, gas and water mixtures for an American oil company, to be published.

(f) Mechanical

Hersey Measurement Co. Inc. work mainly with single phase target meters, but are extending the techniques to two phase.

Micromotion Inc. Are actively developing their coriolis mass flow meters to be used in multiphase flows.

Chemex have marketed their FloComp II automatic well test system. This meter uses the bypass sampling principle, where the gas separates out in a vertical tube and its volume found using a thermodynamic method. The oil and water content is found from the mean density measurement. Though not absolute, the readings require external material properties, the device is very simple in principle (Chemex 1991).

The above are all of the general techniques, though it can be seen that many of the developments are industry specific. The techniques of single phase metering are being applied directly to the considerably more complex multiphase systems, with varying degrees of success.

1.2 Multiphase Fiscal Transfer Metering.

In this special case of multiphase metering, oil is the main fluid and water is the contaminant, in quantities up to 5%. When crude oil is brought ashore, as a combination of oil, water and gas, a 90% Petroleum Revenue Tax is charged. With a barrel of crude being worth approximately $15, small errors in the exact quantity of oil being transferred can

prove very costly for one of the parties. At present, the Karl Fischer titration technique is used to determine the water content of representative samples of the consignment. This involves grabbing samples at a rate proportional to the total flow rate. $1cm^3$ is taken from every $10m^3$, and when the sample contains about 10L, this is further homogenised, and $0.5cm^3$ of this is tested. This amounts to 1 part in 650 million, thus representative sampling and homogenisation are of the utmost importance for the technique to be valid. Problems of slip velocity in partially separated flows, dispersion and distribution must be addressed. A statistical analysis has shown that 10000 samples is enough to be representative of the whole flow.

With the quantities involved, and the real possibilities of large, but short term fluctuations in the flow quality, in future it may prove more practical to continuously monitor the primary samples, rather than resampling as described above.

For pipelines, the transients in the flow are relatively long, whereas in the case of supertankers, most of the water arrives in the first 20 minutes (70% or more by volume). The washing of the tanks at the end of the delivery leads to another large flux of water that must be measured accurately. The device currently available from Endress & Hauser (Aquasyst) utilising capacitance techniques fails at water contents above 40%, and thus cannot measure the first and last stages of a delivery. This is not too significant when the first 20 minutes amounts to only 0.2% of the 36 hours required to empty a tanker, though this does set a limit on the accuracy of the system. Other problems with this technique include the varying material properties of the crude during a delivery.

For example Mexican Isthmus crude could only be bought if an equal amount of low grade Mire crude is also purchased. The delivery proceeds as follows; The Mire is unloaded, 70% water for the first 20 minutes, the Mire tanks are cleaned with Isthmus, the Isthmus tanks are then emptied, and then the whole system is then swilled out. Each of these stages requires independent calibration of the meters for the physical properties of the fluids.

With the current trends in pipeline sharing and the increase in bringing the whole multiphase flow ashore, new measurement techniques are required to monitor precisely what is being pumped into the pipes at the various inlets, both quantity and quality. Other areas of research include microwave and nuclear magnetic resonance meters, and interested parties include Marconi and HiTec (Norway).

A typical sampling station costs £100k, whereas the Endress & Hauser apparatus costs £10k-£15k, leading to the current interest in this method (Miller 1989).

1.3 Multiphase Effluent Metering.

This area can be further divided into two distinct topics, offshore effluent and onshore effluent, each with its own problems. In the first case, £1M of hardware (eg allowances for access, accomodation and safety) is required to keep a man offshore, with 2½ shifts per day, compared with 1½ shifts per day on land and comparatively neglegible housing costs.

The hydrocyclone is now the main type of oil/water separator, however, droplets of 20-30μm diameter or smaller remain in suspension, and there may also be dissolved contaminants. A meter would be required as either a discharge standard monitor or a process control feedback device. An example of both would be a monitor of the output of a sand filter, to determine when the filter needs washing. In many cases, the output liquid is opaque and contains air or gas bubbles that have either degassed from the solution or ingressed through some form of leak. Solids may also be present. At this stage the gas and solid contaminants are generally irrelevant.

The effluent water stream from an offshore installation will typically have a high salt content (10%) and its temperature can vary from 30°C to 120°C, and can lead to salt growths and scale. This is further complicated by dissolved and gaseous CO_2, leading to carbonate scales. Barium and strontium compounds are also present, including their radioactive isotopes.

The oil can vary greatly in viscosity and interfacial tension, leading to corresponding variations in droplet size.

Once out of the ground, the crude undergoes considerable shear at the wellhead choke, which is immediately followed by a heater (to minimise hydrate formation), and the first separator, with its control valves. the resulting droplets can be up to a few mm in diameter, with a mean of between 50 and 100μm. The smallest droplets are of the order 1-2μm, and anything below 30-50μm can get through the primary separator, amounting to 10-300ppm contamination in the wastewater.

This wastewater can be treated with a flocculant additive to enhance the separation. This costs approximately £1000/tonne, and requires considerable storage space, its use should ideally be minimised especially off shore. The process is controlled with intermittent feedback from a standard sampling technique. This comprises just a single aspect of the work of a process control operator. A less involved procedure would prove more reliable, but would not release much manpower.

Further downstream, where several sources of wastewater have been mixed, the system is sampled at least every 12 hours, though more generally the process operators check the effluent three or four times on their rounds during their 12 hour shift. If the supply criteria are known or suspected to be changing, for example when a new well comes into production, the sampling rate is stepped up.

At a more complex station, such as a refinery, the spectrum of contaminants can be much broader than that from a single well, since the quality of the crude from a single well remains almost constant for long periods of time. There can be waxy residues, residual crude and even portions of the refined product and possibly upto 15ppm solids. The fluid contaminants might also include 5000ppm of 3μm droplets as a surge superimposed on the usual 100ppm background contaminants, should a storage tank be cleaned out. Emptying the bottom of storage tanks using pumps induces considerable shear, leading to these small droplets. Also entering into the wastewater system is the rain runoff, which can be contaminated with anything from oil to chemicals to sand.

As for chemical contaminants, spent caustic soda (used to remove sulphites) can cause excursions to pH 8 or 9. The ensuing chemistry can lead to simple soaps and detergents, producing emulsification and aspherical droplets due to modified interfacial effects. One in five samples suffer from these problems and it leads to very inefficient filtering of the contaminants.

Dissolved solids become a problem at concentrations above 100ppm in the effluent stream, though this is much diluted when it reaches the main water course. Culprits include phenols, sulphides, ammonia and phosphates. The latter at 20ppm have recently been seen to cause problems with algae formation. The overall contamination is currently checked using conductivity methods, though generally as alarms rather than for process control. Alternatively, spectral analyses in the infra red can be used on representative samples, with frequencies comparable with those described above. Other light scattering techniques have been found to require considerable maintenance, are not very reliable and are used only as alarms.

The most complex problems are to be found on land at refinery sites, where 16" to 48" storm drains can carry almost any combination of the materials described above, very intermittently.

Thus in conclusion, there are two possible uses for multiphase metering of wastewater systems, the first is a final discharge alarm, which would have to be accurate to ±2-5ppm, to satisfy the National Rivers Authority, and could cost £10k and would sell of order tens per establishment. Anything more than £100k would not be considered. The second would be a process control mechanism, accurate to ±20-30ppm, which could easily sell in the thousands, as no other methods are currently available, and sampling is not practical on the scales involved. To detect 1-2μm droplets would be ideal, though 5-10μm would be quite useful (Chown 1989).

1.4 The detection of sand in liquid or gas flows.

The problems caused by sand appear at the wellhead, where it can seriously interfere with the separation processes, leading to regular cleaning of the separating tanks. The sand also proves to be very destructive to the physical structure because of its abrasive properties.

Typical values for sand production are about 100lbs per day or per 1000 barrels of crude produced, though these figures are very dependent on the current circumstances of the production and also on the past history of the well. Before describing the significance of sand production and how and why it should be monitored and controlled, an overview of the prevailing 'experimental' conditions may be of use.

A typical well in the North Sea stands in 400-600ft of water at 40°F, and at the sea bed, the pipe is 30" in diameter and the oil pressure is about 150psi. 200 feet below the sea bed are the subsurface safety valves. The well then extends through the sea bed to a depth of 5000-15000 feet, where the temperature is 150-350°F and the pressure is 4000-10000psi. The pipe at this point is about 4½" diameter. The bottom of the pipe and the concrete surrounding it are perforated using shaped charges that can penetrate 12" into the surrounding rock formation. In order to enhance the flow of the oil out of the porous medium, several techniques can be employed. One popular method is hydraulic cracking of the rock followed by chemical etching or infilling with Propan polymer® or graded sand. If the well is not naturally flowing, then a secondary recovery technique, such as injecting sea water at the periphery of the field (to force the oil upwards), can be employed (Frances 1989).

The structure of the rock formation at the bottom of the well depends on the physical properties of the rock and also on its age and depth. The perforating gun generates approximately 4 to 8 holes, ½" in diameter per foot of pipe. Thus for a flow rate of up to 40000 barrels per day (in the initial stages of a large well), the flow rate through these small holes will be very high ($\simeq 10 ms^{-1}$). This can loosen particles from the rock formation or from the packing materials. If the flow rate in the riser is not sufficient to carry the particles, then they will settle to the bottom of the pipe and gradually impede the flow.

With a typical platform having 20 wells all feeding into a common separator, it is necessary to know which wells are producing sand so that remedial action can be taken to stop the well blocking, or to at least optimise its oil output versus sand output. One possible method of reducing sand production is to reduce the flow rate through the rock by reperforating the strata. The life of a well can be extended by carefully controlling the oil flow rate from the beginning, increasing the flow rate slowly, allowing the rock to adjust to the new conditions without incurring too much damage. The flow rate is increased to a point where the sand production is considered just acceptable.

The sand can be detected using three different methods, the first being a simple filter (10μm), the second is an impact detector which only works for gas flows and is thus also sensitive to condensates. The third is a differential pressure sensor, one end of which is covered by a thin tube which is eroded by the particles. When the particles break through, an alarm is set off.

With the current cost of platforms, there will be a tendency towards more subsea installations, and horizontal sea bed transport. Horizontal lines are prone to filling , and a weak point can usually be identified. However, a sand detecting meter could remove much of the guess work, but would have to be able to stand temperatures of up to 225^{0}F, be reliable, be calibrated just once, and pose a neglegible risk of leaks.

1.5 Discussions And Conclusions.

The above four sections have briefly described the problems encountered in multiphase and multicomponent metering, and some of the attempts to overcome these problems. The metering of mixtures is a comparatively new subject, and it would seem that tried and tested single phase techniques are being applied to these new situations. From the point of view of numbers sold, devices for metering mixtures total about 5% of the whole flowmetering market (Halsey 1986). However, due to the complexity of the devices, and the savings that can be made if the mixture can be metered directly (rather than by separation followed by single phase metering), the unit price can be considerably higher than for a single phase meter.

Primary metering at the wellhead needs only to be accurate to say 2% for gas and 1% for the liquids, since there is no direct financial penalty for any uncertainty. However, once the materials have been separated, and fiscal transfer is taking place, accuracies in the volumetric metering of ±0.02% (turbine and positive displacement meters calibrated using absolute methods) and in the water content of ±0.02% by volume (titration or distillation) are required. These flowmetering standards have evolved over many years and their revision to accomodate changes in technology is a slow process. It can be concluded (Gold 1986) "that improved measurement accuracy is more likely to be achieved from improved calibration and operating procedures than from the use of different types of flowmeters". This is further reinforced by Halsey (1986), who found that over a large sample of flowmeter users, 55% of meters were over 10 years old, and that only the smaller establishments are quick to take up novel techniques. The metering of hydrocarbons makes up approximately 40% of the whole flowmetering market, making this the largest single industrial use of flowmeters.

It would seem that the areas of general multiphase metering and multiphase fiscal transfer metering provide the largest markets, and this is where most of the effort is being directed. The problems of effluent metering are less well defined and can only become more difficult as the process technologies become more complicated and the legal discharge limits become tighter. Similarly the metering of sand in hydrocarbon flows will prove difficult, as has been seen by the lack of technology in the field.

In principle, all four areas can be approached using several different ultrasonic techniques. The accuracy and applicability of these techniques can only be determined after careful experimental testing, and comparison with the other contenders in the field. In the case of fiscal metering, the device would be competing with the Karl Fischer titration technique, which has become accepted as the standard, so any new technique would have to be very well proven before it was even allowed into the field. Since many of the meters either require or assume homogenised mixtures, it will be to these flows that much of the following work will be addressed.

1.6 Layout of this Work

So far, only oil industry related problems have been covered, however, many other areas of the chemical and process industries also involve the flow of complex media and mixtures.

To show the scope of the problems, figure 1.6a tabulates some of the possible systems that appear in these areas and may be amenable to ultrasonic methods.

The non-invasive or non-destructive testing of each of these systems usually involves the interaction of the system with some sort of waveform, thus;

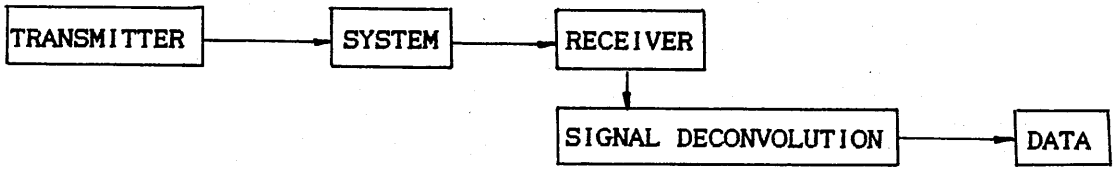

Waveforms that have been used to date include Electromagnetic: Visible, X ray and Gamma ray, Particles: Neutron, Electron and Positron and, of course, all types of mechanical waves.

As has been outlined in the abstract, this work has been a feasibility study of the application of a very specific method to a very general class of problems, namely the ultrasonic interrogation of multicomponent/multiphase flows, with a special reference to liquid in liquid systems.

The information that might be required from a system can be summarised as follows;

		DISCONTINUOUS PHASE		
		Solid	Liquid	Gas
CONTINUOUS PHASE	Solid	Composites Aggregates Laminates Impurities	Fluid inclusions in sedimentary rocks Setting Crystallisation	Internal fractures Bubble entrainment during casting
	Liquid	Sedimentation Elutriation Colloids Suspensions Blood analysis Food processing Wear particles and contaminants in lubrication and hydraulic systems	Emulsions Crude oil settling Water contamination in hydraulic systems Oil Contamination in water systems	Air entrainment Cavitation Boiling
	Gas	Dust/Fallout	Fogs/Mists Aerosols	Mixing processes Sonar balloon detection

Figure 1.6a Table of possible systems where acoustic waves have been used to detect discontinuities.

For a single particle: Position
Velocity
Size
Shape
Composition

For many particles : Spatial Distribution
Velocity Distribution
Size Distribution
Material Properties

An appropriate choice of waveform, for the data range required from the given system will optimise the data acquisition process. A review of the relevant parameters for all the combinations of experimental technique and data required, is far beyond the scope of this work, but they are adequately covered in the literature.

The layout of the rest of this work is now described.

Chapter 2 Is an introductory literature review of the interaction of ultrasonic waves with complex systems, several parts of which will be expanded in detail in later chapters.

Chapter 3 Covers in detail the experimental and theoretical aspects of the multiangle scattering of an ultrasonic wave from a single stationary particle.

Chapter 4 Introduces the problems of back scattering and scattering cross-section and the technique of range gating. This is also extended to cover multiple scattering and the measurement of acoustic velocity and attenuation in mixtures as an alternative method of characterisation.

Chapter 5 Describes larger scale experiments, involving real flowing situations of oil water mixtures, and the use of several ultrasonic techniques to characterise the system.

Chapter 6 Describes the principles of chaotic dynamic systems and how they may be applied to the flow of mixtures. This leads to an improved understanding of the phenomena occurring within the flow and the experimental techniques lead to novel methods of characterising the flow.

Chapter 7 Brings all of the results and conclusions of the previous chapters together and describes where the work can be extended and improved.

This is followed by an alphabetical listing of the **References**.

Appendix A Describes the experimental techniques developed in order to study the scattering of ultrasonic waves from liquid droplets. Several technical difficulties were encountered, and in overcoming them, novel results on the motion of droplets in vertical pipes have been found.

Appendix B Describes the construction and testing of the large scale apparatus.

Appendix C Is a select literature review covering multiphase and multicomponent flows, including flow maps and flow transitions.

Appendix D Is an introduction to chaos as applied to fluid systems, starting from first principles.

Chapter 2: Literature Review: An Overview of the Interaction of Ultrasonic Waves with Complex Systems.

2.1 Introduction

The following sections describe the interaction of ultrasonic waves with complex systems, giving an overview of work that has been carried out and published in the literature, to date. Several of the sections will be expanded in more detail in later chapters.

A general ultrasonic interrogation system has the following form. The ultrasonic signal of a known form interacts with the system in question and the signal is modified by the system in a manner that is characteristic of the system. Useful information will be contained in some or all of the following measurands of the received signal.

- The acoustic velocity
- The attenuation constant
- The angular distribution of the signal
- The Döppler shift
- The phase/transit time of the signal

} and their spatial and temporal variation

Clearly, each measurand will provide different information about the system, either different parameters or if two measurands observe the same parameter, then the quality and quantity of the information will be different.

The interaction of an acoustic wave with a complex system has very many optical analogies, from the simplest reflection and refraction to the more complicated scattering. The work begins with the scattering of a wave from a single sphere. The general problem of the fluid sphere, including longitudinal wave penetration into the body of the sphere, as well as the inpenetrable sphere approximation are considered here. The full theory is derived from first principles in chapter 3. The solid approximation provides a useful comparison with other published works and allows for a greater test of the theoretical predictions in the experiments to be carried out later.

2.2 Single Scatterer

The earliest study of the scattering of waves from spheres dates back to the middle of the nineteenth century with the work of Clebsch (1863) and Strutt (later Rayleigh, 1945 reprint of 1896 work). The early work was carried out in order to explain the scattering of æther waves (later known as electromagnetic radiation) by the atmosphere and dust clouds. This and all the consequent theory is general enough to be applied to any type of scattering, from electromagnetic to acoustic to particle, provided the waveform can be described by simple potential theory. The first century of work in this field has been reviewed by Logan (1965).

All of the early work and many of the modern investigations require the material of the scatterer to be of totally different acoustic properties (namely specific acoustic impedance defined as ρc, where ρ is the density of the medium and c is the speed of sound in the medium) so that the wave does not enter the body of the scatterer. The methods of this analysis have been covered elsewhere (Lenn 1985), and will appear as an approximation to the full derivation in chapter 3.

Clearly, as the physical properties of the scatterer approach those of the surrounding medium, the scatterer will become acoustically invisible, with the amplitude of the scattered wave approaching zero. The table below contains the relevant data for a few of the materials of interest to the project in general.

Material	Density	Speed of Sound	Acoustic Impedance
	ρ/kgm^{-3}	c/ms^{-1}	ρc/Rayls (SI)
Water	1000	1500	1 500 000
Kerosene	810	1324	1 072 440
Air (RTP)	1.2	330	396
Sand	2130	5750	12 247 500
Steel	5900	7800	46 020 000
Erythrocyte	1180	2730	3 221 400

Figure 2.2a Table of some material properties.

Thus it can be seen that the materials chosen for this project, water and kerosene (mimicking the properties of light North Sea crude), are acoustically very similar. Later this will set limits on the approximations that can be made in the theory.

2.3 General Theory

The theory for liquid in liquid scattering was first calculated by Anderson (1950), and is an extension of the works by Rayleigh (Strutt 1894) and Stenzel (1938) taking into account the effects of the wave that enters the scatterer and the fact that the interface between the scatterer and the surrounding medium is flexible. The derivation is such that allowing the various parameters to tend to extremes, reduces the final equation to that of the solid scatterer again. Throughout this work, the approriate form of the equations will be used, except where comparisons are being made between the various approximations. The route taken is the classical method of solving the Greens Equation for the outside, inside and the interface of the scatterer, ie potential theory. The mathematics has been described in the literature (Anderson 1950) and (Morse 1953, 1968), and will be covered in detail in chapter 3. Only the final results will be given here.

Consider figure 2.3a. For a continuous medium of density ρ and speed of sound c, containing a spherical liquid scatterer of radius 'a', density ρ_e and speed of sound c_e, let a plane longitudinal wave of wavenumber k $= 2\pi/\lambda$ and intensity $I = p^2/\rho c$, where λ is the wavelength and p is the pressure of the wave, incident on the sphere from the left.

For the above geometry in a spherical polar coordinate system, the pressure of the scattered wave is given by the following equation for a scatterer of arbitrary material, including solid, liquid and gas.

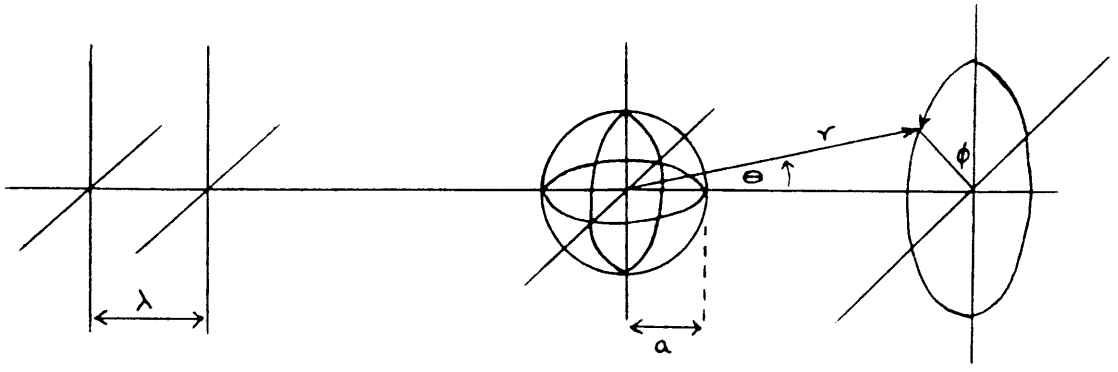

Figure 2.3a Coordinate system for a single scatterer

$$p(r,\theta)=A\sum_{m=0}^{\infty}(2m+1)i^m P_m(\cos\theta)\left[j_m(kr)-\frac{j_m'(ka)-\dfrac{\rho c\, j_m'(k_e a)}{\rho_e c_e\, j_m(k_e a)}\, j_m(ka)}{h_m'(ka)-\dfrac{\rho c\, j_m'(k_e a)}{\rho_e c_e\, j_m(k_e a)}\, h_m(ka)}\right]h_m(kr)$$

Incident Wave

Scattered Wave — Allowing for the material properties of the system and small amplitude internal and surface waves.

Range Effects

(2.3.1)

Where: A = The amplitude of the wave

P_m = m^{th} order Legendre polynomial.

j_m = m^{th} order Spherical Bessel function.

j_m' = The differential of j_m with respect to its argument.

h_m = m^{th} order Spherical Hankel function

h_m' = The differential of h_m with respect to its argument.

2.4 Approximations to the General Theory

As mentioned above, letting $\rho_e c_e \gg \rho c$ reduces the above equation to:

$$p(r,\theta) = A\sum_{m=0}^{\infty}(2m+1)\, i^m\, P_m(\cos\theta)\left[j_m(kr)-\frac{j_m'(ka)}{h_m'(ka)}\right]h_m(kr) \qquad (2.4.1)$$

This will be referred to as the solid approximation when used elsewhere in this work. The mathematics used to derive the above equations is totally general as to the value of ka and $k_e a$, however, a few useful approximations can be derived from the above equations when the $ka \ll 1$ and when $ka \gg 1$. The first case corresponds to the classical Rayleigh/Tyndall

(blue sky) scattering and the second case to the geometric shadow equation (Urick 1965).

In terms of intensities, $I=p^2/\rho c$, with I_o being the incident intensity;

$$ka\ll 1: \quad I(r,\theta) = \frac{16\pi^4 a^6 I_o}{9\lambda^4 r^2}\left(1 - \frac{3\cos\theta}{2}\right) \qquad (2.4.2)$$

$$ka\gg 1: \quad I(r,\theta) = I_o\left[\frac{a^2}{4r^2} + \frac{a^2}{4r^2}\cot^2(\theta/2)\right]J_1^2(ka\sin\theta) \qquad (2.4.3)$$

For $ka\simeq 1$, ie the wavelength is comparable with the circumference of the scatterer, the scattered pressure (or amplitude) is seen to oscillate about the value given by the equation for $ka\gg 1$ (figure 2.4a)

2.5 Scattering Cross-Section

The phenomena of scattering over the whole range of ka is best conceptualised in terms of the differential scattering cross section. The scattering cross section is defined as:

$$\sigma(r,\theta) \propto |p(r,\theta)|^2 \qquad (2.5.1)$$

The proportionality becomes an equality when the incident beam has unit intensity and the receiver subtends a unit solid angle at the scatterer and is unit distance from the scatterer. Thus σ has units of area. The real cross-section is simply given by πa^2. Thus the ratio of $\sigma/\pi a^2$ will give a measure of the effectiveness of the scatterer. Note that σ is a function of θ and r, so the effectiveness of the scatterer depends upon the angle from which it is observed. The total cross section is found by integrating σ over a solid angle of 4π steradians. From now onwards, unless explicitly stated otherwise, σ will refer to σ_{180}, ie the backscattered cross section. The references given above all evaluate σ, and also allow ka to tend to the extremes described previously.

For a solid scatterer, the end result is shown graphically in figure 2.5a. Note that in this and subsequent plots, as ka becomes large, the

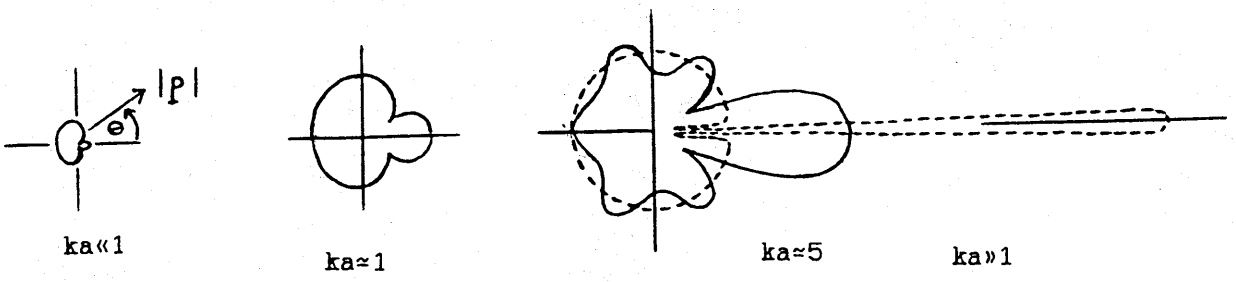

Figure 2.4a Scattering profiles for various ka

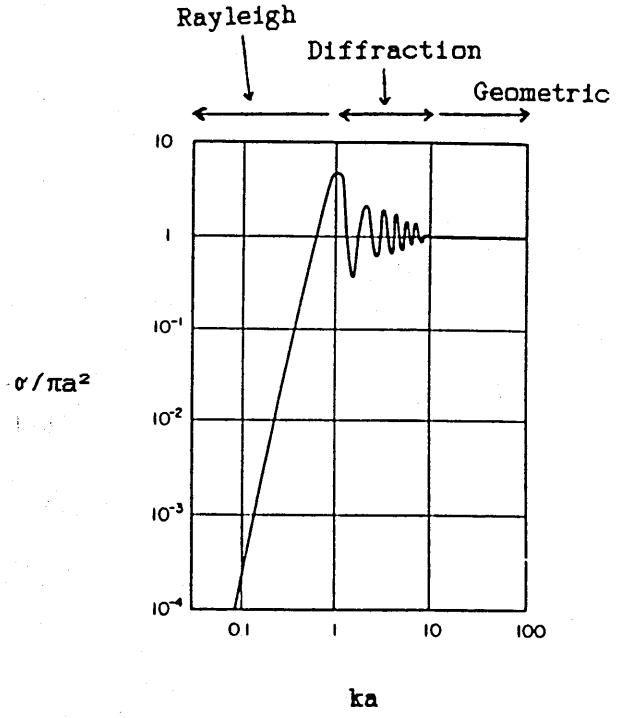

Figure 2.5a Scattering cross-section for a solid sphere

differential scattering cross-section tends towards unity, showing that the scatterer appears to be its real geometrical size.

The diffraction can be considered as the result of the combination of several effects, the most important of which (for a solid scatterer) is the "creeping" wave which moves around the interface between the scatterer and the surrounding medium (Gaunaurd 1985, has covered the theory and Faure 1977, has observed the effect experimentally).

In the case of gaseous and liquid scatterers, the problem becomes more complicated, primarily because of the flexibility of the interface separating the two media. In the case of a liquid scatterer, the wave that enters the sphere undergoes multiple internal reflections and is then re-radiated from the surface, the whole effect tending to reduce the scattering cross section, and provide more complicated interference patterns around ka≈1. It would be expected that a sphere with the same material properties as the surrounding medium (ie $\rho=\rho_e$ and $c=c_e$) would have no effect on the acoustic wave.

The effect of changing from a solid to a fluid scatterer is sketched in figure 2.5b.

However, in the case of a gaseous scatterer, a most significant effect arises, namely; resonance. The compressibility of a gas means that in an acoustic field, the bubble behaves as a classical Helmholtz resonator. When the frequency of the field is identical (see below) to that of one of the partial waves that fit into the resonator, the bubble hits resonance and the motion of its surface becomes extreme. For a gas bubble in a liquid, the most important mode is the monopole, rather than the dipole or any of the other higher order possibilities as sketched in figure 2.5c.

The damping of the motion (thus avoiding the unrealistic and highly embarrassing infinities) is provided by the viscosities of the two media and the thermal properties of the gas (Gaunaurd 1981, Khabeev 1986, Seybert 1988 and Urick 1965).

The frequency of the monopole resonance is given by (Pierce 1981):

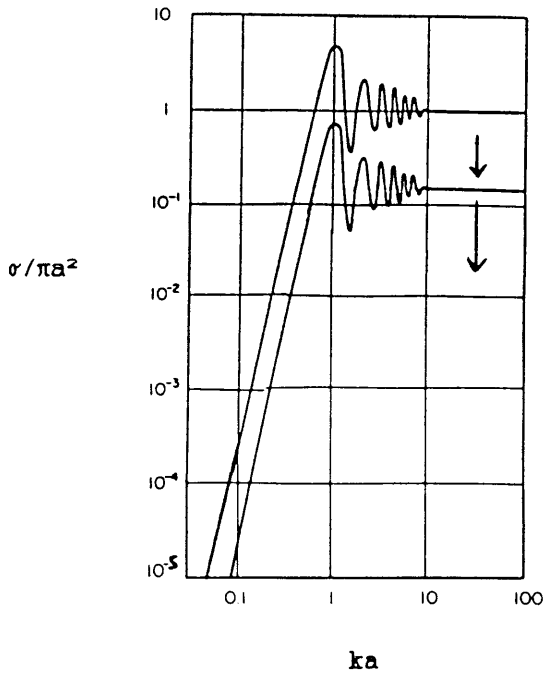

Figure 2.5b. Comparison of scattering cross section for solid and liquid spheres.

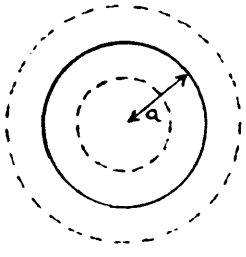

Monopole

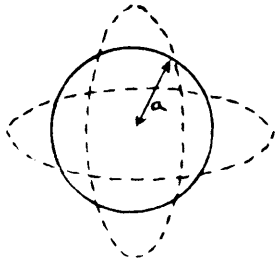

Dipole

Figure 2.5c Gas bubble resonances.

$$f = \frac{\rho^{-1/2}}{2\pi a}\left[3\,\rho_e c_e^2 + \frac{2\gamma\sigma}{a} - \frac{2\sigma}{a}\right]^{1/2} \qquad (2.5.2)$$

Where γ is the ratio of the specific heats of the gas and σ here is the interfacial tension. Taking this into account produces a scattering cross-section as shown in figure 2.5d.

Resonances are not just confined to gaseous scatterers in liquids, but can also be found in other combinations of phases. The variation in cross-section at resonance, and the sharpness of the resonance spike due to the physical properties of the two media (liquids and solids) high density and low compressibility, mean that resonances will be less significant in the flow regimes (confined pipe flow) to be considered later (Brill 1987, Flax 1978, and the five papers by Gaunaurd 1979-1982). Resonances would be expected to appear as spikes on scattering cross-section plots sketched in figure 2.5e.

Note that the scattering cross section of a resonating bubble is a few orders of magnitude greater than its geometric cross section. This means that in a system containing a random distribution of bubbles, a few resonating bubbles will produce a scattered signal greater than that from all the non-resonating bubbles combined. This phenomenon has been utilised experimentally (Medwin 1977).

So far, the only incident waves that have been considered have been longitudinal waves, the only waves that can propagate in the body of a liquid. However when a solid is involved in the system, either as the continuous or discontinuous phase, the possibility of transverse waves also occurs. The whole problem, including conversion between the waveforms and the inclusion of resonances (Gaunaurd 1979) requires a complicated matrix (tensor) approach, but has proved most useful in the elucidation of nuclear scattering from the "liquid drop model" and the "shell model" of the nucleus.

A recent paper (Seybert 1988) has shown that a resonating gas bubble has its motion severely restricted by any rigid boundaries, to the point where resonance is suppressed if the wall is less than 1000a from the bubble. Thus the problem of a few resonating gas bubbles totally masking

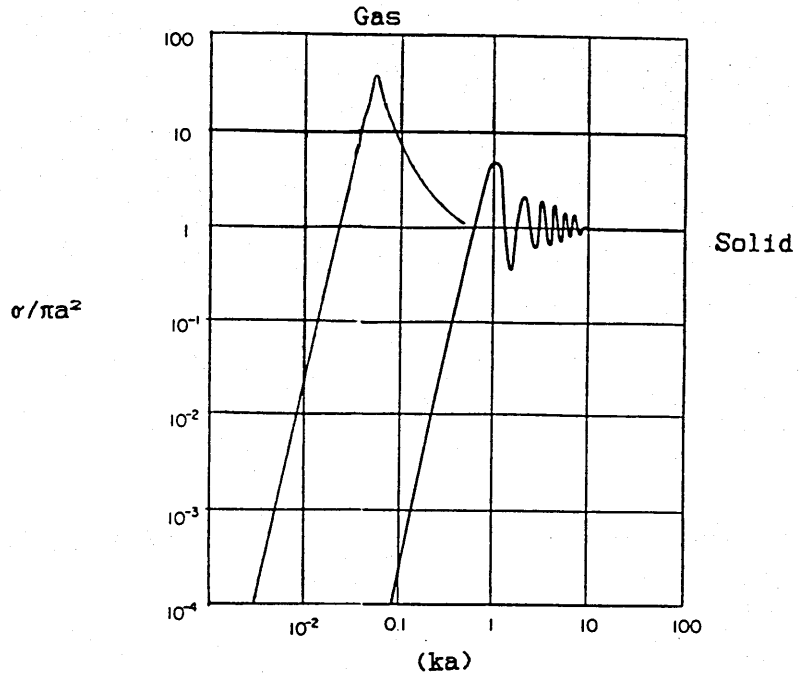

Figure 2.5d. Scattering cross-section of a resonating gas bubble, compared to a solid particle

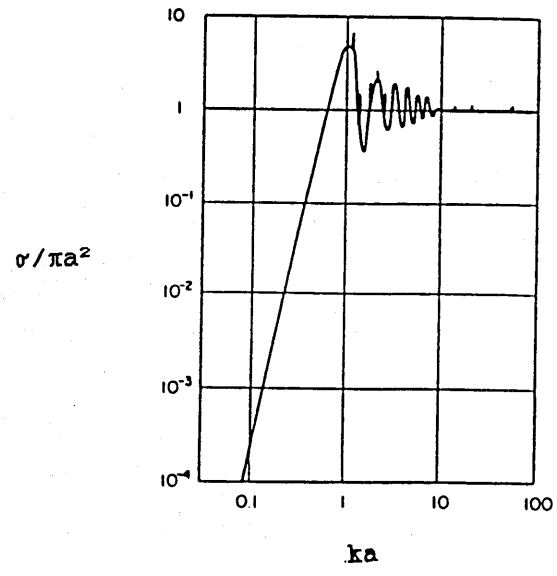

Figure 2.5e Scatering cross-section of a solid sphere, including resonances.

the signal from other scatterers of interest might not occur in the pipe flows under consideration.

2.6 Other Effects of the Material Properties of the Scatterer

The simple potential theory used to derive the equations for the scattering from solids and liquids takes only the density and acoustic velocity into account. Other physical properties such as compessibility can be taken into account (Rayleigh 1944 and Urick 1965). When ka«1 there is also the possibility of the scatterer becoming involved with the bulk motion of the surrounding medium due to the acoustic wave motion. Taking these two effects into account, in the ka«1 limit, changes the equation given previously as (2.4.2),

$$I(r,\theta) = \frac{16\pi^4 a^6 I_o}{9\lambda^4 r^2}\left[1 + \frac{3\cos\theta}{2}\right]$$

to a modified form:

$$I(r,\theta) = \frac{16\pi^4 a^6 I_o}{9\lambda^4 r^2}\left[1 - \frac{K_e}{K} - \frac{3(\rho_e/\rho - 1)}{1 - 2\rho_e/\rho}\cos\theta\right] \qquad (2.6.1)$$

Where K_e is the compressibility of the material of the scatterer and K is the compressibility of the surrounding medium. These effects become minimal for large ka. Figure 2.6a shows plots of this correction factor (for small ka) for various values of the other parameters (Urick 1965).

Generally, in most of the cases likely to be encountered experimentally, the scattered pressures, intensities and cross sections are slightly reduced for solid and liquid scatterers and increased for gaseous scatterers when compared with the simple potential theory.

2.7 Aspherical Scatterers.

So far the scatterer has been spherical in shape. It would be expected that non-spherical scatterers would have a different effect on the

$$\frac{\left[1 - \frac{K_e}{K} - \frac{3(\rho_e/\rho - 1)}{1 - 2\rho_e/\rho}\cos\theta\right]}{\left[1 - \frac{3\cos\theta}{2}\right]}$$

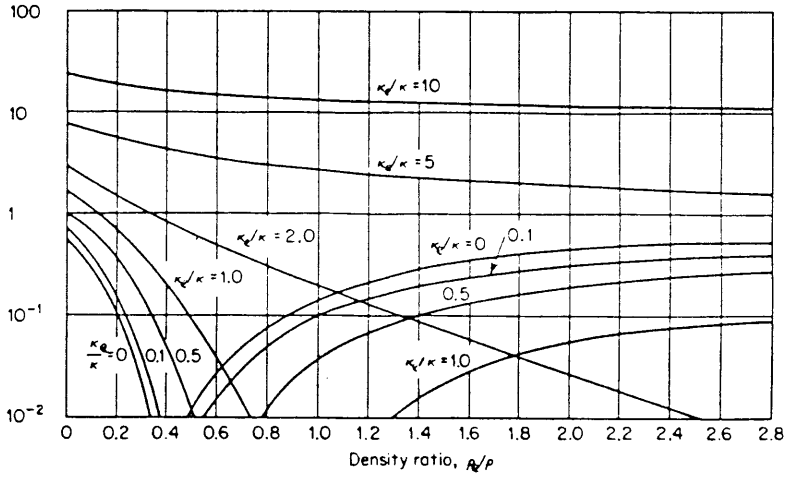

Figure 2.6a. Variation of scattering with material properties (Urick 1965)

acoustic wave. In the first approximation, all scatterers are spherical, but it is necessary to know when this approximation becomes invalid. This problem has been tackled both theoretically (Ahuja 1978, 1979) and experimentally (Sheng 1988). For minor deviations from sphericity, as expected, the spherical approximation remains valid provided the deviations are less than a wavelength from the equivalent spherical radius. When the approximation does break down, it also usually involves a non-homogeneous scatterer eg fish (Foote 1979 and Haslet 1979) or submarines (Urick 1965).

As a final note, now that the theory of scattering has been covered for all three types of discontinuous phase for all values of ka, it is worth noting that acoustic waves are also scattered by the density variations that occur during turbulent flow (Morse 1968 and Korman 1988). This is clearly a non-linear effect, and is a function of Mach number (Lynnworth 1981). As this is essentially scattering from a distribution of turbulent eddies, a simplistic view would be to consider the density fluctuations within the eddy as the primary cause of the scattering and so this scattering would be expected to be a few orders of magnitude smaller than the scattering from a droplet of the same size.

The significance of these results will be discussed in detail as necessary in chapter 3.

2.8 Effects of a Scatterer's Motion.

So far the problem has been concerned with the scattering of a plane ultrasonic wave from a stationary object. If the object is moving then the scattered signal will have a Döppler shift in frequency. For the co-ordinate system shown in figure 2.8a, the frequency shift is given by;

$$\Delta f = \frac{fV}{c}\{\cos\theta\cos\alpha + \sin\alpha\sin\theta\cos\varphi - \cos\theta\} + \text{terms } O(fV^2/c) \qquad (2.8.1)$$

The scattered pressure and intensity profiles will remain as described for the stationary particle.

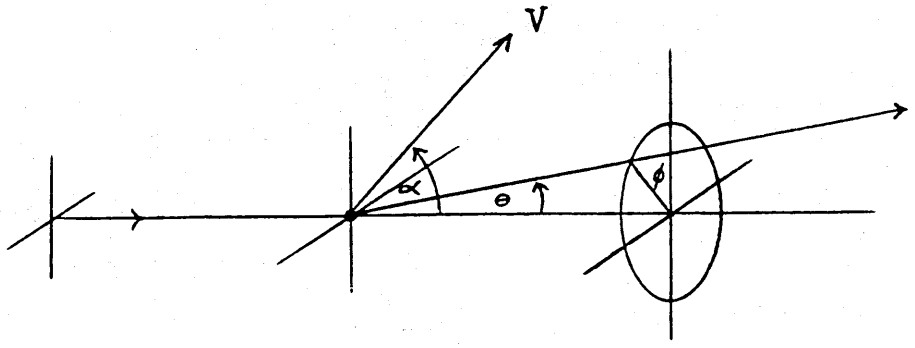

Figure 2.8a Co-ordinate system for Döppler scattering.

2.9 Many Scatterers

The previous sections have considered scattering from just a single particle. However, a simple order of magnitude calculation reveals that in most of the experimental circumstances described in the introduction, the chances of there being just one scatterer in the beam path are minimal. Thus it is necessary to work out what happens when there are several particles simultaneously scattering the ultrasonic wave.

There are two distinct approaches to this problem; to sum over the individual scatterers to give the bulk properties, or to look at the system as a whole and determine the bulk properties as a function of the properties of the two phases. Clearly, both methods should be equivalent, and should predict the same results. However, due to the mathematics involved, the first approach is usually applied when $ka \gg 1$ and the second method when $ka \ll 1$. Each approach gives details of the secondary phase, including void fraction and droplet size distribution.

The two sections below will describe the results of each method in turn.

2.10 Summing Over the Individual Scatterers

The scatterers will have a random size distribution and (chapter 5) a random spatial distribution which are unknown and which are required to be determined. It has been shown (Morse 1953, 1968 and Lenn 1985) that under these criteria, with a Gaussian randomness, that the scattering is predominantly incoherent (ie a random distribution of the phases of each scattered wave at the receiver) and proportional to the first power of the number density of the scatterers N and the average scattering cross-section of the scatterers. Reducing the randomness of the spatial distribution and of the size distribution, in the limit produces an ordered structure of scatterers which scatters a totally coherent wave (eg X ray crystallography) in which the scattered signal is proportional to $N^2\sigma$.

Thus if N(a), the size distribution per unit volume, is assumed Gaussian and $\langle\sigma(a)\rangle$ could be calculated from this, then taking the scattered signal of the form $N^{x}\sigma$, deviations of x from 1 would give more information as to what the size distribution really is.

As for the spatial distribution, this can be determined independently of the size distribution using range gating methods on the scattered signal. The resolution of this method is limited only by the wavelength of the ultrasonic wave.

2.11 Multiple Scattering.

The next problem is what happens when the scattered wave from one scatterer impinges on the other scatterers? This is commonly known as multiple scattering. For a system with dispersed phase fraction α the particles will be separated, on average, by $1.61\alpha^{-1/3}\langle a\rangle$.This is derived from a cubic approximation (figure 2.11a), where $\langle a\rangle$ is the average radius of the particle. The table below (figure 2.11b) gives a few values of this function.

α	Separation/$\langle a\rangle$
0.0001	35
0.001	16
0.01	7.5
0.1	3.5
0.5	2.0

Figure 2.11b Table of particle separation as function of void fraction.

Clearly the simple cubic model breaks down for $\alpha \simeq 50\%$, but other phenomena such as phase inversion occur around this point anyway (see appendices B and C).

Multiple scattering would be expected to produce deviations from the linear function (scattered signal proportional to $N\sigma$), described above. This has been observed experimentally, for $\alpha > 0.1$, in the transport of solids in liquid (Balachandran 1980, 1981 and Jansen 1978, 1979, 1981).

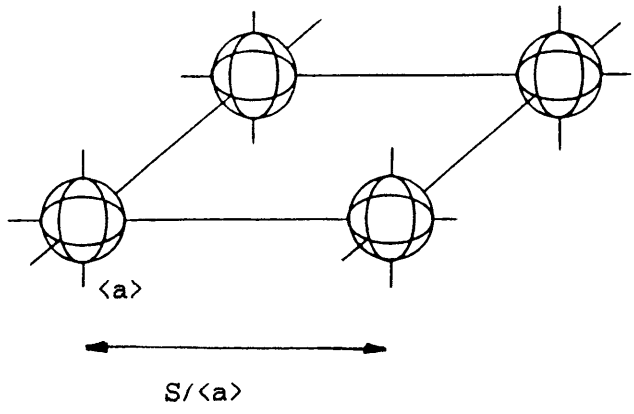

Figure 2.11a. Cubic approximation used to determine particle separation.

There is no exact theory for the multiple scattering problem, with the numerical results always being highly dependent on the approximations made in the definition of the properties of the system. Theoretically, the multiple scattering should lead to the same conclusions as summing over the individual scatterers for the same system. As such, it is beyond the scope of the present work, and will only be entered into when and if it becomes necessary to produce a more accurate solution to the problem (Ma 1983, Twersky 1988 and Tsang 1982). Clearly if the scattering is weak, then effects of multiple scattering will be negligible (see section 4.7).

2.12 Bulk Effects in the Long Wavelength Limit.

In the long wavelength limit, $ka \gg 1$, the scattering from the individual particles becomes very small as described above, dropping off as λ^{-4} (equation 2.4.2) The effect of the single scatterer can be neglected. This phenomenon has been utilised in the selective investigation of suspended materials by choosing the wavelength to ignore silt but to interact strongly with sediment (Lenn 1985 and Jansen 1978, 1979, 1981). However, if all the particles are small, then the combined effect is not neglegible, and the wave "feels" bulk properties characteristic of the mixture rather than those of the individual components. The bulk acoustic properties of the medium are simply the speed of sound (or the acoustic impedance with its implicit density term) and the attenuation constant, and this is the order in which they will be treated below.

2.13 Acoustic Velocity

The speed of sound of an emulsion or suspension was given by (Stakutis 1955);

$$c_2 = \frac{c}{[\{1-(1-\rho_e/\rho)\alpha\}\{1-\alpha+K_e\alpha/K\}]^{1/2}} \qquad (2.13.1)$$

Where all of the symbols have their usual meanings. This equation was seen to have several shortcomings especially for extreme values of α. On

checking with the original (Herzfeld 1930) a typographic error was found, which has been corrected in (2.13.1). An alternative equation derived using full thermodynamic principles for liquid-gas, solid-gas and liquid-vapour systems (Griggs 1982) is as follows.

$$c_2 = \frac{c}{\{[\alpha+(1-\alpha)\rho/\rho_e][\alpha c^2/c_e^2+(1-\alpha)\rho_e/\rho]\}^{1/2}} \qquad (2.13.2)$$

Data for several liquid-gas combinations has been plotted by Griggs, and figure 2.13a is typical of the form of the results

This equation has the same form as the erroneous Stakutis equation for the acoustic velocity in solid-liquid mixtures. As no equation governing the speed of sound in liquid-liquid mixtures has been traced, it would be logical to assume an equation of a similar form.

This conclusion is backed by other work (Piotrowska 1971), which, besides showing the complex nature of this problem (the velocity of sound in an aqueous suspension being highly dependent on whether the solid is organic or inorganic!) reveals the following graph (figure 2.13b) for the experimentally determined acoustic velocity in silicone oil/water emulsions (stabilised with an emulsifier).

2.14 Wave Attenuation.

The attenuation of the waveform is governed by the equation;

$$I(x) = I_o e^{-2\alpha x} \qquad (2.14.1)$$

Where x is the distance from a reference point and α is the attenuation coefficient. The calculation of α for a pure liquid is reasonably straight forward, involving just the thermal and viscous properties, and can be found in any text book (Wood 1946 and Morse 1953,1968). Clearly for a constant physical geometry (see experimental details in chapters 3 and 4) the effect of attenuation will be a constant scaling multiplier throughout a series of experiments, and when ratios are taken, the effect is eliminated.

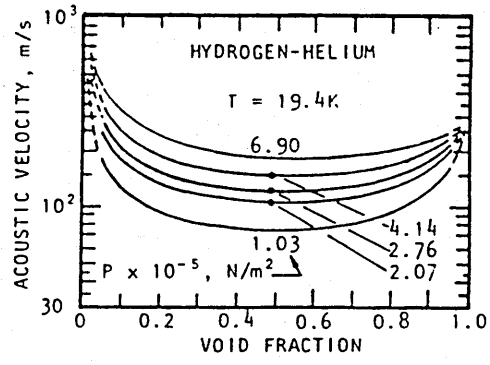

Figure 2.13a. Acoustic velocity for various void fractions of a gas-liquid mixture (Griggs 1982).

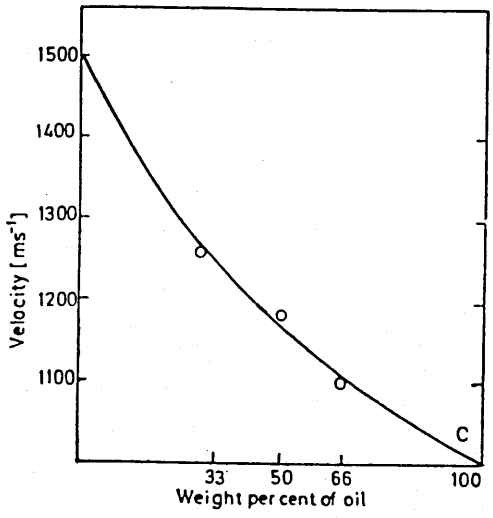

Figure 2.13b. Acoustic velocity for various void fractions of a liquid-liquid emulsion (Piotrowska 1971).

The earliest work on attenuation in a solids suspension were carried out by Epstein (1941) and forms the basis of most modern treatments which extend this to emulsions (Allegra 1972 and Kol'tsova 1974). Generally the attenuation coefficient can be considered as the sum of several parts, thus:

$$\alpha = \alpha_o + \Delta\alpha = \alpha_o + \alpha_s + \alpha_n + \alpha_T \qquad (2.14.2)$$

Where; α_o is the attenuation coefficient of the continuous phase
α_s allows for the inertia of the two liquids at the interface
α_n allows for the viscosities of the two phases
α_T allows for the thermal properties of the two phases

α_s can be subdivided into two further terms, $(\alpha_s)_I$ and $(\alpha_s)_{II}$, the first allows for the scattering caused by the different compressibilities of the two phases and the second allowing for the differences in shear and bulk viscosities between the two phases.

The significance of each of these terms has been found for a stabilised linseed oil emulsion (α=10%) with a mean droplet size of 2μm (Kol'tsova 1974) and are reproduced in figure 2.14a, below;

Type Of Loss / %	λ / MHz				
	3	9	15	21	27
$\Delta\alpha$	100	100	100	100	100
$(\alpha_s)_I$	0	0.4	1	2	3
$(\alpha_s)_{II}$	5	20.6	36	50	60
α_n	11	9	7	6	4
α_T	84	70	56	42	33

Figure 2.14a. Table of relative contributions to the attenuation constant as a function of frequency (Kol'tsova 1974)

$\Delta\alpha$ has been found experimentally for natural oil emulsions (olive, linseed and castor) for $\langle a\rangle=6\mu m$ and is found to be linearly dependent on concentration up to 10% void fraction, for a given frequency, provided that $k\langle a\rangle \ll 1$. As the frequency is increased, a few of the droplets approach $ka \approx 1$ (those at the tail end of the size distribution) and so begin to scatter strongly, thus making the relation $\Delta\alpha$ proportional to Nf^2 outside the error limits, although $Nf^{1.9}$ has been mentioned (Kol'tsova 1974) as a better approximation.

2.15 Phase Shifts.

As a final note, recent experiments (Shiokawa 1986) have revealed that when an ultrasonic wave passes through a suspension of polymethyl methacrylate spheres (mimicing living cells), the phase of the wave is modulated. The phase shifts are dependent on the size (distribution) of the particles and the void fraction, and are linear in the $ka \ll 1$ limits for a void fraction upto 1%. The phase shift produced by a single particle depends on its size and is of the order 10^{-6} degrees.

2.16 Conclusions.

This concludes the review of the interactions of an ultrasonic wave with a discontinuity in a fluid medium, with especial reference to liquid in liquid systems. The theoretical results outlined here will be expanded in an appropriate manner in the next three chapters where they will be investigated experimentally.

Chapter 3: Ultrasonic Scattering from a Single Particle.

3.1 Introduction

In contrast to the previous sections, this chapter will begin with a detailed account of the general theory of the scattering of ultrasonic waves from fluid spheres, followed by the solid and other approximations. This will be followed by appropriate experimental work, designed to investigate and verify the basic theory.

3.2 Theoretical Treatment.

It is clear that the wave scattered from an object will be dependent on several possible variables, which can be grouped as follows;

(i) The properties of the initial incident wave, profile and intensity,

(ii) The difference in material properties of the media inside and outside the scatterer, primarily acoustic impedance, the product of density and acoustic velocity,

(iii) Some function of the position of the observer with respect to the scatterer or the coordinate system.

The following analysis follows that given by Anderson (1950), an alternative approach, using the full Green's equation can be found elsewhere (Morse 1953, 1968)).

Consider a sphere of radius 'a' and acoustic impedance $\rho_s c_s$ surrounded by a medium of acoustic impedance ρc. The centre of the sphere is at the origin of a spherical polar coordinate system, a continuous (sine) wave of angular frequency ω, of infinite extent and unit intensity impinges upon the sphere. The symmetry of the system about the origin, chosen in this way, removes any dependence on φ from the equations (figure 2.3a). This wave of pressure p_o $(=(\rho c I)^{1/2})$ gives rise to an internal wave p_s and a wave, p, emanating spherically from the scatterer. The far field value of p is required to be found. At the surface of the sphere (r=a), both the pressure and the normal

component of the fluid velocities must be continuous. Thus for the acoustic pressure;

$$p(a) + p_o(a) = p_e(a) \tag{3.2.1}$$

and for the radial component of the fluid velocity;

$$u_r(a) + u_{o,r}(a) = u_{e,r}(a) \tag{3.2.2}$$

The acoustic pressure must also satisfy the wave equation;

$$\nabla^2 p = \frac{1}{c^2}\frac{\delta^2 p}{\delta t^2} \tag{3.2.3}$$

Where ∇^2 is the Laplacian in spherical polar coordinates;

$$\nabla^2 p = \frac{1}{r^2}\frac{\delta}{\delta r}\left[r^2\frac{\delta p}{\delta r}\right] + \frac{1}{r^2\sin\theta}\cdot\frac{\delta}{\delta\theta}\left[\sin\theta\frac{\delta p}{\delta\theta}\right] + \frac{1}{r^2\sin^2\theta}\frac{\delta^2 p}{\delta\varphi^2} \tag{3.2.4}$$

With the axial symmetry described above, the general solution to (3.2.3) has the following form (Morse 1968);

$$p = \sum_{m=0}^{\infty} A_m P_m(\mu)\begin{bmatrix} j_m(kr) \\ \\ y_m(kr) \end{bmatrix} e^{-i\omega t} \tag{3.2.5}$$

Where P_m is the Legendre function, $\mu=\cos\theta$, j_m is the spherical Bessel function and y_m is the spherical Neumann function. For $r<a$, terms in y_m cannot be allowed if the solution is to be finite and realistic at the origin, leaving;

$$p_e = \sum_{m=0}^{\infty} B_m P_m(\mu) j_m(k_e r) e^{-i\omega t} \tag{3.2.6}$$

However, outside the sphere, $r>a$, no such restriction exists and the general solution is of the form;

$$p = \sum_{m=0}^{\infty} A_m P_m(\mu)[j_m(kr) + iy_m(kr)]e^{-i\omega t} \qquad (3.2.7)$$

The exact equation for the incident plane wave has the same form as above, with known values for the constant A_m, thus;

$$p_o = (\rho c I)^{1/2} \sum_{m=0}^{\infty} (-i)^m(2m+1)P_m(\mu)j_m(kr)e^{-i\omega t} \qquad (3.2.8)$$

The radial component of the fluid velocity is given by the following equation, for any part of the system;

$$u_r = \frac{-i}{\rho c}\frac{\delta(p)}{\delta(kr)} \qquad (3.2.9)$$

Combining (3.2.6) to (3.2.8) in (3.2.9) leaves the three elements of the velocity as;

$$u_r = \frac{-i}{\rho c}\sum_{m=0}^{\infty}\frac{A_m}{2m+1}P_m(\mu)[\alpha_m(kr) + i\beta_m(kr)]e^{-i\omega t} \qquad (3.2.10)$$

$$u_{o,r} = \frac{-i(\rho c I)^{1/2}}{\rho c}\sum_{m=0}^{\infty}(-i)^m P_m(\mu)\alpha_m(kr)e^{-i\omega t} \qquad (3.2.11)$$

and,

$$u_{e,r} = \frac{-i}{\rho_e c_e}\sum_{m=0}^{\infty}\frac{B_m}{2m+1}P_m(\mu)\alpha_m(k_e r)e^{-i\omega t} \qquad (3.2.12)$$

where;

$$\alpha_m(kr) = (2m+1)j_m'(kr) \qquad (3.2.13)$$

and,

$$\beta_m(kr) = (2m+1)y_m'(kr) \qquad (3.2.14)$$

Where the prime indicates differentiation with respect to the argument.

Substituting the general equations (3.2.6) to (3.2.8) and (3.2.10) to (3.2.12) into the boundary conditions at the surface of the sphere (3.2.1) and (3.2.2) respectively, leaves two equations in two unknowns, A_m and B_m, which can be solved simultaneously, to give ;

$$A_m = -(\rho c I)^{1/2}(-i)^m \frac{(2m+1)}{1+iC_m} \qquad (3.2.15)$$

Where;

$$C_m = \left[\frac{\alpha_m(k_e a)\, y_m(ka) - \beta_m(ka) \cdot \frac{\rho_e c_e}{\rho c}}{\alpha_m(ka)\, j_m(k_e a)} \right] \Bigg/ \left[\frac{\alpha_m(k_e a)\, j_m(ka) - \frac{\rho_e c_e}{\rho c}}{\alpha_m(ka)\, j_m(k_e a)} \right] \qquad (3.2.16)$$

Hence the pressure at any point ouside the sphere can be found using (3.2.7);

$$p = -(\rho c I)^{1/2} \sum_{m=0}^{\infty} (-i)^m \frac{(2m+1)}{1+iC_m} P_m(\mu)[j_m(kr) + iy_m(kr)]e^{-i\omega t} \qquad (3.2.17)$$

To rearrange this into the more usual format, substitutions are made for C_m, α_m and β_m and it is noted that the spherical Hankel function is given by;

$$h_m(kr) = j_m(kr) + iy_m(kr) \qquad (3.2.18)$$

This leaves, with the term $e^{-i\omega t}$ understood;

$$p = (\rho cI)^{1/2} \sum_{m=0}^{\infty} (2m+1)(-i)^m P_m(\cos\theta) \left[\frac{j_m'(ka) - \dfrac{\rho c\, j_m'(k_e a)}{\rho_e c_e\, j_m(k_e a)}\, j_m(ka)}{h_m'(ka) - \dfrac{\rho c\, j_m'(k_e a)}{\rho_e c_e\, j_m(k_e a)}\, h_m(ka)} \right] h_m(kr)$$

(3.2.19)

In the case of the far field, $kr \gg 1$, the above expression can be simplified by noting that (Lenn 1985);

$$(-i)^m h_m(kr) \rightarrow \frac{-i}{kr} e^{ikr}(-1)^m \qquad (3.2.20)$$

And (3.2.19) becomes (2.3.1 from before);

$$p = (\rho cI)^{1/2} \sum_{m=0}^{\infty} (-1)^m (2m+1) P_m(\cos\theta) \left[\frac{j_m'(ka) - \dfrac{\rho c\, j_m'(k_e a)}{\rho_e c_e\, j_m(k_e a)}\, j_m(ka)}{h_m'(ka) - \dfrac{\rho c\, j_m'(k_e a)}{\rho_e c_e\, j_m(k_e a)}\, h_m(ka)} \right] \frac{ie^{ikr}}{kr}$$

(3.2.21)

3.3 Approximations to the General Theory.

When the material of the scatterer has an acoustic impedance that is much greater than that of the surrounding medium, then $\rho_e c_e \gg \rho c$ and equation (3.2.21) reduces to (2.4.1 from before);

$$p(r,\theta) = (\rho cI)^{1/2} \sum_{m=0}^{\infty} (-1)^m (2m+1) i^m P_m(\cos\theta) \left[j_m(kr) - \frac{j_m'(ka)}{h_m'(ka)} \right] h_m(kr)$$

(3.3.1)

The mathematics used to derive the above equations has been totally general as to the values of ka and $k_e a$, however, a few useful approximations can be derived from the above equation when ka«1 and ka»1, as mentioned in chapter 2. The first case corresponding to the classical Rayleigh/Tyndall (blue sky) scattering and the second case to the geometric shadow equation.

In terms of intensities, $I=p^2/\rho c$, with I_o the incident intensity;

$$ka\ll 1;\quad I(r,\theta) = \frac{16\pi^4 a^6 I_o}{9\lambda^4 r^2}\left[1 + \frac{3\cos\theta}{2}\right] \qquad (3.3.2)$$

$$ka\gg 1;\quad I(r,\theta) = \frac{a^2 I_o}{4r^2}\left[1 + \cot^2(\theta/2) J_1^2(ka\sin\theta)\right] \qquad (3.3.3)$$

3.4 Calculating the Scattered Pressure.

In order to calculate the pressure of the scattered wave, so that comparisons with experiments can be made, it is necessary to evaluate equation (3.2.22) for every value $0<m<\infty$, which in turn means evaluating various spherical Bessel functions, Hankel functions and Legendre polynomials, each of which is the sum of an infinite series. The usual technique has involved evaluating the functions from first principles and then truncating each series with some predetermined convergence criteria (Abramowitz and Stegun (1965), Lenn (1985)).

For example, the spherical Bessel function of order m and argument z would be found using the following series;

$$j_m(z) = \frac{z^m}{1.3.5..(2m+1)}\left[1 - \frac{z^2/2}{1!(2m+3)} + \frac{(z^2/2)^2}{2!(2m+3)(2m+5)} - \ldots\right] \qquad (3.4.4)$$

In order to make the calculations simpler, the following steps have been taken.

(i) The spherical Hankel function is split into its two component parts, the Bessel and Neumann functions, as follows;

$$h_m(z) = j_m(z) + iy_m(z) \qquad (3.4.5)$$

This allows the real and complex parts of equation (3.2.22) to be separated and double precision to be used for each part. Equation (3.2.21) then becomes;

$$P = (\rho c I)^{1/2} \sum_{m=0}^{\infty} (-1)^m (sm+1) P_m(\cos\theta) \left[\frac{T_1^2}{T_1^2+T_2^2} + \frac{iT_1T_2}{T_1^2+T_2^2} \right] ie^{ikr} \qquad (3.4.6)$$

Where, $T_1=j_m'(ka)-Bj_m(ka)$, $T_2=y_m'(ka)-By_m(ka)$ and $B=\dfrac{\rho c j_m'(k_e a)}{\rho_e c_e j_m(k_e a)}$

(ii) The spherical Bessel and Neumann functions can be replaced by simple trigonometrical functions which are standard to FORTRAN, and simple recurrence relationships negate the use of the primary level of summation used in previous works. The following substitutions and recurrence relationships were used (Abramowiz 1965);

$$j_0(z) = \sin(z)/z$$
$$j_1(z) = \sin(z)/z^2 - \cos(z)/z$$
$$j_n(z) = (2n-1)j_{n-1}(z)/z - j_{n-2}(z) \qquad (3.4.7)$$

$$j_0'(z) = -\sin(z)/z^2 + \cos(z)/z$$
$$j_1'(z) = (1/z - 2/z^3)\sin(z) + 2\cos(z)/z^2$$
$$j_n'(z) = j_{n-1}(z) - (n+1)j_n(z)/z \qquad (3.4.8)$$

$$y_0(z) = -\cos(z)/z$$
$$y_1(z) = -\cos(z)/z^2 - \sin(z)/z$$
$$y_n(z) = (2n-1)y_{n-1}(z)/z - y_{n-2}(z) \qquad (3.4.9)$$

$$y_0'(z) = \cos(z)/z^2 + \sin(z)/z$$
$$y_1'(z) = (2/z^3 - 1/z)\cos(z) + 2\sin(z)/z^2$$
$$y_n'(z) = (1 - (n+1)(2n-1)/z^2)y_{n-1}(z) + (n+1)y_{n-2}(z)/z \qquad (3.4.10)$$

It is worthy of note that the differential terms are evaluated from the basic function. This approach saves a considerable amount of programming and computer time.

(iii) Similarly, the Legendre polynomials can be found using recurrence relationships as follows;

$$P_0(x) = 1$$
$$P_1(x) = x$$
$$P_n(x) = (2 - 1/n)xP_{n-1}(x) - (1 - 1/n)P_{n-2}(x) \qquad (3.4.11)$$

Before continuing and evaluating the full equation for the scattered pressure, it will be instructive to see how accurate the above functions, (3.4.7) to (3.4.11) are, since recurrence relationships tend to amplify rounding errors of earlier terms. Figure 3.4a gives various comparisons between the above methods of calculation and the values given in Abramowitz (1965).

	Calculated	Published
$j_0(1)$	0.8414709848	0.84147098
$j_1(1)$	0.3011686789	0.30116868
$j_2(1)$	6.2035052011E-2	6.2035052E-2
$j_3(1)$	9.0065811171E-3	9.0066E-3
$j_4(1)$	1.0110158084E-3	1.0110E-3
$j_5(1)$	9.2561158605E-5	9.2561E-5
$j_6(1)$	7.1569362449E-6	7.1569E-6
$j_7(1)$	4.7901257872E-7	4.7901E-7
$j_8(1)$	2.8252435987E-8	2.8265E-8
$j_9(1)$	1.2788330672E-9	1.49137E-9
$j_{10}(1)$	-3.9546077107E-9	7.11655E-11
$y_n(1)$	correct to n=20 to 10 figures, numerical overflow at n=28	
$j_n(10)$	correct to n=18 to 10 figures	
$j_{19}(10)$	8.896627273E-6	8.896627269E-6
$j_{20}(10)$	2.308371975E-6	2.308371961E-6
	First figure lost at n=26	
$y_n(10)$	correct to n=50 to 10 figures, followed by numerical overflow	
$j_4(0.1)$	1.0577E-7	1.0577E-7
$j_5(0.1)$	2.3153E-9	9.6163E-10
$y_n(0.1)$	correct to n=10 to 10 figures, limited by tables.	
$P_n(\cos\theta)$	correct for all $0<\theta<90°$ and $n<10$ to 8 figures.	

Figure 3.4a Table comparing published (Abramowitz 1965) and calculated spherical functions.

The consequences for the finite accurate length of some of the series will be covered in detail later when the full scattering equation is analysed. The use of the full numerical series is also found to produce identical shortcomings due to the rounding errors in the most significant fractions of the series.

3.5 Computer Program to Calculate the Scattered Pressure.

The acoustic pressure scattered by a spherical object is given by equation 3.3.21 and figure 3.5a shows a flow diagram of the FORTRAN program used to evaluate the equation.

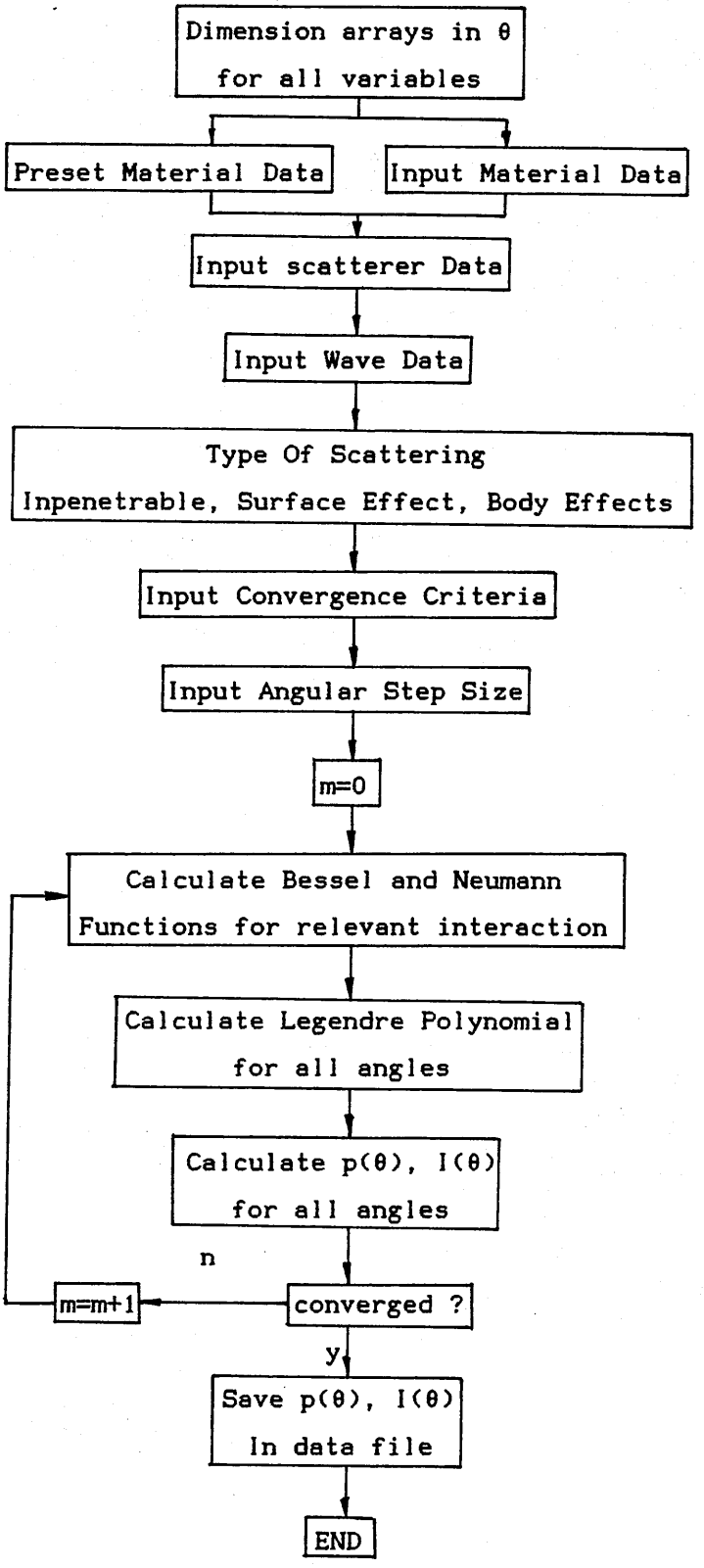

Figure 3.5a Flow diagram of FORTRAN Program to determine scattered pressure.

3.6 Characterising the Acoustic Field of a Transducer.

Before beginning a description of the main experiments, namely ultrasonic scattering from liquid droplets, the concept of the far field must be investigated. the previous sections have already taken the far field into account with the approximation for $h_m(kr)$ given in equation (3.2.21). A more physical description is required before the mathematical approximation can be considered valid.

All of the preceding theory and calculations have required the wavefront to be infinite in space and a perfect sine wave. It is clear that this situation is physically unrealisable. Ultrasonic transducers can only be manufactured to a finite (small) size. The main problem with a continuous wave source are the standing waves that are set up in the apparatus. This can be overcome by using non-sinusoidal waveforms such as pulses of various shapes (Ma 1983 and Stepanishen 1981), but the full analysis for the scattering problem becomes considerably more complicated than that described above. Provided the scatterers are smaller than the length of the wavetrain, then some typical part of the wavetrain (eg the peak) can be assumed to be part of a sinusoidal wave of that amplitude for the analysis of the incident and scattered wave.

The finite size of the transducer (both receiver and transmitter) face provides its own problems. The following arguments will refer to plane transducer faces, but it should be noted that transducers with focussing surfaces are commercially available (Edwards 1983). The near field and far field of an acoustic transducer are defined exactly as their optical counterparts (Fresnel and Fraunhofer respectively), in the first case, the signal at a point must be found by integrating the signal from each point on the transducer taking into account its phase and in the second case, the phase from each part of the transducer can be assumed the same. The far field is the simplest to calculate since the transducer is behaving as a point source with its intensity dropping off as $1/r^2$. The first case of the near field is much more complicated and has been studied experimentally and theoretically (Weight 1984 and Zemanek 1971). Reproduced below are some transducer characteristics, and although not directly comparable (they are for

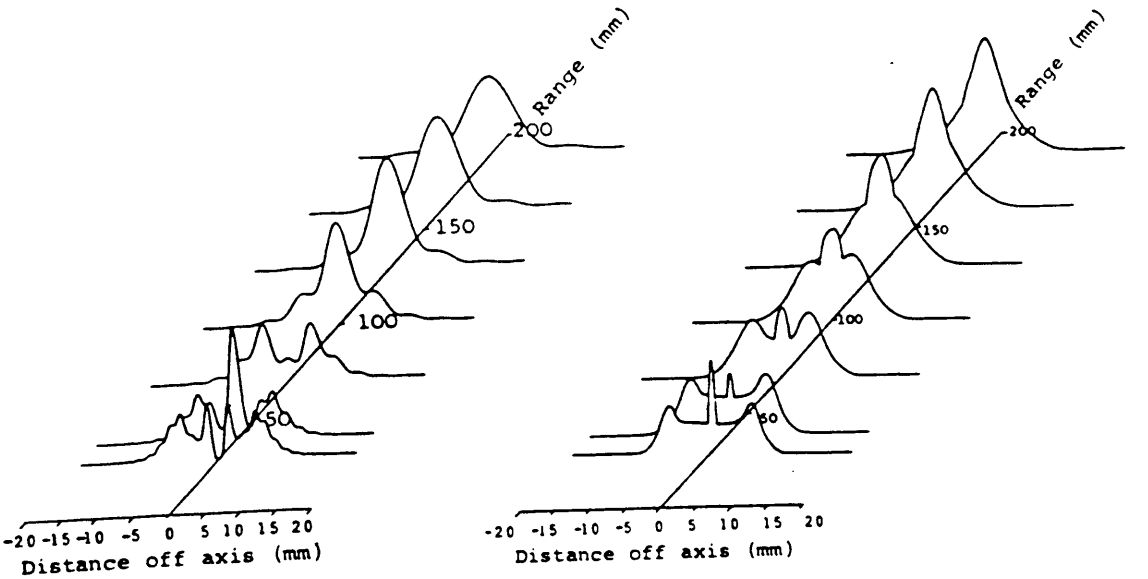

Fig 3.6a Sound pressure as a function of radial position and range (a=19mm, f=2MHz) for a continuous wave excitation and a 1.5λ pulse at that frequency (Weight 1984).

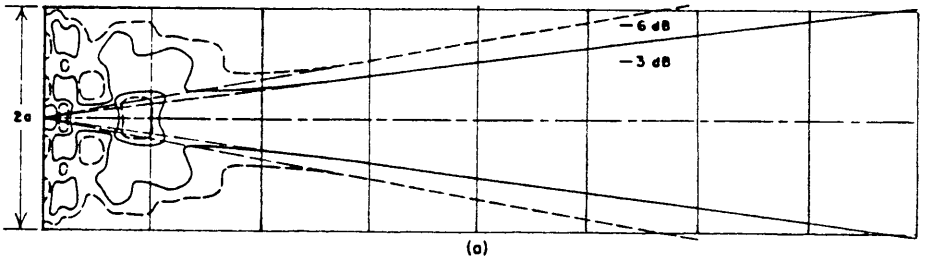

Fig 3.6b Sound pressure contour, showing complex near field (a/λ=2.5), (Zemanek 1971)

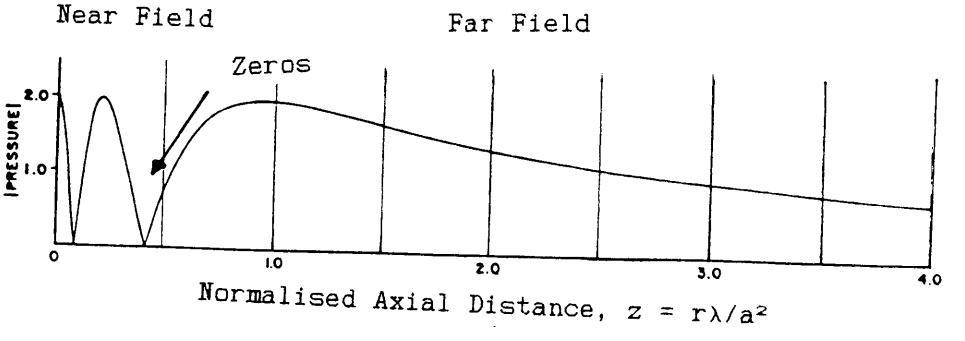

Fig 3.6.c Magnitude of on-axis pressure variations (a/λ=2.5), (Zemanek 1971)

different transducers and from different papers), they should give a feel for what happens in the acoustic field of a typical transducer with a face of radius 'a' (figures 3.6a and b)

Further analysis (including a direct optical analogy) reveals that the greater the ratio a/λ the more beam-like is the resulting far field wave, and in the limit the diffraction edges becoming negligible when compared with the cylindrical beam.

The main aim of this section is to find when the axial position can be considered to be in the far field, since, as can be seen in figures 3.6c and d, a transducer has several 'blind-spots' in its near field, where the amplitude of the pressure wave is zero, and so could not be used to detect anything.

Most sources give a definition of the far field of a finite source as Ka^2/λ, where K is a constant between 0.5 and 2, depending on the author. These methods all involve finding the point closest to the source at which the waves from every point on the source contribute positively. An alternative and much simpler derivation will be given below.

Using the principles of reciprocity, let the transducer be a receiver and let the point in question be a perfect point source (figure 3.6g). The plane face of the transducer will intersect a continuous spherical wavefront. The potential difference generated by the transducer will be proportional to the integral of the instantaneous pressure on the face. For an axial source, the face will intersect more than one wavefront if the axial position is less than a certain critical value. For a distance less than this critical value, a phase pattern identicle to Newton's Rings experiment will be generated on the transducer face and so there will be a possibility of the total pressure being zero. When all of the waveform is contributary, ie a single wavefront, phase $0-\pi$, this will give a minimum distance for the far field.

Using Pythagoras' Theorem, $r = a^2/\lambda - \lambda/4$, thus for all sensible tranducer designs, the term $\lambda/4$ is negligible.

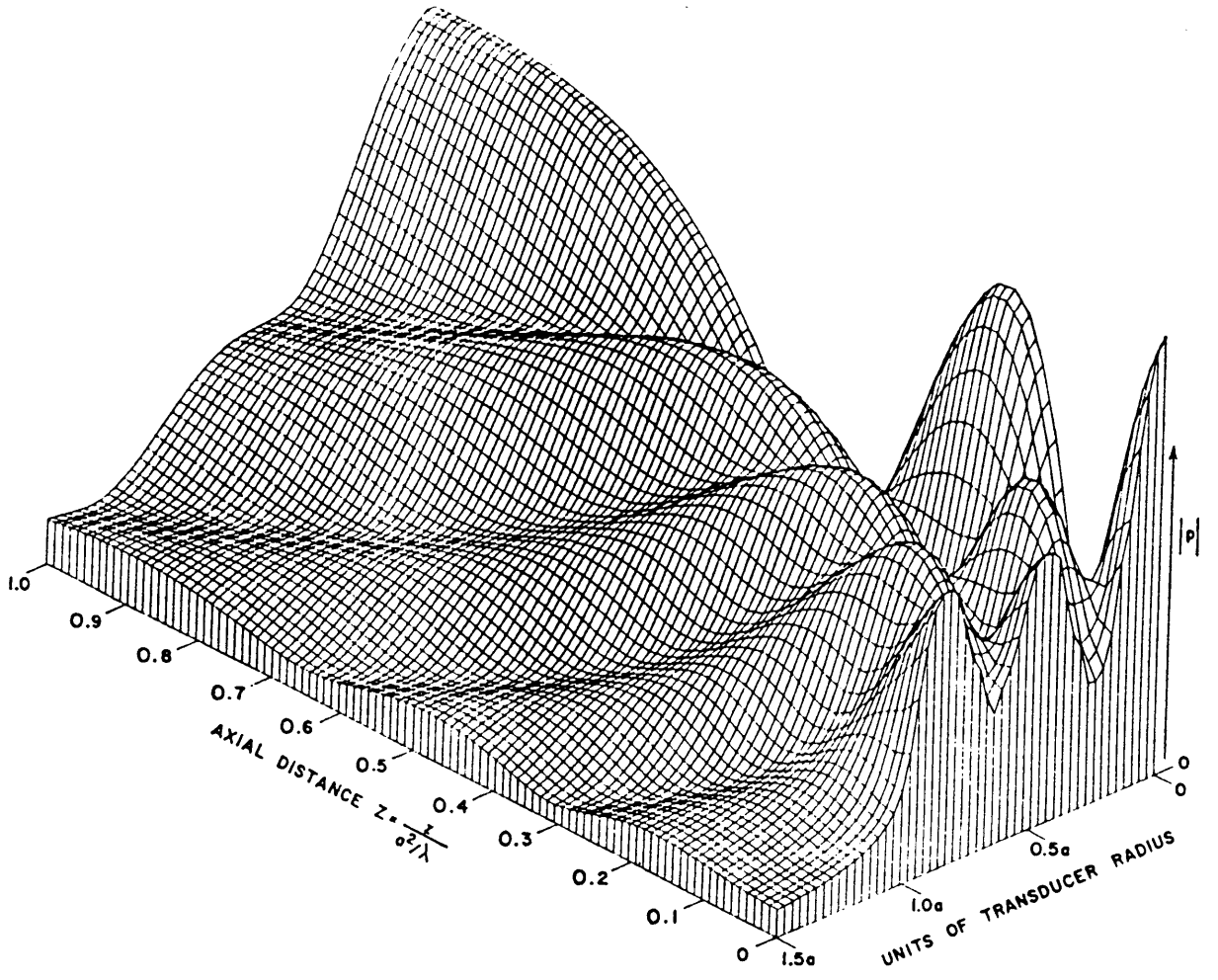

Fig 3.6d A superposition of the last three plots (a/λ=2.5), (Zemanek 1971)

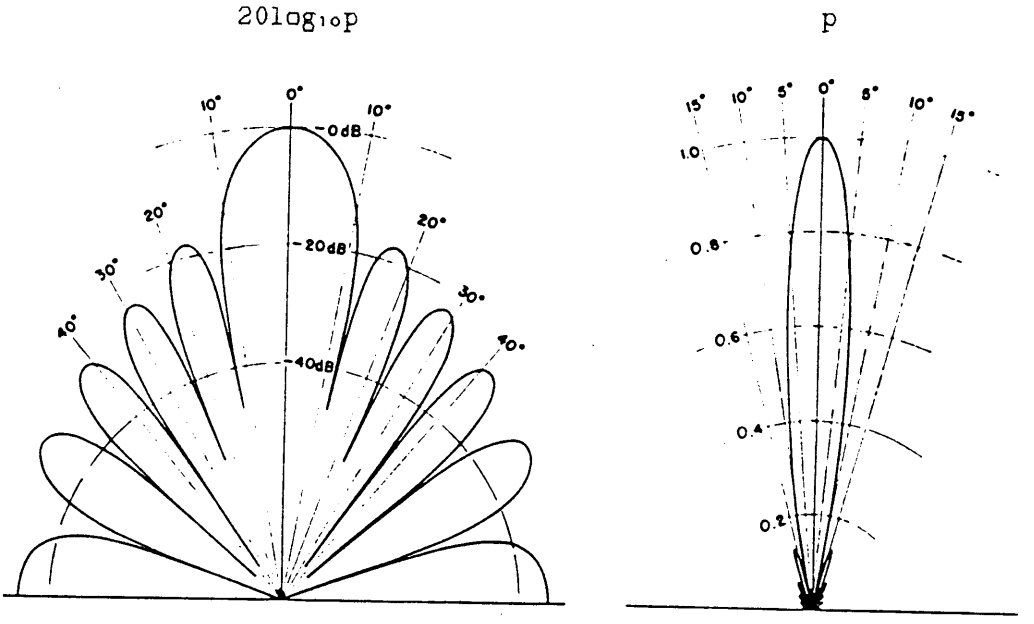

Fig 3.6e Far field beam pattern (a/λ=2.78), (Zemanek 1971)

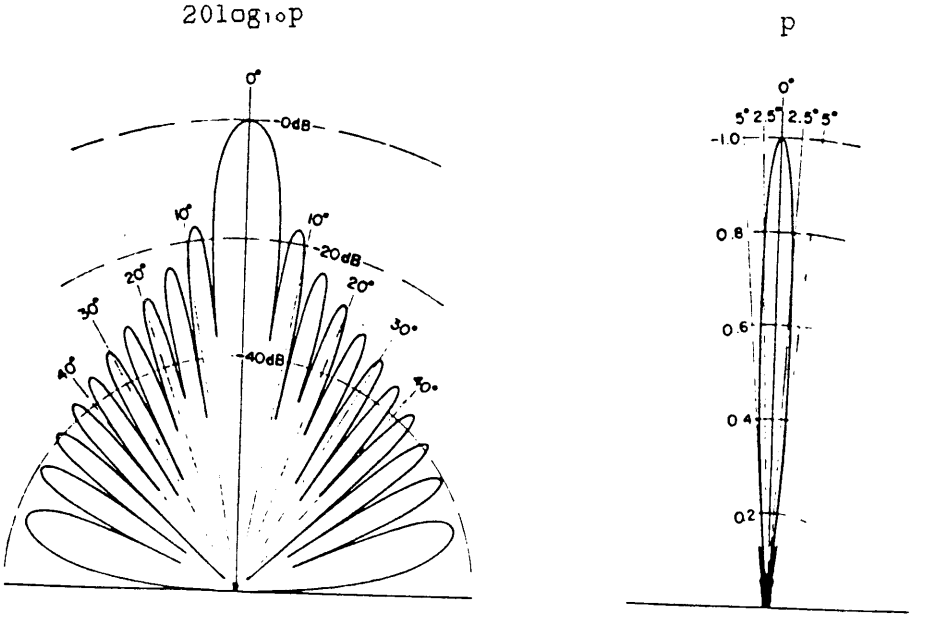

Fig 3.6f Far field beam pattern (a/λ=5.62), (Zemanek 1971)

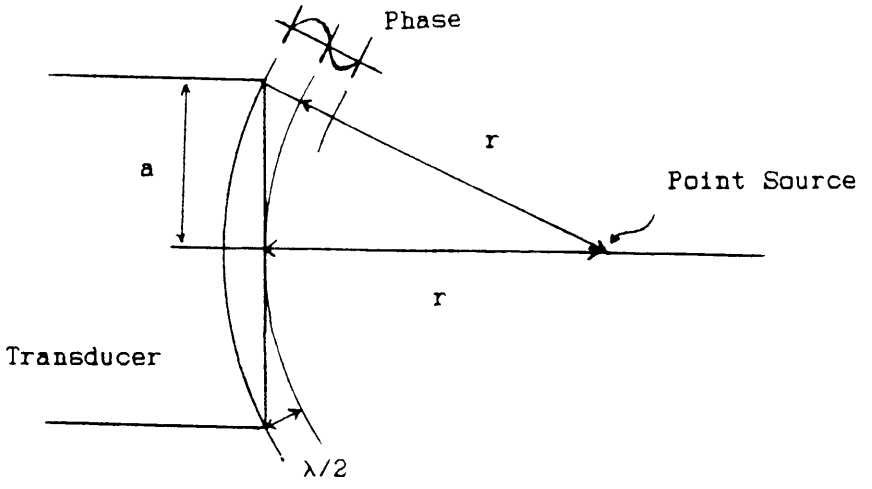

Fig 3.6g Derivation of a far field equation

3.7 Preliminary Ultrasonic Experiments

In order to study the scattering of ultrasound from liquid droplets, an apparatus had to be designed that could suspend the droplet in the acoustic field. An experimental design had to be found that satisfied the following criteria;

(a) The acoustic observation section must have as small an effect on the sound wave as possible, so as not to interfere significantly with the wave scattered from the droplet. This precludes any sort of physical support, which would necessarily be a solid. A solid would strongly scatter any acoustic wave as well as deform the shape of the droplet. The only way around this is to produce a purely hydrodynamic support.

(b) The flow must be laminar, otherwise the droplet would not be stationary in the acoustic field. A turbulent flow could also deform the droplet.

(c) The flow rate has to be able to be controlled accurately enough to bring a single droplet to rest anywhere in the acoustic field, with the buoyancy forces exactly cancelling the hydrodynamic forces.

(d) This flow rate must remain stable over long periods of time ($\simeq$hours) in order to carry out adequate ultrasonic experiments.

(e) The apparatus must be easily dismantled and cleaned, so that repairs can be effected and contaminants removed.

(f) The design must be capable of being modified such that the flow in the observation section can be either (i) upwards or (ii) downwards, depending on whether the droplet is (i) more or (ii) less dense than the surrounding fluid.

A full description of the design and testing of the apparatus is given in appendix A.

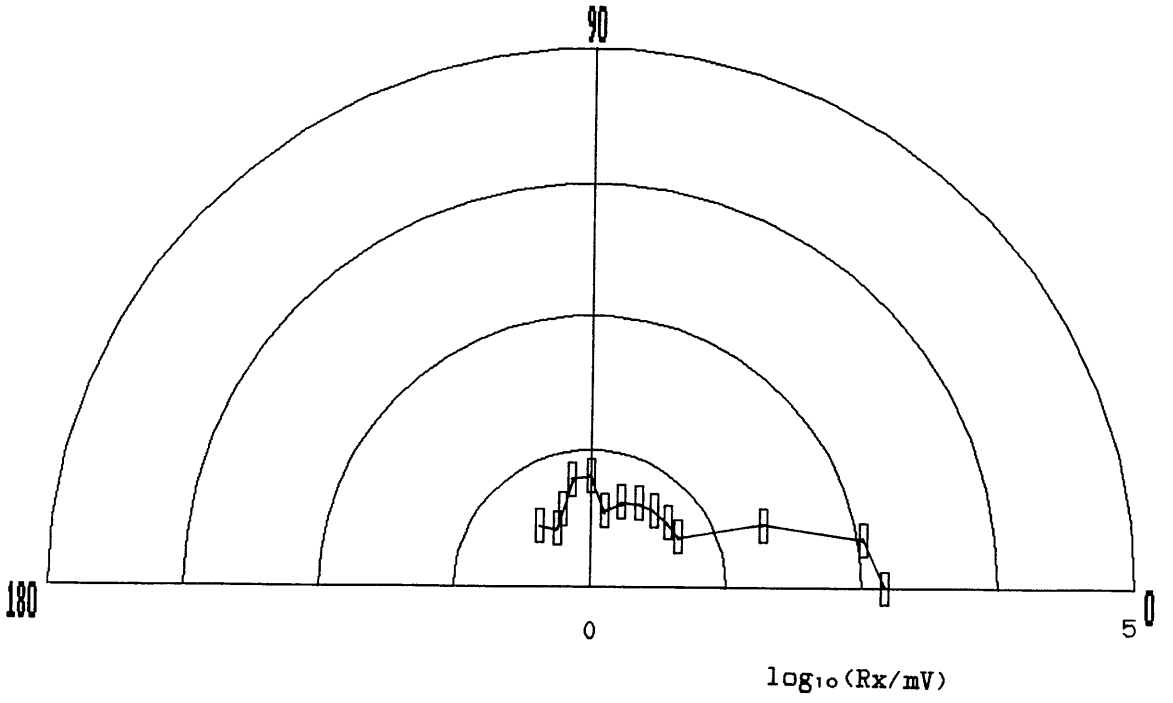

Figure 3.7a Continuous wave scattering from the observation section

Before beginning the scattering experiments from droplets, it was necessary to investigate fully the behaviour of the whole acoustic system. Criteria such as repeatability, accuracy and any possible technical problems have to be eliminated at this early stage.

All of the initial tests were carried out using the downflow apparatus (shown in figure A.2a), with the transmitter being a Schlumberger 1.25MHz ceramic transducer and the receiver being a MatEval 1MHz transducer. The reasons for this choice will be discussed elsewhere. The transmitter was driven with a 10V peak to peak 1MHz continuous sine wave from a Philips digital signal generator. Both transducers are 5cm ± 0.1cm from the centreline of the observation section. Slowly sweeping the receiver from $\theta=0^0$ to 135^0 revealed some sort of weakinterference pattern with peaks at approximately 3^0 intervals. This showed up clearly even though the receiver subtended an angle of 17^0 with respect to the centre of the observation section. In order to appreciate the size of the signal scattered from the observation section, it is plotted in figure 3.7a for an angular step size of 10^0. Because of the fineness of the interference pattern and the fact that θ could only be measured to $\pm 0.25^0$ an average of ten values was taken for each point.

An analysis of the acoustic system, assuming the observation section and the transmitter to be coherent point sources generating an interference pattern and the receiver to be a point also, reveals that there would be an amplitude maximum when;

$$\cos(\theta/2) = (1 + n\lambda/R)/2 \qquad (3.7.1)$$

for all integer values of n. This leads to 33 maximae for $0^0<\theta<180^0$, confirming qualitatively the above results. This means that the signal from the transmitter cannot be assumed to be a narrow beam and the signal in the periphery is comparable with the signal scattered from the observation section. Indeed this is confirmation that the observation section is scattering some of the incident signal.

The scattered signal from the observation section was found to be independent of the static head of the liquid in the section and

independent of the flow rate of the liquid. After several hours, the water started to degas onto the solid surfaces, transducer faces and both inside and outside the observation section, which caused a severe disruption of the acoustic signal. The degassing inside the observation section set an upper limit on the period of a single experiment.

Small leaks in the observation section could be sealed with a tiny dot of cellulose lacquer without affecting the scattered signal.

The problem of the interference pattern on this scale cannot be resolved without resorting to considerably more repeatable apparatus and theoretical complexity. However, the interference pattern could be eliminated from the apparatus by a choice of waveform other than continuous. Two distinct possibilities exist for the form of the driving signal for the transmitting transducer, either some form of modulated sinewave or some sort of spike approximating to a Dirac delta function. A suitable choice of waveform would produce a spatial separation between the wave from the periphery of the transducer and the scattered wave from the observation section (and ultimately from the scattering droplet).

The first experiments along these lines involved the use of a Par 150B spike generator, driving the transducer with a 150V spike of approximately 50ns duration repeated every 0.2ms. The transducer could not respond this quickly, and produced a short pulse of waves at its resonant frequency. The length and shape of the pulse was determined solely by the physical properties of the transducer. The Schlumberger transducer produced a wavepacket 3λ long at a frequency of 1.15 ± 0.04MHz. Assuming the speed of sound in water to be 1450m/s, this meant that the pulse was 3.8mm long in water. A plan of the acoustic system is shown in figure 3.7b and a typical scattered signal is sketched in figure 3.7c

Thus it can be seen that the wave packets were quite distinct for large values of θ, and two separate signals were scattered from the observation section. These two signals were found to be far more complicated than figure 3.7b would imply, since the tube was not just

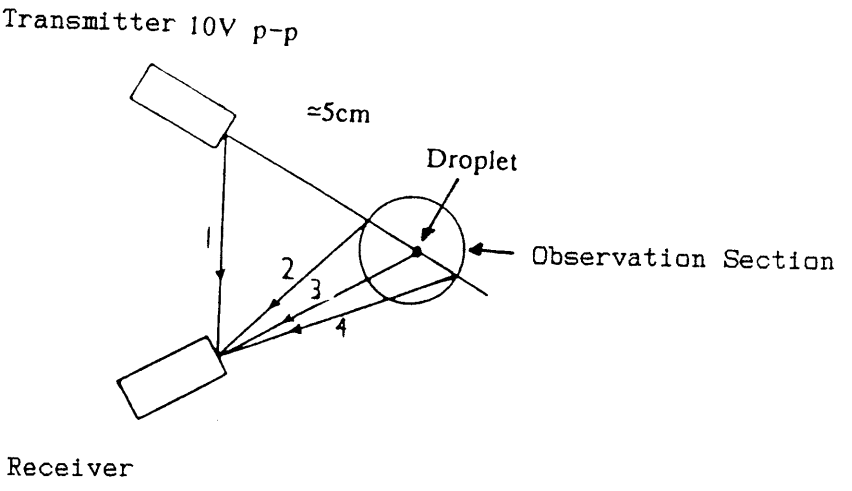

Figure 3.7b A plan of the acoustic system

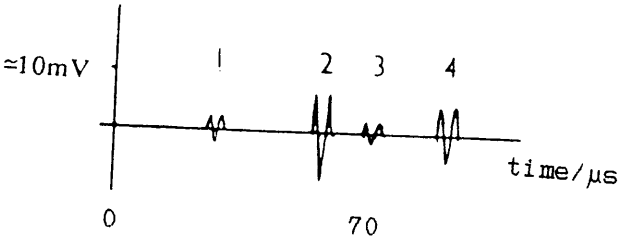

Figure 3.7c A typical scattered signal.

a simple front wall and rear wall, but was cylindrical. The two signals could be resolved for $\theta > 25^0$, below which they became superposed and interfere in a fairly simple manner.

The size of these wall signals was used as a check that the acoustic and electronic system was repeatable from experiment to experiment and from day to day. Figures 3.7d and 3.7e show the scattered signals from the front and rear walls respectively and figure 3.7f is a plot of the path difference between these two signals.

Identical results were found if the transmitter was driven using a 10V p-p signal at a frequency of 1.15MHz for 3 periods of a sinewave.

3.8 Ultrasonic Scattering From Single Droplets.

In order to check the conclusions of the above section, scattering experiments were carried out using all three types of driving signal; continuous sine wave 10V p-p, 150V spike and the modulated sine wave, 3λ at 10V p-p.

In the case of the continuous wave, even more interference phenomenae occurred when a droplet was placed in the observation section. A kerosene droplet $\simeq$1mm in diameter ($ka \simeq 2.3$) produced a minimum signal when it was at the point where the axes of the transducers intersected the axis of the observation section, and produced maxima when moved vertically $\pm$17mm from this point. Again a simple calculation, assuming the observation section to be a line source and the droplet to be a point source confirmed this observation.

The angular scattering was determined for the upper maximum position, and the droplet was moved in and out of the observation section (by adjusting the flow rate), without moving the transducer, so that the signal scattered from the observation section alone could be found.

For small scattering angles, even with the short wavepackets, the wavepacket scattered by the droplet could not be easily distinguished from the waves scattered by the observation section. By moving the

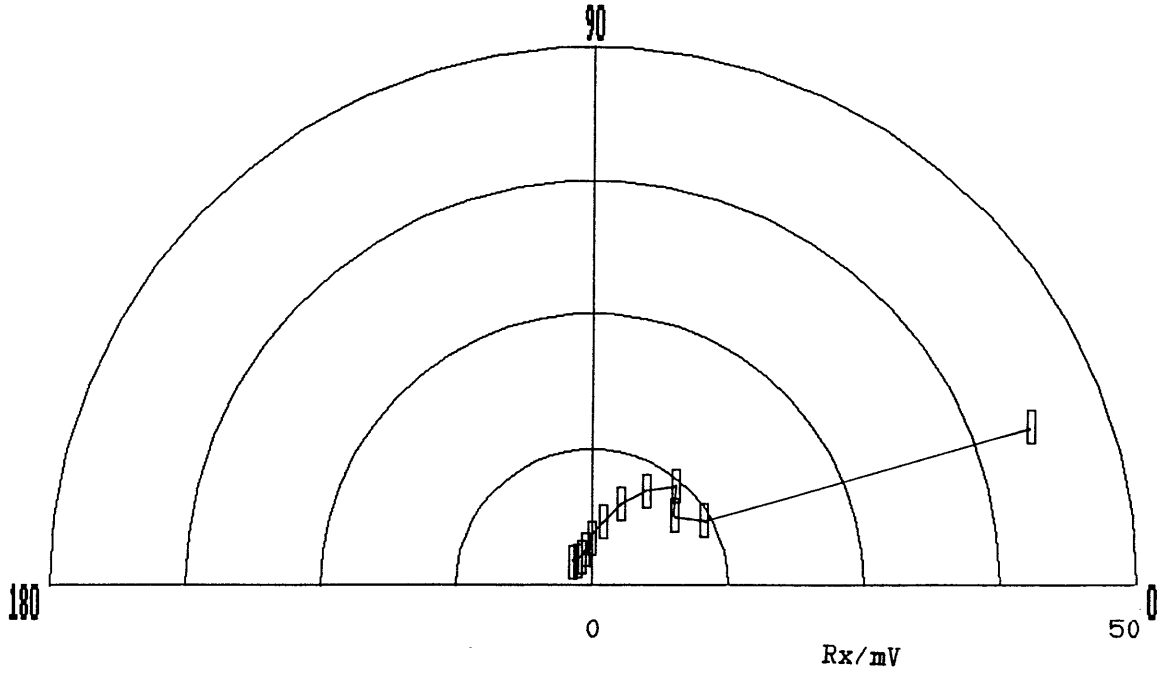

Figure 3.7d Signal scattered from the front wall

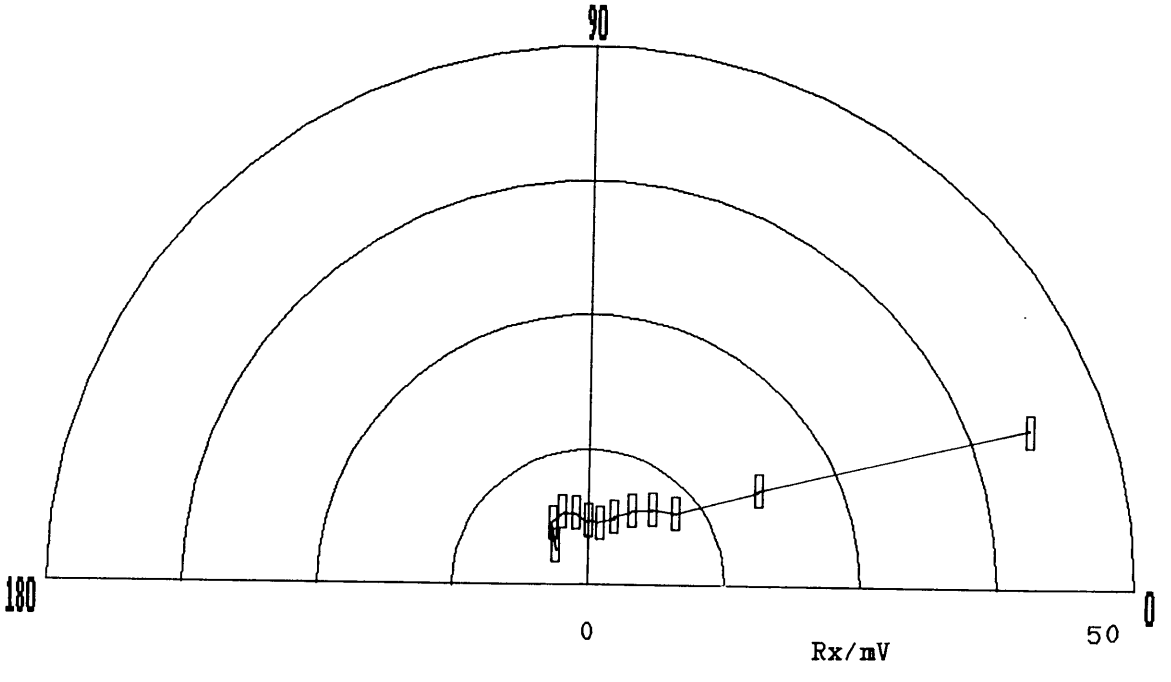

Figure 3.7e Signal scattered from the rear wall

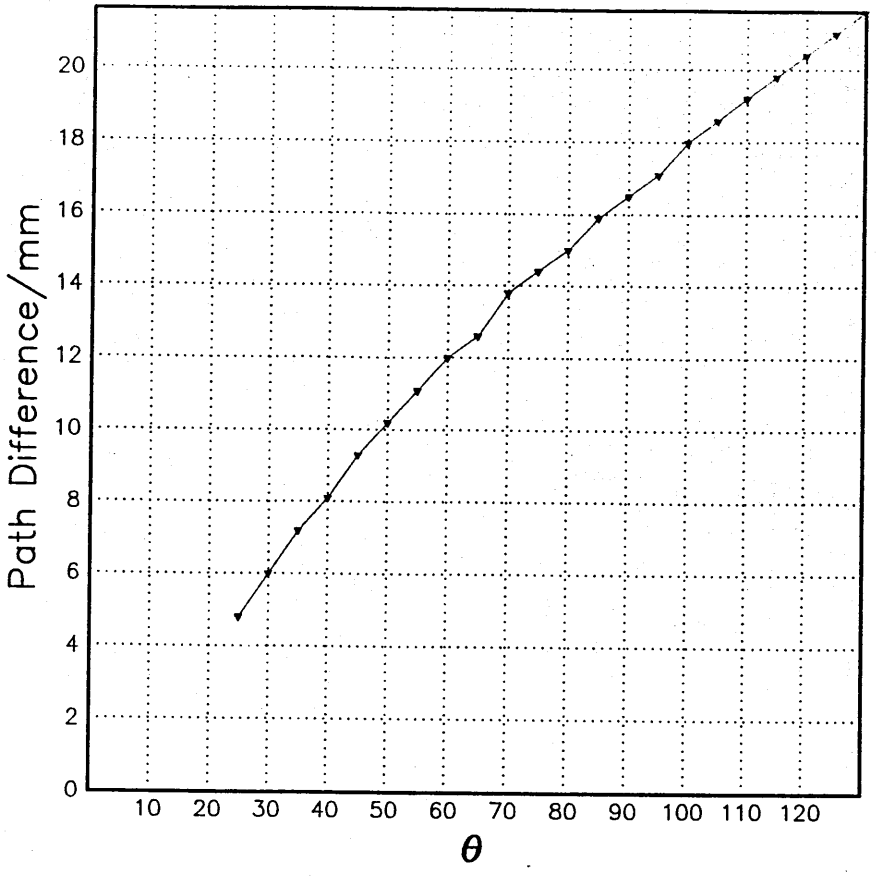

Figure 3.7f Acoustic path difference between the front and rear walls

droplet around in the observation section, it became clear that the phase relationship between the two signals (droplet and observation section) was spatially dependent. To overcome this, the droplet was moved around until a maximum value was found, and so the two signals could be considered to be in phase, and the difference was taken to be the signal scattered by the droplet.

The total signal scattered from the droplet and pipe is given in figure 3.8a and having assumed these two signals to be in phase, the signal from the droplet alone was calculated and is given in figure 3.8b.

It is clear, even from this single experiment, that the scattered signal can be resolved form the background signal, and that scattered lobes are being detected, in qualitative agreement with published theoretical plots, Morse (1953,1968) and Anderson (1950).

Due to the considerable technical difficulties encountered during the above experiment, mainly in finding a maximum signal for each angle, which took a total of over 4 hours, this method was not continued.

The following figures contain scattering data for a series of experiments that used the spike generator to drive the transmitter. The frequencies and particle sizes were chosen to highlight a range of values of ka where interesting phenomena are expected, ie near Rayleigh and diffraction scattering.

The experimental data is tabulated in figure 8.3b' and is plotted along with the theoretical calculations of the scattered pressures (found using the full form of equation 3.2.21.), in figures 3.8c to x. The droplets were sized photographically as described in appendix A. As mentioned above, the peak amplitude is taken as the representative scattered signal and the main frequency component is taken to be that of the continuous sinewave for the theoretical treatment.

The data is a representative part of a series of experiments designed to cover the whole range of materials and droplet sizes. As an aside, the scattering from solid particles of glass, sand and iron was also

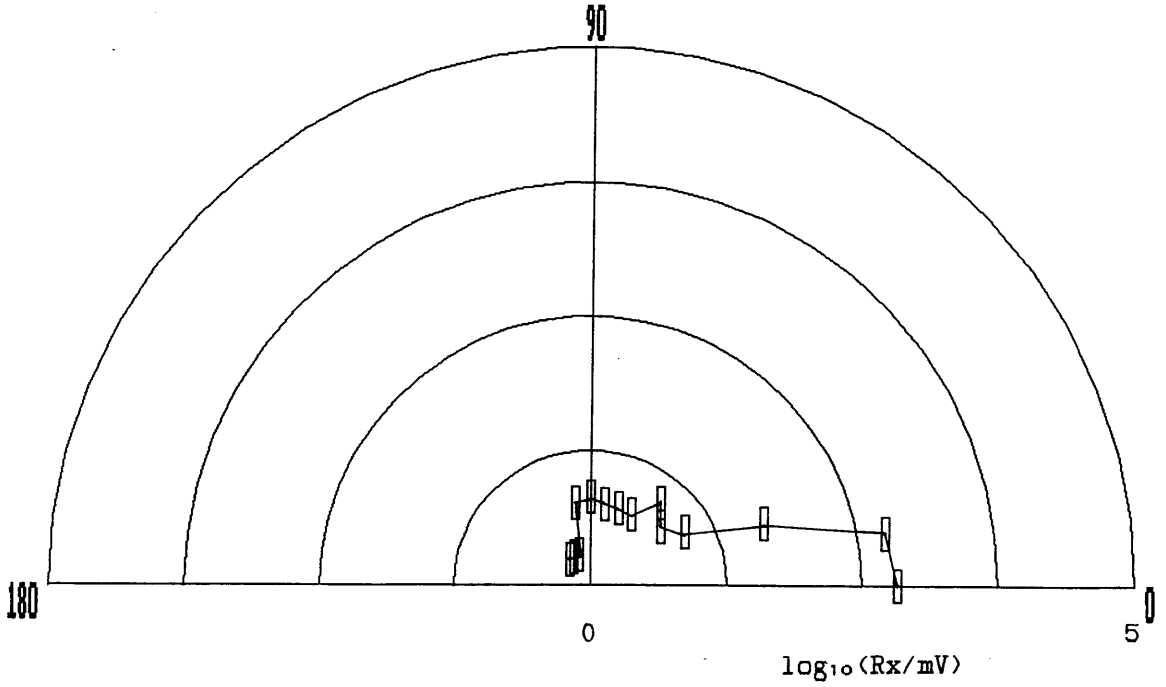

Figure 3.8a The total scattered signal from a kerosene droplet, d≃1mm

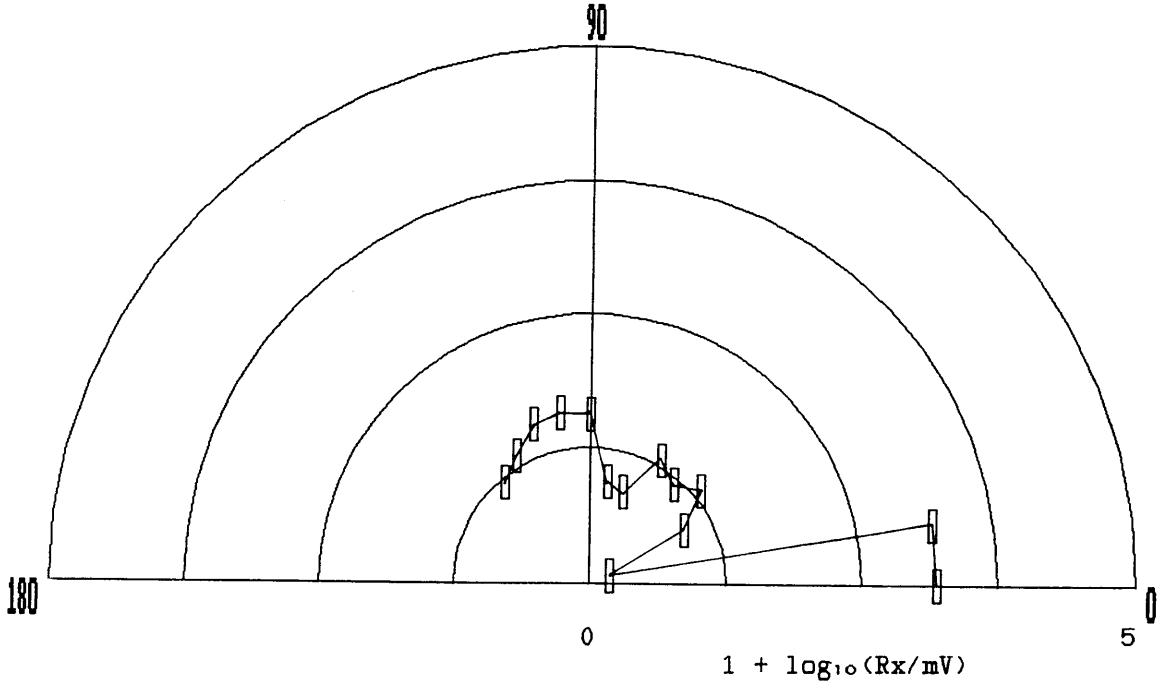

Figure 3.8b The scattered signal from the kerosene droplet, d≃1mm

		θ														
Fig	Detail	0	10	20	30	40	50	60	70	80	90	100	110	120	130	ka
c	kiw 0.89mmr	10	10	8	7	4.4	2.8	1.8	1.8	1.6	2.0	1.8	1.8	1.6	1.6	4.4
d	kiw 0.8mmr	†	6	5	5	3.5	2.2	2.0	1.2	1.6	1.6	1.6	1.6	1.6	1.6	4.0
e	kiw 0.75mmr													1.2	1.6	
f	kiw 1.06mmr	20	15	10	5	2.4	2.4	2.0	2.0	2.0	2.0	1.6	2.0	1.6	1.4	5.3
	kiw 0.255mmr	†	†	†	†	≃.2	≃.2	≃.2	≃.2	≃.2	<.2	.2	.6	.4	.4	1.2
	aiw 0.345mmd												2.6	2.6	2.4	1.7
	aiw ?														1.0	
	kiw 895μmr														1.8p	4.45
	kiw 940μmr														1.6p	4.68
	kiw 790μmr														1.6p	3.94
	kiw 740μmr														1.6p	3.69
	giw 420μmd														1.0	1.05
	giw 250μmd														.2-.3	0.62
	giw 177μmd														<.1	0.44
	giw 149μmd														no signal	0.37
	siw 106μmd														no signal	0.26
	giw 500-600μmd														0.8	1.37
	giw 600-710μmd														1.0	1.63
	giw 710-850μmd														1.0	1.94
	giw 850-1000μmd														1.5	2.30
	giw 1-1.4mmd														2.0	2.99
g	giw 2.3mmd	10	10	8	6	4	4.2	4	4	4	3.4	3.8	4	4	4.8	5.73
h	giw 1-1.4mmd	*≃4	3-4	≃2	≃2	≃1	≃1.5	≃3	≃2	≃1.5	≃1.5	≃1	≃2	≃2	≃2	2.99
i	giw 850-1000μmd	*≃2	≃1	1	1	≃1.5	1	1.5	2	2	2	2	2	1.5	≃1.5	2.30
j	giw 710-850μmd	*.5	≃1	≃1	≃.5	≃.5	1.5	1	2	1.5	2	1.5	1	1	1	1.94
k	giw 600-710μmd	*.5	*.5	*.5	≃.5	.5	≃.5	≃.5	.5	.5	.5	.8	1	1	≃1	1.63
l	giw 500-600μmd	*.2	*.2	*.2	*.2	≃.2	≃.2	≃.4	≃.4	≃.5	≃.5	.8	≃.8	≃.8	≃.8	1.37
	wik 1289μmr														≃1.8	7.03
n	wik 364μmr	†	†	≃.5	≃.5	.4	.6	.8	1	1.2	1.2	1	.8	.8	.5	1.99
o	wik 777μmr	†	†	1	1.6	1.6	1.6	1	2	1.4	1.6	1.4	1.4	1	1.2	4.24
m	wik 989μmr	≃10	10	10	8	6	3	2.2	2	1.6	1.6	1.6	1.2	1.6	1.2	5.40
p	multiple	†	†	†	≃.6	.6	1	1.4	1.6	1.6	1.2	1.2	1	.8	.8	
q	wik 2.2mmd	≃20	≃20	>10	10	5	2	2	2.4	2.2	2	1.6	1.6	1.2	1.6	6.00
r	wik 1.05mmd	†	†	≃1	†	1.2	1.2	2	2	1.6	1.4	1.4	1.2	1.2	1.2	2.87
s	wik 1.22mmd	†	†	≃2	≃2	≃2	≃2	1.6	2	1.2	.8	1	≃.6	.8	.8	3.32
t	wik 1.29mmd	†	†	≃6	4	4.2	2.8	2.8	1.6	1.6	1	.8	<1	1	1	3.52
u	wik 1.44mmd	†	8	2-4	8	5.2	3.2	3	1.6	1.6	1.4	1.2	1.2	≃1.2	1.2	3.93
v	iik 1.4-1.18mmd	†	†	4	4	≃3	1.6	2	2	1.6	≃2	2	1.4	1.2	1	3.52
w	iik 1-1.18mmd	†	≃4	≃2	2	1	?1	2-2.4	2.4	2.4	2	1.6	1.6	1.6	1.6	2.97
x	iik 850-1mmd	†	†	1-2	.5-1	1	1.6	2	2	2	1	1.2	1.2	1.6	1.6	2.52

Figure 3.8b' Sample of experimental data.

Key: Detail: k=kerosene, w=water, s=sand, g=glass, i=iron, i=in,
d=diameter, r=radius
†=too small to measure or indistinguishable from the wall reading
*=difficult reading
Fig= Figure 3.8

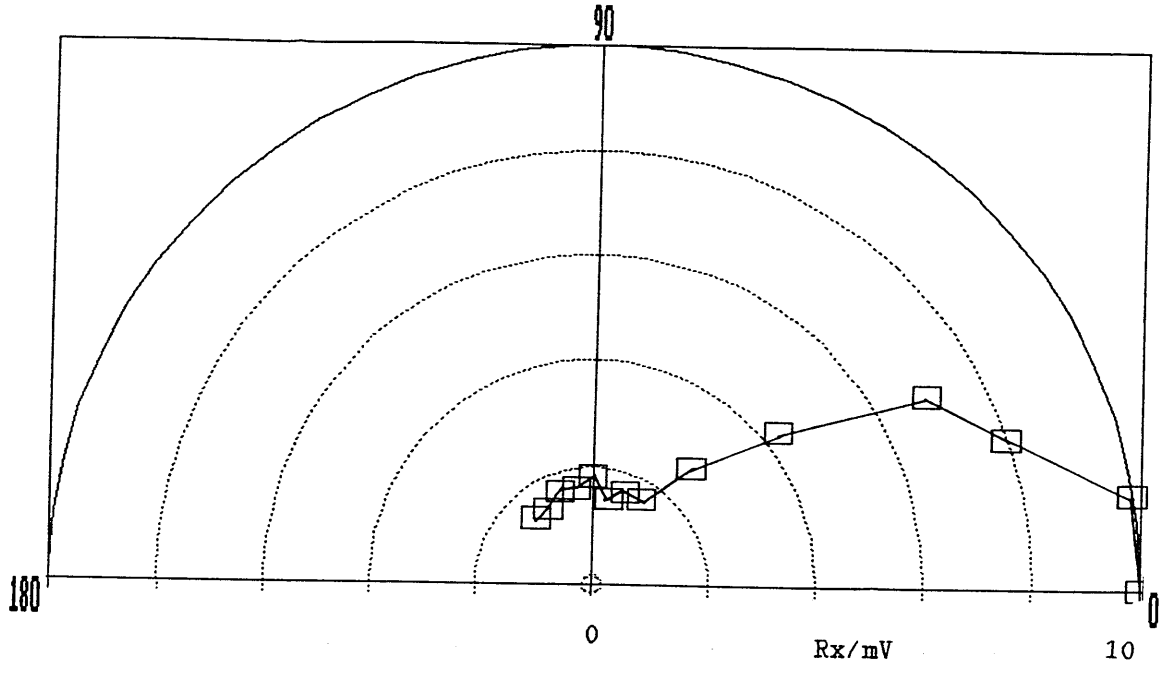

Figure 3.8c Experimental scattering from kerosene in water, ka=4.4

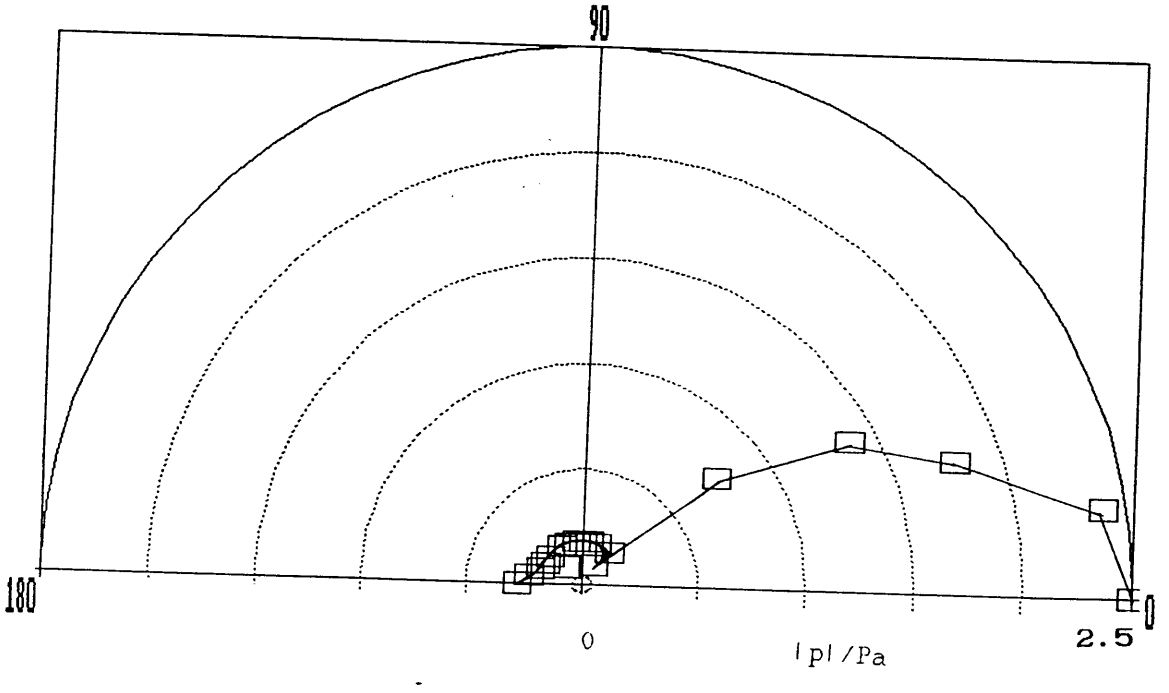

Figure 3.8c' Theoretical scattering from Kerosene in water, ka=4.4

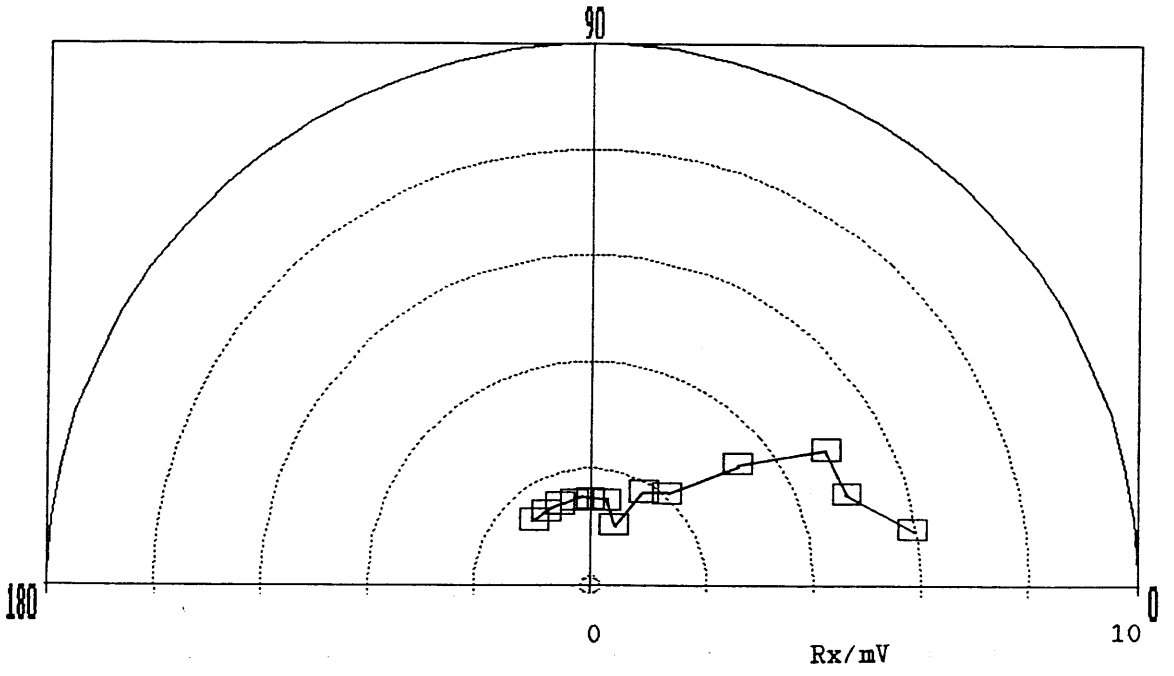

Figure 3.8d Experimental scattering from kerosene in water, ka=4.0

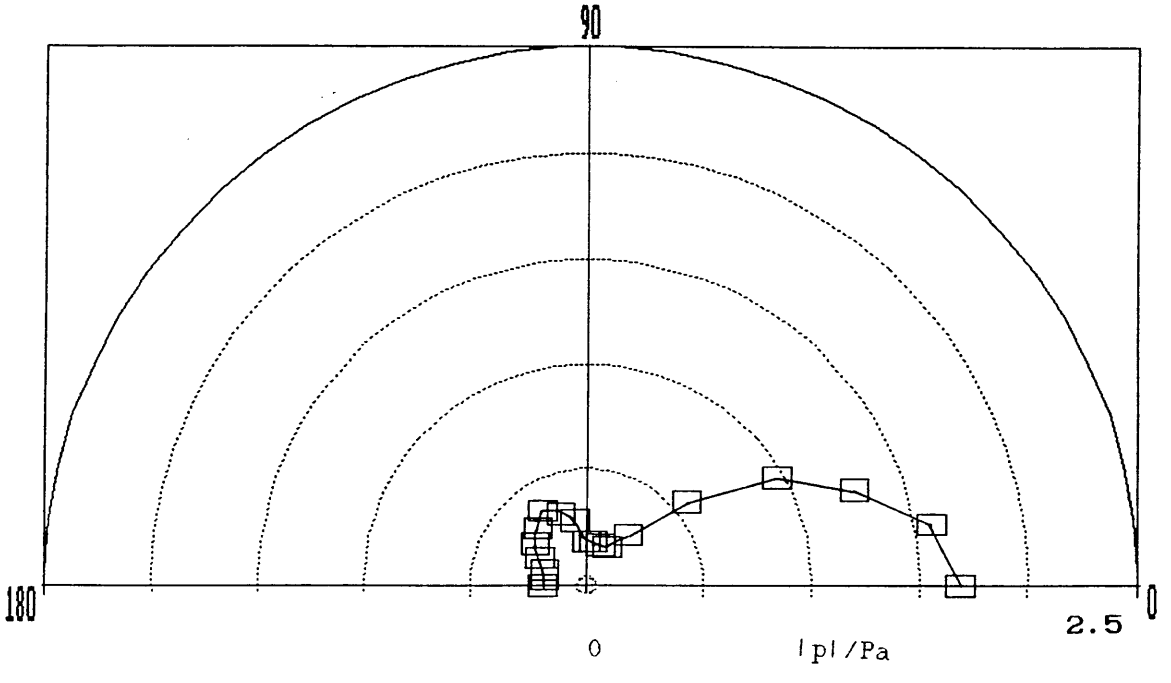

Figure 3.8d' Theoretical scattering from kerosene in water, ka=4.0

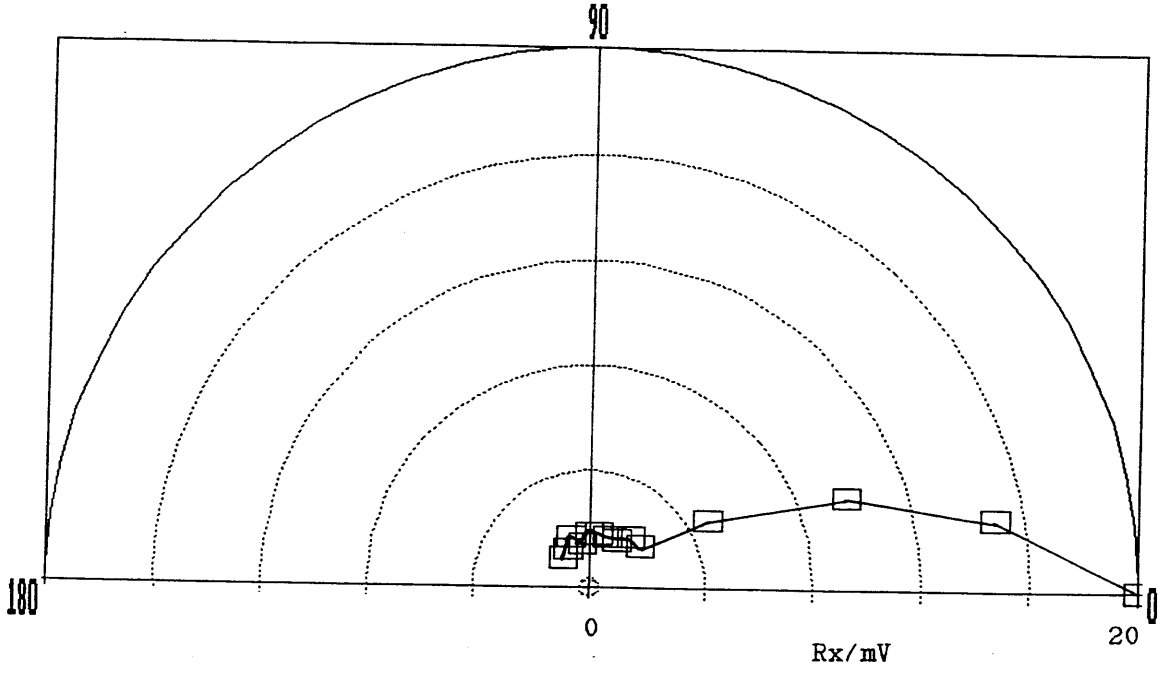

Figure 3.8e Experimental scattering from kerosene in water, ka=5.3

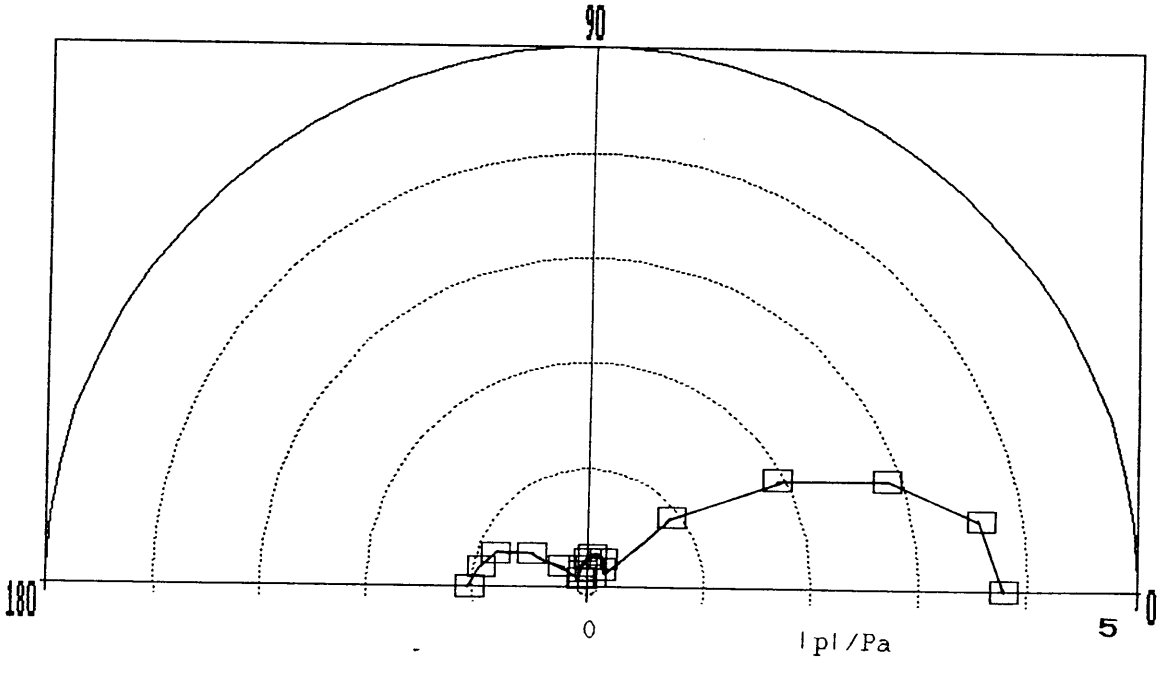

Figure 3.8e' Theoretical scattering from kerosene in water, ka=5.3

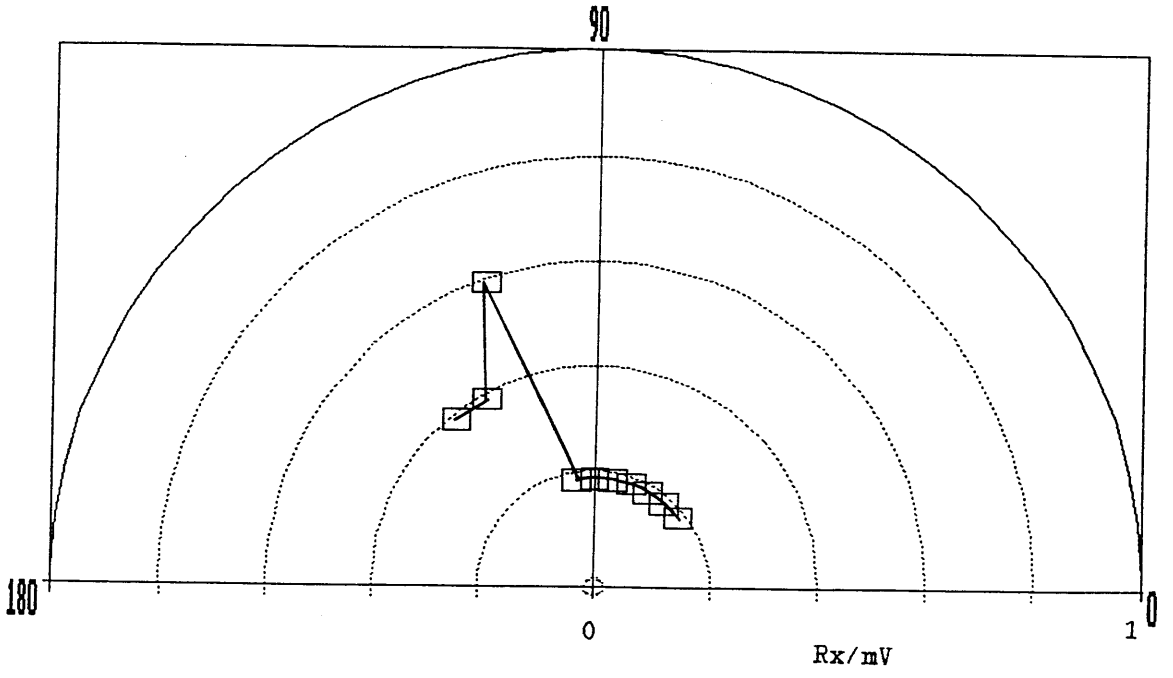

Figure 3.8f Experimental scattering from kerosene in water, ka=1.27

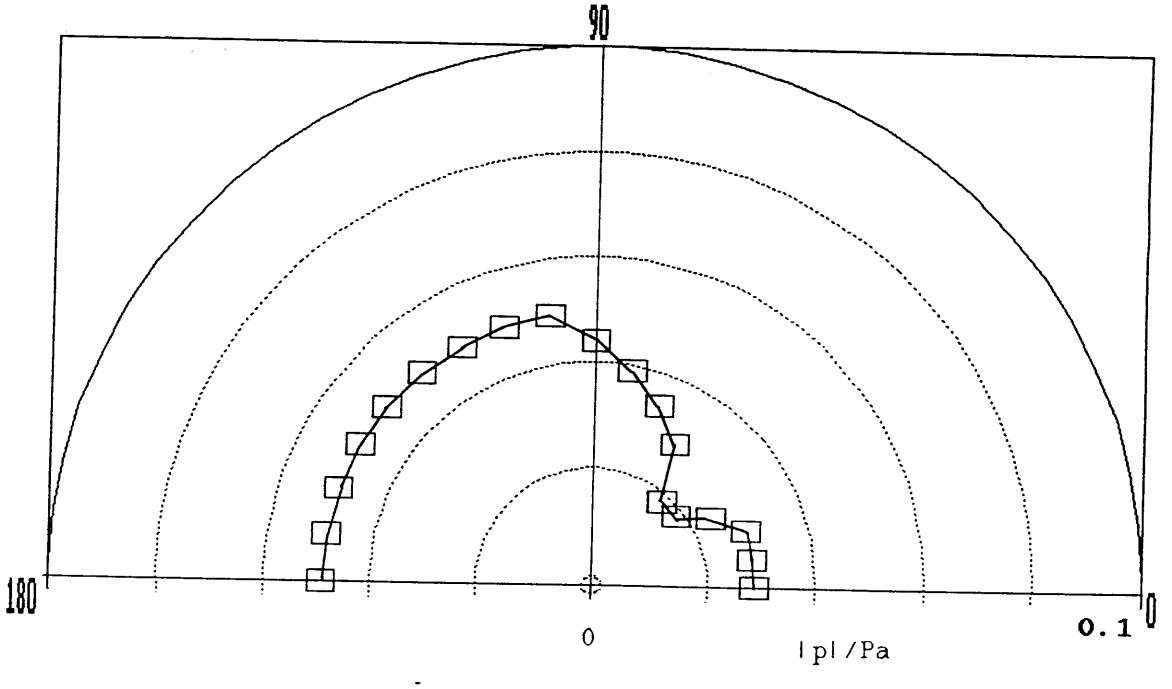

Figure 3.8f' Theoretical scattering from kerosene in water, ka=1.27

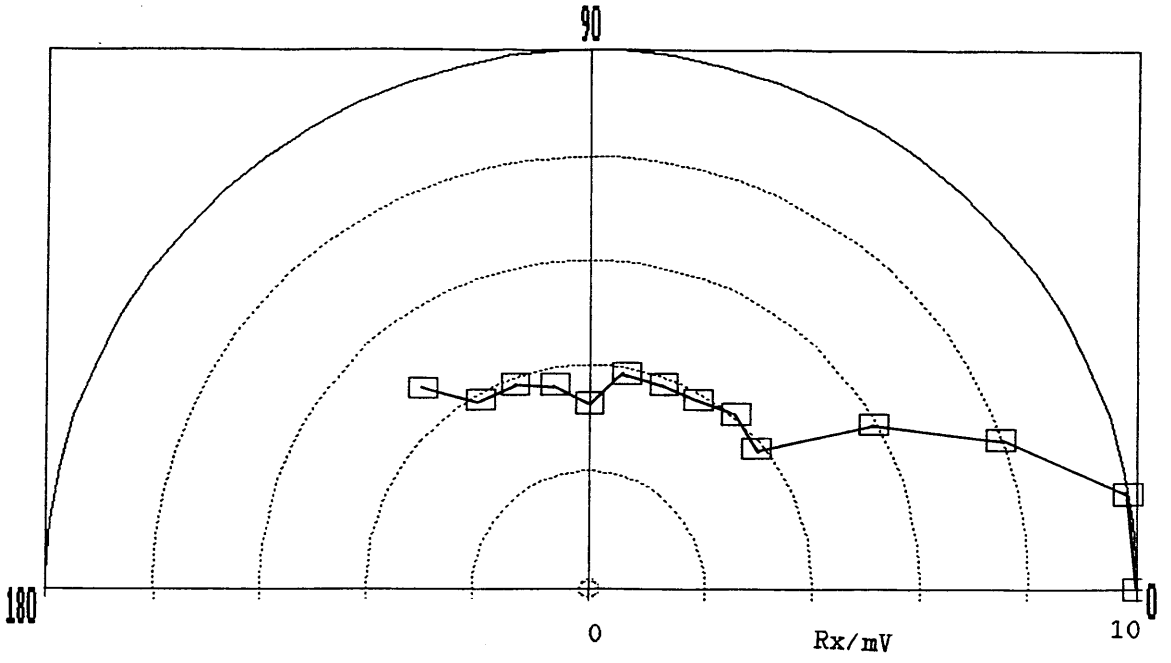

Figure 3.8g Experimental scattering from glass in water, ka=5.73

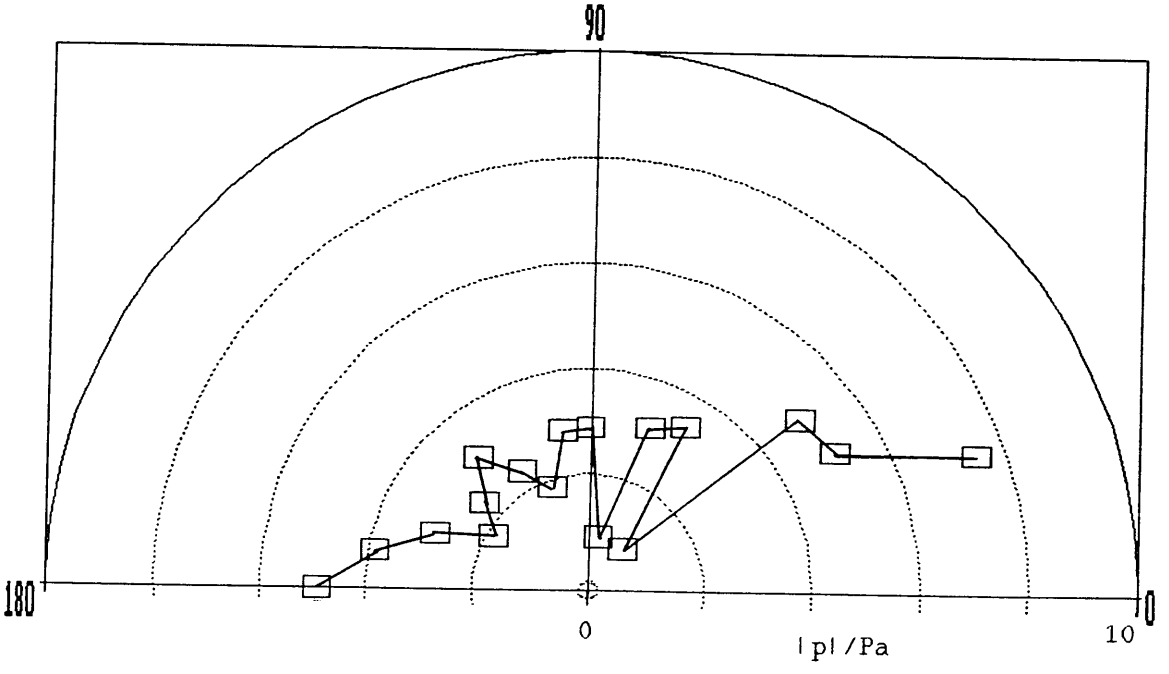

Figure 3.8g' Theoretical scattering from glass in water, ka=5.73

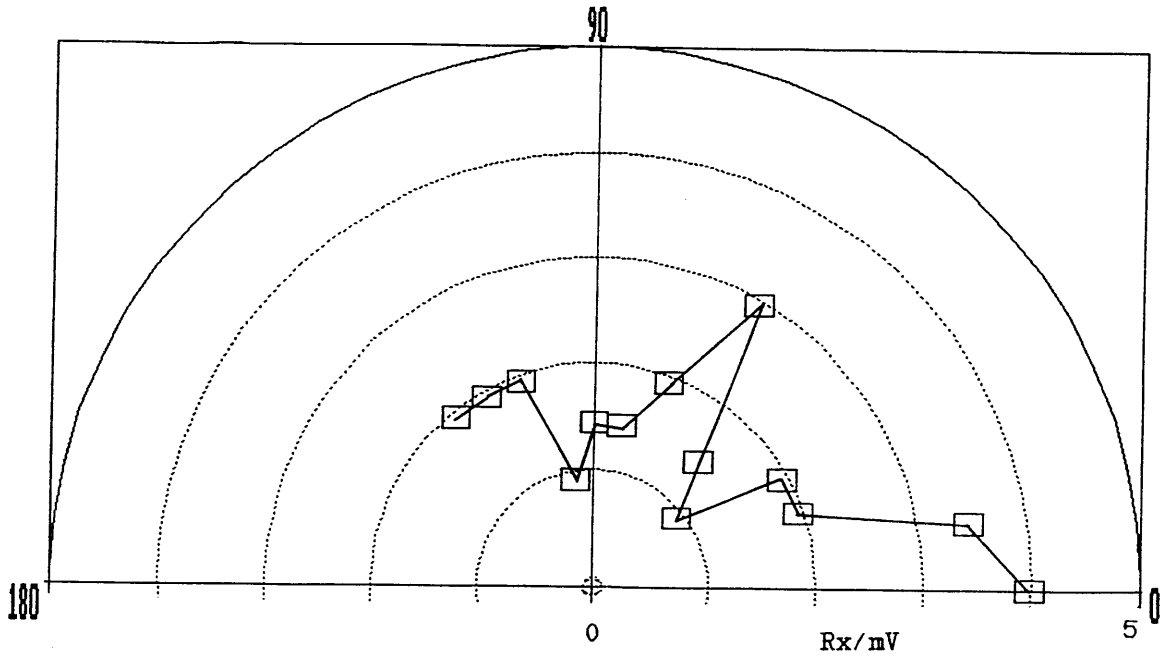

Figure 3.8h Experimental scattering from glass in water, ka=2.99

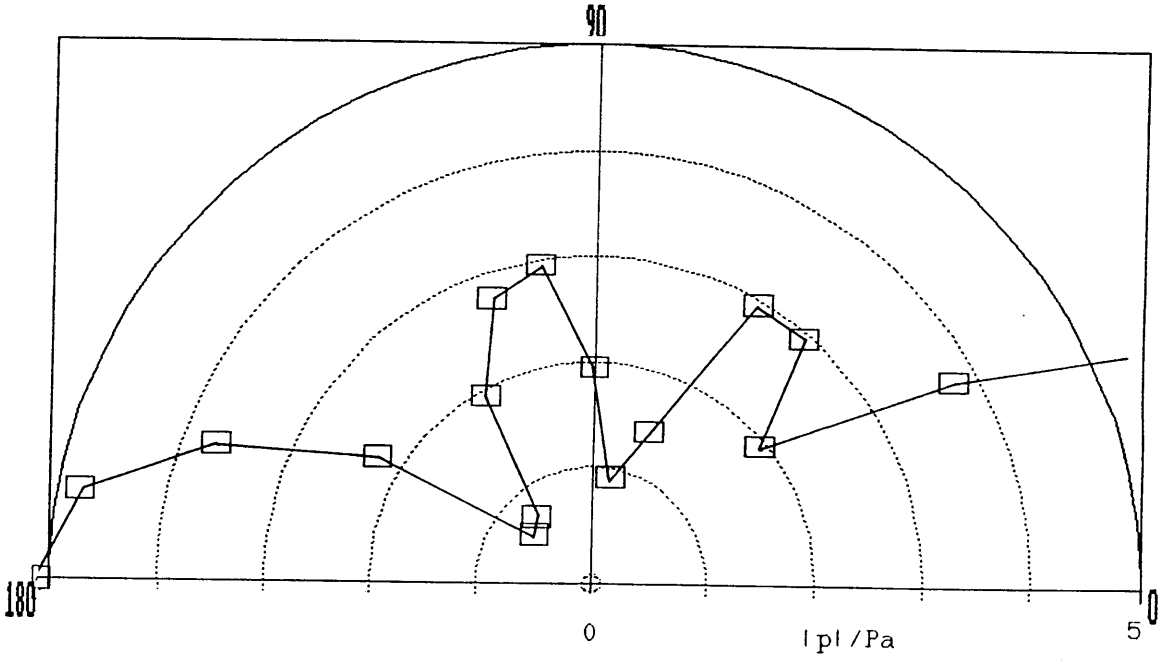

Figure 3.8h' Theoretical scattering from glass in water, ka=2.99

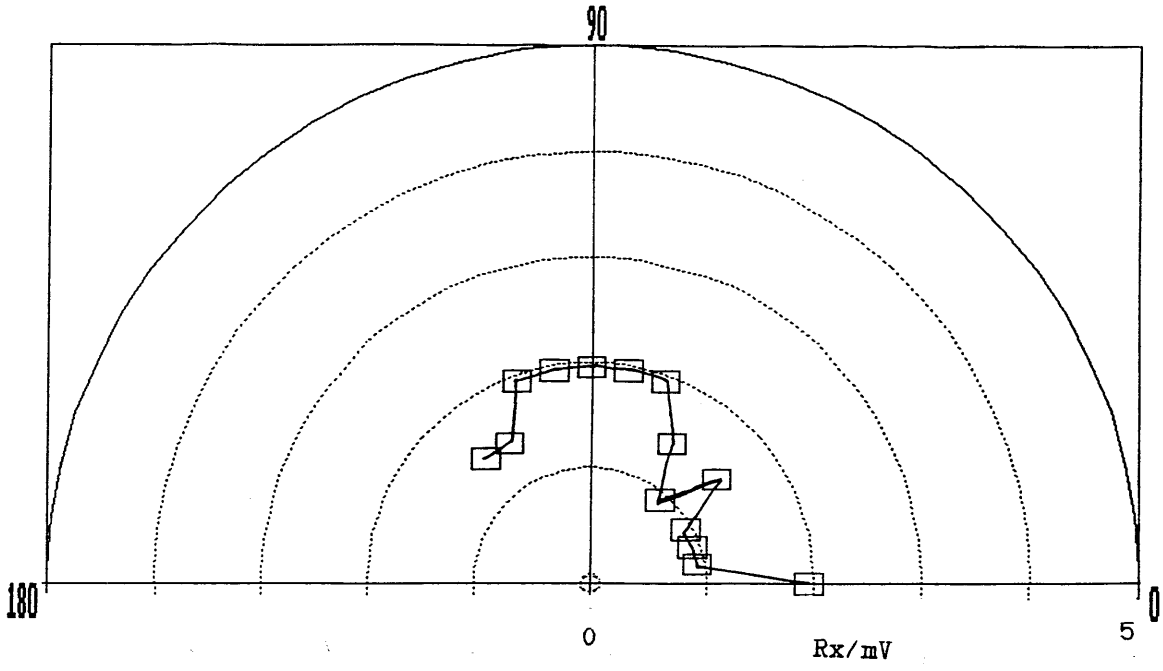

Figure 3.8i Experimental scattering from glass in water, ka=2.30

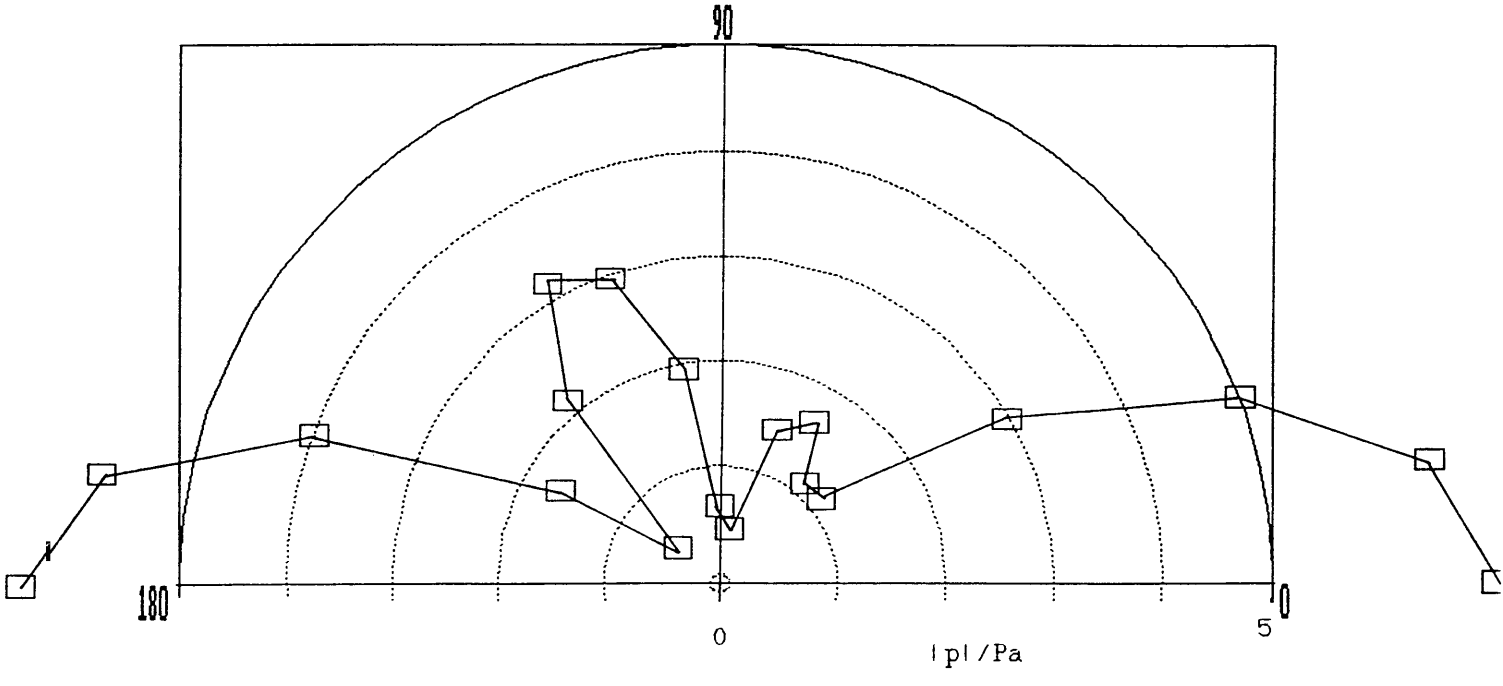

Figure 3.8i' Theoretical scattering from glass in water, ka=2.30

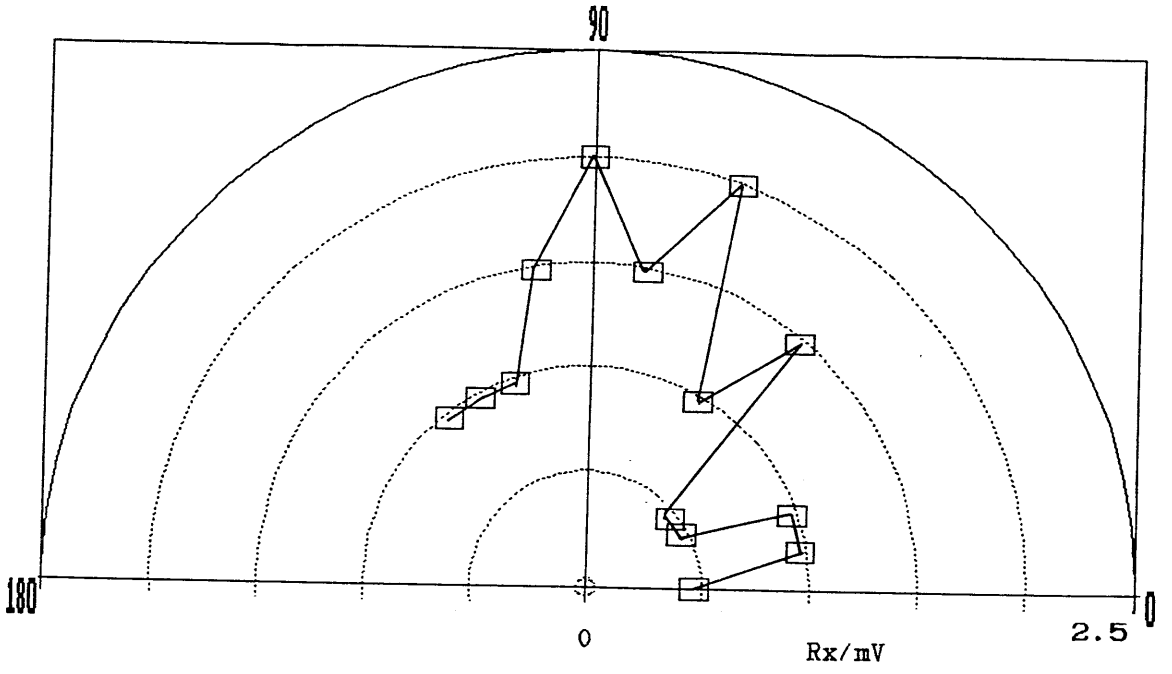

Figure 3.8j Experimental scattering from glass in ater, ka=1.94

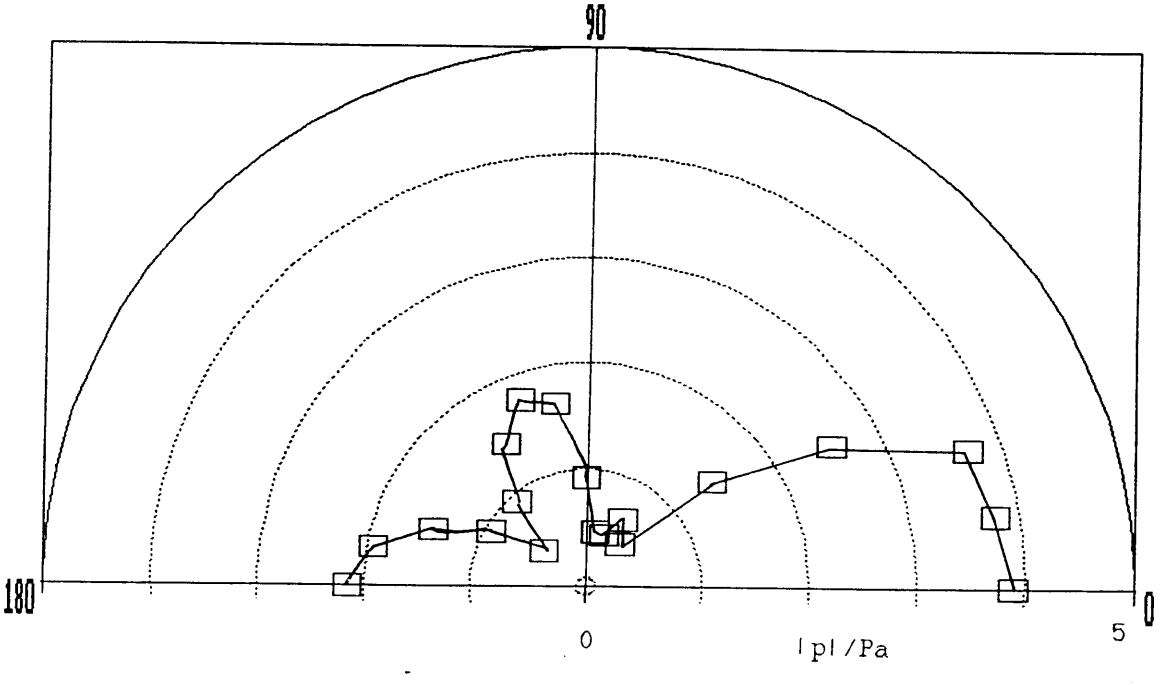

Figure 3.8j' Theoretical scattering from glass in water, ka=1.94

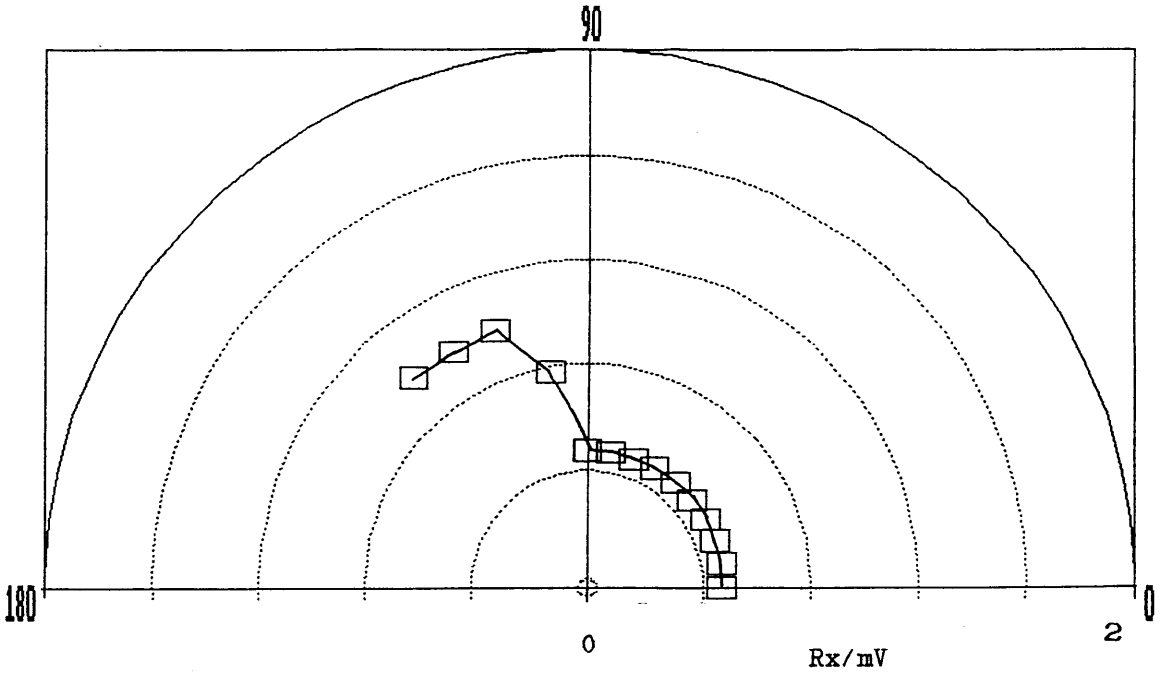

Figure 3.8k Experimental scattering from glass in water, ka=1.63

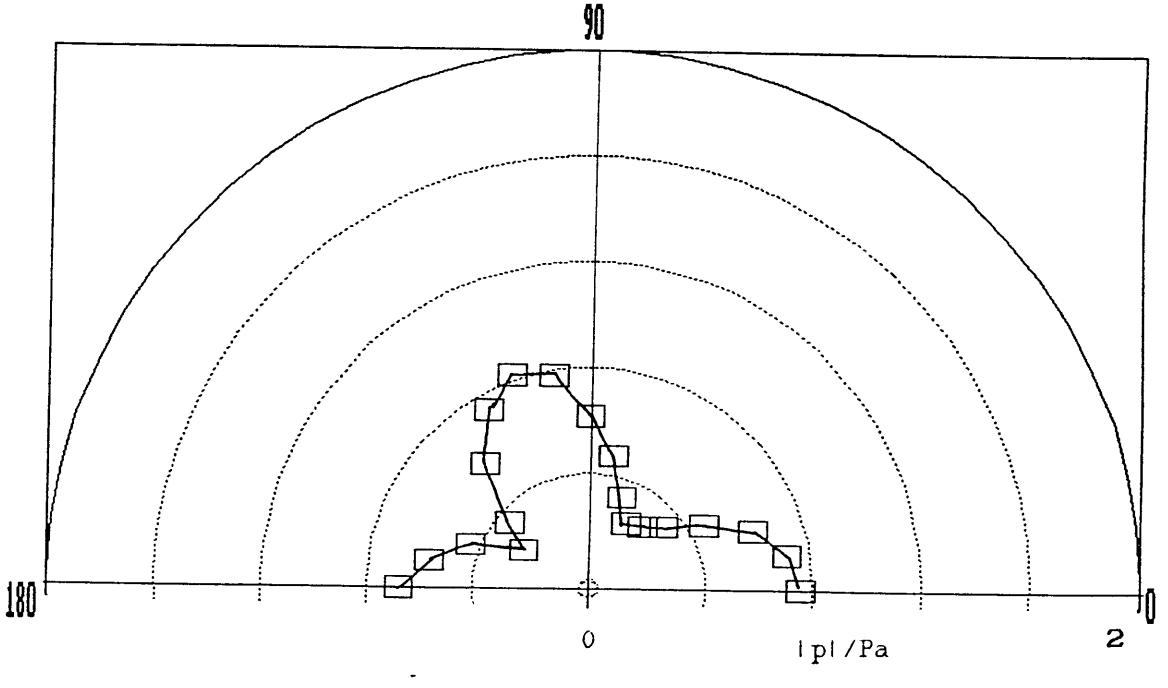

Figure 3.8k' Theoretical scattering from glass in water, ka=1.63

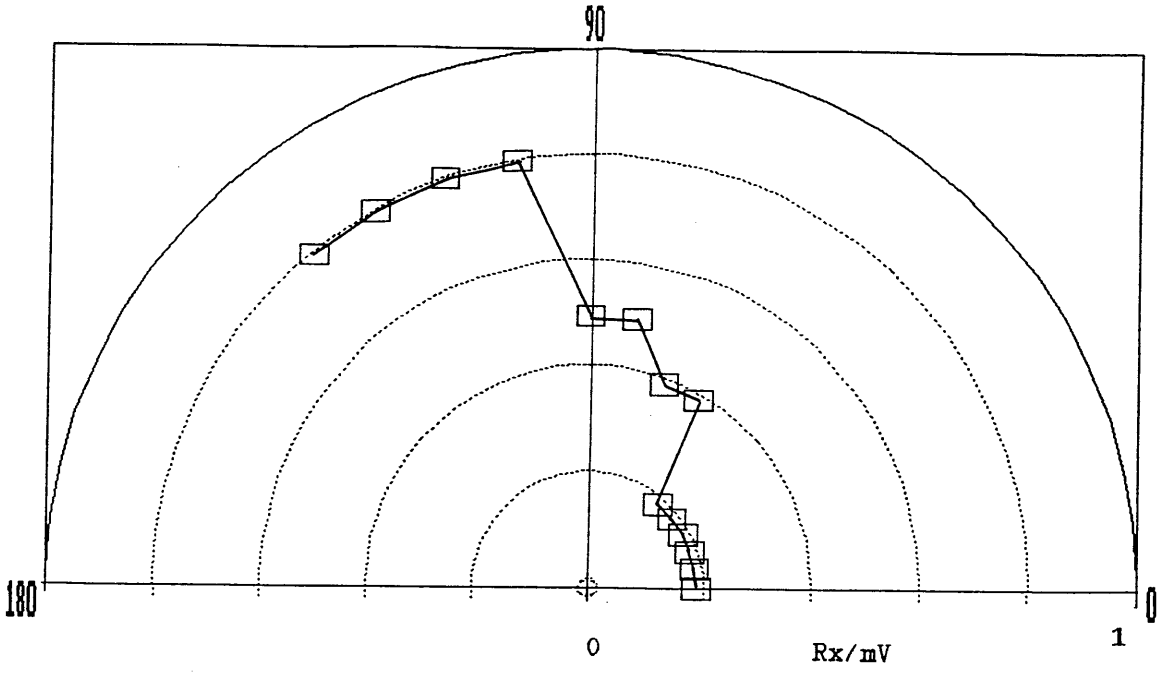

Figure 3.81 Experimental scattering from glass in water, ka=1.37

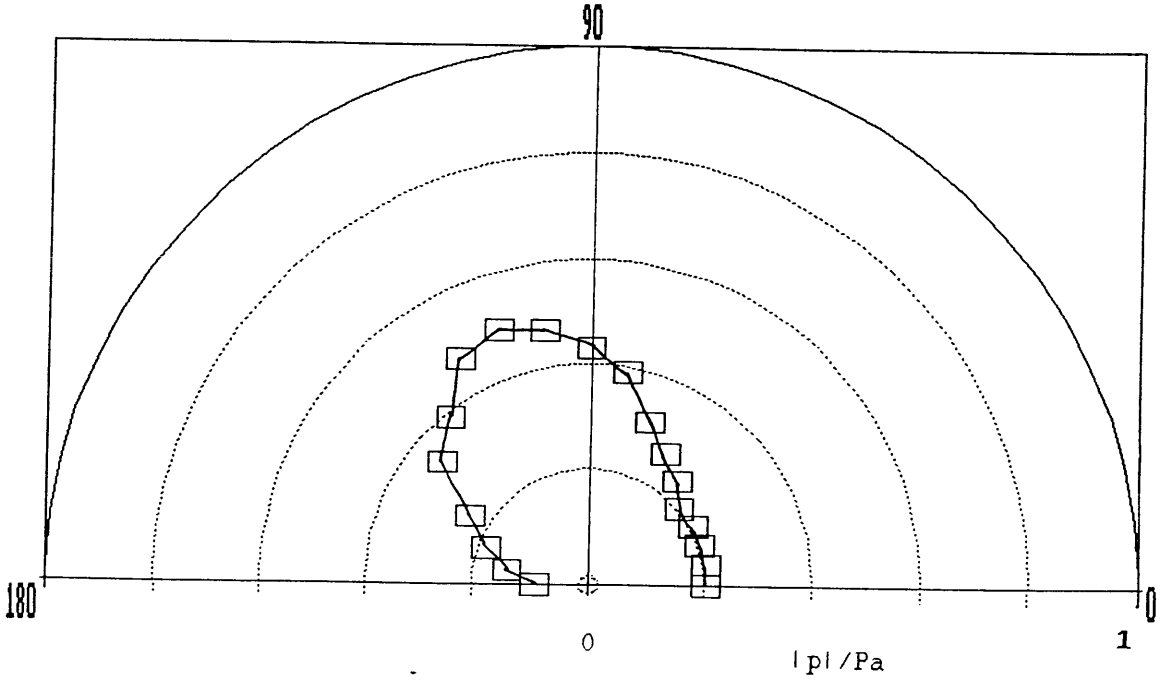

Figure 3.81' Theoretical scattering from glass in water, ka=1.37

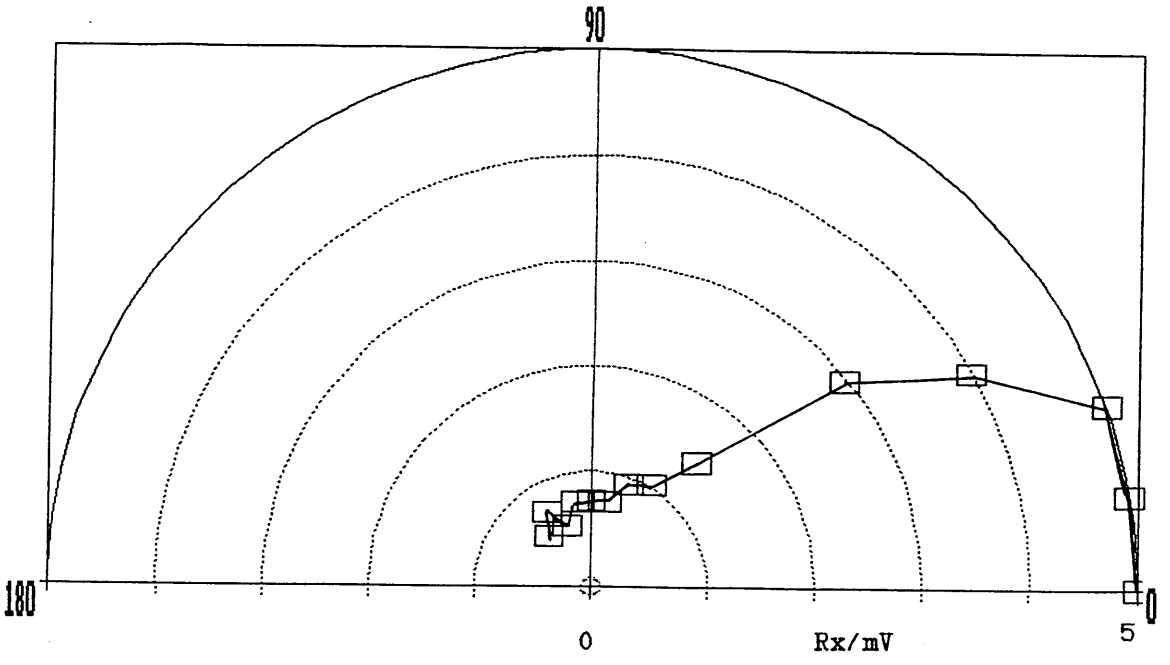

Figure 3.8m Experimental scattering from water in kerosene, ka=5.40

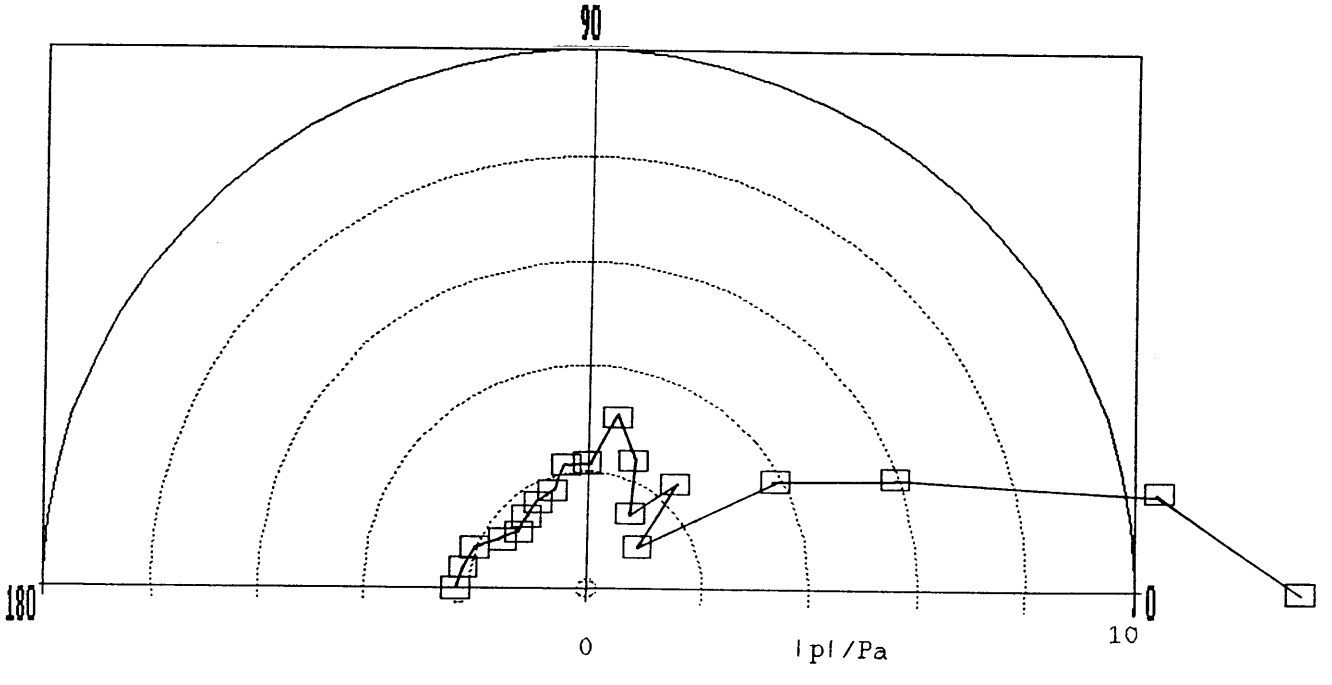

Figure 3.8m' Theoretical scattering from water in kerosene, ka=5.40

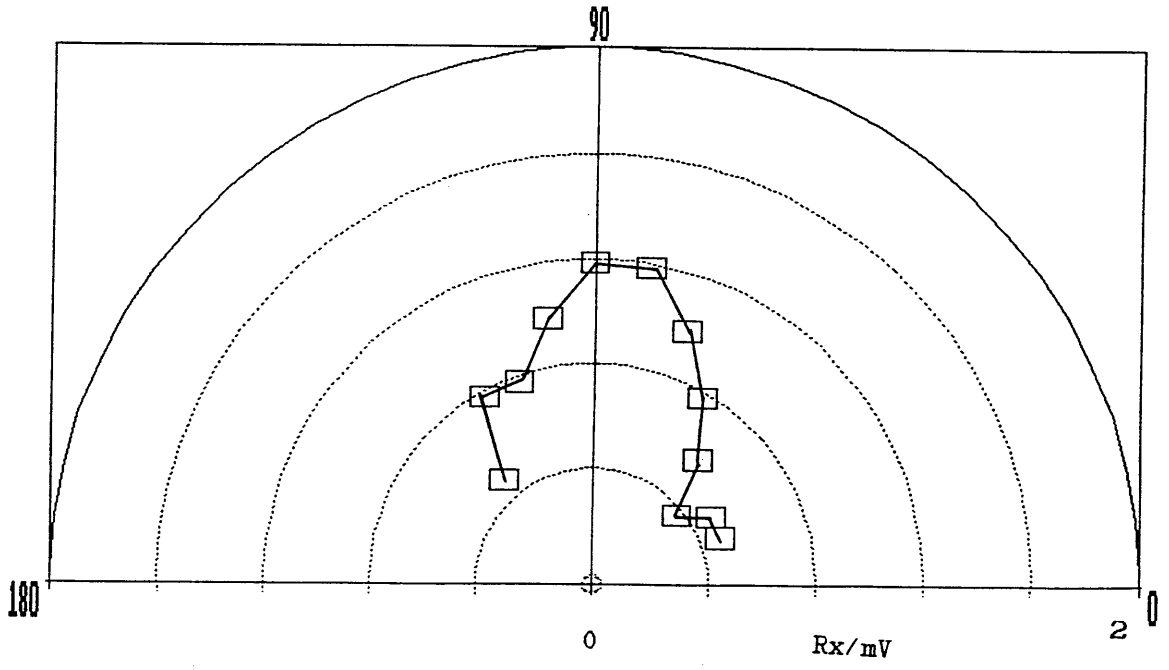

Figure 3.8n Experimental scattering from water in kerosene, ka=1.99

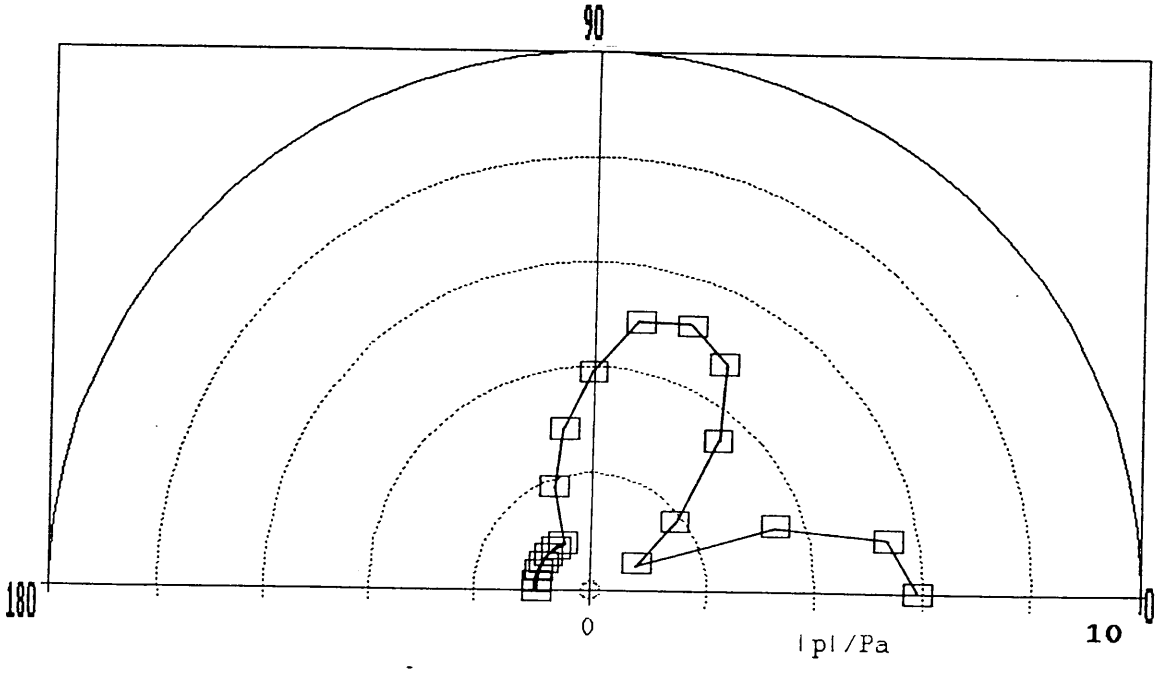

Figure 3.8n' Theoretical scattering from water in kerosene, ka=1.99

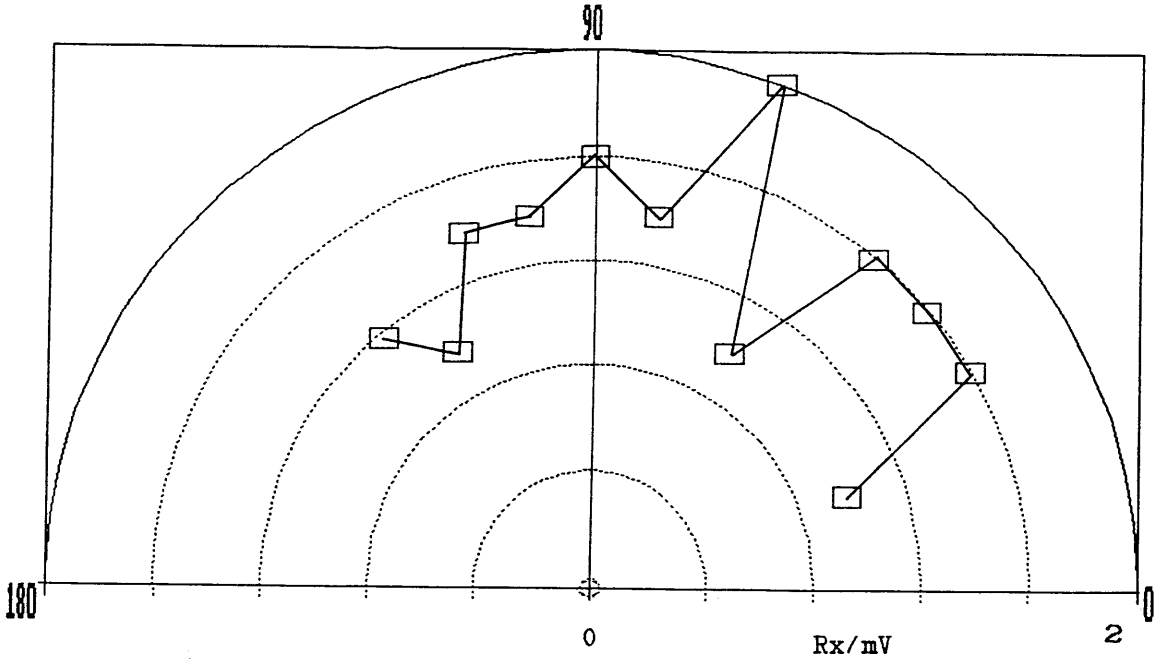

Figure 3.8o Experimental scattering from water in kerosene, ka=4.24

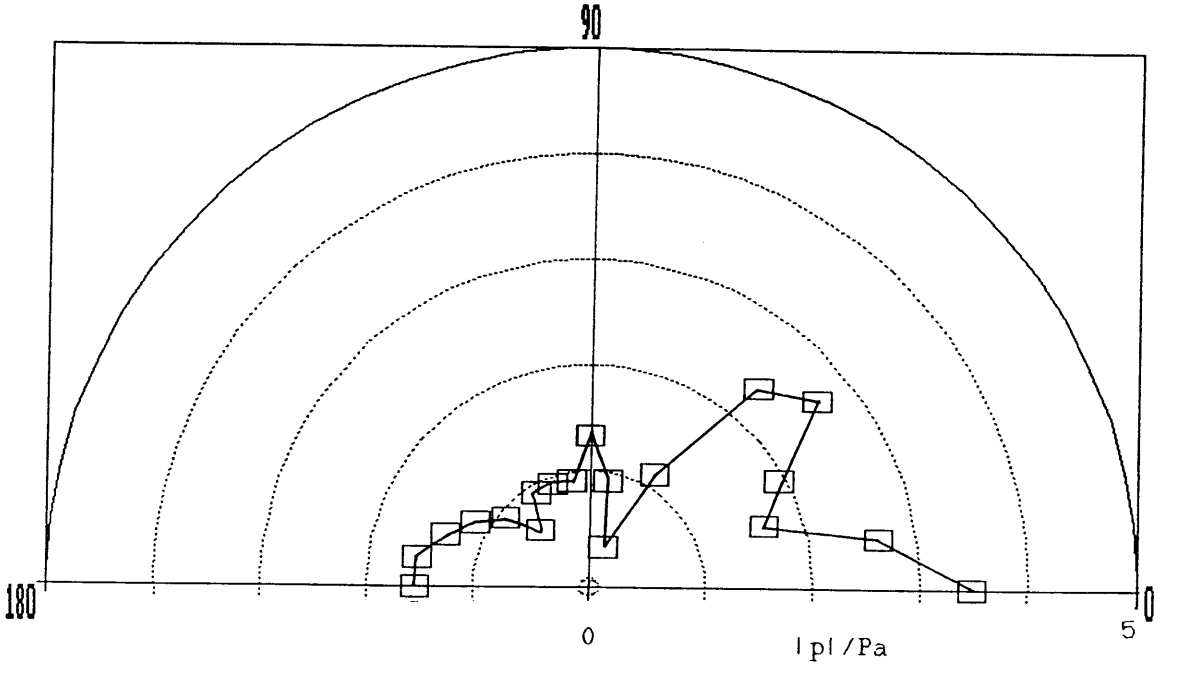

Figure 3.8o' Theoretical scattering from water in kerosene, ka=4.24

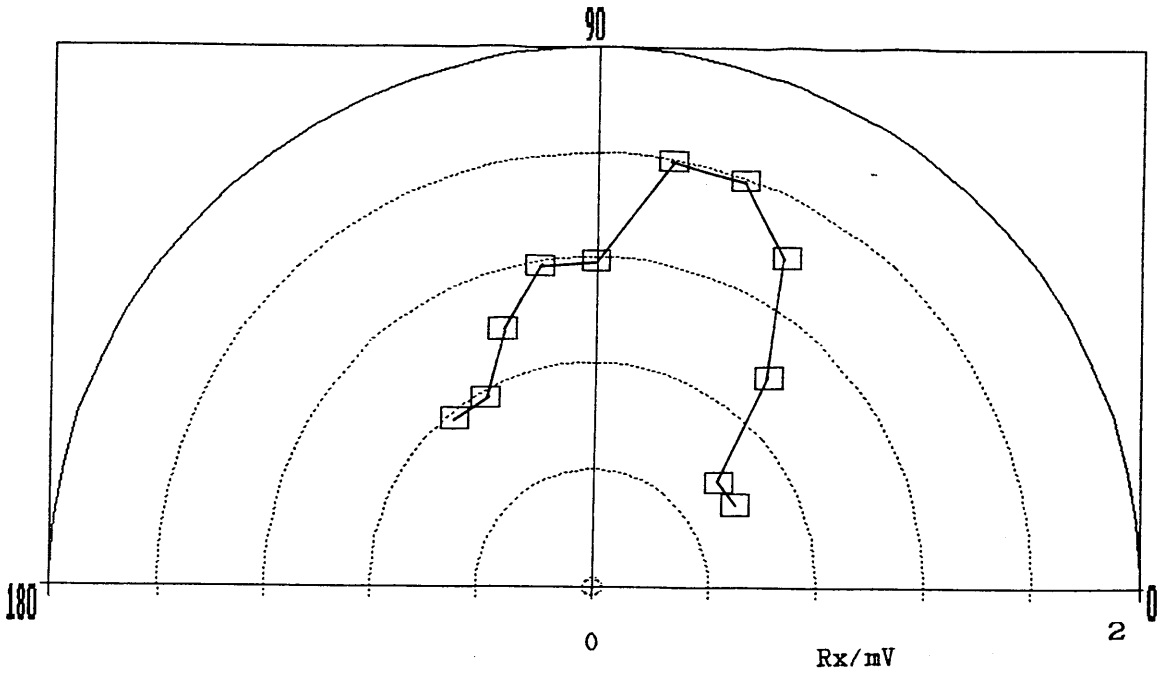

Figure 3.8p Experimental scattering from water in kerosene, ka=5.40

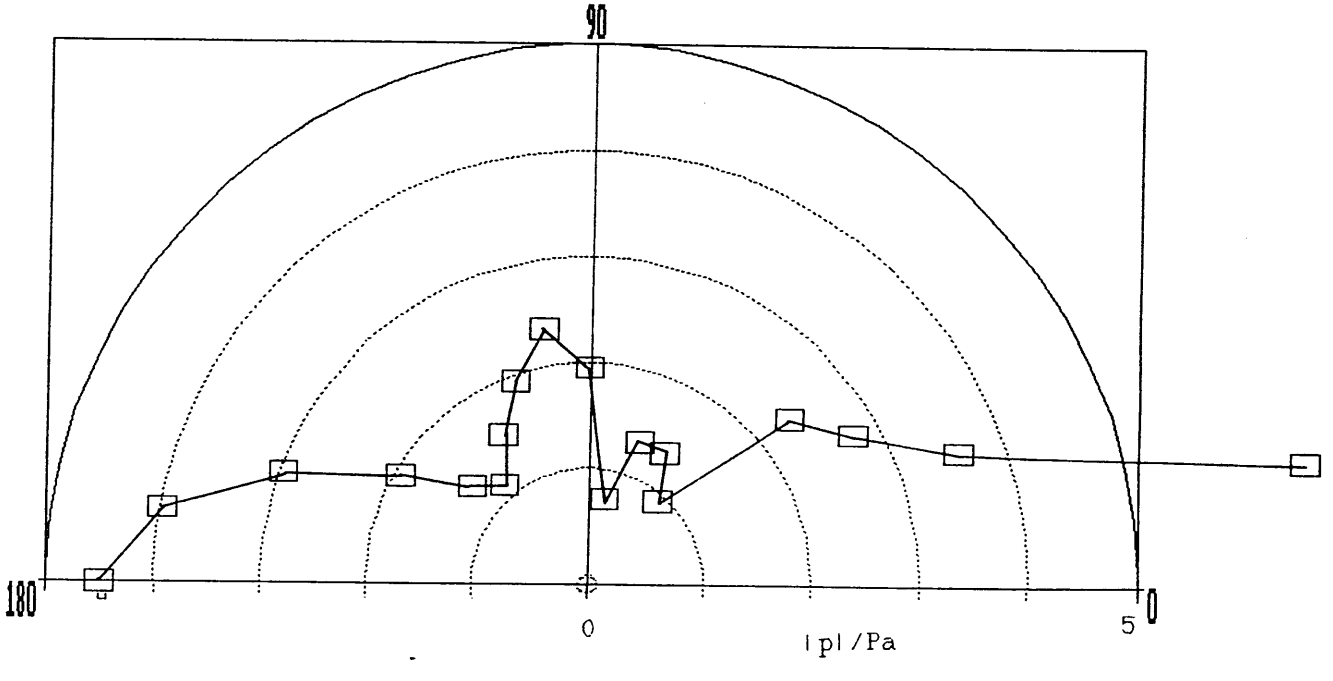

Figure 3.8p' Theoretical scattering from water in kerosene, ka=5.4

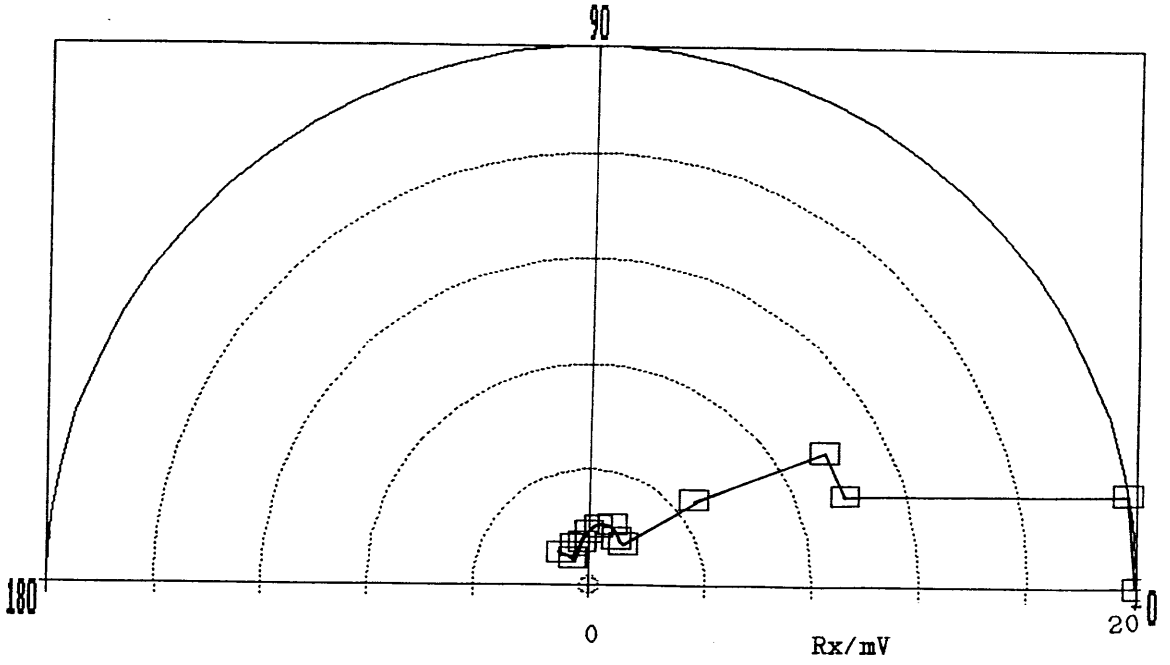

Figure 3.8q Experimental scattering from water in kerosene, ka=6.00

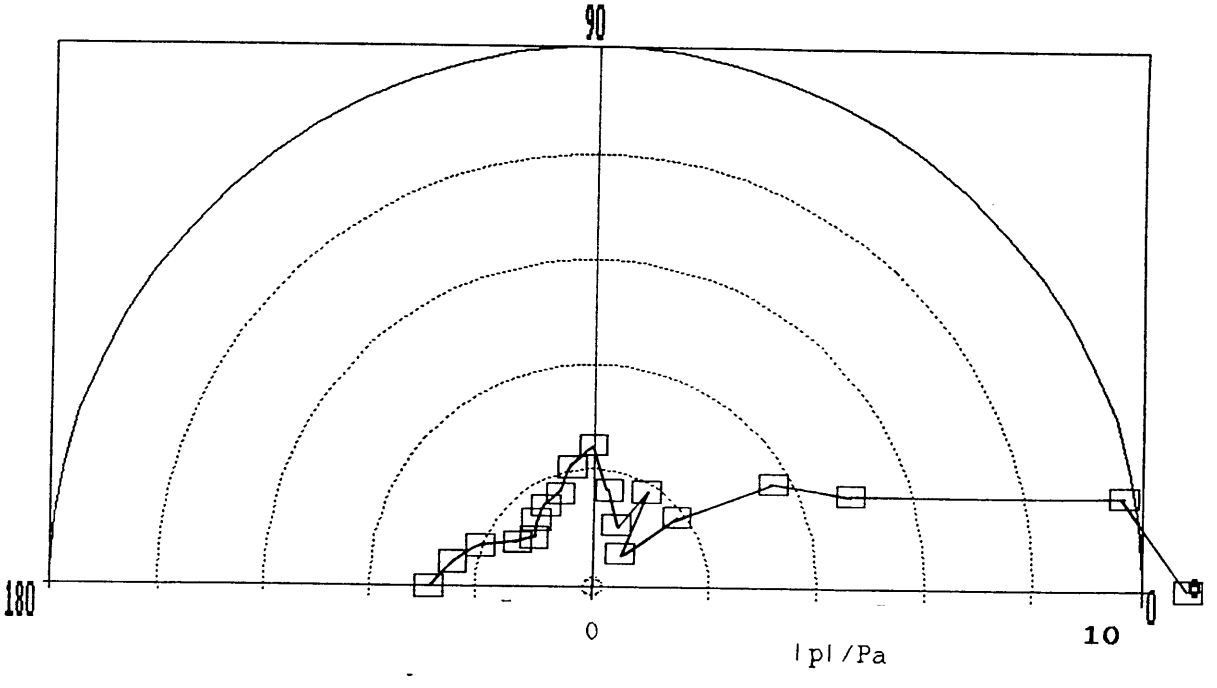

Figure 3.8q' Theoretical scattering from water in kerosene, ka=6.00

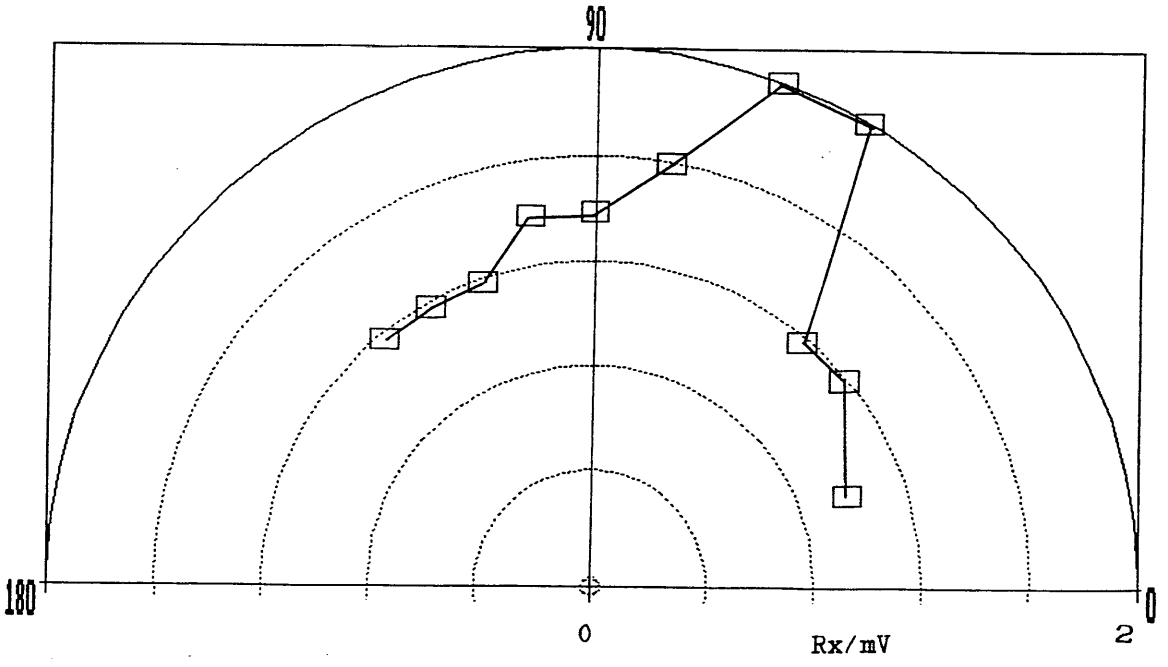

Figure 3.8r Experimental scattering from water in kerosene, ka=2.87

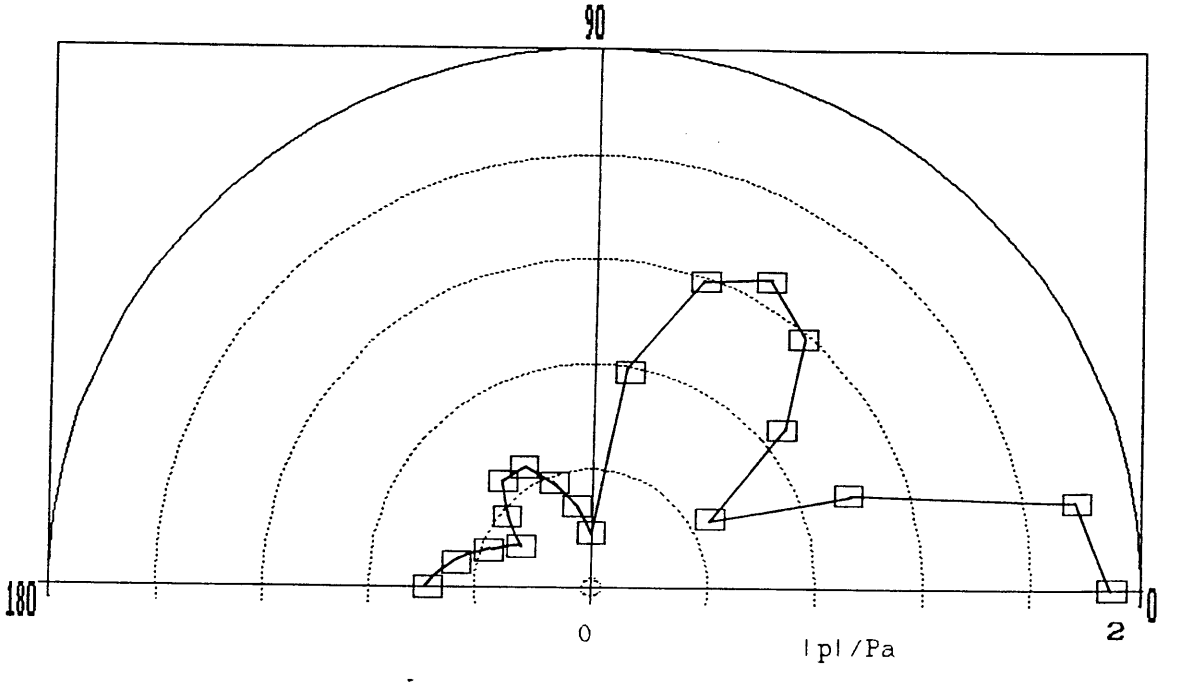

Figure 3.8r' Theoretical scattering from water in kerosene, ka=2.87

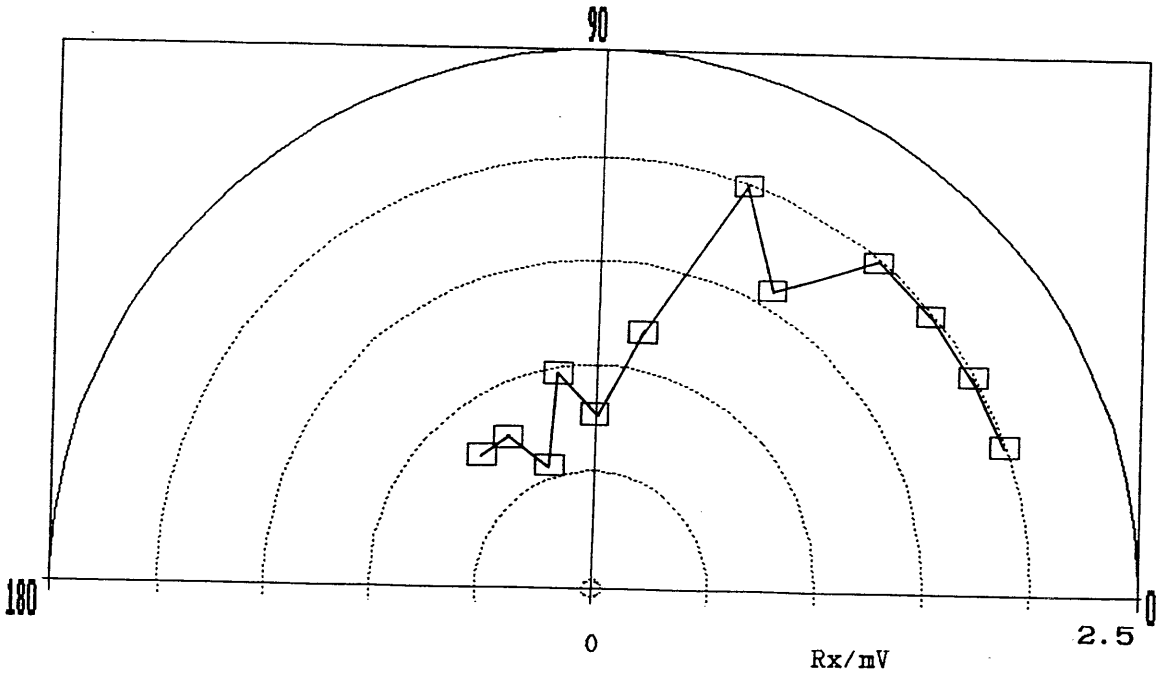

Figure 3.8s Experimental scattering from water in kerosene, ka=3.32

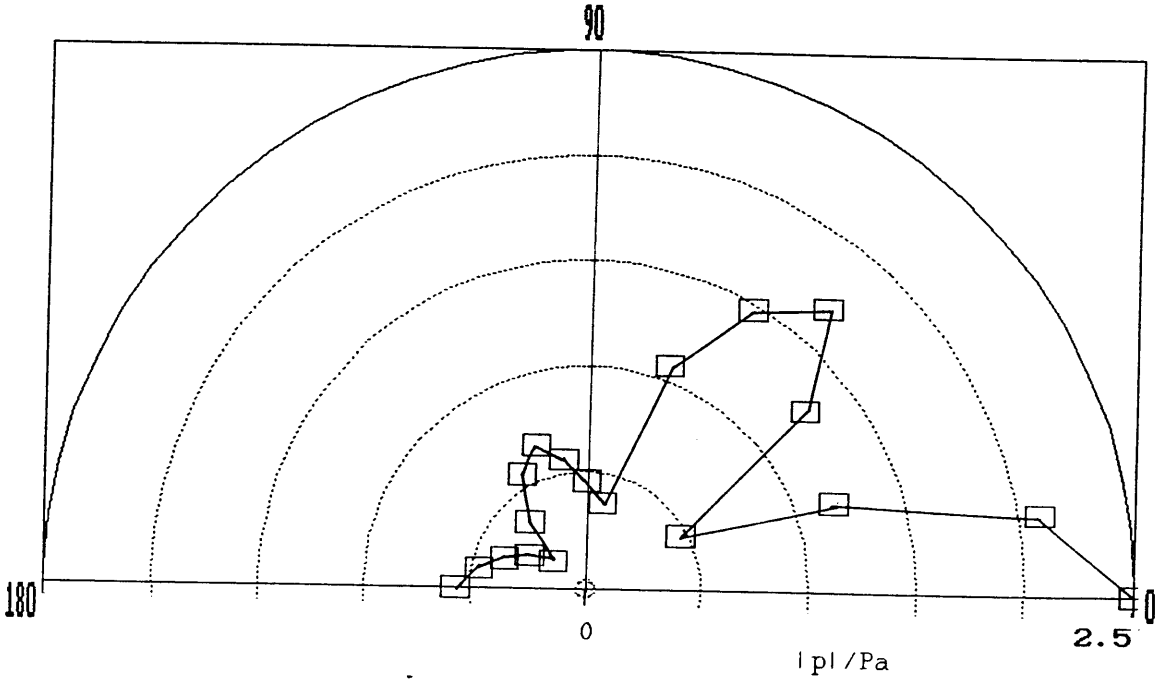

Figure 3.8s' Theoretical scattering from water in kerosene, ka=3.32

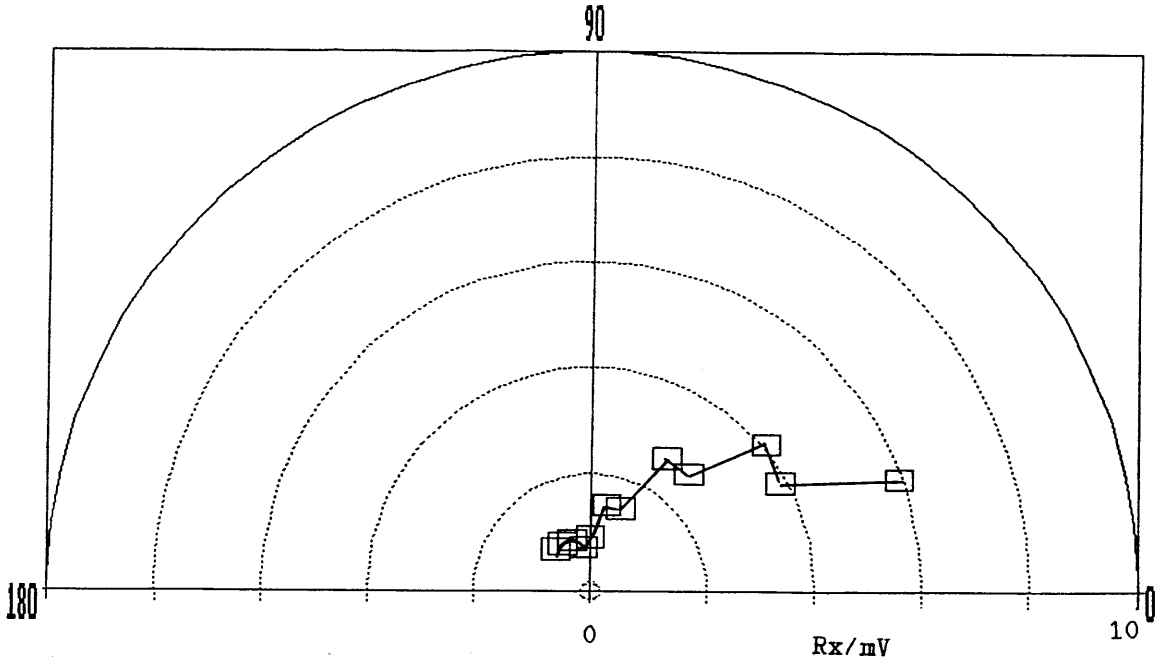

Figure 3.8t Experimental scattering from water in kerosene, ka=3.52

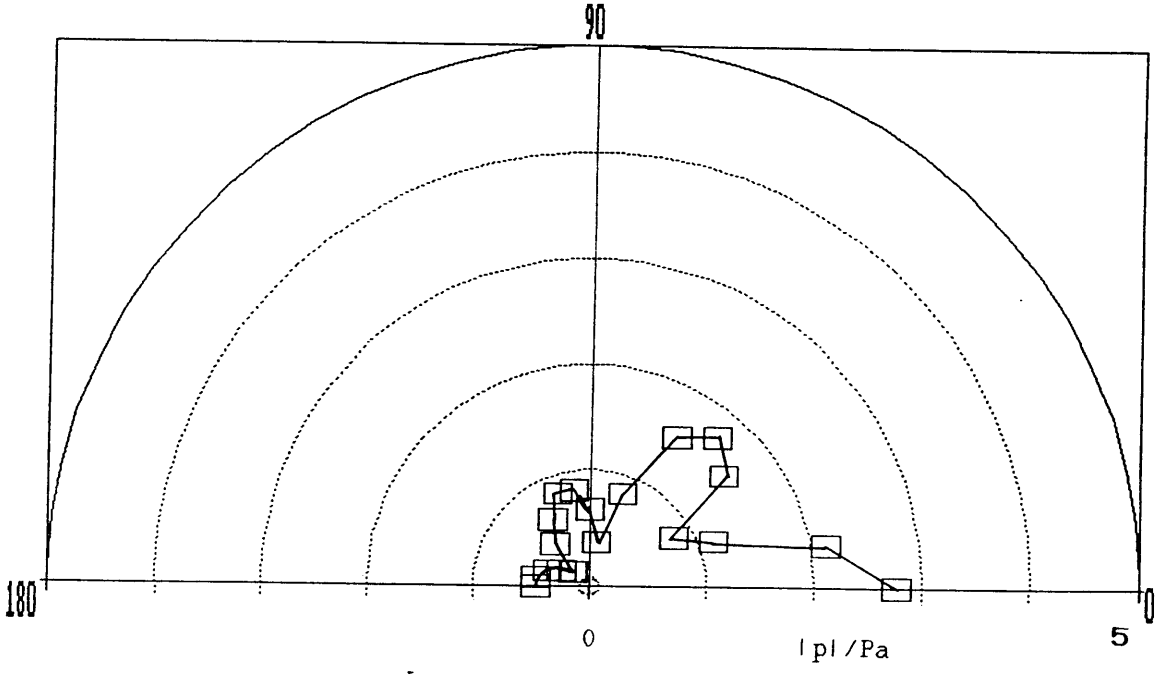

Figure 3.8t' Theoretical scattering from water in kerosene, ka=3.52

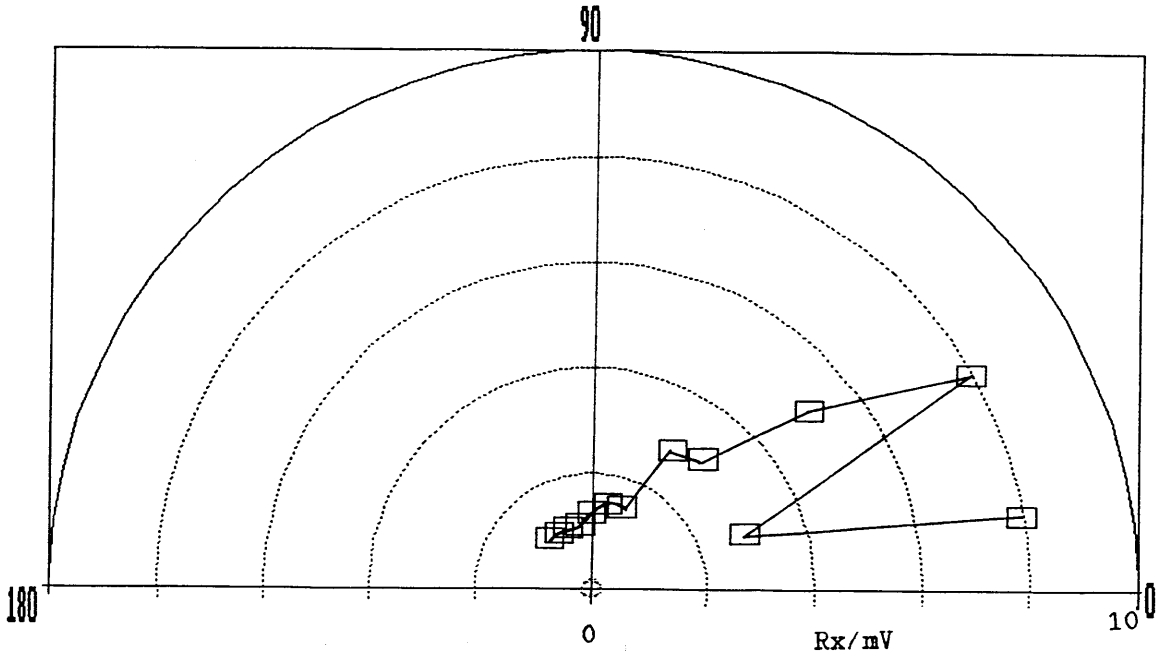

Figure 3.8u Experimental scattering from water in kerosene, ka=3.93

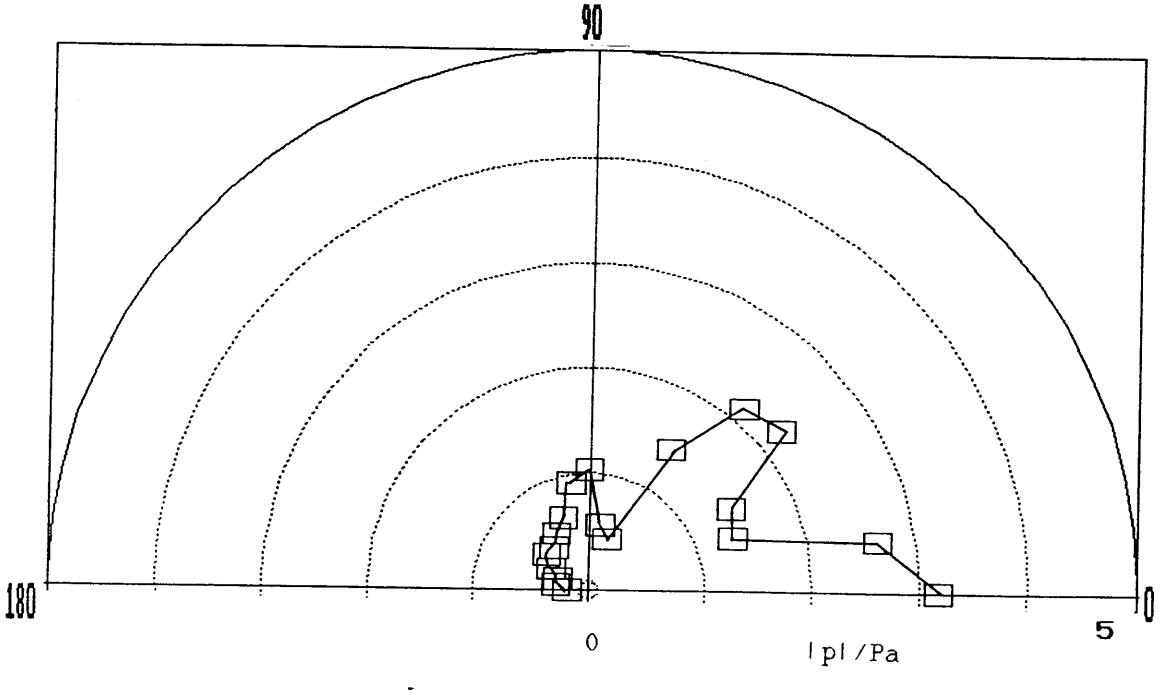

Figure 3.8u' Theoretical scattering from water in kerosene, ka=3.93

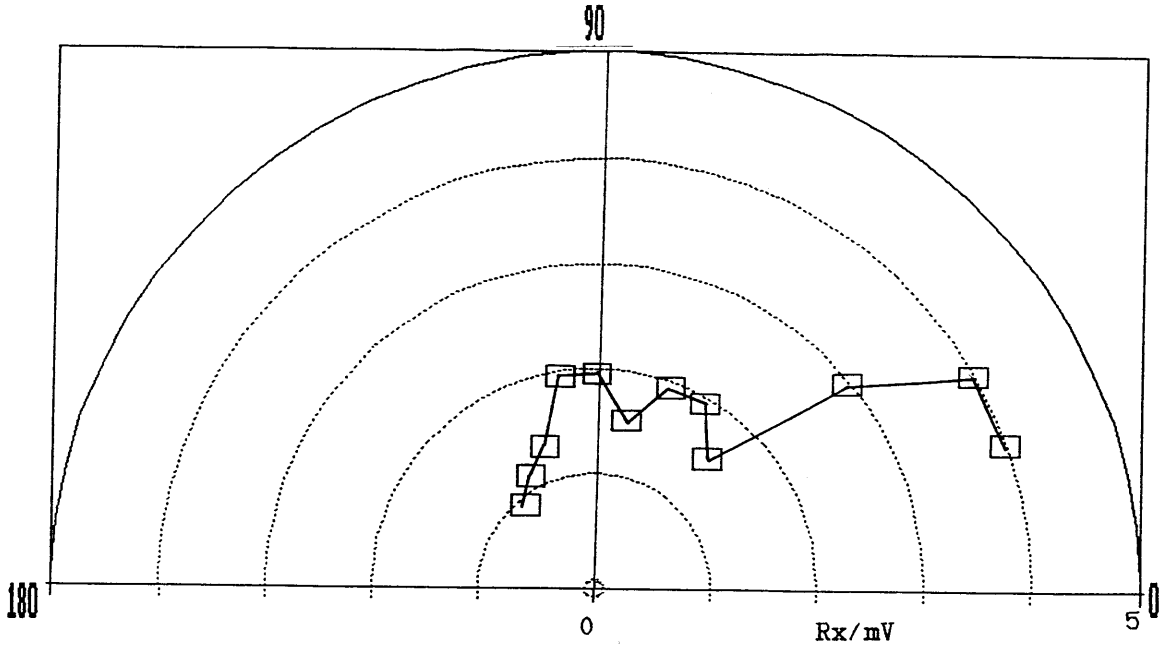

Figure 3.8v Experimental scattering from iron in kerosene, ka=3.52

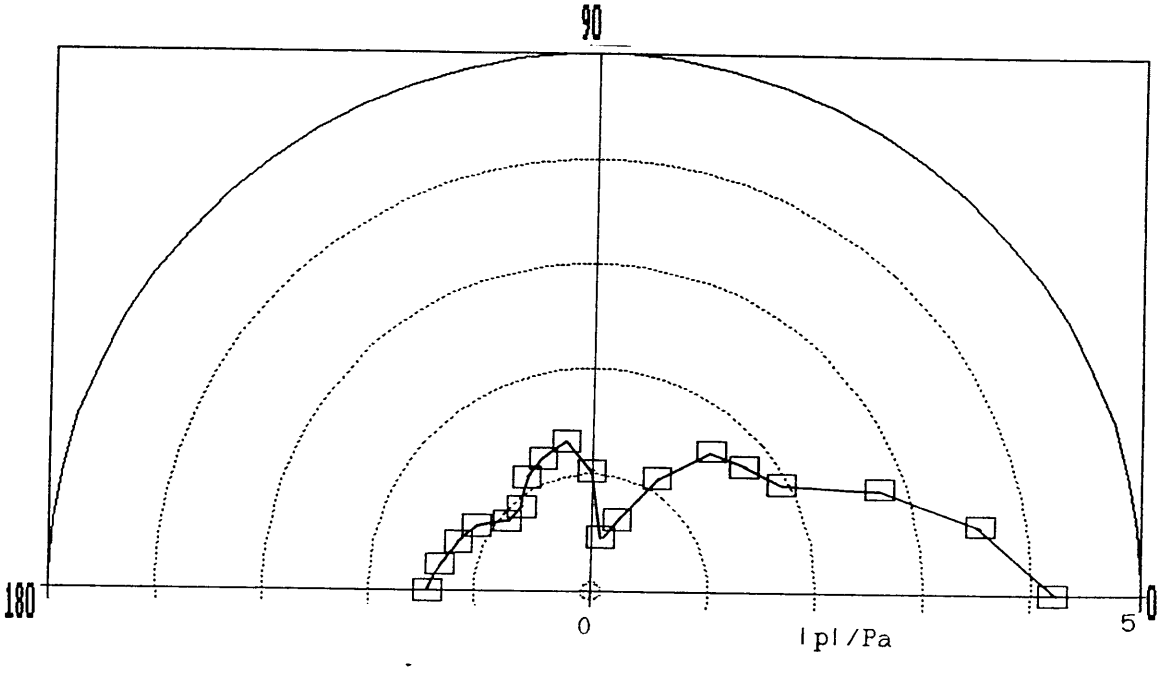

Figure 3.8v' Theoretical scattering from iron in kerosene, ka=3.52

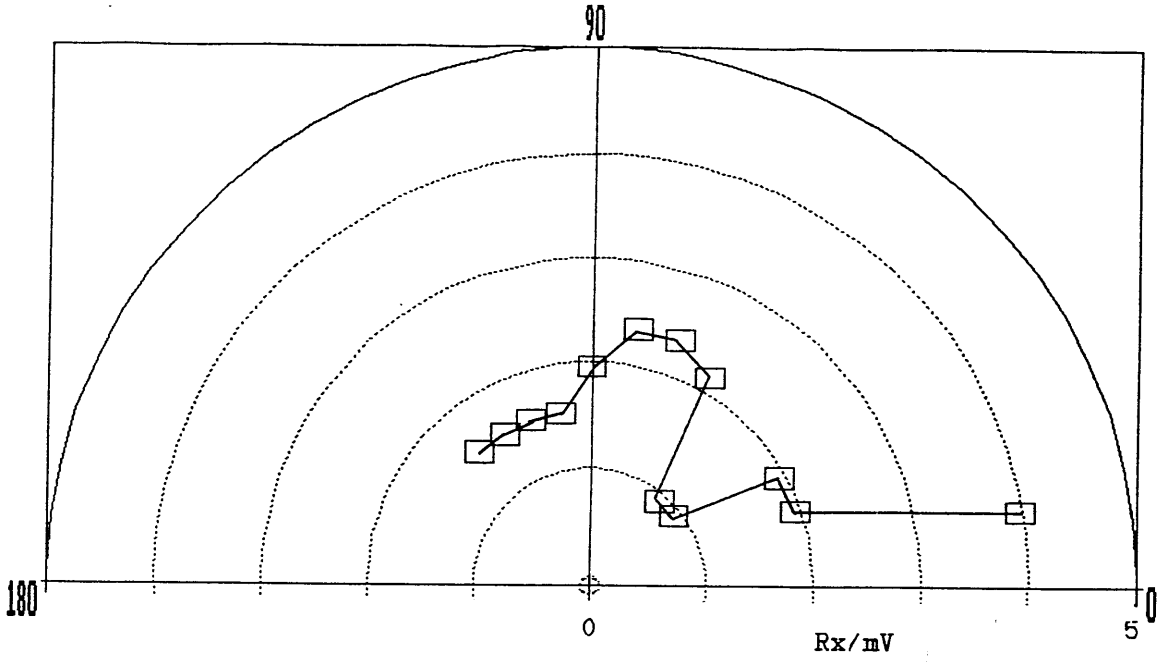

Figure 3.8w Experimental scattering from iron in kerosene, ka=2.97

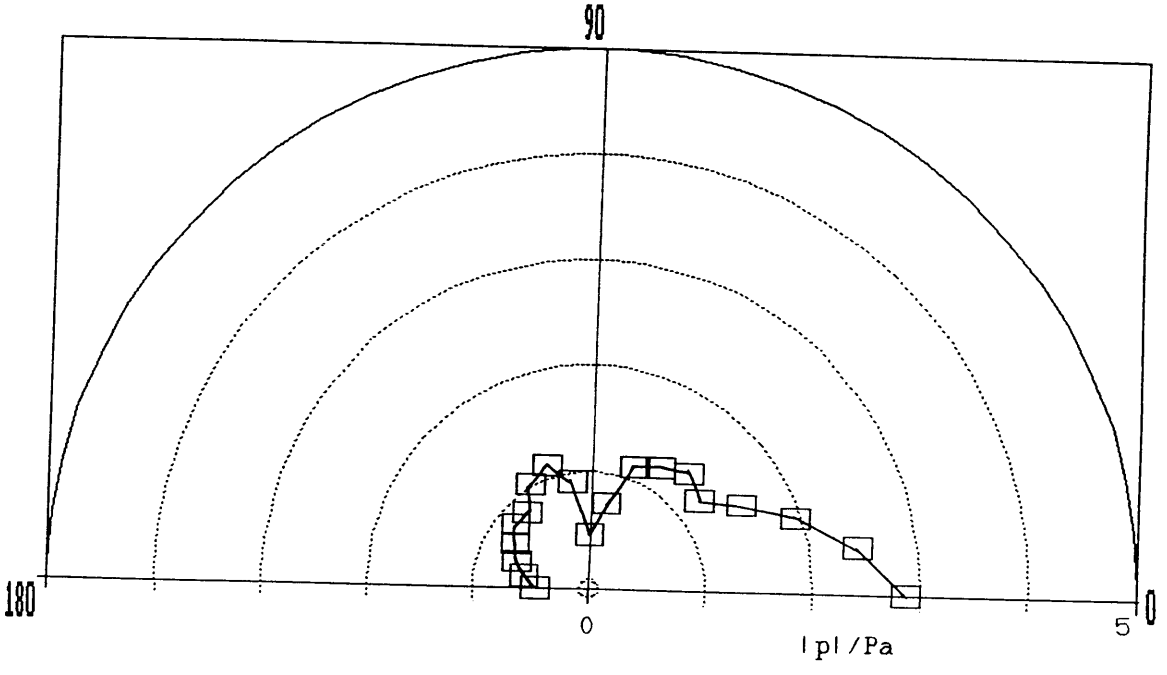

Figure 3.8w' Theoretical scattering from iron in kerosene, ka=2.97

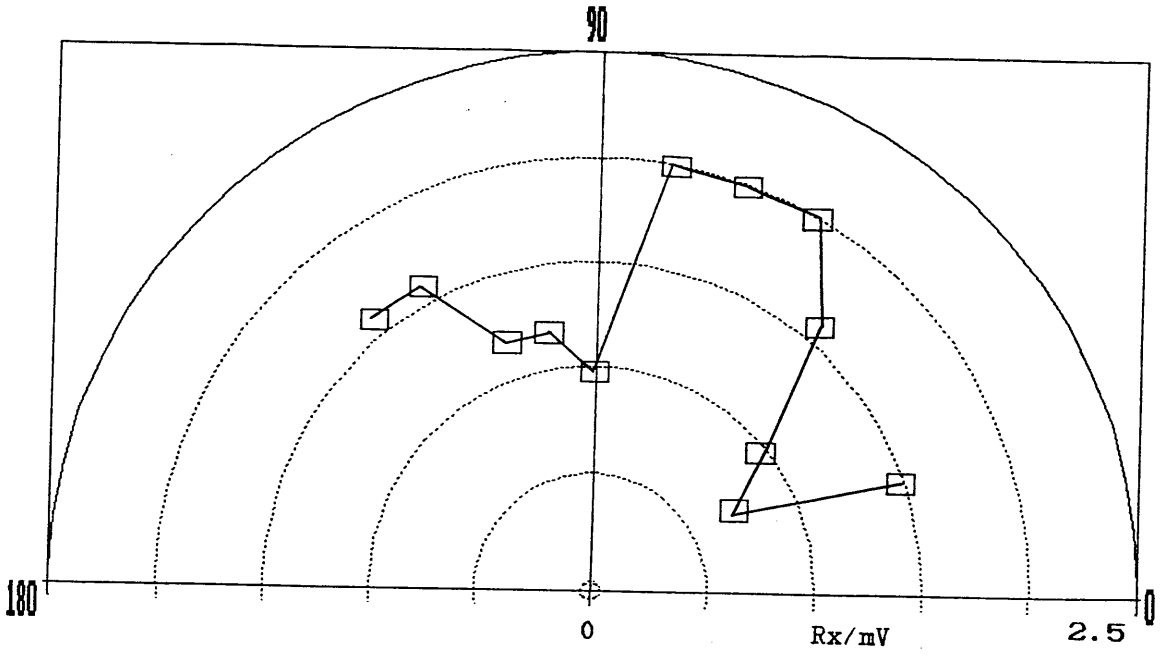

Figure 3.8x Experimental scattering from iron in kerosene, ka=2.52

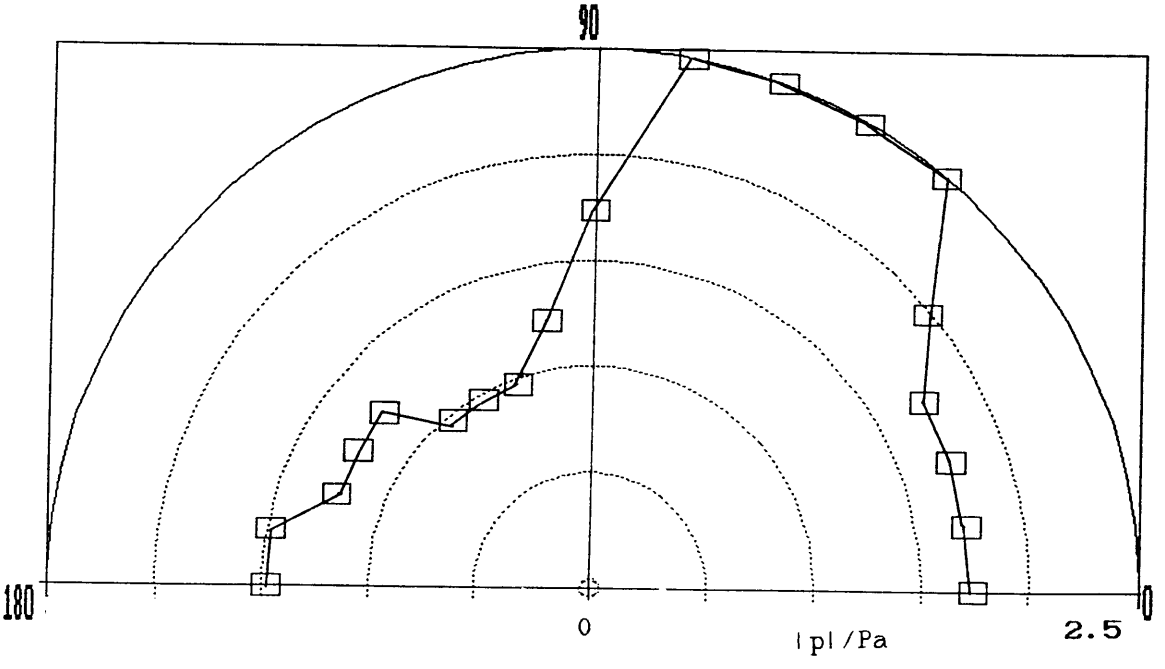

Figure 3.8x' Theoretical scattering from iron in kerosene, ka=2.52

carried out. The fluid flow was not great enough to suspend these particles, and so the particles were graded and dropped through the acoustic observation section one at a time.

The experimental measurements were taken every 10^0 from $+130^0$ to -130^0, with a minimum of 10 measurements at each angle. The droplet was moved through the observation section by varying the flow, thus ensuring the droplet was at the point of maximum acoustic intensity of the beam, and hence producing repeatability from droplet to droplet. The voltage of the peak was measured directly on an oscilloscope. For $\theta<30^0$, the signal from the droplet arrives at the receiver at the same time as the signal from the front and rear walls, producing one combined signal, as described in the last section. Thus the droplet was moved in and out of the observation section, till the change in signal due to the presence of the droplet was found to be a maximum, implying the signal scattered from the droplet is in phase with those from the walls and that the droplet is on the axis of the transmitted signal.

None of the experiments showed any discrepancy between $V(+\theta)$ and $V(-\theta)$ greater than the experimental error that could not be accounted for (and eliminated) as a changing experimental parameter, such as an impurity on the wall of the observation section.

3.9 Discussion and Conclusions.

Starting from first principles, this chapter has considered the scattering of an acoustic wave from a fluid sphere. The ultrasonic properties of the experimental apparatus have been studied in detail, so as to reveal the best method for determining the scattered pressure from individual spheres.

The use of the full scattering equation when comparing theoretical and experimental scattering profiles, has produced good agreement over the full range of scatterer parameters (acoustic impedance and size), in the general shapes and sizes of the signals. Nodes and peaks in the scattered profile occurring at approximately the correct angles and

the relative sizes of the peaks also show good agreement. The effect of approximating the general theory, ie assuming the fluid spheres to be solid, has not been considered at this stage, but will be detailed in the next chapter.

Section 3.8 listed a series of results over a range of scatterer properties. Figures 3.9a, b and c, contain a selection of these in the form of three series of results from which several qualitative but important conclusions can be made, as published in Oddie et al (1989,1990) and Lenn et al (1990).

In each case, increasing the size of the scatterer increases the forward scattered signal, in agreement with the theory. Where a distinct broad minimum is found in theory, a dip in the scattered profile is found experimentally. The sharper dips cannot be resolved, due to the finite size of the receiver. In general there is a simple linear scaling between the experimental and theoretical results across the whole range of scatterer properties displayed here.

There are also a few inconsistent results, for example the spikes appearing on a few of the results. These are not directly attributable to experimental error, since all of the data is a compilation of the results from scattering angles of $+\theta$ and $-\theta$, and the spikes were observed on both. An error analysis of these scattering experiments will be given in chapter 4, where quantitative conclusions will be outlined.

At this stage the qualitative conclusion is that an individual particle produces a unique scattering profile and can be sized using just the profile of the scattered pressure, with the position and amplitude of the nodes and lobes, or possibly, the ratio of the scattered pressure through two different angles (see chapter 5 for details of this latter method in use)

The following chapter will consider characterising the particles using the wave scattered through a single angle, as a function of frequency (ie ka instead of just the radius a).

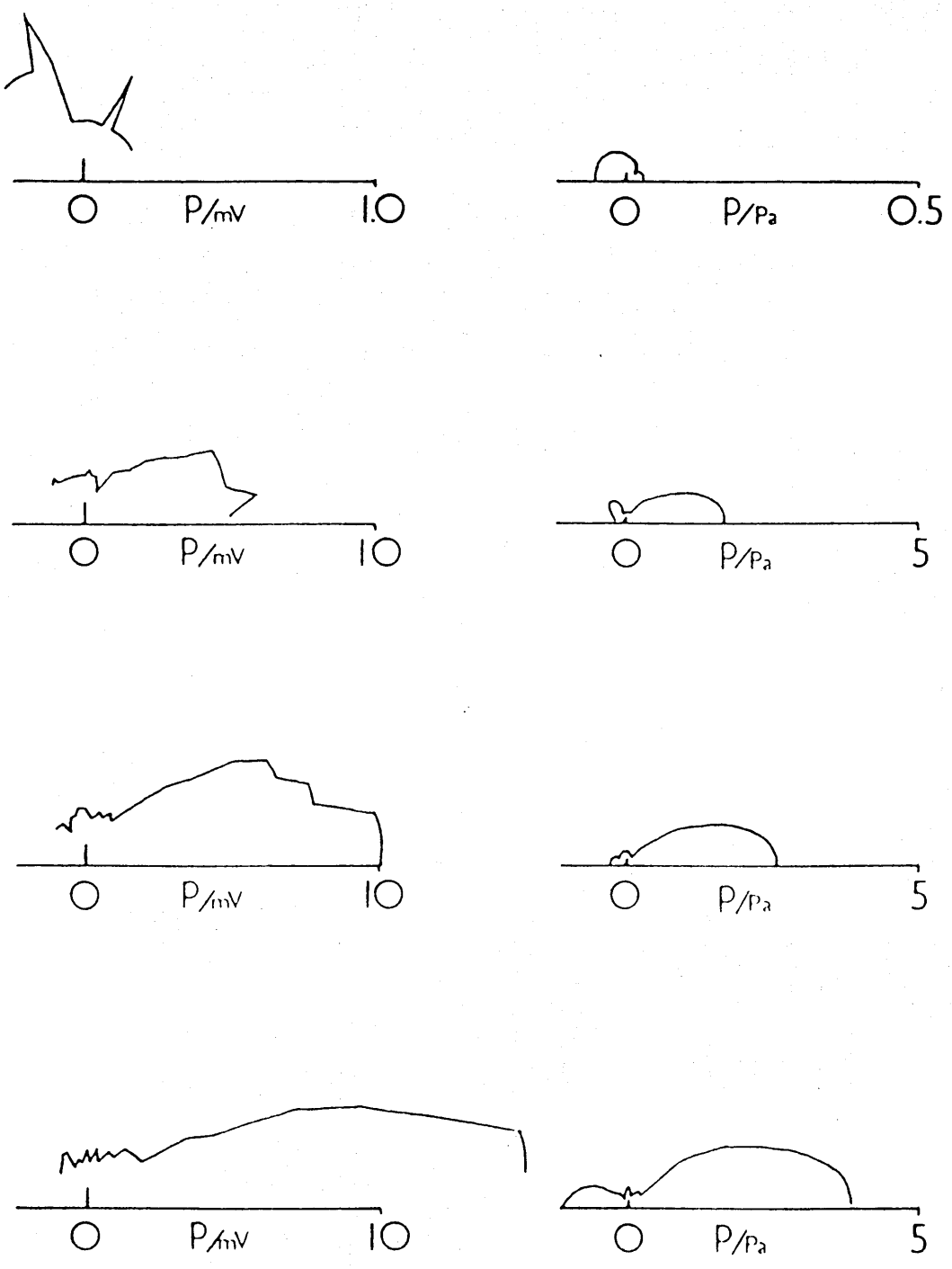

Figure 3.9a Scattering profiles for kerosene droplets in water.
ka=1.27, 4.0, 4.4 and 5.3

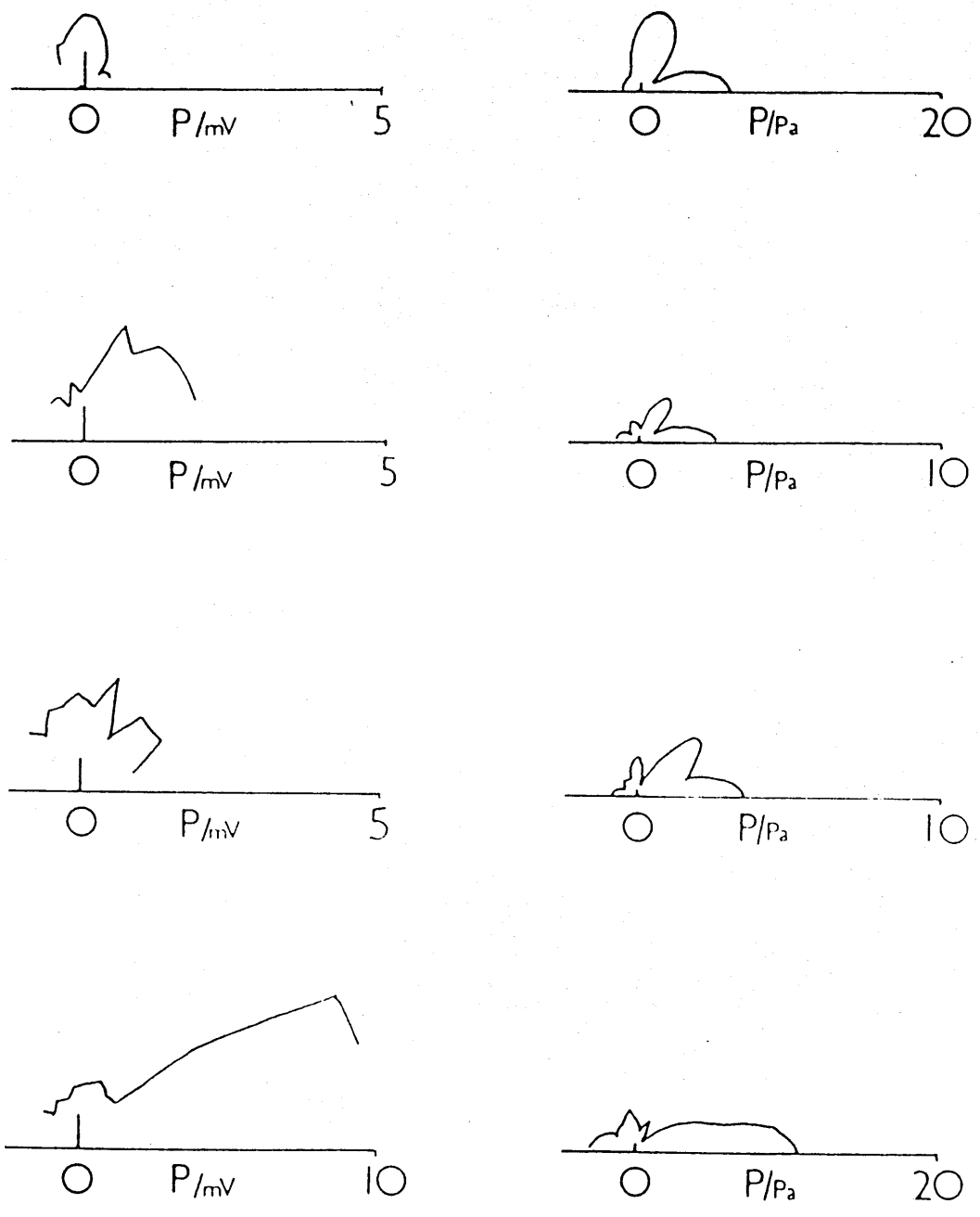

Figure 3.9b Scattering profiles for water droplets in kerosene.
ka=1.99, 3.32, 4.24 and 6.00

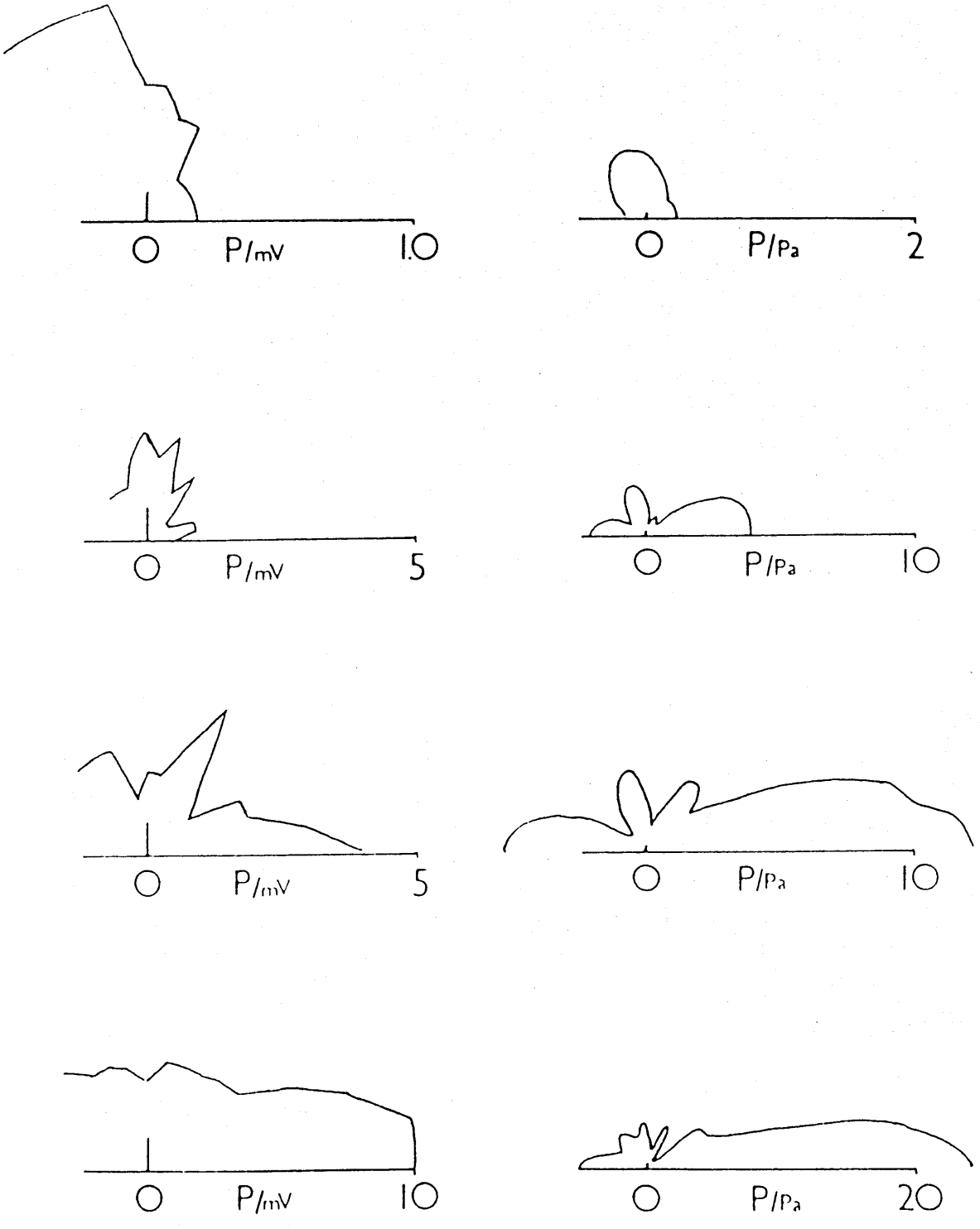

Figure 3.9c Scattering profiles for sand particles in water.
ka=1.37, 1.94, 2.99 and 5.73

Chapter 4: Scattering Cross-Section of a Single Particle.

4.1 Introduction and Theory

An alternative view of scattering, in contrast to the single particle size, multiple angle scattering of the previous sections, is to consider a single angle and then vary the particle size. The principle is best expressed in terms of the 'differential scattering cross-section' (briefly detailed in chapters 2 and 3), which is defined as follows;

$$\sigma(r,\theta,\varphi) \propto |p(r,\theta,\varphi)|^2 \qquad (4.1.1)$$

Following the previous approach, the dependence on φ is removed by the symmetry of the system, and r is chosen to be a unit constant distance, in the far field, and merely acts as a scaling factor. Thus (4.1.1) reduces to;

$$\sigma(\theta) \propto |p(\theta)|^2 \qquad (4.1.2)$$

The real, or geometric, cross section of the scatterer is given by πa^2. Therefore, the ratio $\sigma(\theta)/\pi a^2$ will give a measure of the effectiveness of the scatterer at that angle. The total cross section is found by integrating $\sigma(\theta)$ over a solid angle of 4π steradians.

The more usual approach is to find σ_{180}, ie, the backscattered cross section. However, due to the physical limitations of the apparatus, the largest angle that could be attained was 130^0.

From previous arguments, note that $p(\theta)$ is proportional to the voltage shown on the oscilloscope, and consequently;

$$\frac{\sigma(\theta)}{\pi a^2} \propto \frac{|V(\theta)|^2}{\pi a^2} \qquad (4.1.3)$$

These values can be found directly from the data in table 3.8b'.

4.2 Computer program to determine scattering Cross-Section.

The computer program listed and described in section 4.5 was modified, so as to calculate $\sigma(\theta)/\pi a^2$ and the resulting flow chart is given below.

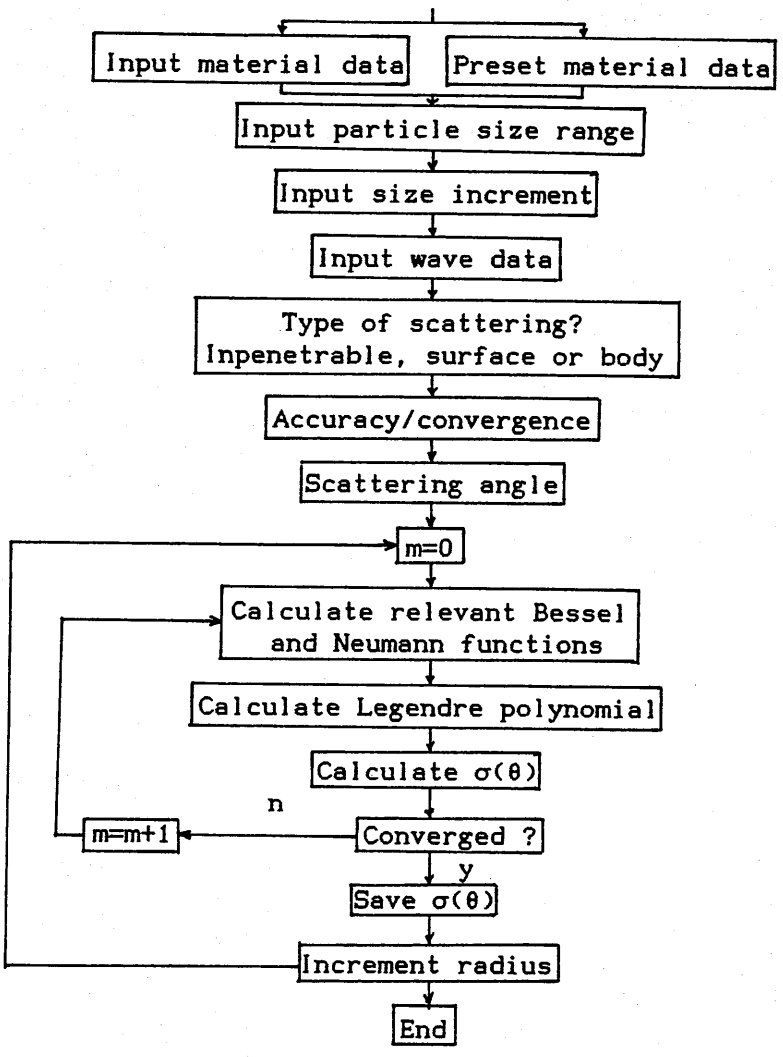

Figure 4.2a Flow diagram of the computer program to determine scattering cross-section.

4.3 Theoretical and Experimental Data at 130°.

The scattering cross-section at 130° is calculated directly from table 3.8b', and the theoretical value is found using the full form of the scattering equation, the results being tabulated below in figure 4.3a and appearing graphically in figures 4.3b to d

Detail	V_{130}/mV	ka	$\log_{10}(\|p\|^2/\pi a^2)$
kiw 0.89mmr	1.6	4.4	0.012
kiw 0.8mmr	1.6	4.0	0.105
kiw 0.75mmr	1.6	3.7	0.160
kiw 1.06mmr	1.4	5.3	-0.256
kiw 0.255mmr	0.4	1.27	-0.0969
aiw 0.967mmd	2.4	2.4	0.895
aiw 0.753mmd	1.0	1.9	0.352
kiw 895µmr	1.8p	4.45	0.109
kiw 940µmr	1.6p	4.68	-0.040
kiw 790µmr	1.6p	3.94	0.116
kiw 740µmr	1.6p	3.69	0.173
giw 420µmd	1.0	1.05	0.857
giw 250µmd	.2-.3	0.62	-0.088
giw 177µmd	≤.1	0.44	-0.398
giw 149µmd	no signal	0.37	
siw 106µmd	no signal	0.26	
giw 500-600µmd	0.8	1.37	0.430
giw 600-710µmd	1.0	1.63	0.472
giw 710-850µmd	1.0	1.94	0.321
giw 850-1000µmd	1.5	2.30	0.525
giw 1-1.4mmd	2.0	2.99	0.549
giw 2.3mmd	4.8	5.73	0.744
giw 1-1.4mmd	≃2	2.99	0.549
giw 850-1000µmd	≃1.5	2.30	0.525
giw 710-850µmd	1	1.94	0.321
giw 600-710µmd	≃1	1.63	0.472
giw 500-600µmd	≃.8	1.37	0.430
wik 1289µmr	≃1.8	7.03	-0.207
wik 364µmr	.5	1.99	-0.211
wik 777µmr	1.2	4.24	-0.120
wik 989µmr	1.2	5.40	-0.329
multiple	.8		
wik 2.2mmd	1.6	6.00	-0.171
wik 1.05mmd	1.2	2.87	0.221
wik 1.22mmd	.8	3.32	-0.262
wik 1.29mmd	1	3.52	-0.166
wik 1.44mmd	1.2	3.93	-0.0535
iik 1.4-1.18mmd	1	3.5	-0.166
iik 1-1.18mmd	1.6	2.97	0.438
iik 850-1mmd	1.6	2.52	0.581

Figure 4.3a Table of experimental scattering cross-sections at 130°
The key for the details is the same as for figure 3.8b' above.

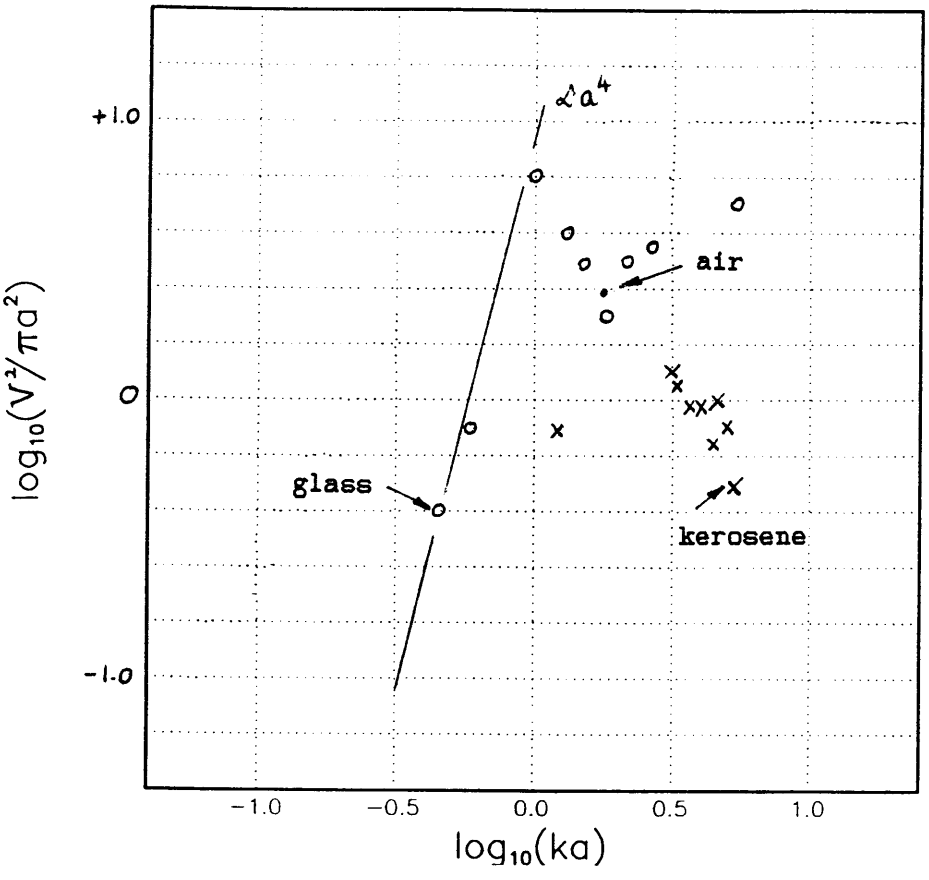

Figure 4.3b Experimental σ_{130} For kerosene, air and glass in water.

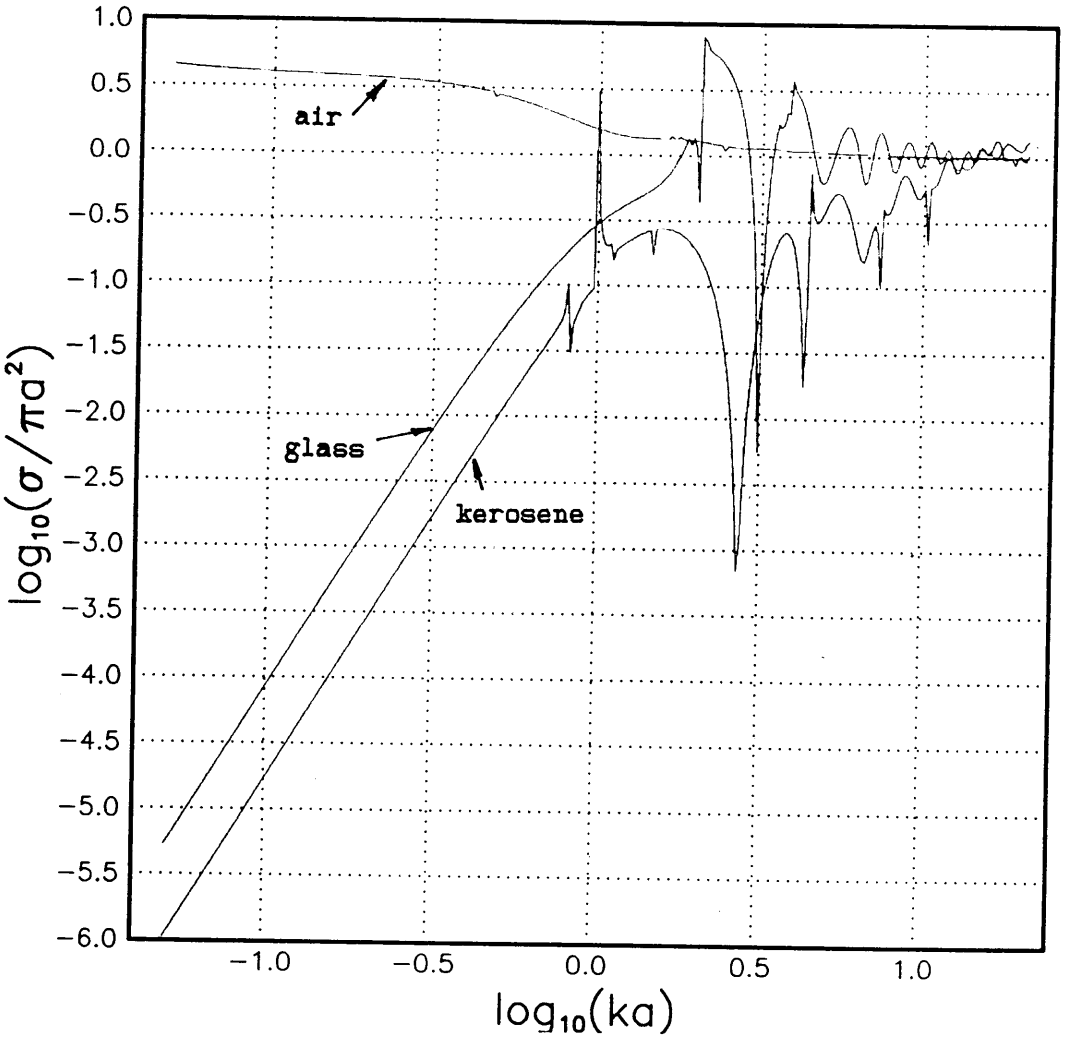

Figure 4.3b' Theoretical σ_{130} For kerosene, air and glass in water, assuming an extended reaction.

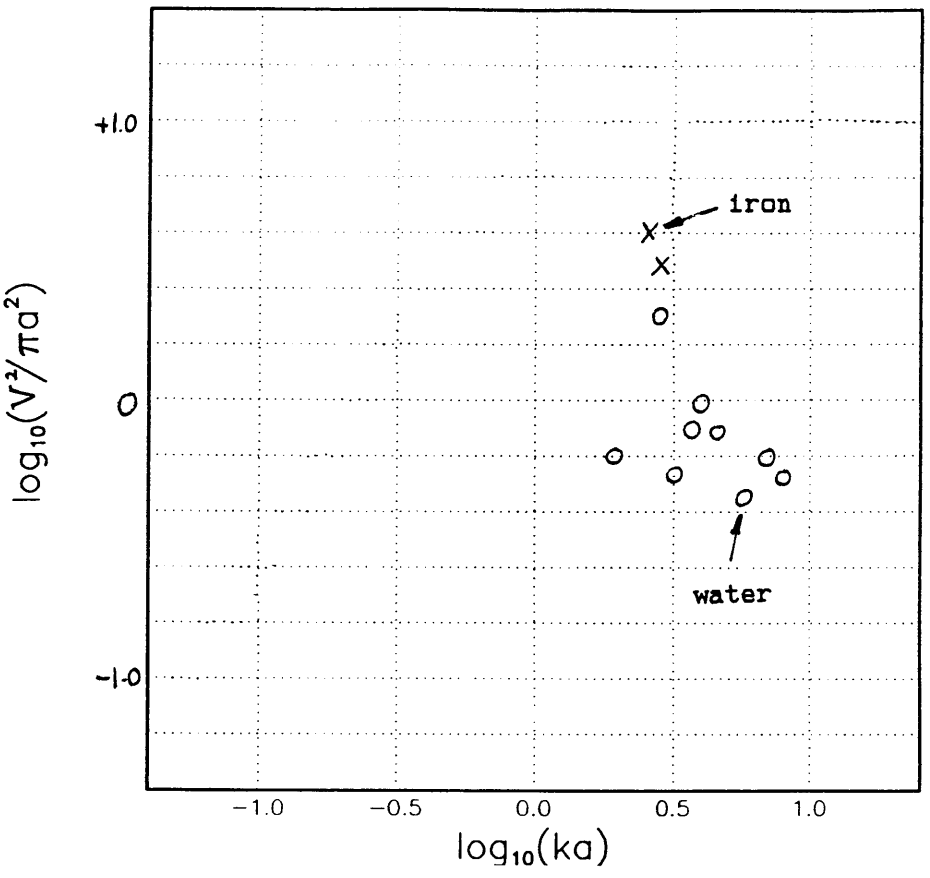

Figure 4.3c Experimental σ_{130} for water and iron in kerosene.

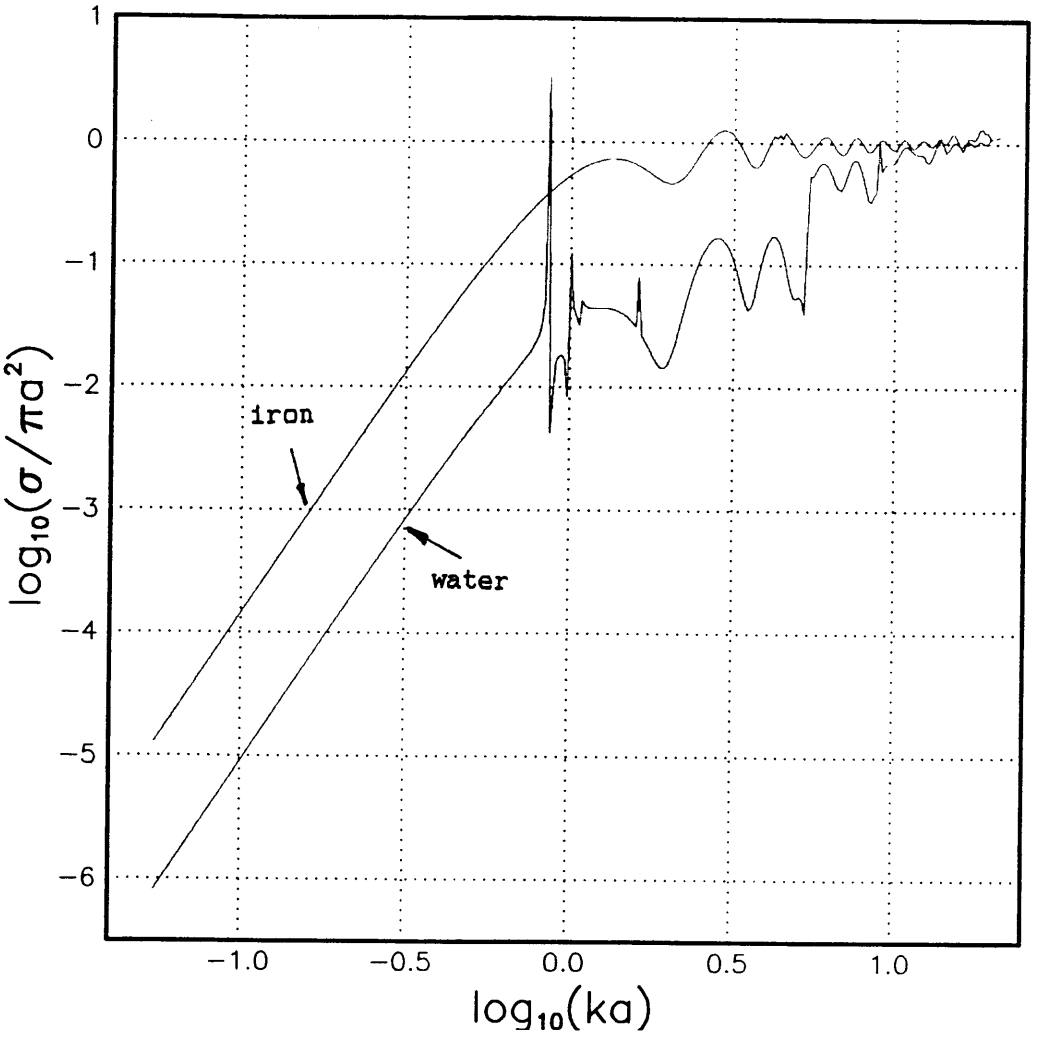

Figure 4.3c' Theoretical σ_{130} For iron and water in kerosene, assuming an extended reaction.

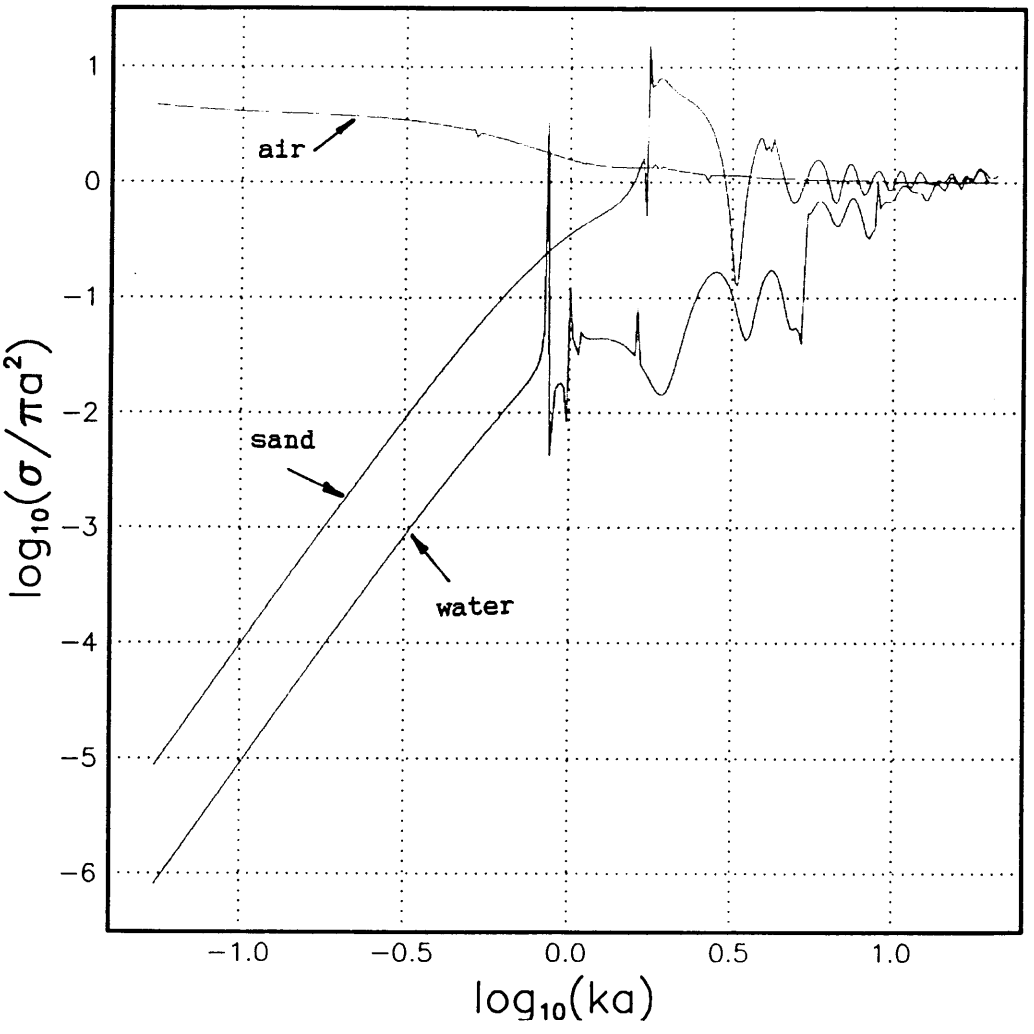

Figure 4.3d Theoretical σ_{130} For air, sand and water in kerosene, assuming an extended reaction.

All of the above experiments, including those of chapter 3, have involved the direct measurement of the scattered signal using a Tektronix 2215 oscilloscope. The gain of the oscilloscope was adjusted during each reading to maximise the size of the signal on the screen.

Direct reading errors amount to no more than half of the smallest division on the screen at that scale. The smallest scale used was 2mV/division, leading to an error of ±0.1mV. The droplets were sized photographically as described in appendix A, leading to errors of less than 5% in diameter. The solid particles were generally from reliable sources (BDH Chemicals Ltd) and were all sieved using standard meshes, to produce narrow size distributions, though these were not quantified.

4.4 Backscattering Introduction.

As has been described in the previous sections, the apparatus was limited to $0° < \theta < 130°$. In order to obtain information about the differential backscattering cross section, ie with $\theta = 180°$, a totally different approach must be taken.

4.5 Backscattering Apparatus.

During this part of the experiment, a prototype range gated backscattering cross correlation flowmeter was made available for test purposes. The circuit design and construction is that of Pogaridis (1988). The design was also rebuilt so that the whole of the timing circuit was digital and so could be controlled by a BBC microcomputer. The latter design was found to produce inferior results during the initial comparative experiments, and so the original circuit was used during the main series experiments.

The basic principles of the system are as follows;

(a) The transducer is driven at its resonant frequency (2MHz) for a short period of time, usually producing a small and integral number of wavelengths($\simeq 3\lambda$).

(b) The driving circuit is then switched off, and the transducer lies dormant.

(c) A predetermined time later, a receiving circuit is activated, again for a finite duration, for the transducer to behave as a passive receiver. These times determine the size and position of the observation window relative to the front face of the transducer.

(d) For this work, this signal is then analysed. For the cross correlation flow meter, this signal would then be filtered, amplified and then compared with the signal from an identical system that is a known distance further down the pipe, the correlation peak giving the time for the scatterer to move between the two transducers.

(e) In contrast to all commercially available backscattering systems, the amplifiers in this circuit are balanced so that they are not saturated when an object passes through the observation window. This leaves an output signal that is a function of the scattered pressure incident on the face of the transducer.

4.6 Theoretical and Experimental Data at 180°.

Two separate experiments were carried out. The first involved the flow of a kerosene emulsion past the face of the tranducer, such that at any instant, the droplets in the observation window were approximately monodisperse and the window was narrow enough, and the emulsion dilute enough for the signal from an individual droplet to be observed. The emulsion was generated by injecting a known volume of kerosene in a known period of time through a capillary tube. The time for the droplets to rise to the observation window was noted alongside the reading, and the droplets were also photographed. As has been noted in previous sections, the photographic method was the best way to determine the droplet sizes.

The second experiment involved dropping glass and iron beads of known sizes through the observation window. As with the last section, the backscattered cross section was calculated directly from the output voltage and the measured size of the particle. The various results and calculations appear tabulated below in figure 4.6a. The particle data was entereded into the previous computer program and plots for the backscattered cross-section were found for the various material combinations. Various experimental results can be found in figures 4.6b to h. The results will be fully discussed in section 4.9.

Medium	Size	Signal		ka	log10(ka)	$\|V\|^2/\pi a^2$	log10($\|V\|^2/\pi a^2$)
Emulsion 0-18s	430μmr	Saturated		3.7	0.568	4.975E6	6.70
20s	190μmr	1.5V		1.6	0.204	1.984E7	7.30
30s	160μmr	1V		1.4	0.146	1.243E7	7.09
50s	120μmr	.5V		1.0	0.000	5.526E6	6.74
60s	110μmr	.5V		0.95	-0.0223	6.576E6	6.81
90s	91μmr	.25V		0.79	-0.102	2.402E6	6.38
120s	79μmr	.1V		0.68	-0.167	5.100E5	5.71
giw	2.3mmd	>1.7-Sat	Saturated	10	1.000	6.800E5	5.83
giw	1-1.4mmd	1.5-Sat	1.5-sat	4.33-6.1	0.636-0.785	2.86E6-1.88E6	6.46-6.27
iiw	1-1.18mmd	1.5-Sat	1.5-Sat	4.33-5.1	0.636-0.708	2.86E6-2.06E6	6.46-6.31
giw	850-1mmd	1.2	1.2-1.5	3.7-4.3	0.568-0.633	2.54E6-1.83E6	6.40-6.26
iiw	850-1mmd	1.2-Sat	1.2-Sat	3.7-4.3	0.568-0.633	2.54E6-1.83E6	6.40-6.26
giw	710-850μmd	1.2	1	3.1-3.7	0.491-0.568	3.03E6-2.12E6	6.48-6.33
giw	600-710μmd	?1	.8-1	2.6-3.1	0.415-0.491	3.54E6-2.52E6	6.55-6.40
giw	500-600μmd	1	1-1.5	2.2-2.6	0.342-0.415	5.09E5-3.54E6	6.71-6.55
giw	420μmd	1	1-1.2	1.8	0.255	7.22E6	6.86
giw	250μmd	.7	.5-.75	1.1	0.0414	1E7	7.00
giw	177μmd	.3	.4	0.77	-0.113	3.66E6	6.56
giw	149μmd	.1	.1-.2	0.65	-0.187	5.27E5	5.76
giw	90-106μmd	0.02	0.02	0.35-0.46	-0.456--0.337	6.28E4-4.5E4	4.80-4.66

Figure 4.6a Table of experimental data for calculating σ_{180}.
The key for the details is the same as for figure 3.8b' above.

4.7 Theory of Multiple Scattering.

The last section considered backscattering from what was considered a very dilute and monodisperse system of droplets, and, with a narrow enough gate, the individual scattered pulses could be resolved. It has also been seen in chapter 3, that the wave scattered from an individual droplet can be many orders of magnitude weaker than the

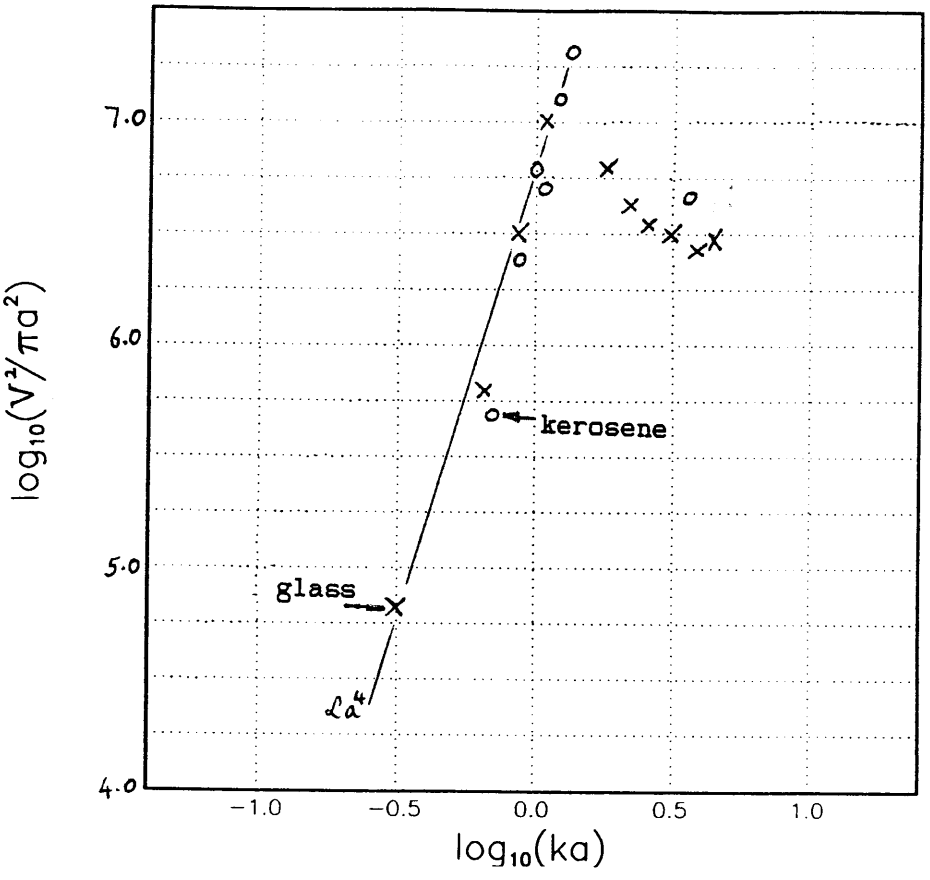

Figure 4.6b Experimental σ_{1so} for glass and kerosene in water.

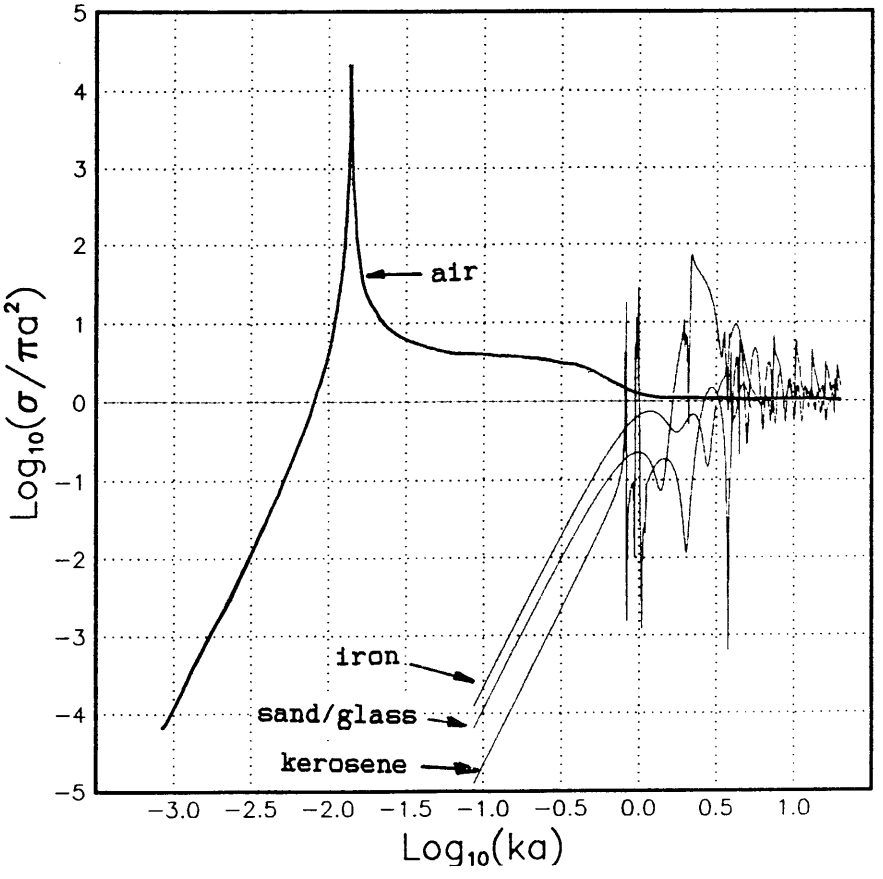

Figure 4.6c Theoretical σ_{180} for air, iron, sand/glass and kerosene in water, assuming an extended reaction.

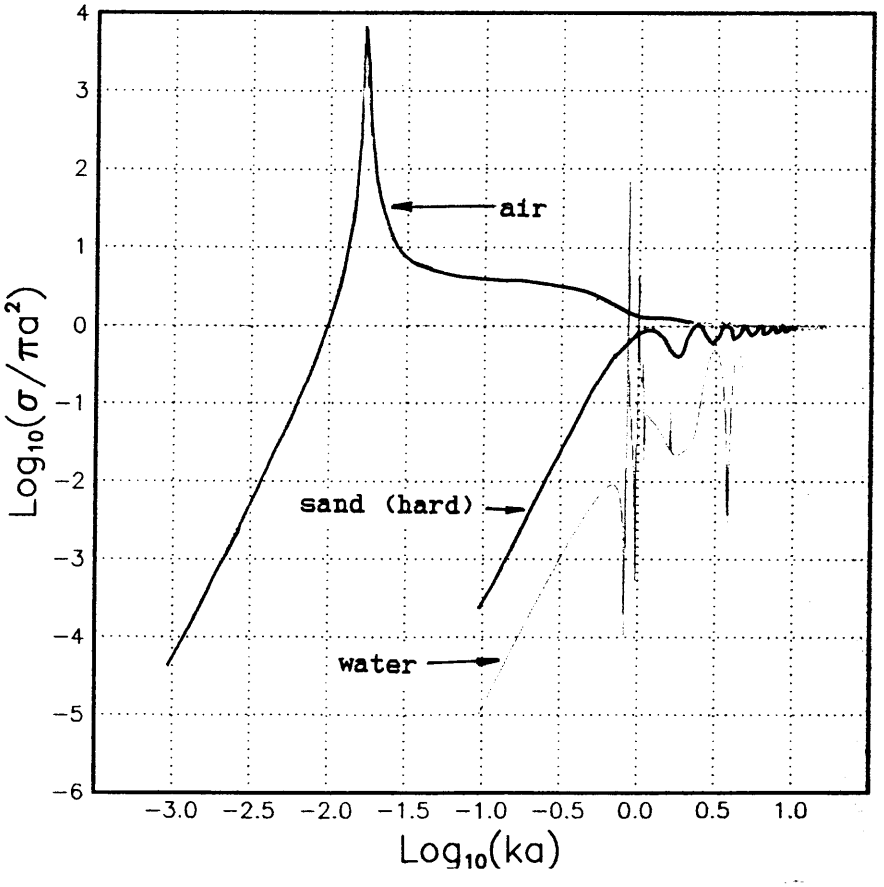

Figure 4.6d Theoretical σ_{1so} for air, sand (hard) and water in kerosene.

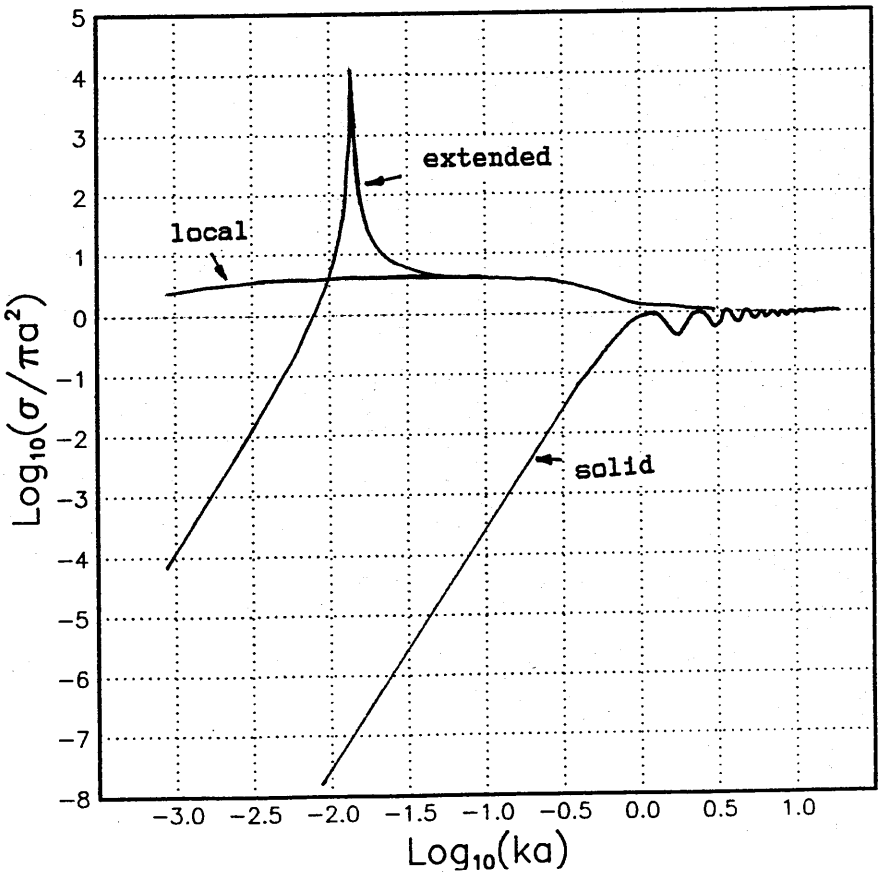

Figure 4.6e Theoretical σ_{180} for air in water with local, extended and solid reactions.

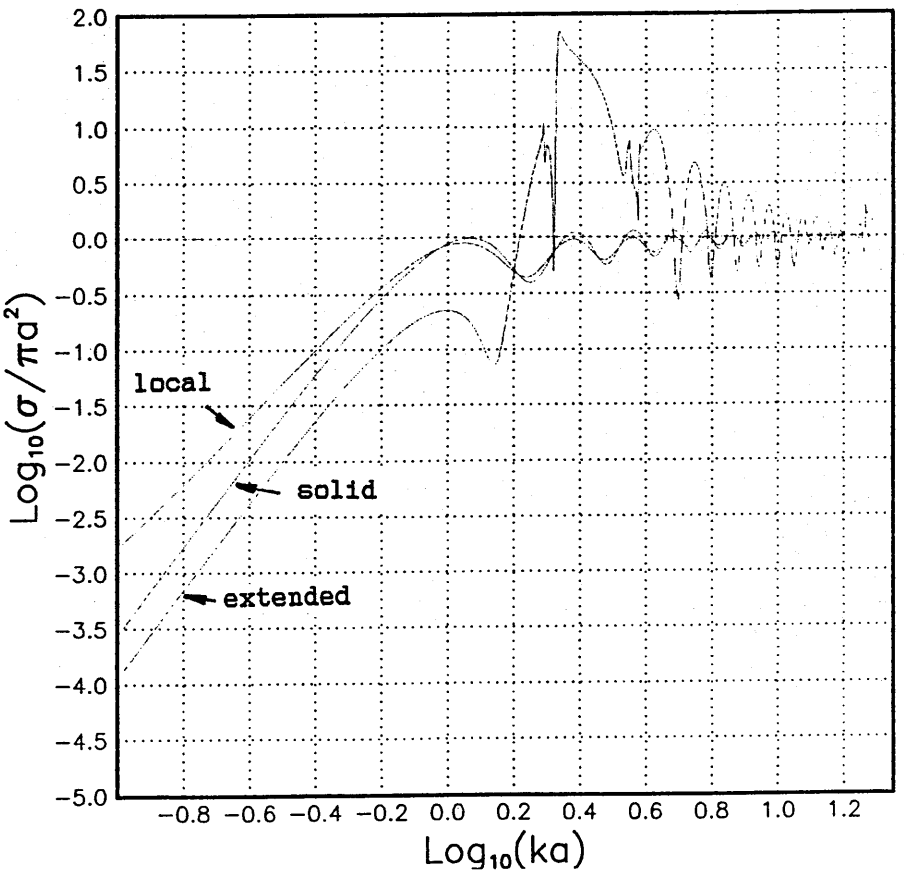

Figure 4.6f Theoretical σ_{180} For sand in water with local, solid and extended reactions.

extended reactions.

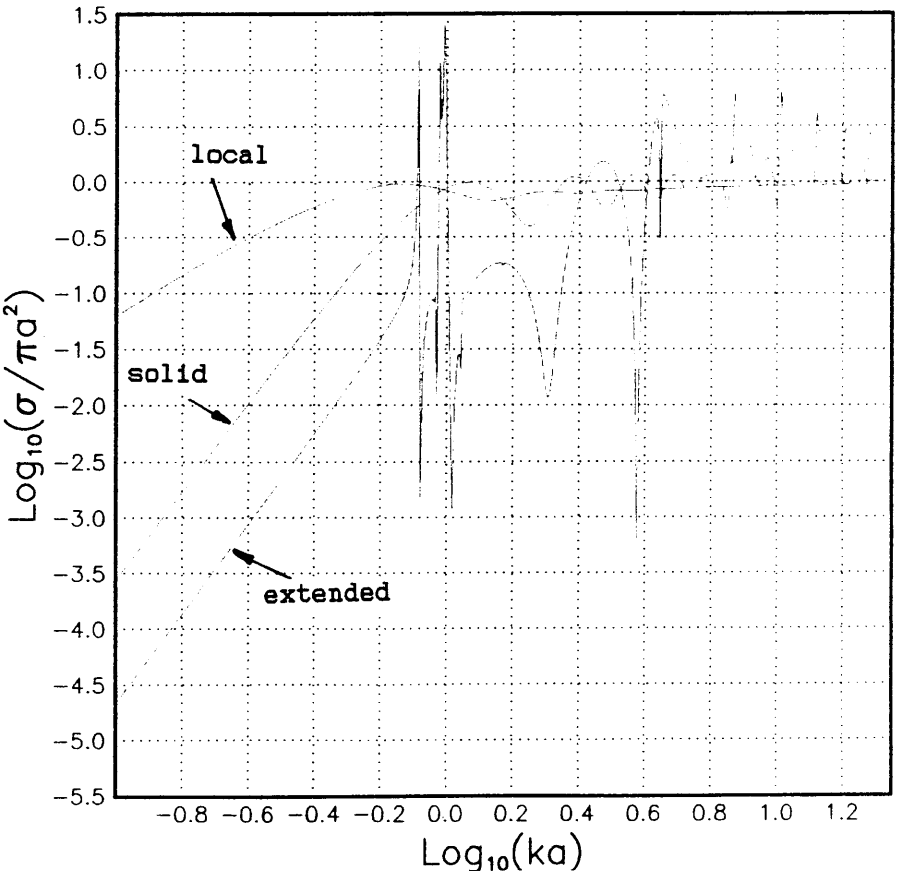

Figure 4.6g Theoretical σ_{1so} for kerosene in water with local, solid and extended reactions.

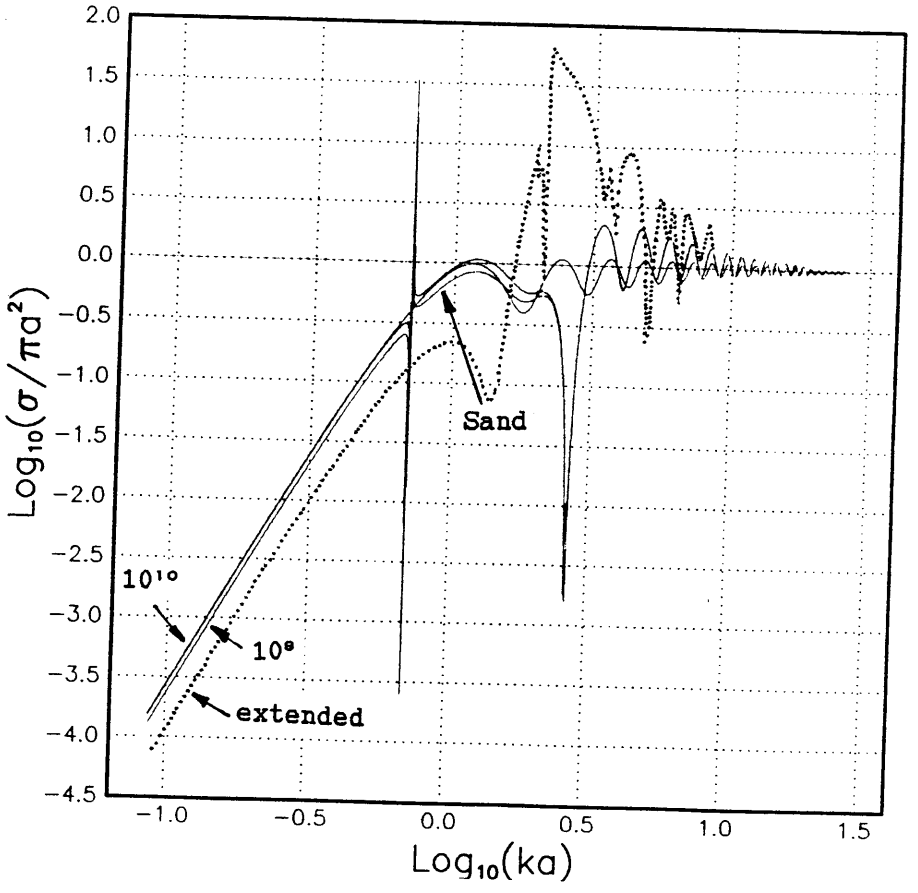

Figure 4.6h Theoretical σ_{180} comparing solid, extended (Z=10^{10}, 10^{8} and Sand) in water.

incident wave. Thus it would be expected that multiple scattering will be a very weak and possibly undetectable effect.

A more rigorous analysis of the multiple scattering problem outlined in chapter 2 will now be undertaken. The method is that of Morse (1953).

Consider a sphere of radius a containing N scatterers. The position of the nth scatterer is given by the vector r_n with respect to the centre of the sphere O, as shown in figure 4.7a. Let an incident plane wave of unit intensity be of the form;

$$p_i = e^{ikr\cos\theta} \qquad (4.7.1)$$

The wave is scattered from each particle with an angular distribution function $f(\theta)$ (=$p(r,\theta)$ of chapter 3). Thus at the point P, the first order scattered wave is given by the sum of the individual scattered waves;

$$p_s = \sum_{n=1}^{N} \frac{f(\theta_n)}{R_n} e^{[i(k_o.r_n + kR_n)]} \qquad (4.7.2)$$

The second order scattered wave, ie the wave wave scattered by particle n and then rescattered by particle m towards point P, will be of the form;

$$p_s = \sum_{m=1}^{N} \sum_{n=1}^{N} \frac{f(\theta_{n-m})f(\theta_m)}{(r_n-r_m)R_m} e^{[i(k_n.(r_n-r_m)+kr_m)]} e^{[i(k_o.r_m + kR_n)]} \qquad (4.7.3)$$

Equations of this form and higher order terms are not solvable for finite distributions, without specific details of the particle spatial and size distributions. However, the form of the equation leads to

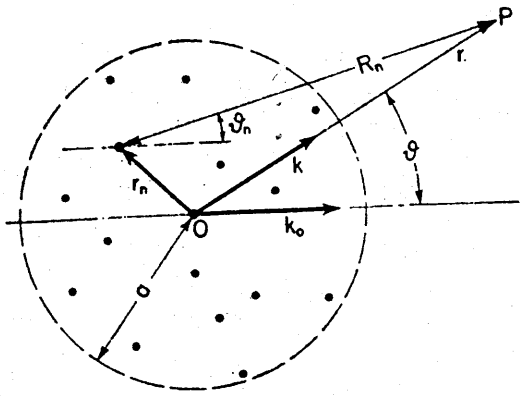

Figure 4.7a Angles, position and propagation vectors for the scattering of a plane wave by an ensemble of scatterers.

several conclusions. Firstly, the rescattered pressure goes as the square of the angular scattering function and thus for non resonating particles (Morse 1953) will always be much smaller than the first order scattering. It would also be expected that for a large number of uniformly sized particles that are randomly distributed, that the scattering will be predominantly incoherent and thus small in amplitude, ie the sum of the exponential terms in (4.7.3) will be small. Hence second order scattering will be neglected.

Returning to the first order scattering (4.7.2) and taking the phase of the incident wave to be zero at the origin. When r»a this reduces to;

$$p_s \simeq e^{ikr} f(\theta) \sum_{n=1}^{N} e^{i(k_0-k).r_n} \qquad (4.7.4)$$

Each component of the wave at P has its own phase and the resulting intensity is a function of this phase. If the spatial distribution is totally random, so will be the phases, leading to incoherent scattering. Regular arrays of scatterers produce coherent scattering. Intermediate distributions will produce combinations of both types of scattering.

The intensity of the scattered wave is given by $|p_s|^2$, leading to;

$$|p_s|^2 = \frac{|f(\theta)|^2}{r^2} \sum_{m,n=1}^{N} e^{i(k_0-k).(r_m-r_n)} \qquad (4.7.5)$$

Where r_m-r_n is the vector from the nth to the mth scatterer. By separating the m=n terms, the equation becomes;

$$|p_s|^2 = \frac{|f(\theta)|^2}{r^2} N + \sum_{n\neq m}^{N} e^{i(k_0-k).(r_m-r_n)} \qquad (4.7.6)$$

The first term is the intensity that would be measured if the N scatterers sent out their waves independently, producing random phase relationships at the observer. This is the incoherent part of the scattered wave. The second term is the coherent part of the scattered wave, which takes into account the phase relationship between each wave. Again, a purely random distribution leads to incoherent scattering only (Morse 1953), thus the scattered intensity is proportional to the first power of the number of scatterers;

$$|p_s|^2 = N \frac{|f(\theta)|^2}{r^2} \qquad (4.7.7)$$

The coherent scattering term leads (eventually) to an N^2 dependency. Should the effects of multiple scattering become significant in the later experiments the above outline will be expanded in detail.

4.8 Speed of Sound and Attenuation Effects.

These factors have already been discussed in some detail in chapter 2, where the general interaction of the acoustic wave with many scatterers was considered. This is an appropriate place to investigate some of those conclusions experimentally. The simplest method of measuring the speed of sound in a material is to take a known length of the material and find the time of flight of an acoustic pulse across the material. This technique has several drawbacks which lead to poor accuracy ($\simeq \pm 1\%$) mainly caused by problems of identifying the position of the received peak, and identifying the real length of the system since the transducer is of finite thickness.

These problems can be eliminated using an interferometric method. The usual technique involves using a single transducer and reflector (Gooberman 1968), driving the transducer at a constant voltage (at the resonant frequency of the transducer) and measuring the current passing through the transducer. As the fluid cavity varies in length it moves in and out of resonance and the current shows minima and maxima respectively. These resonances occur every half wavelength of the incident sound wave. This method has the advantage over the static

transducer, fixed frequency, time of flight methods in that only the properties of the cavity are involved in the calculations.

A novel approach to the resonant cavity method was adopted which involved letting the refelector be a passive receiver (voltage detect), thereby measuring the intensity of the sound in the cavity. Thus by moving the receiver, the effective cavity moved in and out of resonance and again the received voltage has maxima every $\lambda/2$.

The final apparatus is sketched in figure 4.8a.

In order to minimise the effects of lash in the threads of the micrometer and receiver support, all motion for any one measurement was carried out in one direction. Part of a typical received signal is shown in figure 4.8b, showing that the maxima are easier to distinguish than the minima. The subsidiary peaks imply non-parallelicity of the transducers but are easily distinguished and not counted (Gooberman 1968). To further reduce the errors caused by end effects, the length of the cavity must be varied by as much as possible, and the motor speed must be carefully controlled at each end of the traverse.

The resonant frequency of the transducers used was found to be 1.1MHz and the frequency supplied by the signal generator was stable and accurate to 5 figures as confirmed by the timer counter. The position of an individual peak could be found to ±5μm using the digital voltmeter and the motorised micrometer in a single direction. Moving backwards and forwards around the peak led to errors of ±25μm in position. The micrometer had a range of 50mm and was checked at both ends using a standard 25mm micrometer, with agreement to ±5μm.

Thus the speed of sound could be found knowing only the frequency and the length required to produce a given number of peaks. For water , over several readings and a range of temperatures, the speed of sound was found to be $1480.2\pm0.6 ms^{-1}$ with a temperature coefficient of $+2.0 ms^{-1}$ per $0.1^{0}C$. These errors are only five times greater than the best published (Kaye 1986). For kerosene, c was found to be $1324.0 ms^{-1}$ and for Dielectric 180, $c=1295.5 ms^{-1}$.

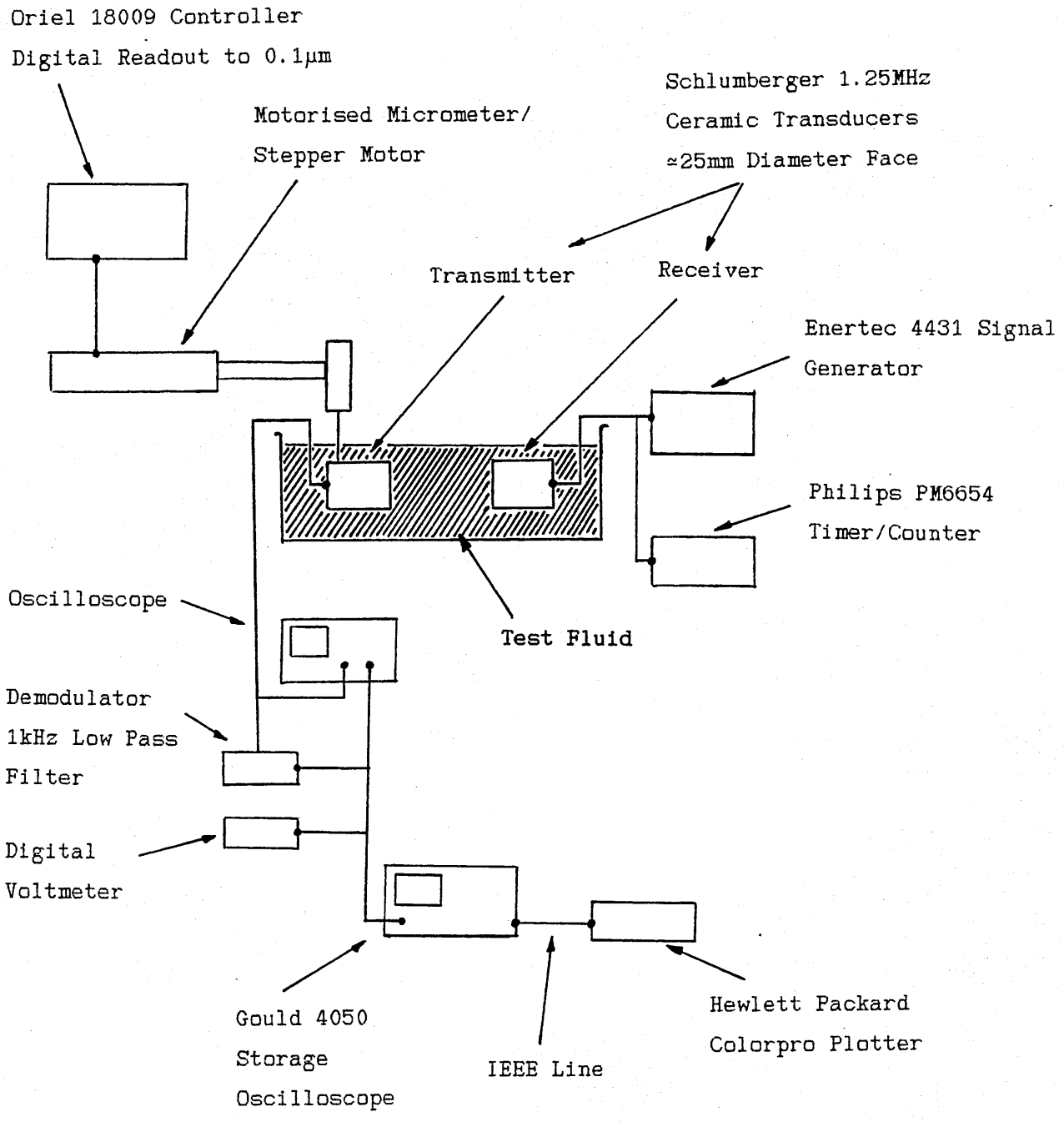

Figure 4.8a Schematic of the moving transducer acoustic interferometer.

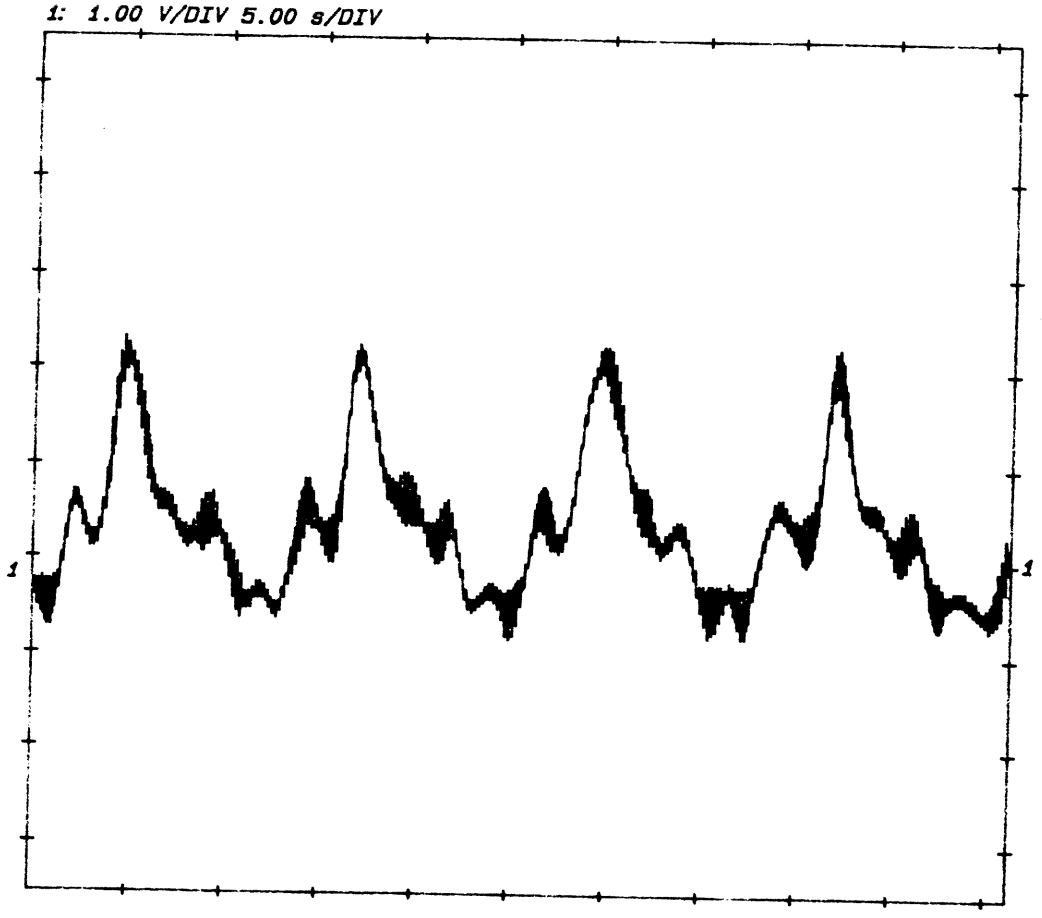

Figure 4.8b Part of a typical received signal from the interferometer

The finite size of the transducers and apparatus preclude this technique from producing realistic values for attenuation, as the geometric factors cannot be eliminated from the fluid effects. Problems of producing repeatable emulsions means that attenuation measurements were not be made at this stage, since attenuation is very sensitive to the particle size distribution (Lenn 1985, Morse 1953).

Figure 4.8c shows the results of determining the speed of sound in a very well mixed emulsion (droplets estimated <1μm), using the pulse reflection method and the interferometric method.

As for the measurement of attenuation coefficients, several technical problems had to be overcome. First and foremost, there was effects of particle sizes even when ka was very small and the individual reactions were in the Rayleigh region. All methods that could be practically devised showed a dependence on the transducer and apparatus geometry which would not transfer easily between experimental situations. Thus absolute attenuation coefficients could not be practically determined.

4.9 Discussions and Conclusions.

This chapter has involved a different theoretical approach and experimental techniques to those described in chapter 3. Although two different frequencies have been utilised ie 1MHz at 130^0 and 2MHz at 180^0, the results were made directly comparable by the use of the dimensionless ka as the axis of the scattering cross-section plots.

A slope characteristic of the 4th power law was evident for both the kerosene droplets and the glass beads/sand particles at both angles for ka<1, a direct experimental confirmation of the Rayleigh scattering theory. For ka>1, a more complicated behaviour including scattering cross-section maxima and minima are observed for both solid and liquid scatterers. The scattering cross-section of the solids being generally greater than their liquid counterparts, by an amount approximately in line with the theory.

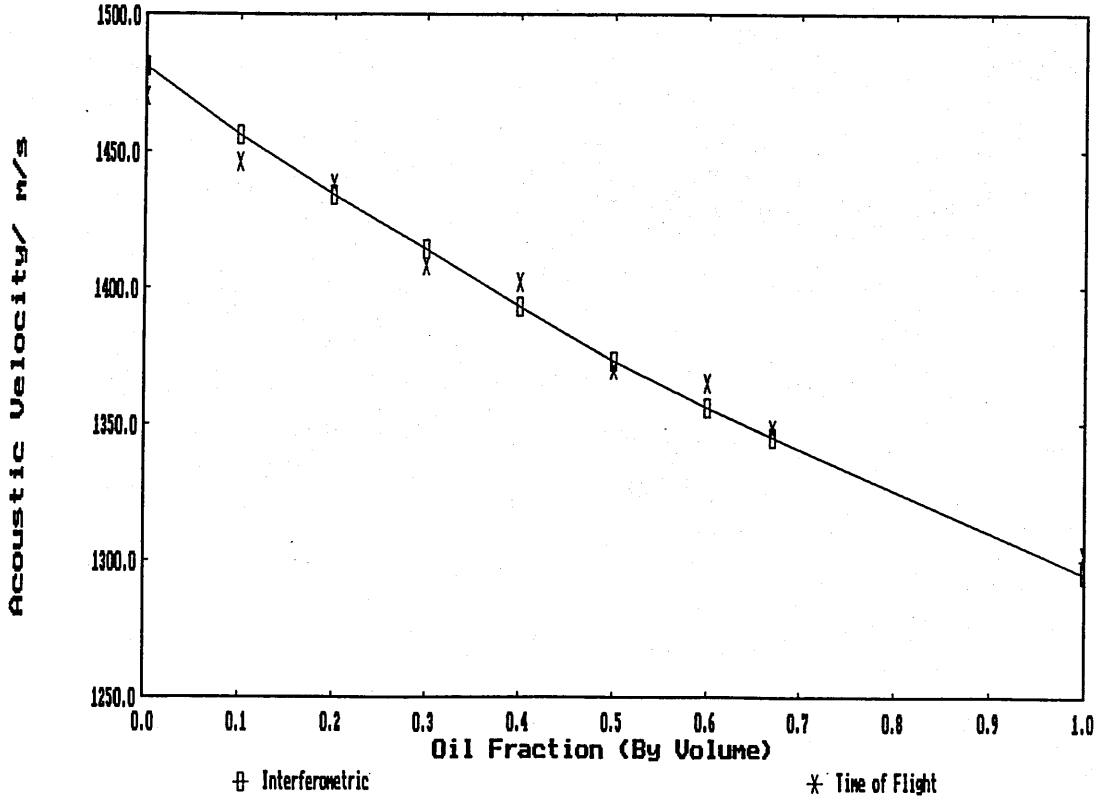

Figure 4.8c Speed of sound in a water/kerosene emulsion using the pulse reflection and interferometric methods.

There is a lot more detail in the theoretical plots, resonant spikes, steps etc, than is resolvable by the experiments. The few air results confirm that for ka>1, the scattering cross section of the air bubble is of the same magnitude as the equivalent solid and slightly greater than the equivalent liquid scatterer. The behaviour of air bubbles for ka<1 could not be observed in this apparatus, since the flow rates required to hold them stationary could not be maintained accurately enough. However, the theory shows that for ka<1 the resonance effects of the bubbles overcome the size effects down to ka≈0.016, where the main resonance occurs, after which the 4th power law becomes evident.

The experiments at 180^0 extend the range of ka for the scattering from liquid droplets and again, the 4th power law is observed for ka<1, and more interestingly, around ka=1 a few liquid droplets were observed with scattering cross sections greater than the equivalent solid particle. These results are all in line with the theoretical predictions for the extended scattering from liquid droplets, since treating the liquid droplet as a solid would lead to scattering that is always smaller than the scattering from a sand particle of the same size.

For ka>1 a reduction in σ was seen as is characteristic of diffraction scattering, though, as with the experiments at 130^0 there was not sufficient data or resolution to observe the finer theoretical predictions.

The theory of a local reaction type of scattering approximation would have produced scattering for ka<1 with a slope ≈2. This is not observed experimentally for solid or liquid scatterers and therefore this model is not valid for the acoustic interaction.

The magnitude of the scattering from gas bubbles for ka<1 has not been investigated experimentally, as described above, however, the theoretical predictions agree with those published elsewhere. The large resonance might cause some problems in subsequent experiments if air bubbles cannot be eliminated or separated from the liquid droplet flow.

As a final note, a novel method of determining the acoustic velocity has been proposed and tested, which is not only very accurate but also simple in design and operation. The simple time of flight method ($\simeq\pm1\%$ due to length measurement and timing) is not capable of detecting any deviation from linear in the $c(\alpha)$ plot. It must be noted that the homogeneity of the emulsion is very important if either method for determining the acoustic velocity is to produce reliable results. Droplet density waves must be avoided as well as large droplets, since these will complicate the measurement, especially in the interferometer. A similar method for determining the attenuation coefficient that was absolute and independent of transducer geometry has yet to be devised.

Thus far the ultrasonic investigations have been of fairly simple and small scale systems where the experimental parameters are easily controlled. The following chapters will apply some of these ultrasonic methods to a larger scale system, more representative of the industrial environments described in chapter 1.

Chapter 5: Larger Scale Experiments.

5.1 Introduction.

This chapter describes experiments carried out on a two-component flow loop, extending the work of the last few chapters to a much larger scale, where the number, position and size of the scatterers are less well defined. In order to maintain continuity with the preceding and following chapters, only those experiments directly related to the ultrasonic investigations are considered here. A full description of the design, testing and operation of the flow loop appears in appendix B. The droplet flow regime is generated using a jet mixer, and so the chapter begins with the physical characterisation of these droplet flow regimes.

This is followed by the application of the angular scattering and Döppler techniques to characterising the droplet flow regime. Limitations to these ultrasonic techniques are described in detail.

5.2 Testing The Jet Mixer.

The two critical parameters that determine the droplet size distribution from a well designed jet mixer are the flow rate and nozzle size. This requires a jet Reynolds number ($Re=\rho v l/\mu$) that is much greater than the Reynolds number of main pipe flow (Fernando 1990). For low void fractions (<10%) the resulting emulsion can be considered to be 'frozen' into the main flow for several diameters downstream of the injection point (horizontal pipes). Beyond this, the swirl generated by the injector decays to the point where the droplets can move under gravity to the pipe wall. The resulting increased void fraction at the pipe wall enhances the chance of coalescence, and the droplets can be considered lost from the main flow. As in the previous sections, the emulsion properties were chosen such that the droplets produced Rayleigh and near diffraction scattering, and had diameters comparable with those produced in normal pipe and mixer systems.

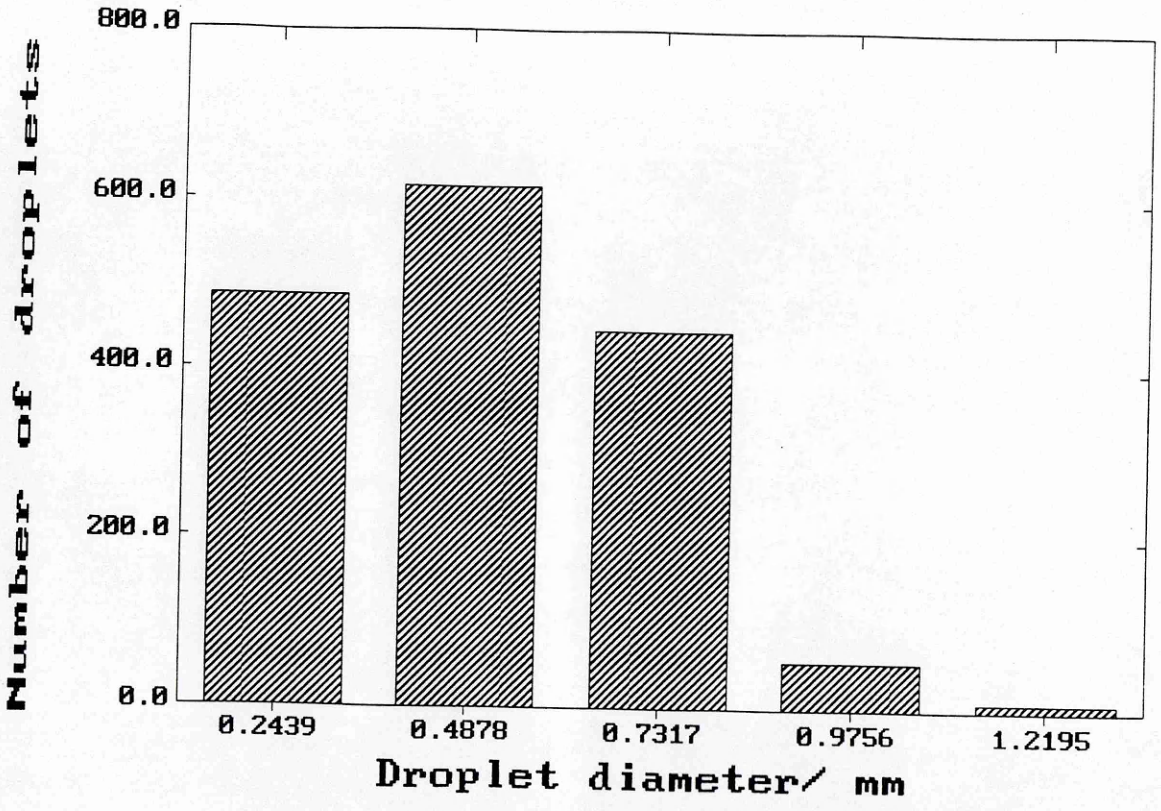

Figure 5.2a Typical droplet size distribution for a jet size of 3.57mm water flow rate $2\times10^{-3}m^3s^{-1}$ and oil flow rate (jet) $0.38\times10^{-3}m^3s^{-1}$

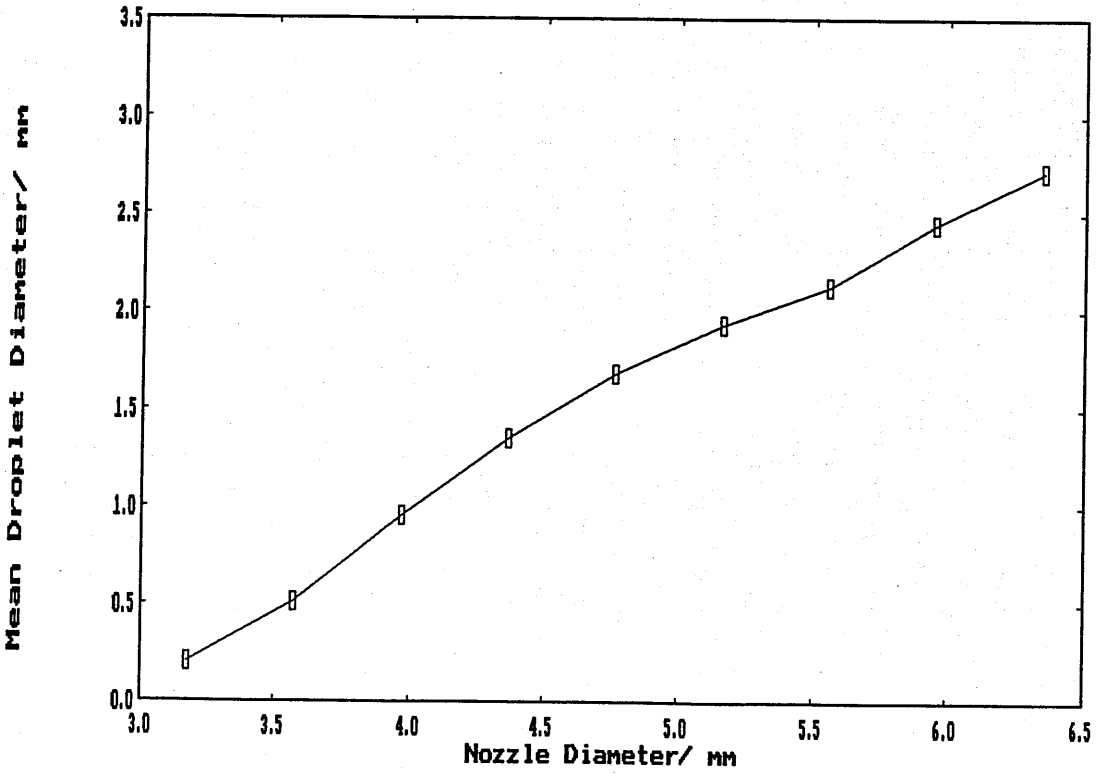

Figure 5.2b Mean oil droplet diameter as a function of nozzle size, for the same flow parameters as figure 5.2a, ie water flow rate $2\times10^{-3}m^3s^{-1}$ and oil flow rate (jet) $0.38\times10^{-3}m^3s^{-1}$

A series of experiments were carried out using varying nozzle sizes, whilst keeping the volumetric flow rates in both the jet and main pipe constant. Thus the void fraction remained constant for each experiment.

Rather than trying to interpret high speed photographs of the resulting emulsion a few diameters downstream of the injector, the flow was abruptly brought to rest (the resulting pressure surges were large, but not catastrophic!) and still photographs were taken through the pipe wall. The droplets in the resulting images were sized manually, using not fewer than 1000 droplets per image. No attempts were made to analyse the resulting size distributions and only a simple mean droplet diameter was calculated. A typical example of the resulting size distribution is shown in figure 5.2a.

The mean droplet diameter is plotted as a function of nozzle diameter in figure 5.2b. As expected, a simple relationship is evident. Almost identical curves (within experimental error) were found when the water flow rate was varied whilst keeping the jet (oil) flow rate constant. That the mean droplet diameter is largely independent of the main flow rate will prove useful in later experiments.

5.3 Angular Scattering Experiments.

Several technical problems had to be overcome before these experiments could be carried out successfully. Firstly, the gas bubbles generated by the cavitation at the flow controlling valves (described in appendix B.5) had to be eliminated, or at least reduced to the point where they did not interfere with the experiment. Thus a series of experiments was carried out to investigate the scattering from the gas bubbles in an otherwise single component flow. Secondly examination of figure 5.3a reveals that the scattering from an emulsion in the test section spool piece was not as well defined (both spatially and angularly) as in the single droplet experiments described in chapters 3 and 4.

It is clear from figure 5.3a that the signal (from a single pulse from the transmitting transducer) could be scattered by several droplets, each with a different scattering angle. A range gating system was thus

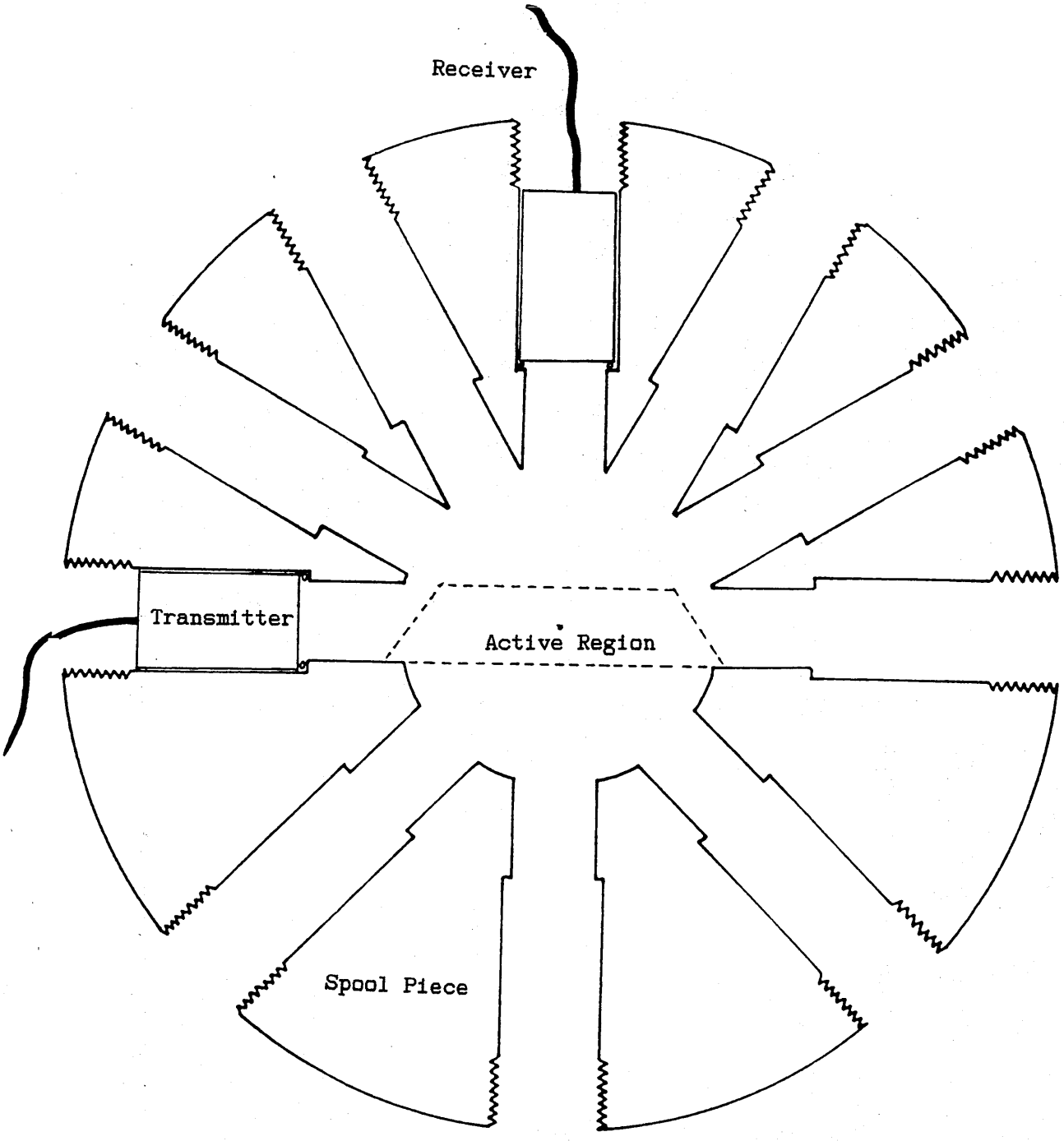

Figure 5.3a General scattering geometry in the spool piece, neglecting edge diffraction effects

constructed which could control the effective volume where the scatterer(s) could reside.

The whole circuit consisted of a series of counters driven by an external clock which controlled the relative positions (in time) of the active periods of the transmitter and receiver. It was also capable of operating a single transducer as both a transmitter and receiver (compare section 4.5).

The circuit is reproduced for completeness in figure 5.3b, including timing diagrams for the various elements of the circuit. A photograph of the final constructed circuit appears in figure 5.3c with an annotated photograph of the final electronics package appearing in figure 5.3d where a typical transmitted pulse and the receiving gate are just visible on the oscilloscope screen. By using only switches (no amplifiers etc), the effect of the electronics remains linear and so the results are directly comparable with the previous angular scattering experiments. It should also be noted that when a 3λ pulse was used, the scattering from a droplet on the axis of the pipe is taking place in an almost identical physical geometry to the experiments of chapters 3 and 4, ie the relative positions of the transducers and droplets and the size of the active volume.

Thus the theory of the ultrasonic interaction with a complex system has been given, and much of the basics investigated and proved experimentally. Now the work can be extended onto a larger scale of flow.

5.4 Comparing Experiment and Theory.

As can be seen from figure 5.3a the spool piece allowed angular scattering measurements in increments of 15^0 from 0^0 (forward scatter) to 150^0 subtended at the centreline of the pipe. The range gating circuit could be used to reduce the effective volume of the pipe within which the scatterer could lie. For scattering angles greater than 45^0 the volume was quite well defined at about $1cm^3$ on the axis of the pipe

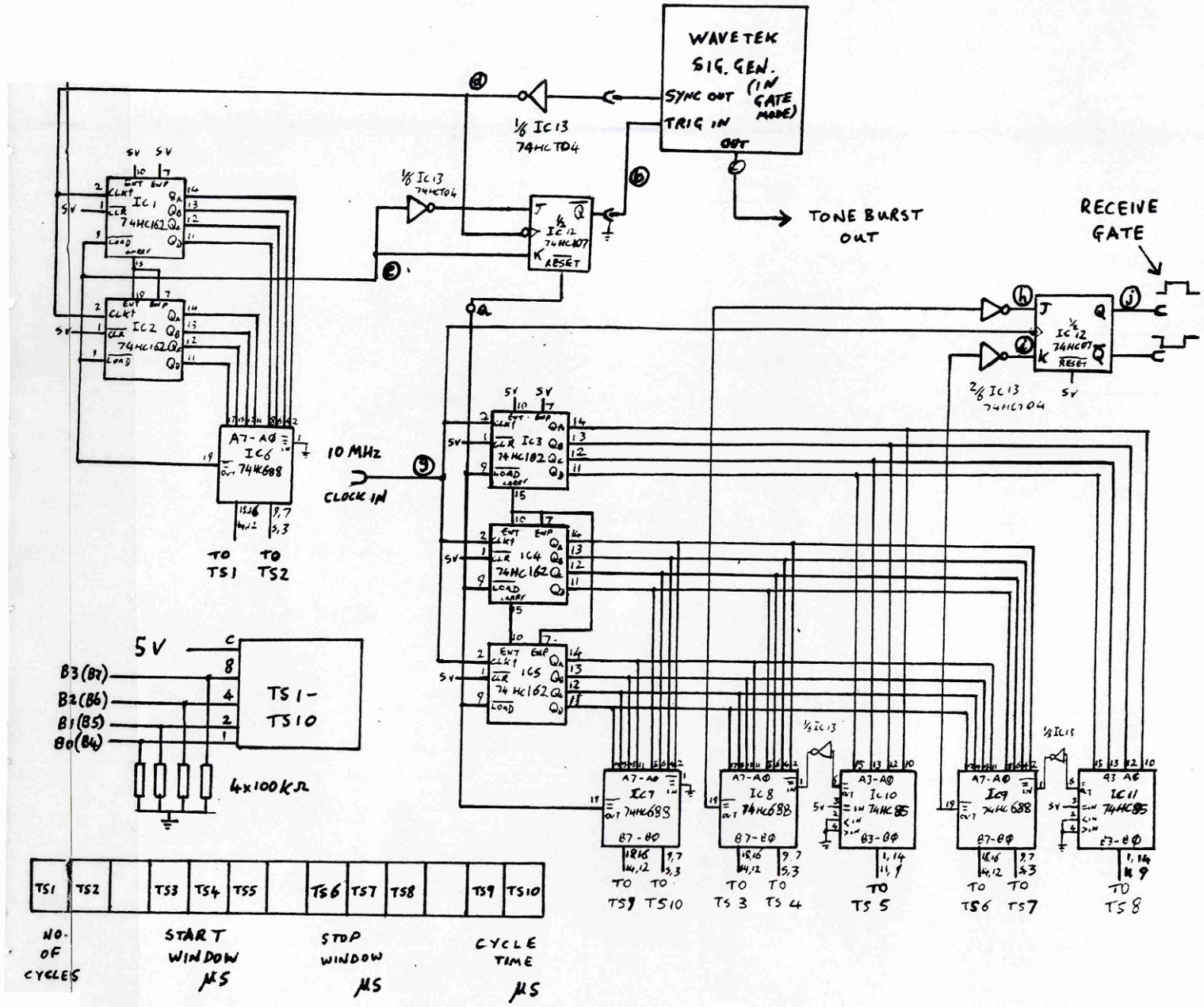

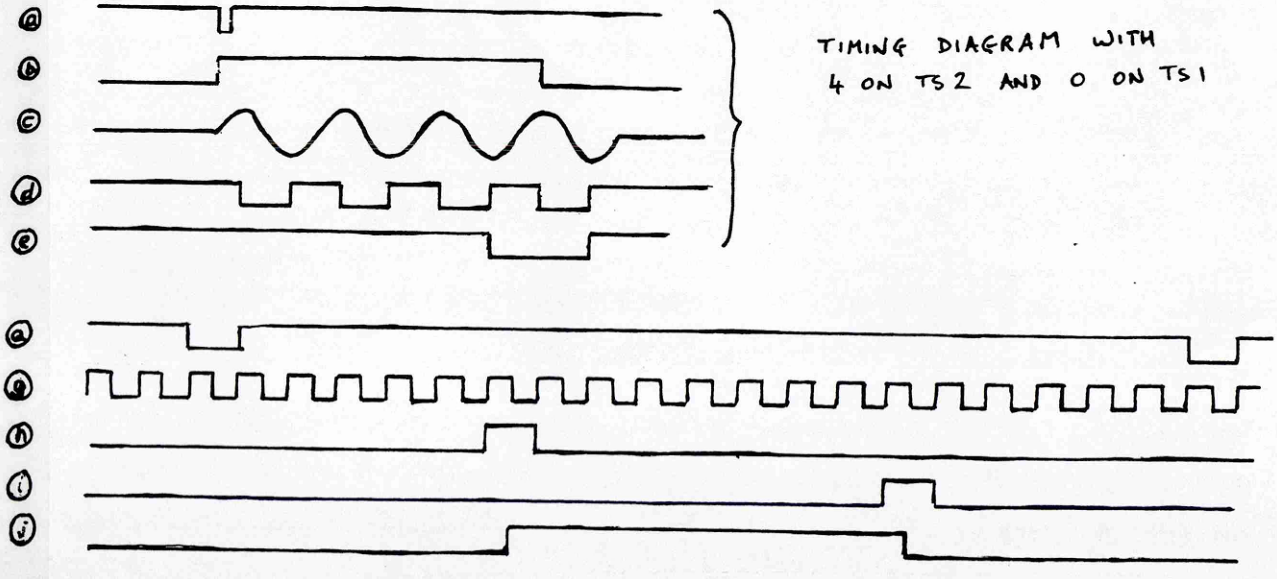

Figure 5.3b Range gating circuit diagram and timing diagrams

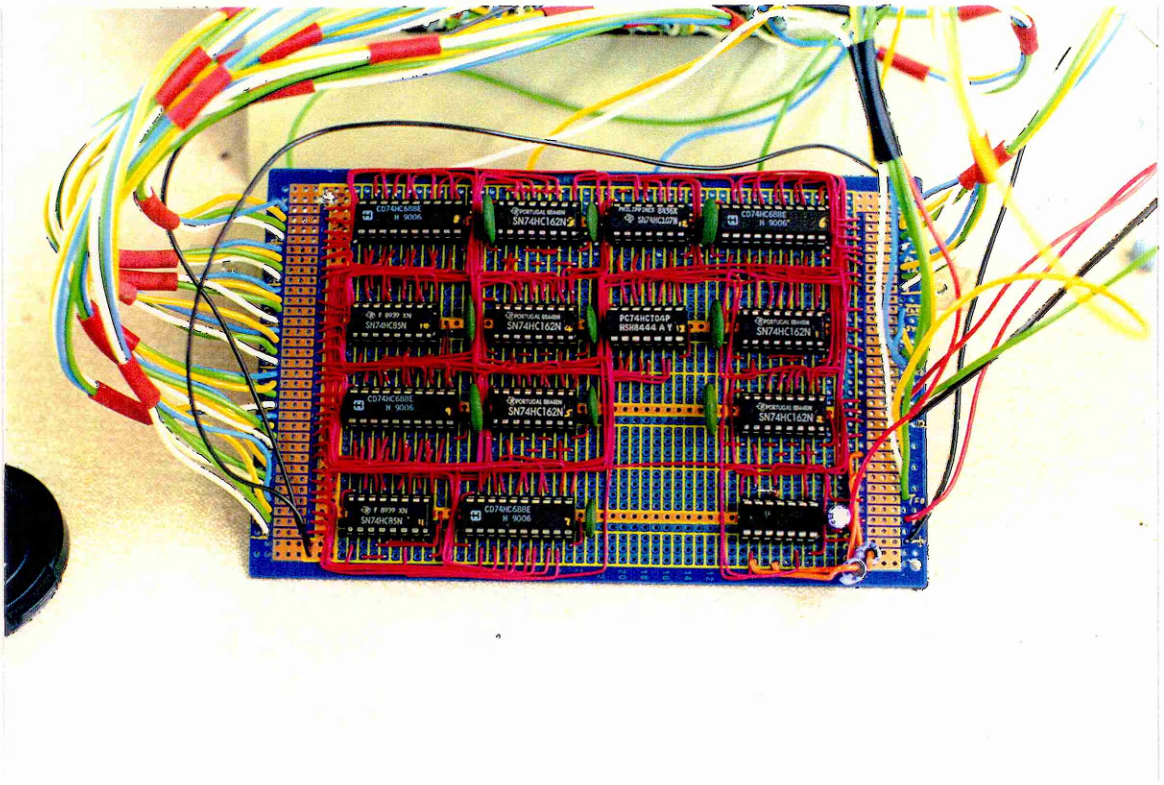

Figure 5.3c Photograph of the finished range gating circuit

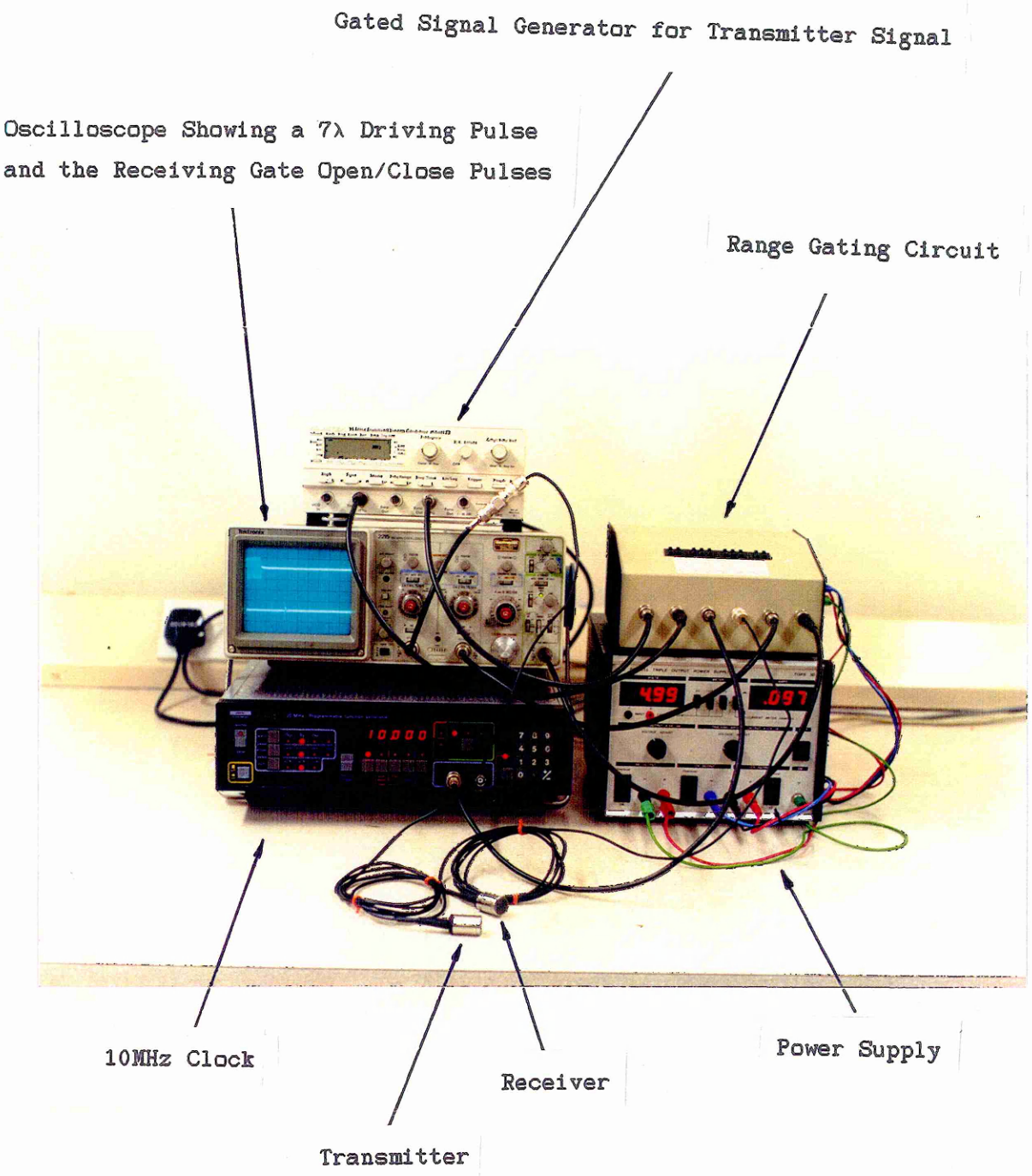

Figure 5.3d Photograph of the final electronics package and ancillaries

(figure 5.4a) when using a 3μs gate received 60μs after the beginning of the transmitted toneburst.

For scattering angles smaller than 45^0, the scattering volume became less well defined, as the range gating principle completely failed in forward scatter. The forward scattered signal could not be measured due to the simultaneous arrival of the transmitted signal. Though the volume where the scatterer could lie increased, this was partially compensated for by the resulting transmitter/receiver geometry which tended to keep the effective scattering angles within the whole scattering volume close to that of the receiver angle.

Because of the geometry of the spool piece, and the fact that only four transducers were available for the experiments, it was necessary to generate each scattering profile in stages. This involved shutting down the flow loop and rearranging the transducer positions until all the angles had been covered.

The scattered pressure incident on the receiver was measured directly as a voltage on an oscilloscope (as in chapters 3 and 4). The largest signal constantly present across the whole width of the gate was taken as the appropriate measurement.

Figures 5.4b, c and d show some typical scattering profiles from oil droplets in water. This series of experiments kept the main water flow rate and jet flow rate (oil) constant. Thus by varying the nozzle size, emulsions with varying mean droplet diameters (with corresponding variations in number density) can be created as described in section 5.2.

From these plots several points are immediately clear. The general shapes are reminiscent of those from single droplets (sections 3.8 and 3.9). The various lobes, and more importantly, nodes that are present in the scattering profiles are in good agreement with the theoretical predictions for the scattering from an individual droplet of the mean diameter (see associated figures 5.4b', c' and d'). The ratio of the scattered signals through any pair of angles also provides a good test of the theory. The ratio of the signals scattered through 30^0 and 150^0

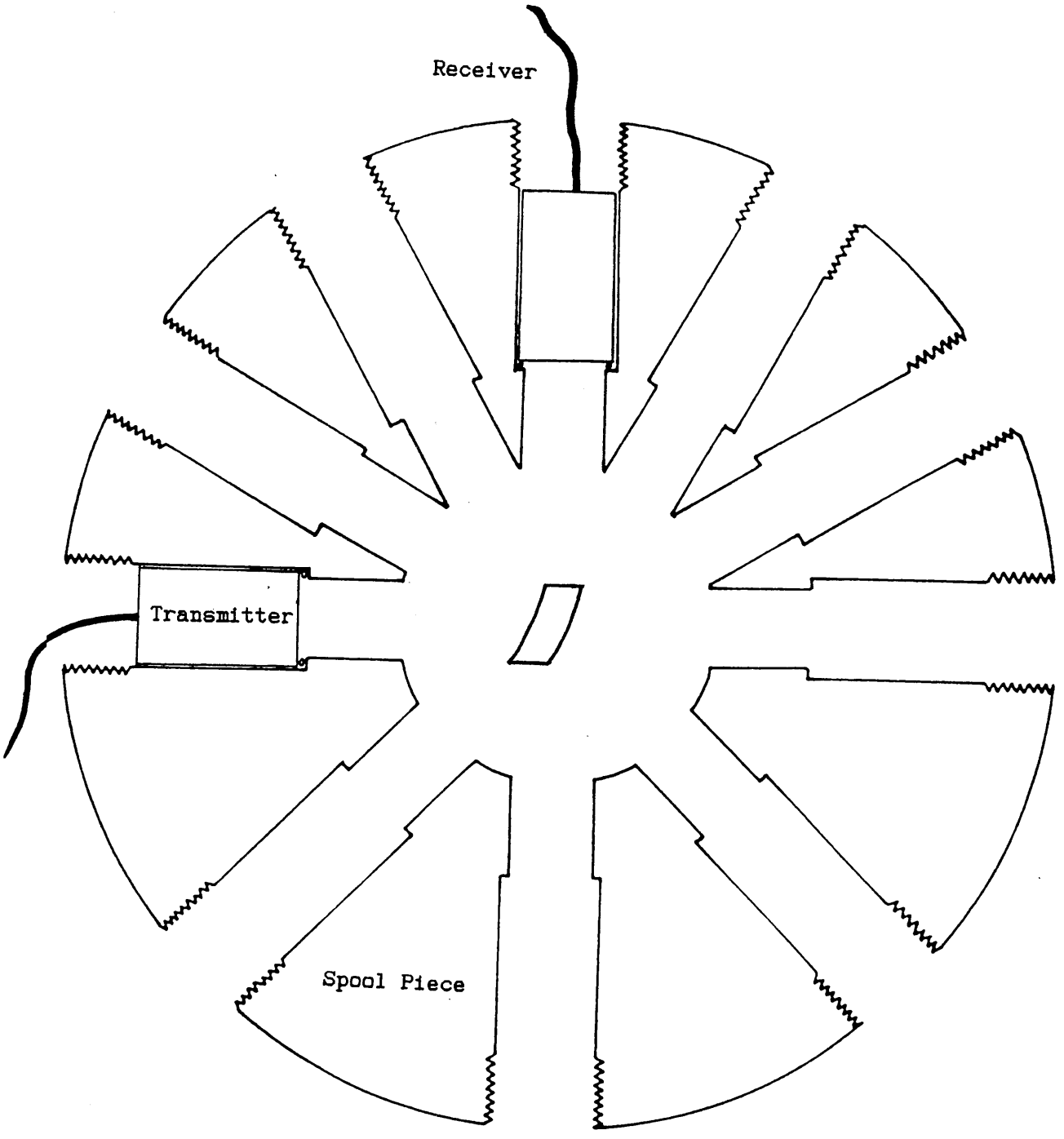

Figure 5.4a Effective scattering volume with a 6μs receive gate 60μs after the initial toneburst (full scale).

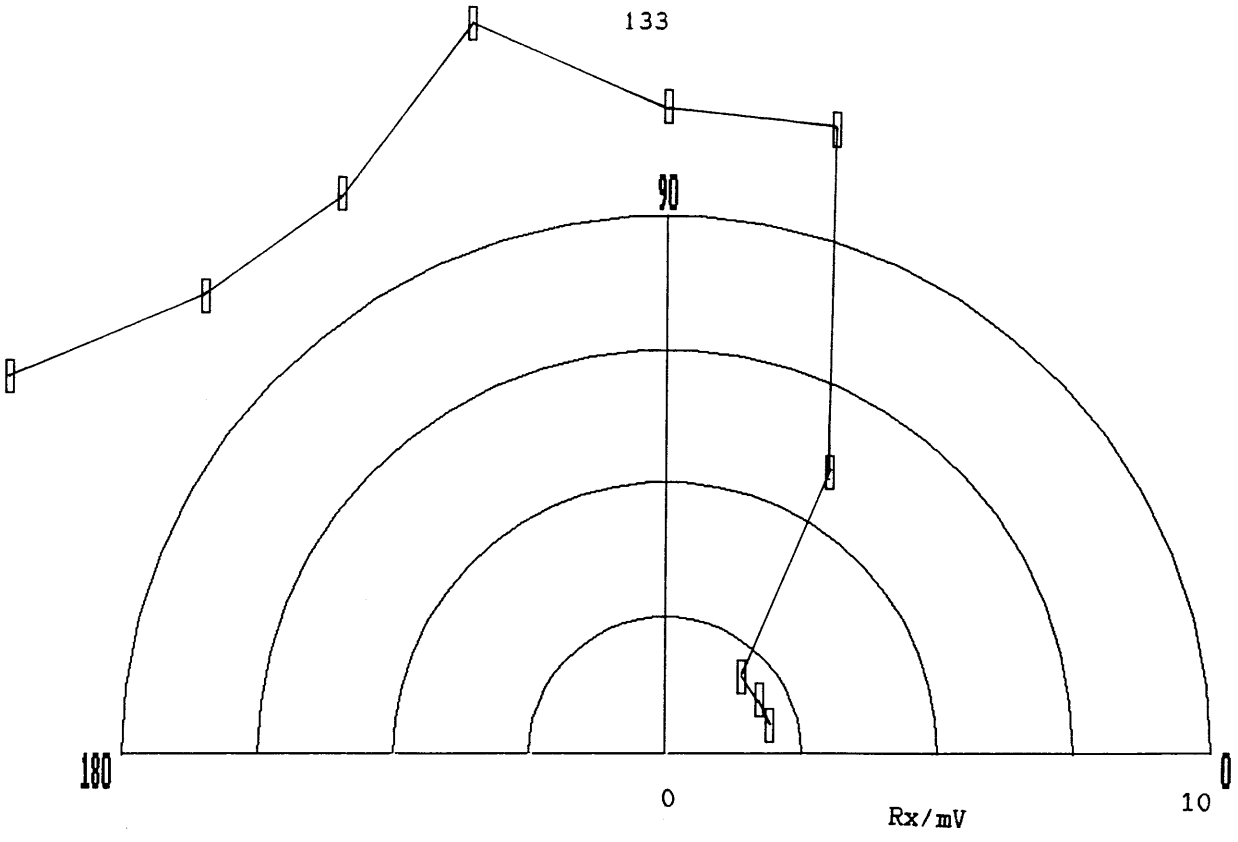

Figure 5.4b Scattering from oil droplets in water. Water flow rate = $1.95\times10^{-3}m^3s^{-1}$ (120Hz), jet flow rate = $3.85\times10^{-4}m^3s^{-1}$ (460Hz), void fraction=16%, nozzle diameter=1/8", $\langle d\rangle$=0.2mm, ka=0.42

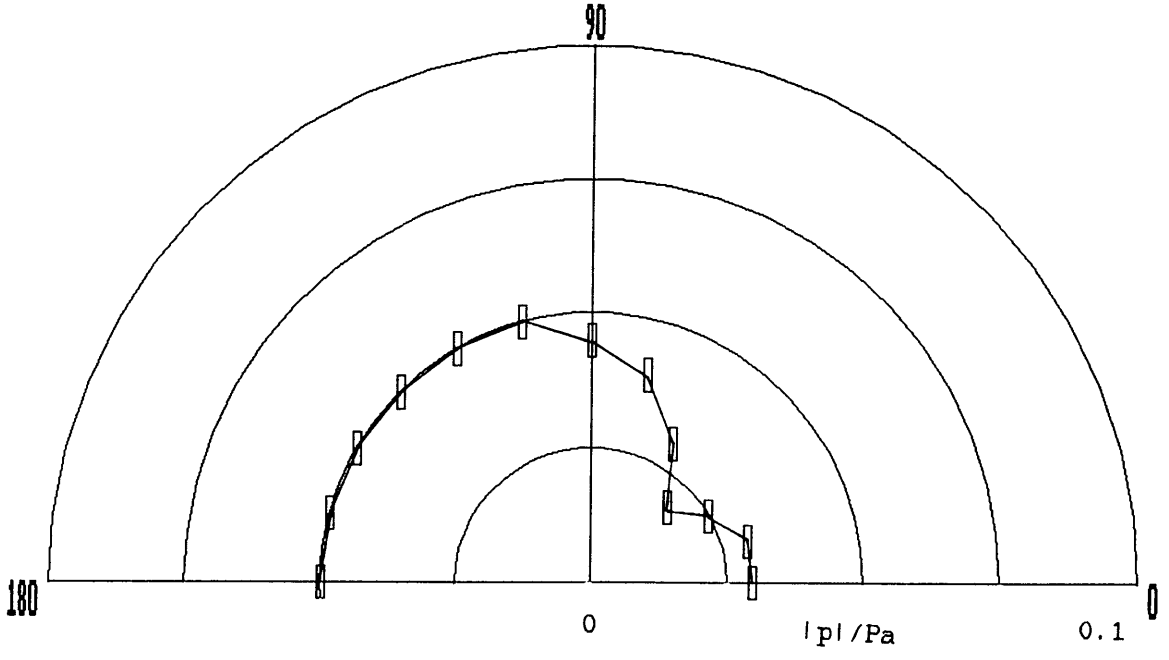

Figure 5.4b' Scattering from a single oil droplet in water, ka=0.42

(Theoretical)

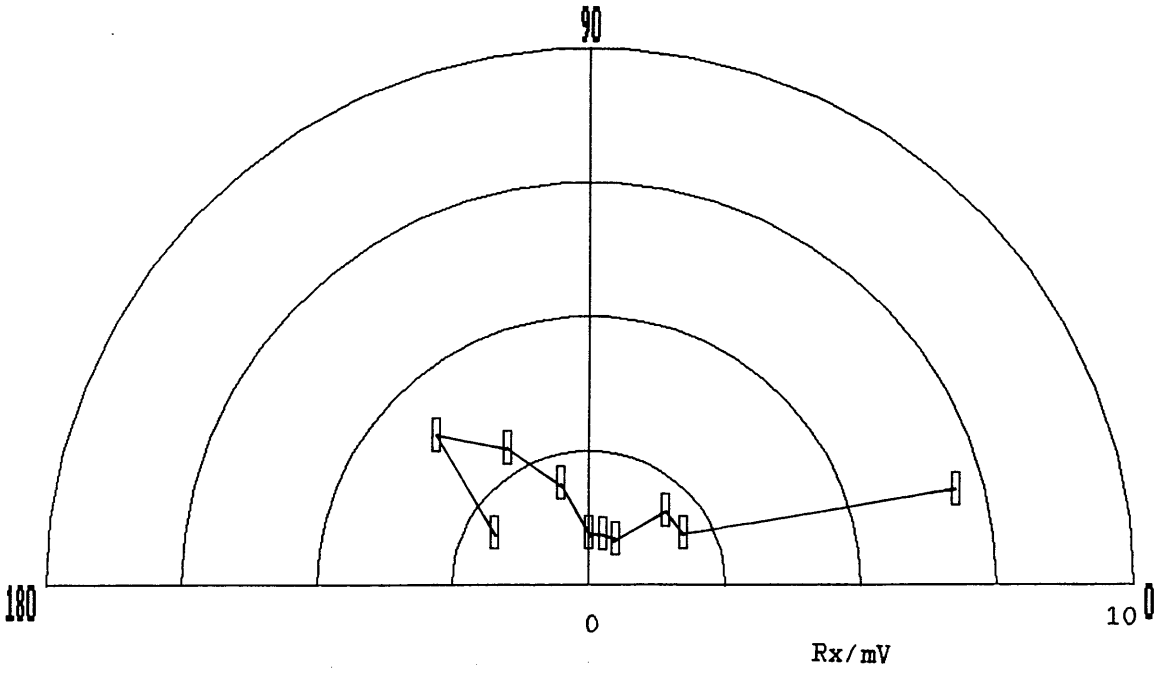

Figure 5.4c Scattering from oil droplets in water. Water flow rate = $1.95\times10^{-3}m^3s^{-1}$ (120Hz), jet flow rate = $3.85\times10^{-4}m^3s^{-1}$ (460Hz), void fraction=16%, nozzle diameter=3/16", <d>= 1.67mm, ka=3.5

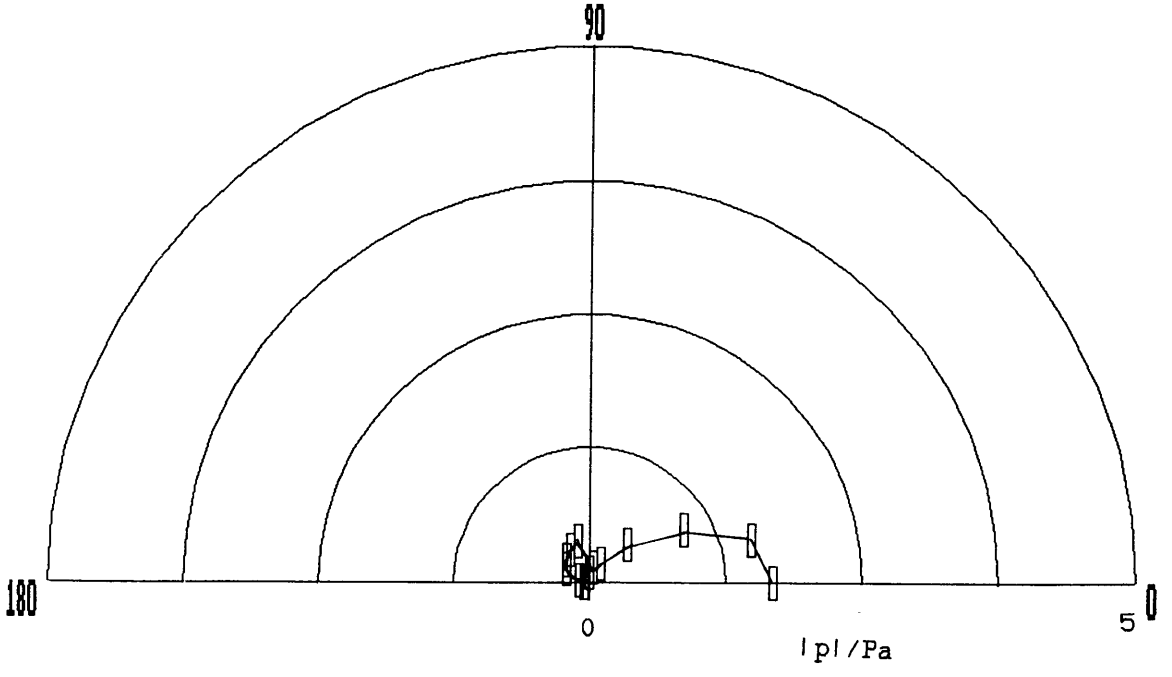

Figure 5.4c' Scattering from a single oil droplet in water, ka=3.5
(Theoretical)

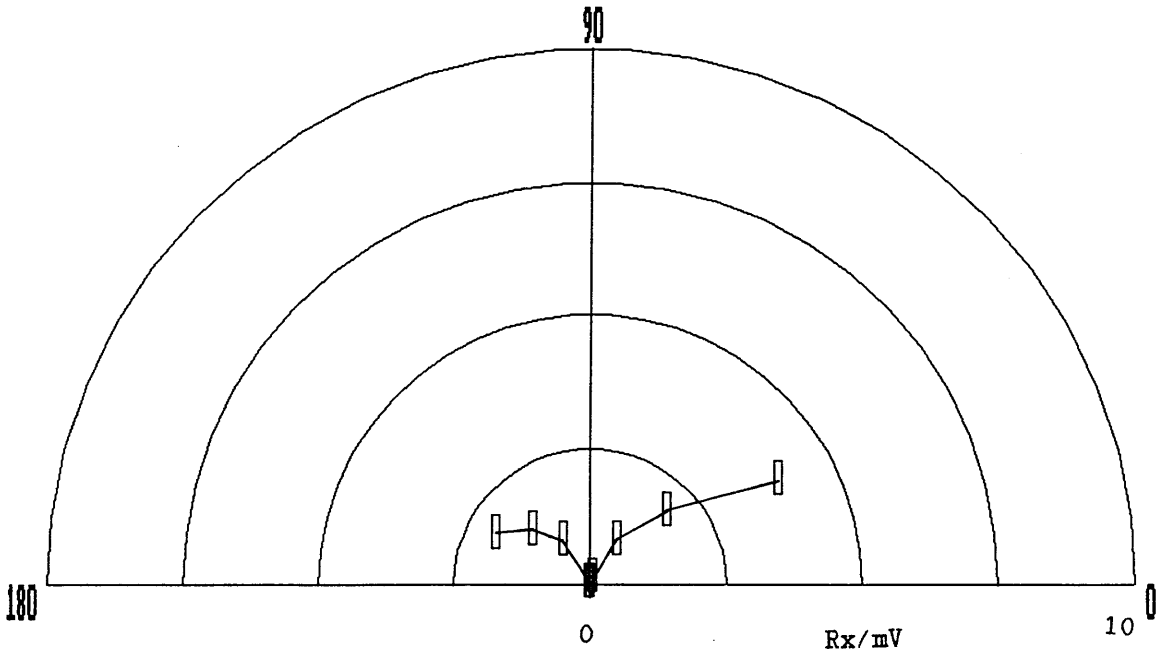

Figure 5.4d Scattering from oil droplets in water. Water flow rate = $1.95\times10^{-3}m^3s^{-1}$ (120Hz), jet flow rate = $3.85\times10^{-4}m^3s^{-1}$ (460Hz), void fraction=16%, nozzle diameter=1/4", <d>=2.72mm, ka=5.7

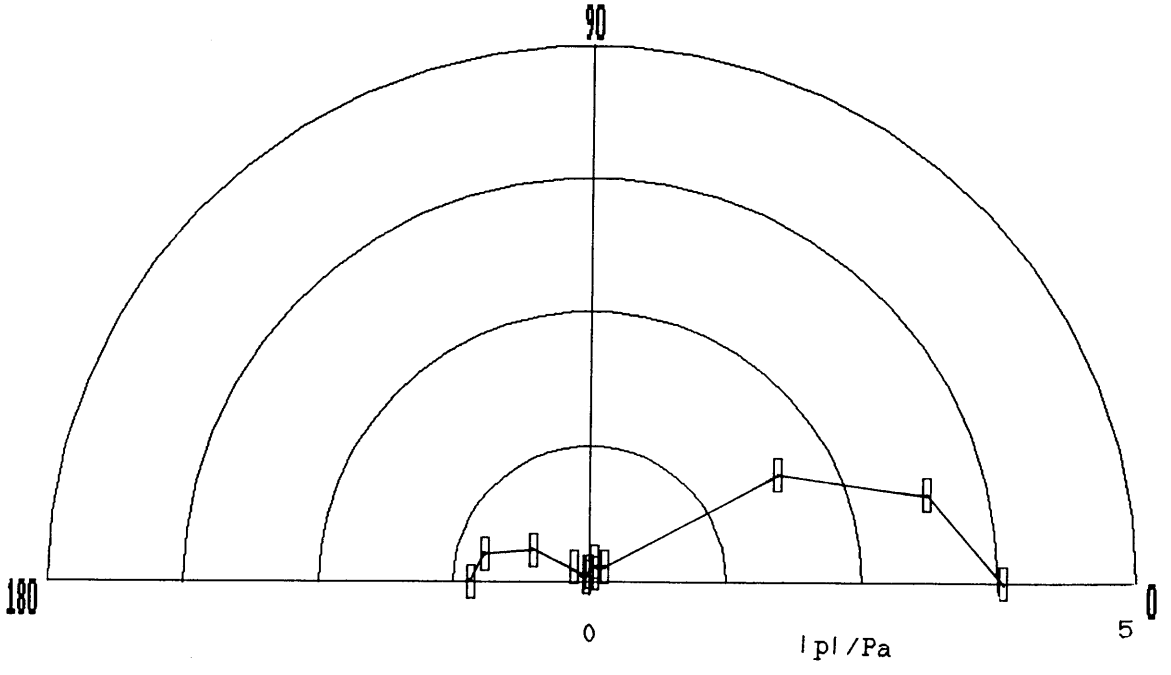

Figure 5.4d' Scattering from a single oil droplet in water, ka=5.7 (Theoretical)

are found for the three sets of data shown in figures 5.4b, c and d, and are listed below.

ka	V_{30}/V_{150} (Experiment)	V_{30}/V_{150} (Theory)
0.42	0.14	0.5
3.5	3.5	3.2
5.7	2.0	2.8

Figure 5.4e Table comparing theory and exeriment for the ratio of thescattered pressures at 30^0 and 150^0 for various ka

From these values and the figures, a few points are immediately clear. The scattering in figure 5.4b is typical of Rayleigh scattering with larger signals being backscattered. The overall scale of the signal in figure 5.4b when compared with figures 5.4c and d (and their theoretical plots) which are typical of diffraction scattering at first appears at odds with the single scatterer profiles until number densities are considered.

For a monodisperse flow, the particle separation can be found from equation 2.11, which reduces to $S \approx 3\langle a \rangle$ for this set of experiments, since the void fraction is constant at 16%. Thus for $\langle d \rangle = 0.2$mm, 1.67mm and 2.72mm the number densities of the scatterers is approximately $3.7 \times 10^4 cm^{-3}$, $65 cm^{-3}$ and $15 cm^{-3}$ respectively. It can now be seen that the particles in the Rayleigh scattering region will produce comparable signals to the diffraction scattering emulsions due to the number density effect ($\approx a^{-3}$) counteracting the weak scattering effect ($\approx a^4$).

The assertion that the scattering intensity from an ensemble of particles goes as the first power of the number density can now be checked experimentally. By keeping the jet properties constant (size and flow rate) and varying the main water flow rate, the void fraction can be varied at will. This also provides a check that the mean droplet size is independent of the main flow rate, the flow loop being shut down and photographs of the resulting emulsion being taken for each experiment. No change in the mean droplet size could be detected for the flow rates considered here. However for very low water flow rates (below the range

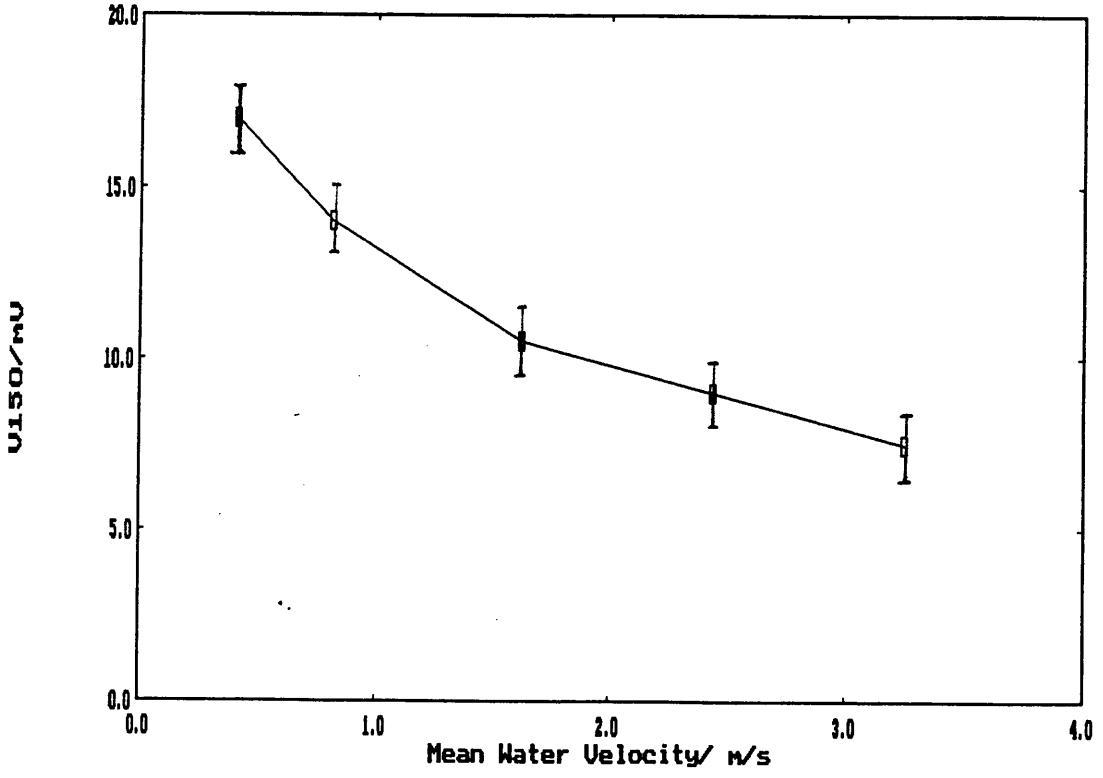

Figure 5.4f Scattered pressure in volts as a function of water flow rate with constant jet properties. Scattering angle=150°, jet flow rate = $3.85\times10^{-4}m^{3}s^{-1}$ (460Hz), nozzle size=1/8"

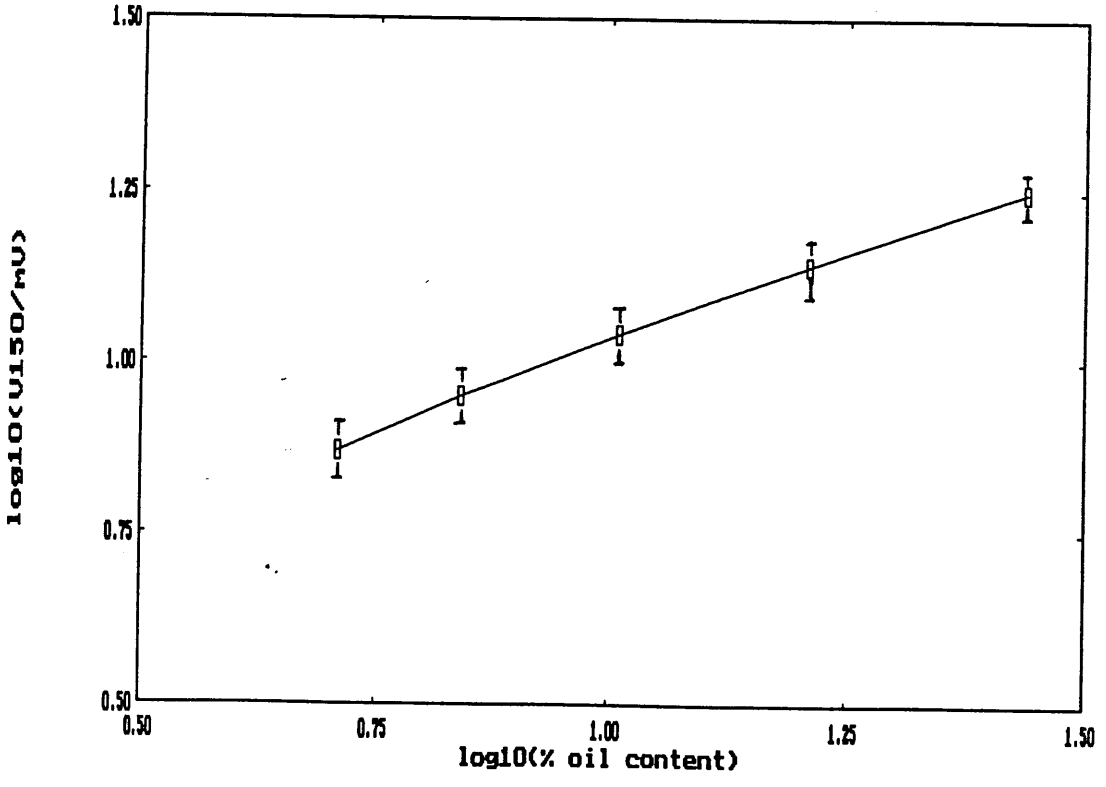

Figure 5.4g Log/log plot of scattered pressure as a function of void fraction, measured in volts and % oil content respectively. Physical paramaters as figure 5.4e

of the water meter) a reduction in the droplet size was observed, probably due to recirculation in the jet mixing zone.

Figure 5.4f shows the scattered voltage at 150^0 as a function of water flow rate, for a 1/8" jet nozzle (therefore small droplets and Rayleigh scattering). Converting the liquid flow rates into a void fraction allows figure 5.4g to be plotted. the least squares slope through the points is found to be 0.502, which, within the experimental errors (0.502±0.12 from the worst possible case through the error bars) can be taken as 0.5.

Thus: Voltage α (void fraction)$^{1/2}$

Pressure α (number density))$^{1/2}$

Intensity α Number Density

Using larger jet sizes, lower jet flow rates or smaller scattering angles all tend to produce less good results, since the number densities are much reduced, there are the scattering nodes to contend with and the signals are generally smaller.

Another important conclusion concerns the number of scatterers involved in the scattering. From the equation and table of section 2.11 and the above flow data, it is seen that there are approximately 10^3 scatterers involved in each measurement. Thus the effects of multiple scattering need not be allowed for (even when the droplets are only separated by a few radii on average), when the scattering is weak.

During all of the previous experiments, great care has been taken to eliminate the effects of air bubbles coming out of solution in the flow loop. This is achieved by increasing the pressure of the whole loop (by partially closing the outlet valves) to the point where bubbles are no longer evident in the pipe, either visibly in the flow or eventually appearing on the upper walls of the pipes when the flow is suddenly switched off.

A check for the presence of air bubbles in an apparently 'clean' flow would be to use them to scatter ultrasound exactly as in the previous sections. A water flow was set up with no back pressure in the system,

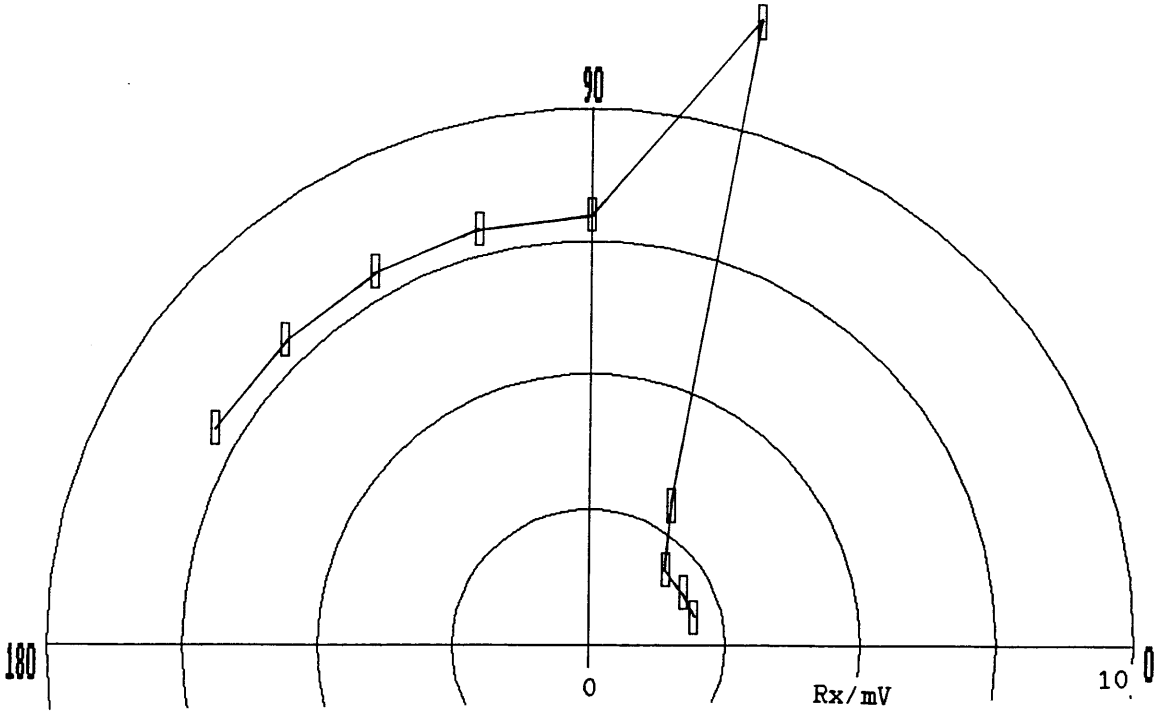

Figure 5.4h Scattering from air bubbles in water. Water flow rate = $9.4\times10^{-4}m^{3}s^{-1}$ (58Hz)

leading to visible clouds of bubbles moving down the pipe. The angular scattering from these bubbles was measured and the results are plotted in figure 5.4h.

Again Rayleigh scattering is evident, and this was confirmed photographically with a mean diameter of 0.17mm. It is clear from the figure 5.4h that the most effective bubble detector would work at scattering angles of between 75^0 and 150^0. Minimising this signal by increasing the back pressure in the flow loop proved to be as good a method of eliminating the air bubbles as visual observation.

To quantify the amount of air in the flow is very difficult as its origin is not directly controllable, however, when the flow is stopped, the bubbles rise to the upper surface after several seconds, where they can be photographed, exactly as in the sizing measurement. This enables an estimate of void fraction to be made. For the unrestricted flow the void fraction is approximately 0.01%.

Comparing figure 5.4h with figure 5.4b shows that a 0.01% air flow produces similar scattering to a 16% oil flow when both are in the Rayleigh scattering regime. This is in line with the earlier theoretical result (figure 4.3b') that the scattering from air bubbles for $ka<1$ is always much greater than from similar sized liquid droplets. This is a serious drawback since optimising the scattering from the liquid droplets (Rayleigh scattering from many small droplets) leads to a very sensitive air meter.

5.5 Acoustic Döppler Measurements.

As was outlined in section 2.8, the acoustic wave scattered by a moving particle undergoes a frequency shift dependent on the particles velocity and the angles between the velocity vector and the directions of the incident and scattered waves. The general equation for the frequency shift is given by equation 2.8.1 for the coordinate system shown in figure 2.8a.

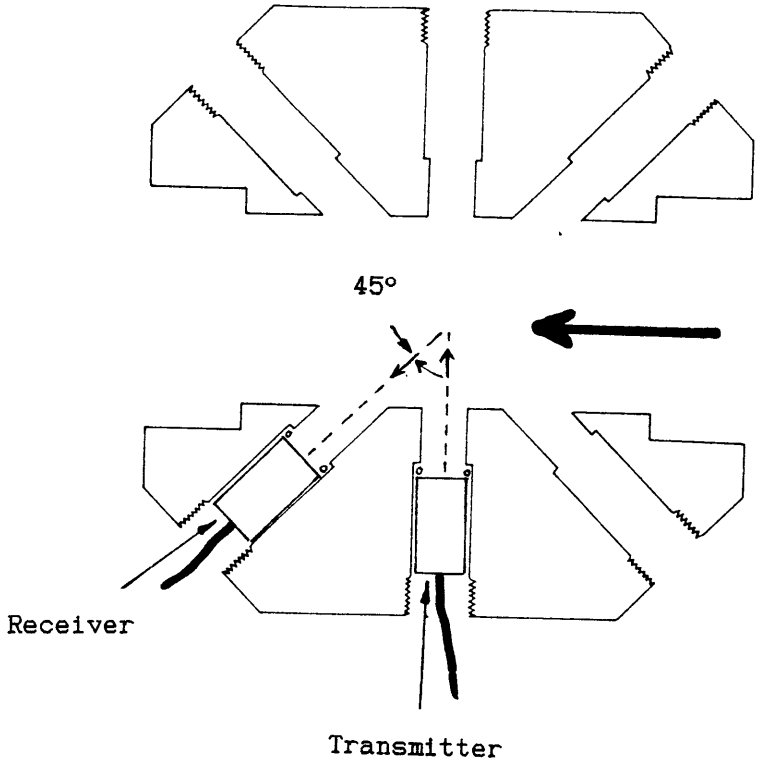

Figure 5.5a Döppler scattering geometry in the spool piece.

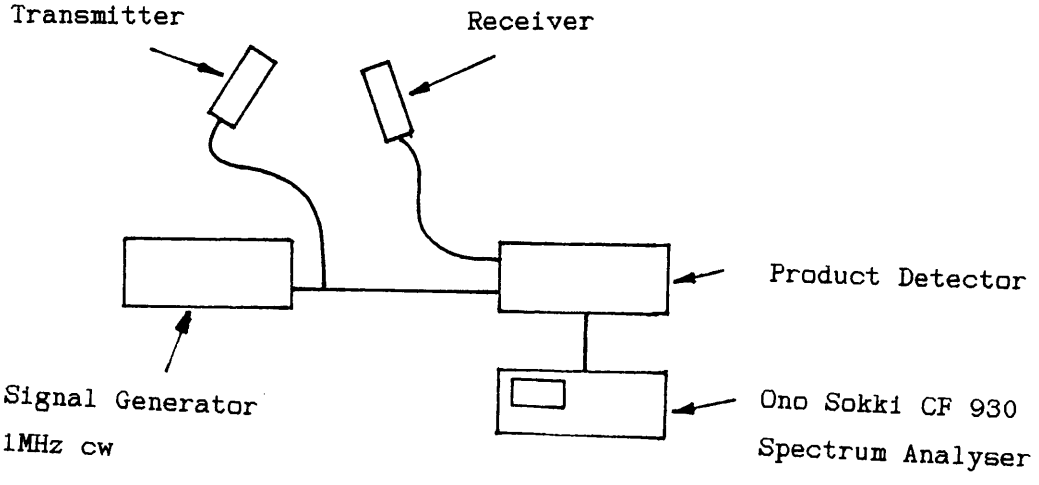

Figure 5.5b Block diagram of the circuitry used to determine the Döppler frequency shift.

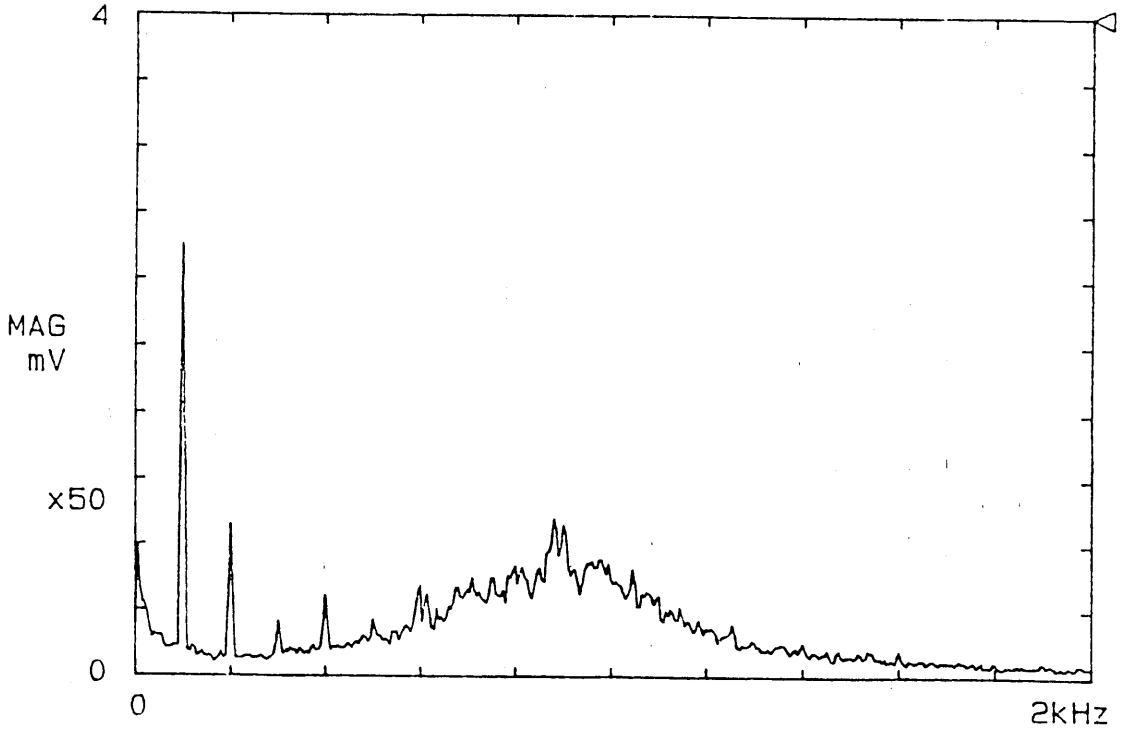

Figure 5.5c Typical spectrum analyser output

The simplest Döppler scattering geometry from the point of view of the analysis and interpretation available within the spool piece is shown in figure 5.5a. This geometry leads to a frequency shift given by;

$$\Delta f = \frac{fV\cos 45^0}{c} \qquad (5.5.1)$$

A block diagram of the circuitry used to determine this shift is given in figure 5.5b. Full details of the design, testing and analysis of this circuit can be found elsewhere (Lenn 1985).

Figure 5.5c shows a typical demodulated signal printed from the screen of the spectrum analyser, with the peak frequency being determined visually in conjunction with the cursor on the screen.

A series of experiments was carried out in the horizontal flow section, keeping the jet parameters constant (an oil flow rate of 460Hz or $5.85\times10^{-4}m^3s^{-1}$ and nozzle size of 1/8") and varying the water flow rate. A plot of the Döppler frequency shift versus the water flow rate is plotted in figure 5.5d. Clearly, the total flow rate is due to a combination of the oil and water flow rates. Thus assuming no slip between the two fluids, figure 5.5e is a plot of the velocity inferred from the Döppler measurement versus mean velocity and centreline velocity, the latter assuming a fully developed turbulent velocity profile.

5.6 Discussion and Conclusions.

This chapter has required the extensive use of a two-component flow loop, incorporating a jet mixer/injector. Very simple methods have been used to characterise the flow including visual observation and photography, especially of the emulsion/droplet flow regime

The spool piece was designed to incorporate a range of ultrasonic techniques, however, in the end, considerations of time allowed only the new technique of droplet sizing by angular scattering and the old technique of ultrasonic Döppler velocimetry to be analysed in detail.

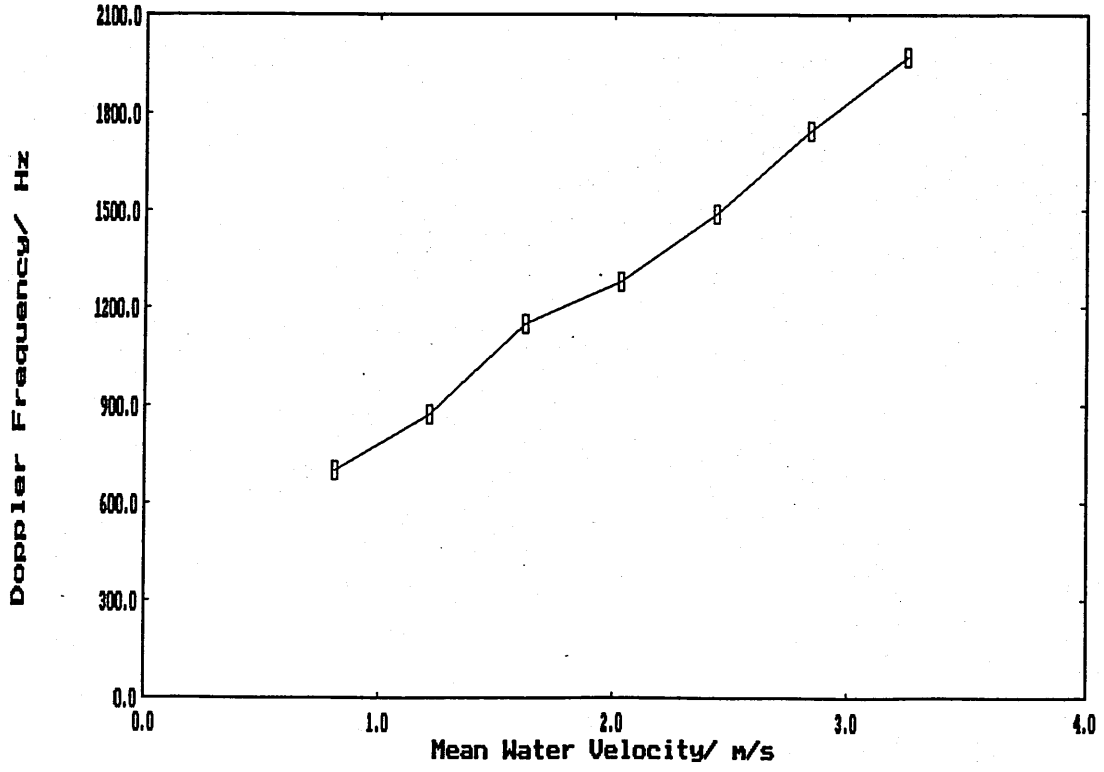

Figure 5.5d Plot of Döppler shift vs water flow rate for constant jet properties.

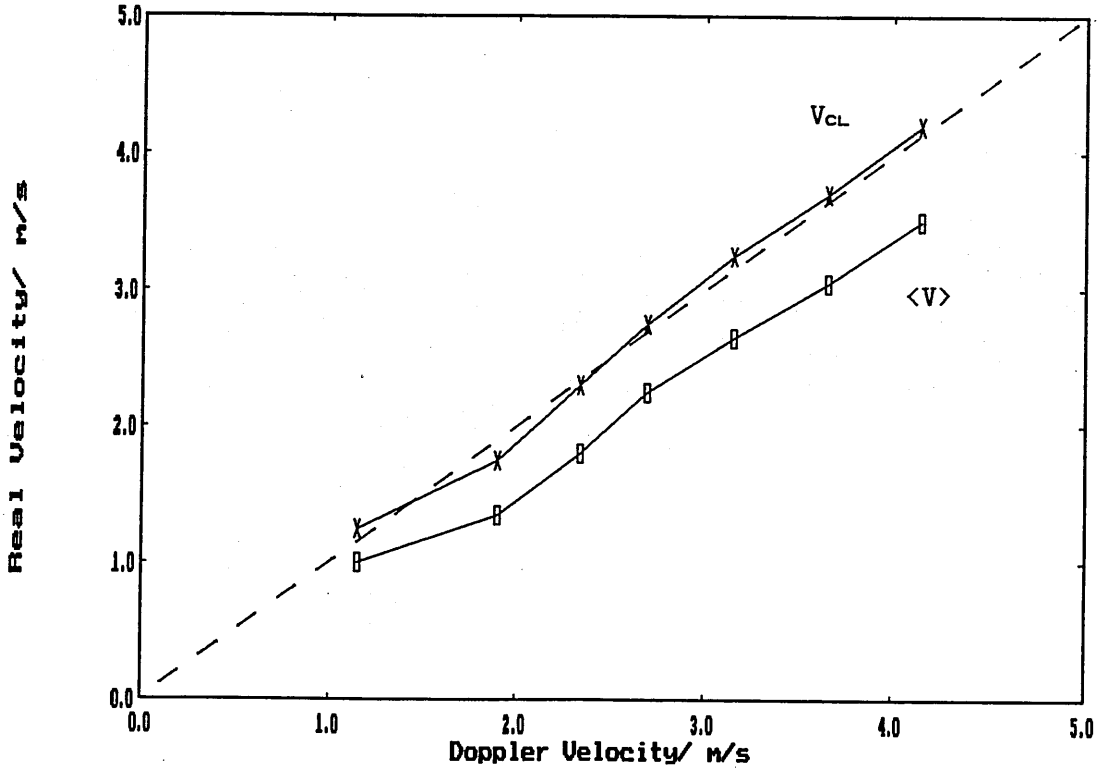

Figure 5.5e Plots of Döppler implied velocity vs centreline and mean velocities assuming no slip.

The flow loop could produce all of the flow regimes required and the jet mixer/injector gave a flexible enough range of droplet sizes (in fair agreement with other published theoretical and experimental results (Fernando 1990)), for a representative series of angular scattering experiments to be carried out.

A simple range gating circuit was designed and constructed to define more accurately the scattering volume and scattering angles. This allowed angular scattering measurements to be made around the axis of the pipe, the results of which are in line with those expected from theory, only after an allowance is made for the number density of the scatterers. Rayleigh scattering and diffraction scattering have both been observed from appropriate droplet flows, with the scattering nodes approximately agreeing with the appropriate nodes of the single droplet of the mean diameter.

The classical assumption that the scattered intensity is proportional to the number density of scatterers has been proved experimentally, thus also confirming that the droplets are randomly distributed.

A final scattering experiment has confirmed the previous theoretical conclusion that scattering from gas bubbles with $ka<1$ is much greater than from the equivalent oil droplets. An air fraction of approximately 0.01% produces similar scattering to a 16% oil fraction, both for $ka<1$. Thus air is the critical parameter in the effective application of the scattering technique.

A standard Döppler method was used to determine the velocity of the flow. The result confirms that the Döppler method is measuring the centreline velocity. These calculations assume that the speed of sound in the main flow is that of water. For the void fractions involved, a correction must be made for the speed of sound in the emulsion. This is not a trivial exercise, as the droplet distribution in the flow and especially near the transducer sections may not be uniform. Any corrections for this effect will tend to reduce the Döppler implied velocity to somewhere between the centreline velocity and the mean velocity.

Thus the droplet flow can be sized and the velocity determined usng only ultrasonic methods. Multi angle scattering methods can be used to determine coarse differences in size distributions leading to Rayleigh scattering and diffraction scattering, as well as finer details within the diffraction scattering regime. Even for large void fractions, (≈20%) the weakness of the scattering negates the problems of multiple scattering, meaning that the individual scatterers can be summed statistically, making the analysis simpler than it might have been. Similarly, Doppler methods can be used to determine velocities within the flow, the weakness of the scattering meaning that attenuation is not a problem in detecting the signals. Incorporating void fraction measurements using speed of sound methods (chapter 4) would allow a comprehensive characterisation of the whole flow. Other standard techniques not investigated here, such as range gated backscatter and range gated cross-correlation would allow number density distributions and velocity distributions to be defined also.

Chapter 6: Detecting Chaos in an Oil-Water Flow.

6.1 Introduction.

Thus far this work has concentrated on the ultrasonic characterisation of an oil-water flow in the droplet flow regime. Clearly, as both components of the flow are fluids, they can appear in many different configurations across the pipe. Obvious flow regimes such as stratified, wavy and annular, provide fairly simple interfacial geometries to study and quantify. These are just a few of the qualitative descriptions of two-phase and two-component flows that have appeared in the literature. The published literature on flow regimes and flow regime maps has been briefly reviewed in appendix C along with some of the semi-empirical relationships that have been derived to predict flow transitions.

One possible approach towards producing a unified view of multiphase and multicomponent flows involves generating large databases of experimental data. From measurements of parameters such as time series of differential pressure or electrical impedance, combined with thresholding, spectral and visual methods, methods can be devised that can predict the flow parameters and flow regime of an unknown system. The accuracy of these systems varies greatly with flow regime, since there is no physical basis for the techniques used.

An alternative approach, which may lead to a better understanding of the physics of the flow of mixtures, is to impose a tractable model upon the flowing system. It has been shown experimentally, and often verified theoretically, that a flowing system goes through several transitions as the flow rates are increased. For low flow rates, a simple laminar flow always appears, and at high enough flow rates, something approaching fully developed turbulence is evidenced. This type of behaviour is also observed in simple experimental and numerical systems that are described as chaotic.

This chapter will show experimentally that the droplet flow regime has somewhere between five and six degrees of freedom, implying that the

flow can be modelled using five or six variables, thus indicating that two-component flows display chaotic behaviour. A detailed discussion of chaos and fluid flows can be found in appendix D, which is a literature review that starts from first principles and finishes with the few published works that have detected chaos experimentally in multiphase flows.

6.2 Oil-Water Experiments and Data Analysis.

As mentioned above and in appendix D, a few attempts have been made to investigate multiphase flows from a chaos perspective. The following paragraphs describe a preliminary proof of principles for the application of some of these methods, to oil-water flows.

In the end, three sets of experimental data were available for analysis. One from the flow loop built for this project (chapter 5 and appendix B) and the rest from the oil-water loop at Schlumberger Cambridge Research.

The Cranfield data comprised a measure of the amplitude of a continuous 1MHz ultrasonic beam scattered through 150^0 in a vertical oil-in-water disperse flow with a water superficial velocity of $0.4ms^{-1}$ and an oil holdup of 0.05. The Schlumberger data involved two different oil-water flows. Firstly, an oil-in-water dispersion with a water superficial velocity of $0.4ms^{-1}$ and an oil holdup of 0.05 monitored using a resistive method. Secondly a vertical water-in-oil disperse flow with an oil superficial velocity of $0.4ms^{-1}$ and a water holdup of 0.1 was monitored using a capacitive method.

Exact experimental details of the Schlumerger work is not available. However, that the data was gathered via a 12bit 1kHz A-D converter for 5 seconds is sufficient for the present purposes. The data was sent directly to the Cranfield computer center VAX over JANet, the academic network transmission system.

The experiments carried out on the Cranfield loop consisted of taking the scattered 1MHz signal, extracting the modulating envelope (1kHz

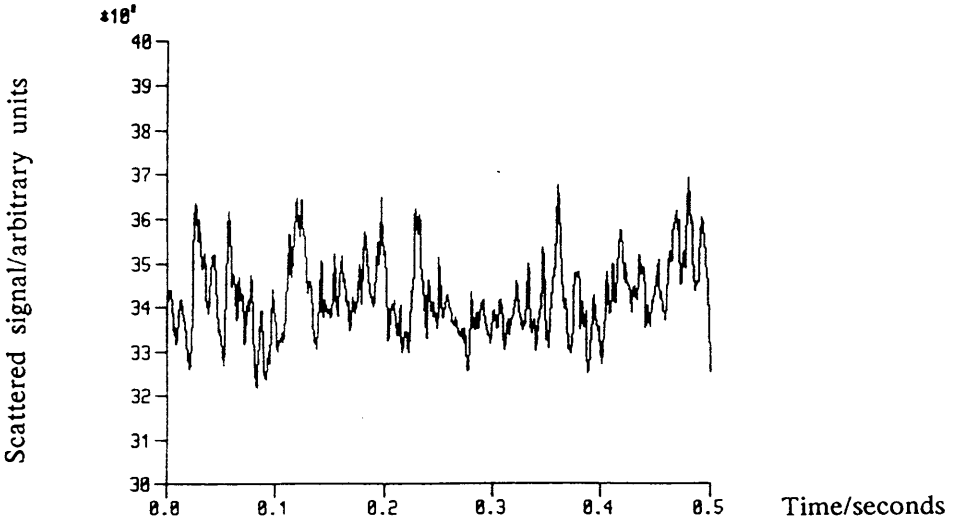

Figure 6.2a. Data from the ultrasonic measurement of a vertical oil in water flow.

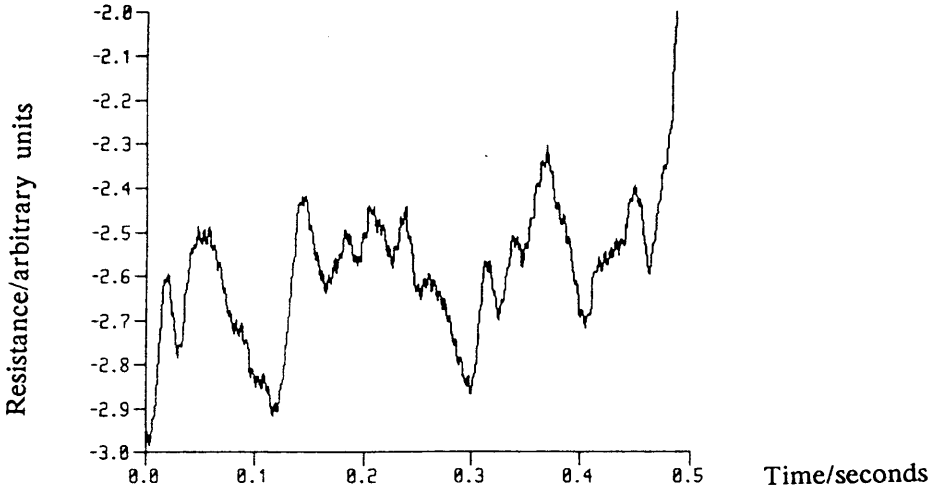

Figure 6.2b. Data from the resistive measurement of a vertical oil in water flow.

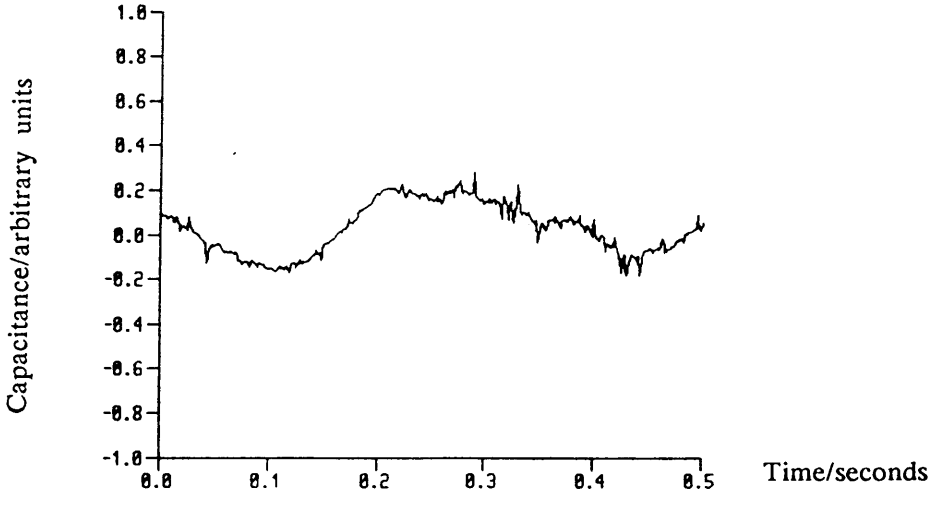

Figure 6.2c. Data from the capacitive measurement of a vertical water in oil flow.

low pass filter), sampling and digitising the signal using the built in A-D of a Horizon S100 data processor and computer. The data was first saved in machine code on the Horizon disk and then sent via the serial port to an Opus personal computer. The data file transfer package Kermit was then used to send the data to the VAX mainframe where the analysis would be carried out.

Thus three sets of data were available for analysis and portions of each are reproduced in figures 6.2a, b and c. It is immediately clear that the transfer function of the capacitive measuring system has filtered out many of the higher frequency components of the signal, leaving a characteristic frequency of about 3Hz. This frequency lies within the region 1-20Hz expected for the density waves of the droplet flow regime (Drahos 1989). The resistive and ultrasonic data show similar dominant frequencies, but also contain much more information at the higher frequencies.

6.3 Identifying the Attractor Governing the Dynamics of the Flow.

The instantaneous state of the system can be considered as a point in a multidimensional phase space, with each orthogonal coordinate representing an independant parameter governing the underlying dynamics. As the system evolves in time, the trajectory of this point traces out an object in all of the coordinates. The trajectories of all physically realisable systems tend towards a finite attractor whose shape and complexity are determined by the underlying dynamics.

If the system is chaotic, the trajectory has a sensitive dependence on initial conditions, though the gross shape of the attractor is independent of the initial conditions. In the full expansion of the phase space, the trajectory of the chaotic system never repeats itself, and hence, if the attractor is to remain finite, must have structure on every scale less than that of the attractor, ie infinite structure and a fractal by definition. The trajectories produced by non-chaotic systems must necessarily lie on closed loops or (hyper) surfaces.

Thus, in order to construct an attractor for a dynamical system, a knowledge of all the independent variables governing the behaviour is required. Simultaneous measurement of all of these variables would allow the attractor to be drawn and analysed. For most systems, even the number of underlying variables is not known, so measuring them would prove difficult to say the least.

However, it has been shown that an attractor can be reconstructed from the time series of a single experimental variable (Packard 1980, Takens 1981 and appendix D). The level to which the reconstructed attractor resembles the real attractor, depends on how representative of the behaviour of the system, the data is. Thus the data shown in figure 6.2c would be expected to reproduce a less realistic attractor than the other two sets of data, since its information content is much less.

6.4 Reconstructing the Attractor.

The attractors were reconstructed using the method of delays, by taking the experimental time series ($X_0(t)$) and creating other sets of data from this using the method of delays, ie $X_1(t)= X_0(t+\tau)$, $X_2(t)= X_0(t+2\tau)$, ... $X_n(t)= X_0(t+n\tau)$. Figures 6.4a to d show projections f the reconstructed attractor for the resistive data onto the planes $(X(t),X(t+\tau))$, $(X(t),X(t+3\tau)$, $(X(t),X(t+5\tau))$ and $(X(t),X(t+7\tau))$. In this case, τ was taken as the data interval (1ms), however, any multiple of this could be used, though large values reduce the effective amount of data at large n. It is clear from these figures that the trajectory is starting to become less "knotted" as the delay is increased, implying that a low dimensinal phase space will be able to totally unwind and contain the attractor.

6.5 Determining the Dimension of the Attractor.

The number of dimensions in which the attractor is plotted, the embedding dimension M, is increased until the attractor (if strange) is totally unwound, and never crosses itself. Ideally the next integer

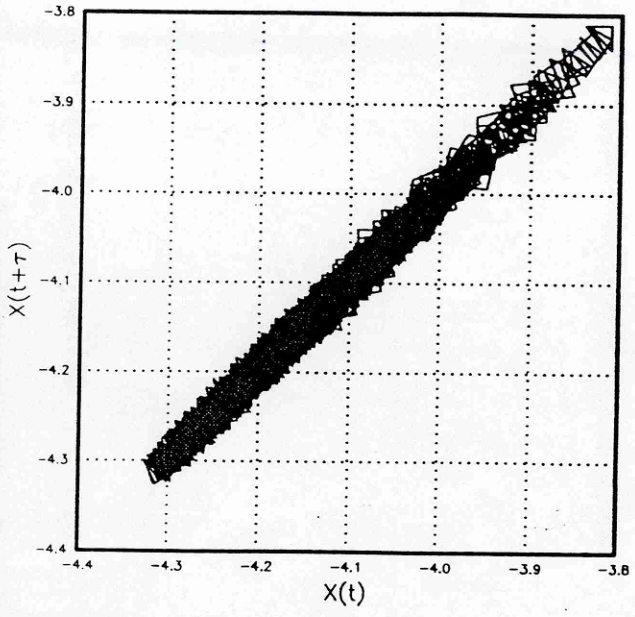

Figure 6.4a. The attractor for the resistive data reconstructed in X(t),X(T+τ) space.

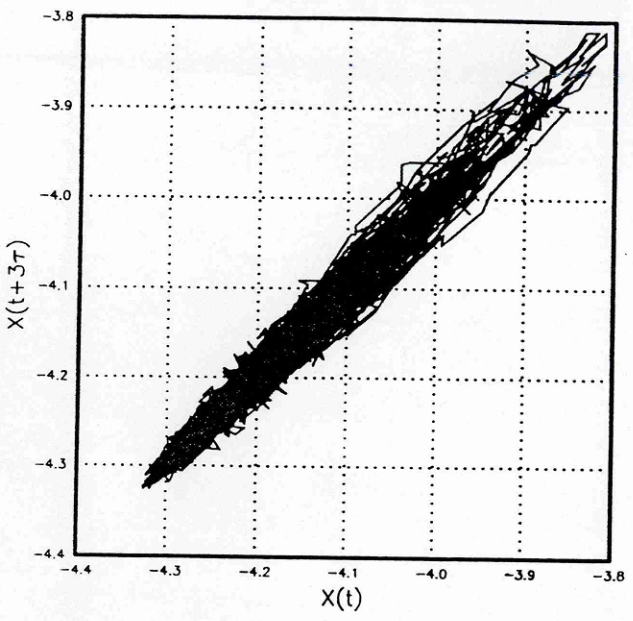

Figure 6.4b. The attractor for the resistive data reconstructed in X(t),X(T+3τ) space.

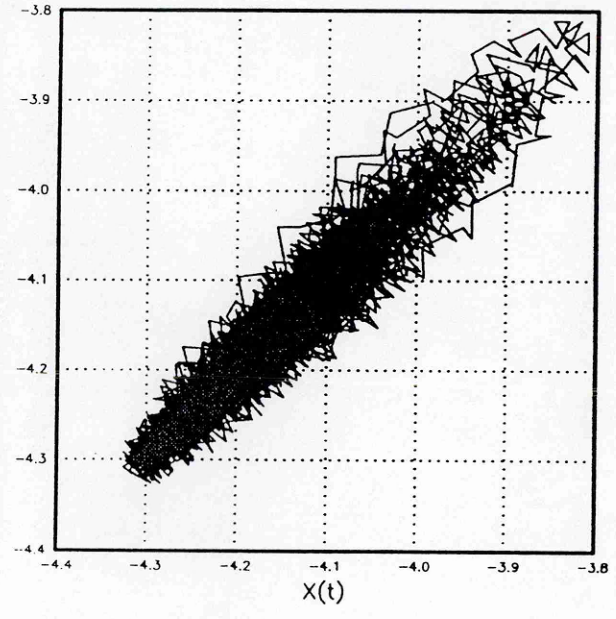

Figure 6.4c. The attractor for the resistive data reconstructed in X(t),X(T+5τ) space.

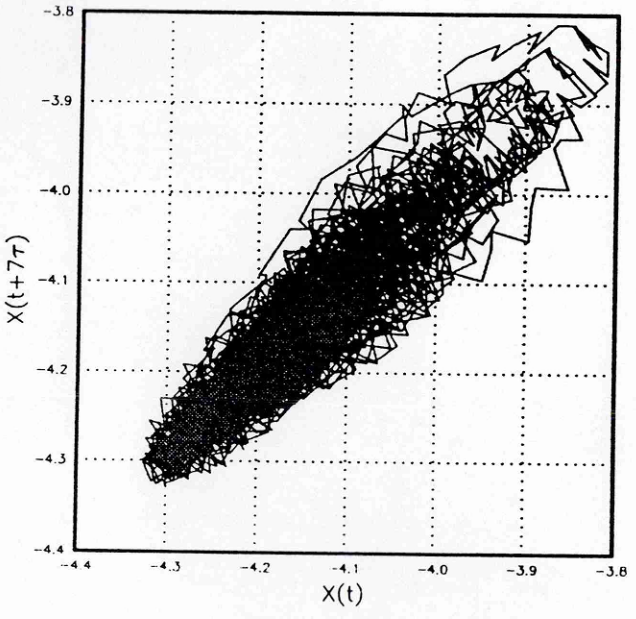

Figure 6.4d. The attractor for the resistive data reconstructed in X(t),X(T+7τ) space.

higher than the fractal dimension of the attractor would totally unwind the attractor and any increases in M beyond this would lead to no further expansion of the attractor. Limitations of the experimental data usually means that an embedding dimension considerably higher than the fractal dimension is usually required before the attractor stops crossing itself. This, and the fact that it is not a simple procedure to visualise objects in more than 3 dimensions, means that a more mathematical approach must be taken to determine the fractal dimension of the attractor and the next higher integer for the embedding dimension.

Several different numerical methods have been proposed in the literature for finding the fractal dimension directly from the experimental data. These are mostly modifications and improvements to the method proposed by Grassberger and Procaccia (1984) modified in Moller (1989) and Dvorak (1990).

A correlation integral is defined as follows:

$$C(\varepsilon) = \lim_{N\to\infty} \lim_{\varepsilon\to 0} \frac{1}{N^2} \sum_{\substack{i,j \\ i\neq j}}^{N} \theta(\varepsilon - |R_i - R_j|) \qquad (6.5.1)$$

where θ is the Heaviside step function that tests whether R_j lies within a hypercube of side 2ε of R_i. R_i and R_j are points on the reconstructed attractor in the M dimensional phase space as described in the previous section.

For an attractor with a fractal dimension D, by definition (Grassberger 1984);

$$C(\varepsilon) \underset{\varepsilon\to 0}{\simeq} \varepsilon^D \qquad (6.5.2)$$

Thus a plot of $\log_{10}C(\varepsilon)$ versus $\log_{10}\varepsilon$ will have a slope of D, provided the phase space has a dimension $>D$ and the attractor is fully

expanded. For the latter criterion to be met, both experimentally and theoretically (Packard 1980), requires an embedding dimension $M>2D+1$.

Figure 6.5a shows the main features of a plot of $\log_{10}C(\varepsilon)$ versus $\log_{10}\varepsilon$ for various values of embedding dimension. As the value of M is increased, there is a range of ε where the slope$\simeq$M, above this region, the ε is too great, and is encompassing a greater volume of the attractor than that over which the fractal definition $C(\varepsilon)\simeq\varepsilon^D$ is valid. Below this value, ε is less than the data quantisation step e, so further reductions in ε cannot separate the data points. As M is further increased, the slopes tend towards a constant value, the fractal dimension of the attractor. Convergence occurs around $M\simeq 2D+1$.

The region of linearity is also limited by the number of data points, since a single correlation gives $C(M,\varepsilon)=1/N^2$ as a lower limit. These criteria all provide limiting values of ε over which the analysis can be carried out. The correlation integral is defined in the limit $\varepsilon\rightarrow 0$. The assumption here is that the behaviour of the attractor at these intermediate values of ε is the same as that as $\varepsilon\rightarrow 0$. In order to increase confidence that this is the case, it has been proposed that the linear region of the graph should cover at least a decade of ε. This means that the size of an attractor that can be determined from a given data set is limited by the data itself. These factors will be further quantified in a later section.

These methods have been applied to the ultrasonic and resistive data, and the resistive results are plotted in figures 6.5b to e for various values of M.

The slopes of the linear portions of the graphs have been determined using a least squares method and are plotted as a function of the embedding dimension, M, for both the ultrasonic and resistive data in figure 6.5f.

The 'linear' part of the graph is obtained by finding the slope of the line joining each pair of consecutive points. A least squares line is found for those points between which the individual slopes deviate by less than 10% from the mean.

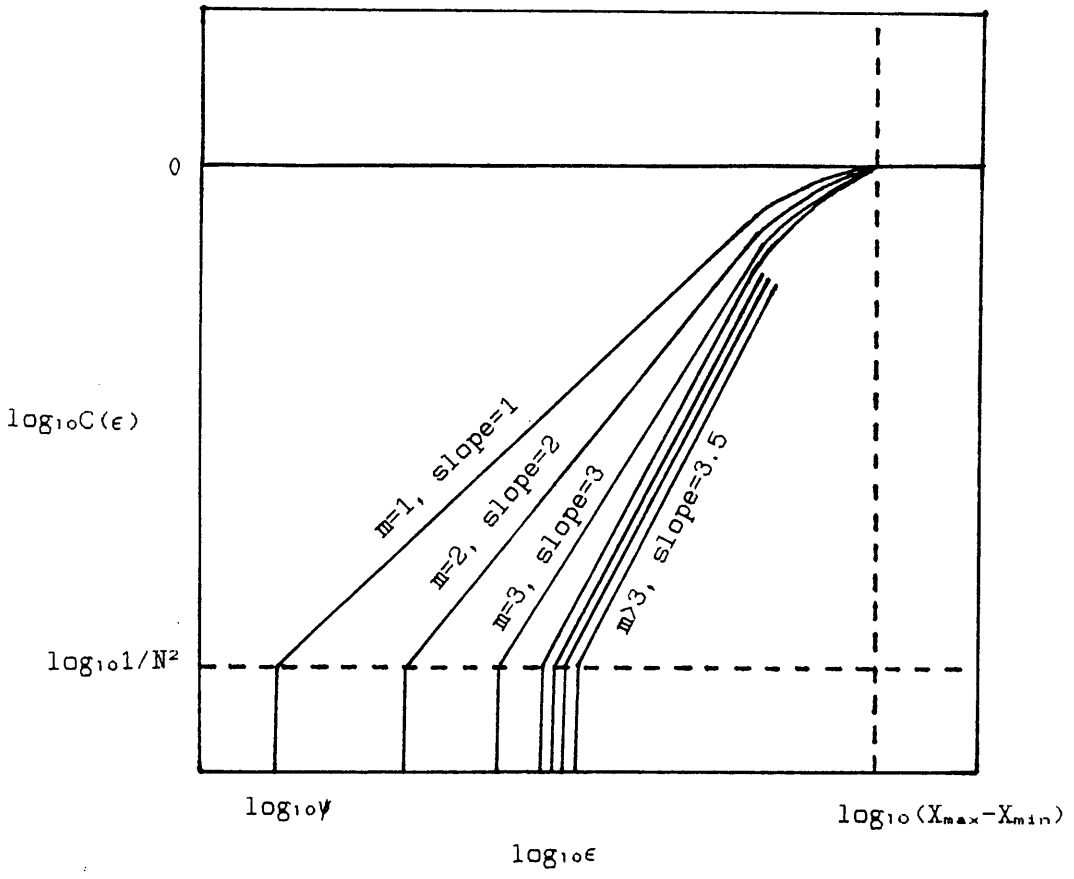

Figure 6.5a. A sketch of the plot used to determine the Hausdorff dimension,

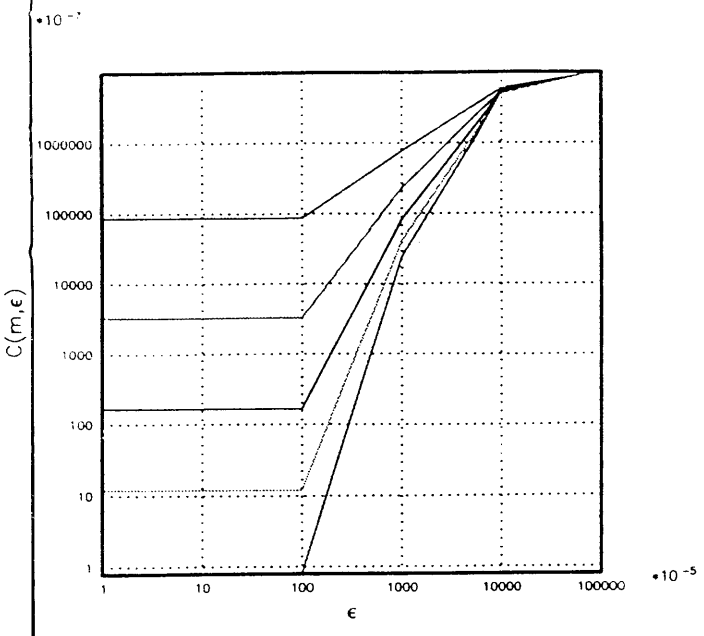

Figure 6.5b. Plot of $\log_{10}C(\epsilon)$ vs $\log_{10}\epsilon$ for the resistive data with M=1,2,3,4 and 5

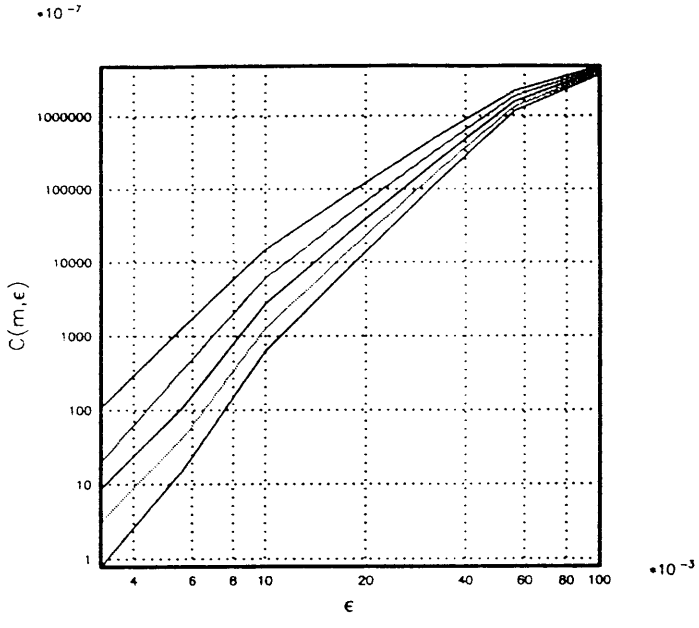

Figure 6.5c. Plot of $\log_{10}C(\epsilon)$ vs $\log_{10}\epsilon$ for the resistive data with M=6,8,10,12 and 14

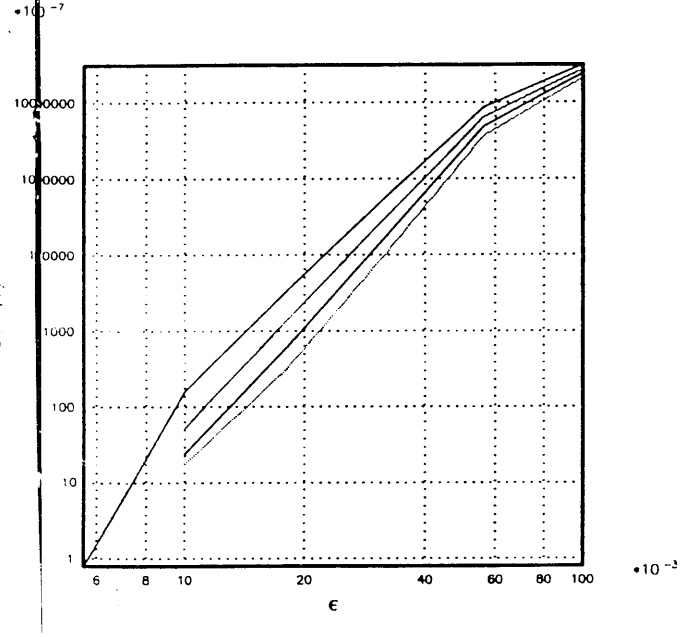

Figure 6.5d. Plot of $\log_{10}C(\epsilon)$ vs $\log_{10}\epsilon$ for the resistive data with M=18,22,26 and 30

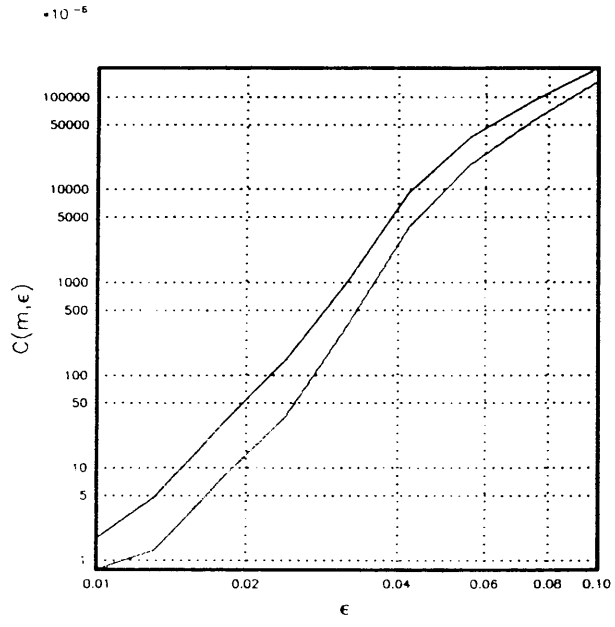

Figure 6.5e. Plot of $\log_{10}C(\epsilon)$ vs $\log_{10}\epsilon$ for the resistive data with M=30 and 40

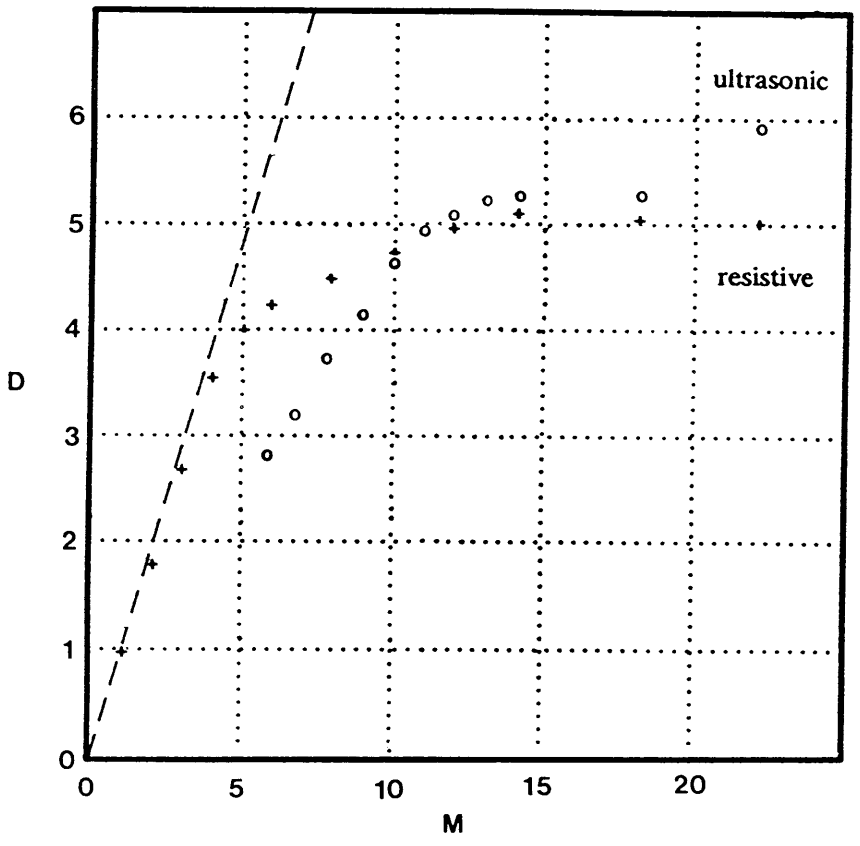

Figure 6.5f. Plot of attractor dimension vs embedding dimension for the resistive and ultrasonic data, also showing the line for white noise (dashed).

As expected, for M«D, the correlation saturates and the curve follows the line for white noise. As M is further increased, deviations from the white noise line occur, and for M›12, D has tended towards a constant value of between 5 and 6 for both the ultrasonic and resistive data.

6.6 Errors.

At present, an exact quantification of the errors of this series of experiments is not possible. However, a published numerical analysis provides a useful analogy and starting point (Holzfuss 1986).

A numerical system consisting of a 5-torus, constructed from a time series with a Fourier spectrum of 5 incommensurate frequencies, has been studiedwith reference to the errors inherent in the numerical routines used to calculate attractor dimensions. A value of 5±0.5 was found for the Grassberger-Procaccia algorithm, and although this looks a little pessimistic for the limited data presented here, this value for the error will suffice, till a more rigorous analysis of the data is carried out.

Taking the analysis to extremes, figure 6.5a shows values of the correlation integral (resistive data) for embedding dimensions of 30 and 40, the straightest portions of which lead to attractor dimensions of 6.4 and 6.8 respectively. Similar problems are found for the ultrasonic data as can be seen in figure 6.4f. This would suggest that there is an upper limit to the dimensionality of any analysis that can be carried out on the data. This limit must be inherent in the data file.

Consider a system producing a signal made up of S bits with an external noise of Q bits, the digitising error e or what ever, and let the system have reached its current complex behaviour via a period doubling route, for as good a reason as not. As the system is allowed to evolve, the error in the initial data will be amplified, till it becomes comparable in amplitude with the signal itself. This implies a sensitive dependece on initial conditions and hence chaos.

For a system such as a logistic equation (appendix D.2), the number of iterations or measurements required for this to happen is given by:

$$n=S-Q \qquad (6.6.1)$$

Thus when the points on the attractor are reconstructed from a single time series of data, the later coordinates of any point are unrelated to the earlier coordinates, and so for M>S-Q, the analysis becomes invalid. Alternatively, the analysis is only valid for embedding dimensions that satisfy:

$$M \lessapprox \frac{\log_{10}(\text{Signal/Noise})}{\log_{10}(2)} \qquad (6.6.2)$$

Along with the criterion relating the maximum analysable fractal dimension to the length of the data file (Ruelle 1990):

$$D \lessapprox -\log_{10}(1/N^2) \qquad (6.6.3)$$

Noting that for convergence of the correlation $N \simeq 2D+1$, then;

$$M \lessapprox 1 - 2\log_{10}(1/N^2) \qquad (6.6.4)$$

and this means that both the quality and the quantity of the data set strict limits on the dimensionality of attractors that can be detected. For the resistive data with 5000 points of 7 digit data, this means;

$$M_{max}(\text{Quality}) \simeq 23$$
$$M_{max}(\text{Quantity}) \simeq 15$$

and the most stringent criterion is set by the quantity of the data, and this is still sufficient to allow the attractor dimension ($D \simeq 5 \rightarrow M_{convergence} \simeq 11$) to be found.

6.6 Discussion and Conclusions.

The flow of multiphase and multicomponent mixtures in pipes is one of the greatest unsolved problems of modern process engineering. The complexity of the behaviour has meant that all but the simplest phenomena have remained unexplored, both experimentally and theoretically. The droplet flow regime in an oil/water flow in a vertical pipe has been investigated using ultrasonic and resistive techniques, and the data analysed using the Grassberger-Procaccia algorithm. The dimension of the attractor governing this flow lies somewhere between 5 and 6 and is the same for both methods of measurement, as is implicit in the theory.

As yet, there exists no general method of solving the equations governing an arbitrary fluid flow, especially the flow of any type of combination of materials and phases. Indeed, there is no unified approach to predicting, even semi-empirically, the transition boundaries wihin these flows. There is a need for objective and reliable diagnostic criteria, since confidence in the flow pattern maps used in design and operation is limited (Drahos 1989).

Many of these systems display complex and erratic behaviour, often qualitatively described as chaotic. The systems can be interrogated using many different physical principles and the results can be analysed using either a non-parametric or parametric approach. The first involves the usual statistical analysis in the amplitude, time and frequency domains, leading to 'characteristic' distribution and correlation functions. Stochastic discriminants, such as moments of various orders, or shape comparisons can then be used to identify the flow. The parametric approach requires a semi-empirical model to be generated in terms of power series, based on time series from the system. These methods have a limited success, though are in common use and their implementation has been reviewed in (Drahos 1989).

It has become clear that the spectral methods do not provide an adequate tool for quantifying and characterising the behaviour of these systems (Mayer-Kress 1986). The determination of other independent quantities from the experimental data, such as the

Hausdorff-Besicovich or 'fractal' dimension provides another route to quantifying the behaviour. The fractal dimension gives a measure of the number of degrees of freedom governing the dynamics of the system, with non-integer values indicating chaotic behaviour.

The determination of fractal dimensions for the flow of mixtures has received very little experimental attention. The few instances being reviewed in appendix D.7

Thus far, this chapter has described the analysis of a single flow condition, with fixed experimental parameters. For flows other than this specific (droplet) system, this method of analysis should provide a useful and quantitative discriminator between flow types. The (fractal) attractor dimension gives a measure of the complexity of the behaviour and a rough guide to the number of parameters governing the dynamics of the system. It would be expected that different types of behaviour would be governed by different parameters.

Clearly, a point on the usual flow regime maps (eg appendix C), represents a time average of the behaviour in a cross-section of the pipe, or for a controlled experiment, the inlet conditions. As the attractor dimension takes into account the temporal behaviour of the system, it is more closely related to the dynamics of the system. It is proposed that a flow regime map, drawn in terms of fractal dimension contours will provide better detection of flow transition boundaries and eliminate all of the vague transitions. The variation of fractal dimension with flow conditions should also assist in the analysis of developing flows and also in the analysis of the more complicated, yet developed flows.

Any flow map drawn in this way must take into account single phase flows, as these are special cases of the flow of mixtures. As most flow transitions in mixtures occur for mean Reynolds numbers considerably less than those required for classical turbulence, sudden jumps in fractal dimension might be expected around the single phase flow transition (ususally on the axes of flow maps).

The simpler flow regimes will produce attractors with dimensions that could be found from an analysis of the dynamics of the behaviour, for example;

Smooth stratified	→ 0
Periodic (linear and non-linear) waves	→ 1
Aperiodic (non-linear) waves	→ 1→2
All other flow regimes	→ >2

In view of the computer time that would be required to map the main areas and transitions of flow regime maps, it might be possible to develop an analogue or digital circuit to determine the fractal dimension of a signal in real time. Circuits already exist (Pyragas 1987, Namajunas 1988 and Cenys 1988) that can determine the next highest integer.

It is not possible at this stage to show that the fractal dimension is not an integer (implying chaos), due to the size of the errors inherent in the analysis (D±0.5).

However, that the dimension is this small, implies that a low number of parameters and equations are governing the dynamics of the system, and maybe, an analytical approach to finding the equations might be worthwhile.

Absolute proof of chaotic behaviour requires the calculation of the Lyapunov exponents of the attractor, and for at least one of them to be posistive. At this stage it is sufficient that a low dimensional attractor has been detected to justify further work in this area. This work offers the possibility of at least flow regime detector which is purely quantitative.

Chapter 7: Conclusions, Comments, Future Work and Directions.

The first part of this work has involved a study, starting from first principles, of the characterisation of complex flows using scattered ultrasound. This has been followed by a study of the more fundamental aspects of these and other measurements to provide a more global view of the flows themselves.

7.1 Ultrasonic Conclusions.

The aim of this thesis was to develop a non-invasive meter capable of characterising a disperse two component flow. In the process of attaining this goal it became clear that there is indeed a need for such a meter and that ultrasonic techniques could provide the appropriate physical principles.

Much of classical scattering theory for liquid and solid particles has been investigated and proved experimentally from the various angular scattering profiles, to the Rayleigh fourth power law to diffraction type scattering effects. Although only using a short toneburst rather than a continuous wave, this work has served to fill in some large unexplored gaps in experimental ultrasonics.

It has been shown that ultrasonic methods can determine droplet sizes, droplet velocities and void fractions, and on the small and easily controllable scale agreement with theory is good. However, on the larger scale, the effects of gas contamination of the flow has been quantified, and therefore this work clearly shows the operational limits of the ultrasonic techniques. The scattering from very low number density air bubbles is comparable with that from high concentration oil dispersions, their effect on speed of sound measurements will also be disproportionately large. This is a very serious limitation which would have to be taken into account if these principles are to be applied in the field.

7.2 Conclusions of the Chaotic Analysis of Complex Flows.

Flow maps derived for diverse systems show many qualitative similarities. Simple systems governed by a small number of equations and parameters can show very complex behaviour, indeed the sort of behaviour usually expected of more complex systems.

Almost all fluid systems undergo a series of simple transitions, as some external parameter is varied, prior to the onset of turbulence. If there is finite symmetry within the flow, the first transition from laminar flow will involve this symmetry being broken either spatially or temporally. These transitions are governed by simple underlying equations from the macroscopic point of view, analagous to equations of state or equations of motion.

From the microscopic point of view, ther are a very large number of degrees of freedom within the fluid system, but these must interact to produce an effective macroscopic behaviour with an effective number of degrees of freedom which is much smaller. Thus for a liquid dispersion, the classical argument, similar to single phase 'turbulent' flows would be that the number of degrees of freedom of the system is proportional to the number of droplets in the system.

It has been shown experimentally that the whole system follows a low dimensional attractor and is governed by between five and six variables ie five or six first order equations with each parameter scaled according to some dimensionless group.

For instance, the dimensionless groups that have already been extensively utilised to theoretically model the flows (J.C.R. Hunt, DAMTP Cambridge) may offer an insight into the number of parameters required to characterise the flows, namely;

Reynolds Number $Re = \rho vR/n$ Inertia/viscous forces

Morton Number $Mo = gn2\Delta\rho/\rho2\sigma3$ A useful multiphase flow parameter

Eotvos Number $Eo = d2g\Delta\rho/\sigma$ Gravity/surface tension forces

Froude Number	Fr = v2/gR	Inertia/gravity forces
	L = d/R	Droplet/pipe length scale

This may indicate that an analytical approach to the phenomena might be worthwhile, though very difficult with five or six variables.

These techniques could be extended across the whole of the flow maps, producing results in the form of fractal dimension contours.

It would be expected that the more obvious flow boundaries would show up as sharp changes in dimension. This may be analogous to the behaviour around classical phase transitions (entropy and dimensions). This should be able to detect between wavy stratified and wavy annular flows, where spectral methods fail.

There is an analogy here with an ideal gas in an engine. Classically, there are six degrees of freedom for every atom of the gas. However, the whole system is totally defined in a PVT plot, each point on this plot showing some instantaneous state of the system. These three parameters thus characterise the system which can thus be considered as effective degrees of freedom. For the gas, there are laws (albeit statistical) that connect the behaviour of the individual atoms to the behaviour of the gas. The ensemble average of the deterministic behaviour of the individual elements allows this connection to be made.

For the case of multiphase/multicomponent flows, the flow must be deterministic, since the external parameters can be controlled and the component particles are real and confined. The equations connecting the behaviour of the parts to that of the whole are not yet known. Indeed, equations governing the behaviour of the whole are at best semi-empirical.

7.3 Recommendations for Future Work.

There are many ways in which the ultrasonic experiments can be improved such as absolute quantification of the incident and scattered acoustic waves rather than the ratios and relative values used here. This would merely serve as fine tuning of the basic principles which have been proved here. Extending the range of ka in the scattering experiments would be interesting, especially if ka could be tuned to some of the theoretically predicted resonant spikes, which would provide very stringent tests of the scattering theory.

The standard techniques of range gated cross correlation, spatial filtering and spectral methods (applied to the various signals) could be tried on the liquid/liquid system.

Many fundamental questions about the transition to turbulence in the general fluid system have yet to be addressed, such as; how if at all is the work described here related to classical turbulence? Is the huge transition in a straight pipe around Re=2000 related to the order of the symmetry of the flow? What is the attractor for fully developed turbulence, is it finite?

On a simpler note the following work could be approached with considerably less effort.

Absolute proof of chaotic behaviour requires the determination of Lyapunov exponents (positive), since the methods of finding the dimension of attractors lead to values that are not conclusively fractional.

This route requires considerable computer power. An analogue/digital circuit has been designed to find the next highest integer to the fractal dimension. Maybe a circuit could be built to detect the Hausdorff dimension in real time.

Once these techniques have been perfected a systematic survey of multiphase/multicomponent flows could be undertaken.

References

Abramowitz M.; Stegun I.
A Handbook Of Mathematical Functions.
Dover,1965

Agrawal S.S.; Gregory G.A.; Govier G.W
An analysis of horizontal stratified two phase flow in pipes.
Can. J. Chem. Eng. 51 280-286 (1973)

Ahuja A.S.
Scattering Of Sound In Suspensions Of Spheroidally Shaped Particles.
J. Acoust. Soc. Am. 1979,66(3) pp801-805

Ahuja A.S.; Hendee W.R
Effects Of Particle Shape And Orientation On Propagation Of Sound In Suspensions.
J. Acoust. Soc. Am. 1978,63(4) pp1074-1080

Allegra J.R.;Hawley S.A.
Attenuation Of Sound In Suspensions And Emulsions: Theory And Experiments.
J. Acoust. Soc. Am. 1972,51(5:2) pp1545-1564

Ambari A.; Gauthier-Manuel B.; Guyon E.
Direct Measurement Of The Tube Wall Effect On The Stokes Force.
Phys. Fluids 1985,28(5) pp1559-1561

Ambari A.; Gauthier-Manuel B.; Guyon E.
Wall Effects On A Sphere Translating At A Constant Velocity.
J. Fluid Mech. 1984,149 pp235-253

Andereck C.D.; Liu S.S.; Swinney H.L.
Flow regimes in a circular Couette system with independently rotating cylinders.
J. Fluid Mechanics. 164 155-183 (1986)

Anderson V.C.
Sound Scattering From A Fluid Sphere.
J. Acoust. Soc. Am. 1950,22(4) pp426-431

Awrejcewicz J.; Mrozowski J.
Bifurcations and chaos in a particular Van-der-Pol - Duffing oscillator.
J. Sound and Vibration. 132(1) 89-100 (1989)

Baker O.
Simultaneous flow of oil and gas.
Oil Gas J. 53 185 (1954)

Balachandran W.; Beck M.S.
Solids-Concentration Measurement And Flow Measurement Of Slurries And Sludges Using Ultrasonic Sensors With Random Data Analysis. Part 2: Flow Velocity Measurement.
Trans. Inst. M. C. 1980,2(4) pp199-206

Balachandran W.; Briggs R.
Ultrasonic Sensors For Monitoring Flows And Sludge Solids Concentrations In Water And Waste Water Treatment.
Wat. Sci. Tech. 1981,13 pp581-588

Barkla H.M.; Auchterlonie L.J.
The Magnus Or Robins Effect On Rotating Spheres.
J. Fluid Mech. pp437-447

Bell K.J.; Taborek J.; Fenoglio F.
Interpretation of horizontal in-tube condensation heat transfer correlations with a two phase flow regime map.
Chem. Eng. Prog. Symp. Ser. 66 150-163 (1969)

Bénard H.
Les tourbillons cellulaires dans une nappe liquide.
Revue generale des sciences pures et appliquées. 190011 1261-1271, 1309-1328.

Biagé M.; Delhaye J.M.; Nakach R.
The flooding transition; An experimental appraisal of the chaotic aspect of liquid film flow before the flooding point.
AIChE Symp. Ser. vol 85 n269. 26th national heat transfer conference Philladelphia, PA, USA 6-9 August 1989 pp274-279.

Boussinesq J.
Theory analytique de la chaleur.
vol 2. p 172. Gauthier-Villars, Paris (1903)

Boussinesq J.
Hydrodynamique.
J. Comp. Rend. 1913 pp1124-1129

Brill D.; Gaunaurd G.
Resonance Theory Of Elastic Waves Ultrasonically Scattered From An Elastic Sphere.
J. Acoust. Soc. Am. 1987,81(1) pp1-21

Cenys A.; Namajunas A.; Pozela J.; Pyragas K.; Tamasevicius A.; Ulbikas J.
A new method for quantitative characterisation of chaotic oscillations in semiconductors.
Acta Phys. Pol. A. (Poland) vol A73(3) pp365-368 March 1988.

Chandrasekhar S.
Hydrodynamic and hydromagnetic stability.
Oxford (1961)

Charles M.E.; Govier C.W.; Hodgson G.W.
Horizontal pipeline flow of equal density oil-water mixtures.
Can. J. Chem. Eng. 39(1) pp27-36 Feb 1961.

Chemex.
FloComp II Technical data handbook.
Chemex, PO Box 70130, Bakersfield, Ca 93387. (1991)

Cheng K.C.; Yuen F.C.
Flow visualisation studies on secondary flow patterns in straight tubes downstream of a 180 deg. bend and in isothermally heated horizontal tubes.
J. Heat Transfer. 109 49-54 (1987)

Choe W.G.; Weinberg L.; Weisman J.
Observation and correlation of flow pattern transition in horizontal, co-current gas-liquid flow.
Two-phase transport and reactor safety. Eds. Veziroglu T.N.; Kakac S. Hemisphere (Washington) 1978.

Chown P.K.
Private communication 1989

Clebsch A.
Ueber die Reflexion an einer Kugelflache.
j. fur Math. 61 pp195-262 (1863)

Clift R.; Grace J.R.; Weber M.E.
Bubbles, Drops and Particles.
Academic 1978

Coles D.
Transitions in circular Couette flow.
J. Fluid Mechanics. 21 385 (1965)

Dean T.
The design, manufacture and testing of the Texaco subsea three phase meter.
North Sea flow measurement workshop 1990. 23-25 October 1990.
National Engineering laboratory, East Kilbride, Glasgow.

Dean W.R.
Note on the motion of fluid in a curved pipe.
Phil. Mag. 4 208-223 (1927)

Dinham E.L.
Private communication 1989

Doherty M.F.; Ottino J.M.
Chaos in deterministic systems: Strange attractors, turbulence and applications in chemical engineering.
Chem. Engng.Sci. 43(2) 139-183 (1988)

Dowty E.L.; Hatton G.J.; Durrett M.G.; Dean, T.L.; Jiskoot M.A.
Design and performance of a three-phase subsea metering system.
SPE paper 22375 (1992)

Drahos J.; Cermak J.
Diagnostics of gas-liquid flow patterns in chemical engineering systems.
Chem. Eng. Process. 26 147-164 (1989)

Dükler A.E.; Taitel Y.
Flow pattern transitions in gas-liquid systems: Measurement and modelling.
Multiphase Science and Technology. vol 2. Springer (1986) p 1-94.

Dvorak I.; Klashka J.
Modification of the Grassberger-Procaccia algorithm for estimating the correlation exponent of chaotic systems with high embedding dimensions.
Phys. Letts. A. 145(5) pp225-231 (April 1990).

Eaton B.A.; Andrews D.E.; Knowles C.R.; Silberberg I.H.; Brown K.E.
J. Petrol. Technol. 19 815 (1967)

Edwards P.L.; Jarzynski J.
Scattering Of Focused Ultrasound By Spherical Microparticles.
J. Acoust. Soc. Am. 1983,74(3) pp1006-1012

Epstein P.S.
On the absorption of sound by emulsions and suspensions.
Contributions to applied mechanics, Theodor von Karman anniversary volume. CalTech 1941 pp162-188

Faure A.; Maze G.; Ripoche J.
Observation Of Ultrasonic Surface Waves On Plane And Cylindrical Solids By Optical Methods.
J. Appl. Phys. 1977,48(3) pp869-875

Fernando L.M.
Jet mixing of water in crude oil pipelines.
PhD Thesis, DFEI, CIT. 1990.

Fiegenbaum M.J.
Quantitative universality for a class of nonlinear transformations.
J. Statist. Phys. 19 25-52 (1978)

Flax L.; Dragonette L.R.
Theory Of Elastic Resonance Excitation By Sound Scattering.
J. Acoust. Soc. Am. 1978,63(3) pp723-731

Fluenta.
Nonintrusive measurement of gases and liquids.
WIOM 300 Technical data handbook. Fluenta July 1991

Foote K.G.
Fish Target Strength-To-Length Regressions For Application In Fisheries Research.
Ultrasonics Int. Conf. Proc. 1979 pp327-332

Franca F.; Acikgoz M.; Lahey R.T.; Clausse A.
An application of fractal techniques to flow regime identification.
5th International conference on multiphase production. Cannes, France. 19-21 June 1991. Organised by Bhrg. Editor Burns A.P.
Published by Elsevier

Furness R.A.; Heritage J.E.
Redwood Flowmeter Directory.
IBC Technical Services. 1989

Gaisford S.G.; Watjen J.P.; Bjornsen B.G.
Composition monitor and monitoring process using impedance measurements.
International patent application No PCT/US89/04494

Gaunaurd G.
The Mittag-Leffler Expansion And The Interpretation Of Poles In The Scattering Amplitudes Of Waves Echoed From Fluid Spheres.
Abstract Only J. Acoust. Soc. Am. 1979,66(Suppl.1) ppS81

Gaunaurd G.; Uberall H.
R-Matrix Theory Of Sound Scattering From Fluid Spheres Via The Mittag-Leffler Expansion.
J. Acoust. Soc. Am. 1980,68(6) pp1850-1857

Gaunaurd G.C.; Kalnins A.
Resonances In The Sonar Cross Sections Of Coated Spherical Shells.
Int. J. Solids Structures 1982,18(12) pp1083-1102

Gaunaurd G.C.; Uberall H.
Resonance Theory Of Bubbly Liquids.
J. Acoust. Soc. Am. 1981,69(2) pp362-370

Gaunaurd G.C.; Uberall H.
Numerical Evaluation Of Modal Resonances In The Echoes Of Compressional Waves Scattered From Fluid-Filled Spherical Cavities In Solids.
J. Appl. Phys. 1979,50(7) pp4642-4660

Gaunaurd G.C.; Uberall H.
Identification Of Cavity Fillers In Elastic Solids Using The Resonance Scattering Theory.
Ultrasonics 1980,Nov. pp261-269

Gaunaurd G.C.; Uberall H.
Relation Between Creeping-Wave Acoustic Transients And The Complex-Frequency Poles Of The Singularity Expansion Method.
J.Acoust. Soc. Am. 1985,78(1) pp234-243

Gerrard H.G.; McNeill D.B.
Theoretical And Experimental Physics.
Chapman-Hall 1960

Gold R.C.
Flowmetering in the Oil Industry.
Flow Measurement (Special Issue) June 1986 pp63-66

Gooberman G.L.
Ultrasonics: Theory and Application
English Universities Press. 1968.

Görtler H.
Einige bemerkungen über strömungen in rotierden flussigkeiten.
ZAMM 24 210 (1944)

Govier G.W.; Aziz K.A.
The flow of complex mixtures in pipes.
Van Nostrand. (1972)

Grassberger P.; Procaccia I.
Dimensions and entropies of strange attractors from a fluctuating dynamics approach.
Physica 13D 34-45 (1984)

Griggs E.I. et al
Acoustic Velocities Of Two Phase Mixtures Of Cryogenic Fluids.
Heat Transfer 1982, Proc. 7th Int. Conf. Munich 1982,6-10 Sept.
pp225-230

Hadamard J.S.
Comp. Rend. Acad. Sci. 152 pp1735-1738 (1911)

Hadley G.
Concerning the cause of the general trade winds.
Philos. Trans. 29 58 (1735)
in Lorenz E.N.
The nature and the theory of the general circulation of the atmosphere.
World Meteorological Organisation (1967).

Hagiwara Y.
Experimental studies on chaotic behaviour of liquid film flow in annular two-phase flows.
Physiochemical Hydrodynamics. 10(2) pp135-147 (1987).

Halsey D.M.
The Character of Swirl in Turbulent Pipe Flow With Reference to its Effect on Flowmeters.
Thesis TTPhD DFEI 1986

Harmathy T.Z.
Velocity of large drops and bubbles in media of infinite or restricted extent.
AIChE. J. 6(2) pp281-288 (1960).

Haslett W.G.
The Fine Structure Of Sonar Echoes From Underwater Targets, Such As Fish.
Ultrasonics Int. Conf. Proc. 1979 pp307-320

Hausdorff F.
Dimension und äusseres Mass.
Math. annalen. 79 157-179 (1919)

Hayes E.R.
The Prediction of Droplet Motion and Breakup Using a Vortex Model for Turbulent Flows.
PhD Thesis, DFEI, CIT. (1988)

Hayward A.T.J.
Flowmeters; A basic guide and source-book for users.
Macmillan, 1984

Hayward P.
Minimum Hydraulic Conditions For Automatic Sampling.
Petrole Et Techniques 1983,295

Hénon M.; Pomeau Y.
Two strange attractors with a simple structure.
Turbulence and Navier-Stokes equations. Ed. Temam R. Lecture notes in Math. 565 29-68 Springer (1976)

Herzfeld K.F.
Propagation Of Sound In Suspensions.
Phil. Mag. 1930,9(59) Suppl. pp752-769

Hewitt G.F.; Roberts D.N.
Studies of two phase flow patterns by simultaneous X-ray and flash photography.
Report AERE-M29159. UKAEA Harwell 1969

Holzfuss J.; Mayer-Kress G.
An appraoch to error estimation in the application of dimension algorithms.
Proceedings of an international workshop at the Pecos River Ranch, New Mexico. September 11-16, 1985. Ed. Mayer-Kress,G. pp 2-5
Springer-Verlag, 1986. pp114-122.

Hoogendorn C.J.
Gas-liquid flow in horizontal pipes.
Chem. Engng. Sci. 9 pp205 (1959)

Hopf E.
A mathematical example displaying features of turbulence.
Communs. pure and applied maths. 1 pp303-322 (1949)

Jansen R.H.J.
The In Situ Measurement Of Sediment Transport By Means Of Ultrasound Scattering.
Delft Hydraulic Laboratory, Publ. 203, July 1978

Jansen R.H.J.
An Ultrasonic Doppler Scatterometer For Measuring Suspended Sand Transport.
Ultrasonic Int. Conf. Proc. 1979 pp366-371

Jansen R.H.J.; Gosse J.G.
Field Measurements Of Sediment Transport; Problems And Prospects.
IAHR Workshop Of Part. Motion And Sed. Transport: Measurement Techniques And Experimentl Results. Rapperswill (Switzerland) April 6-8, 1981 pp20.1-20.4

Jeffries H.
Some cases of instability of fluid motion.
Proc. R. Soc. Lond (A). 118 195-208 (1928)

Jones S.W.; Thomas O.M.; Aref H.
Chaotic advection by laminar flow in a twisted pipe.
J.Fluid Mechanics. 209 335-357 (1989)

Jurman L.A.; Bruno K.; McCready M.J.
Periodic and solitary waves on thin, horizontal, gas-sheared liquid films.
Int. J. Multiphase Flow. 15(3) 371-384 (1989)

Kadanoff L.P.
Roads to chaos.
Physics today. 46-53 Dec 1983

Kaye G.W.C.; Laby T.H.
Tables Of Physical And Chemical Constants.
Longman 1986

Khabeev N.S.; Shagapov V.Sh.
Oscillations Of A Gas-Vapor Bubble In An Acoustic Field.
Fluid Dynamics 1986,21(3) pp405-408

Kolmogorov A.N.
Local structure of turbulence in an incompressible liquid for very large Reynolds numbers.
Compt. Rend. Acad. Sci. URSS. 30 299-303 (1941)
Compt. Rend. Acad. Sci. URSS. 32 16 (1941)

Kol'tsova I.S.; Mikhailov I.G.; Saburov B.
The Propagation Of Ultrasonic Waves In Natural Oil Emulsions.
Russian Ultrasonics 1974,4(1) pp50-55

Korman M.S.; Beyer R.T.
Nonlinear Scattering Of Crossed Ultrasonic Beams In The Presence Of Turbulence In Water.I: Experiment.
J. Acoust. Soc. Am. 1988,81(1) pp339-349

Ladenberg R.
Ann. Physik 23 p447 (1907). Full exposition in Gerrard

Lahey R.T.; Clause A.; Dimarco P.
Chaos and Non-Linear Dynamics of Density-Wave Instabilities in a Boiling Channel.
Heat Transfer, Philadelphia 1989 pp256-261

Landa P.S.; Rozenblyum M.G.
Method for evaluating the embedding dimension of an attractor from experimental results.
Sov. Phys. Tech. Phys. 34(1) 6-10 (1990)

Landau L.D.; Lifshitz E.M.
Course of theoretical physics.
Vol 6. Fluid Mechanics. Pergamon (1959)

Lenn C.P.
The Measurement Of Size And Concentration Of Fine Sand Suspensions Using Scattered Ultrasound.
Thesis, PhD Cranfield Institute Of Technology, 1985.

Lenn C.P.
Multiphase Flow Instrumentation Market Survey
DFEI Report TR/18/214/73 May 1987

Lenn C.P.
Ultrasonic Sensors and Systems: Absorption and Scattering of Ultrasound.
Short Course Notes. DFEI, CIT, June 1991

Lenn C.P.; Oddie G.M.
The use of Ultrasonic Methods for Monitoring Secondary Components (Solid, Liquid and Gas) Entrained in Bulk Liquid Flows.
International Conference on the Monitoring of Complex Flows. London 1990. IBC Technical Services.

Levich V.G.
Physiochemical Hydrodynamics.
Prentice-Hall 1962

Lin C.C.
The theory of hydrodynamic stability.
Cambridge (1955)

Lockhart R.W.; Martinelli R.C.
Proposed correlation of data for isothermal two-phase, two-component flow in pipes.
Chem. Eng. Prog. 45 39-48 (1949)

Logan N.A.
Survey Of Some Early Studies Of The Scattering Of Plane Waves By A Sphere.
Proc. IEEE. 1965,53 pp773-785

Lorenz E.N.
Deterministic nonperiodic flow.
J. Atmos. Sci. 20 130-141 (1961)

Lugt H.J.
Vortex flows in nature and technology.
Wiley (1983)

Lynnworth L.C.; Carey C.A.; Pederson N.E.
Nonintrusive (noninterfering) ultrasonic techniques to measure gas mass flow rates.
Report No. AEDC-TR-74. National technical information service, U.S. Department of commerce (October 1974).

Ma Y.; Varadan V.K.; Varadan V.V.; Bedford K.W
Multifrequency Remote acoustic Sensing Of Suspended Materials In Water.
J. Acoust. Soc. Am. 1983,74(2) pp581-585

Malkus W.
Reported by Lorenz E.N. On the prevalence of aperiodicity in simple systems.
Global analysis. Ed. Grmela M. Marsden J.E.. Lecture notes in maths. 775 53-75 Springer (1979)

Mandhane J.N.; Gregory G.A.; Aziz K.A.
A flow pattern map for gas-liquid flow in horizontal pipes.
Int. J. Multiphase flow. 1 537-553 (1974)

Mayer-Kress G.
Introductory remarks: Dimensions and entropies in chaotic systems: Quantification of complex behaviour.
Proceedings of an international workshop at the Pecos River Ranch, New Mexico. September 11-16, 1985. Ed. Mayer-Kress,G. pp 2-5 Springer-Verlag, 1986.

Medwin H.
Counting Bubbles Acoustically: A Review.
Ultrasonics 1977,Jan pp7-13

Miles R.N.
An approximate solution for the spectral response of Duffing's oscillator with random input.
J. Sound and Vibration 132(1) 43-49 (1989)

Miller D.S.
Internal flow systems.
British Hydromechanics Research Association. Fluid Engineering Series, Vol 5. (1978)

Miller J.S.S.
Private communication 1989

Moller M.; Lange W.; Mitschke F.; Abraham M.B.; Hubner U.
Errors from Digitising and Noise in Estimating Attractor Dimension.
Phys. Letts. A. 138(4,5) p176-182 June 1989

Morimoto Y.
Variation of bifurcation diagram in difference equation: $X(t+1)=AX(t)\{1-X(t)-BX(t-1)\}$.
Trans IEICE. E72(1) 1-3 (1989)

Morse P.M.; Feschbach H.
Methods Of Theoretical Physics. Vols I+II
McGraw-Hill 1953

Morse P.M.; Ingard K.U.
Theoretical Acoustics.
McGraw-Hill. 1968

Mullin T.; Lorenzen A.; Pfister G.
Transition to turbulence in a non standard rotating flow.
Phys. Letts. 96A(5) 236-238 (1983)

Namajunas A.M.; Tamasevicius A.V.
Determination of the number of degrees of freedom of a chaotic system using an analog electronic device.
Lit. Fiz. Sbornic. 28(3) 401-403 (1988)

Newell A.C.; Rand D.A.; Russell R.
Turbulent transport and the random occurrence of coherent events.
Physica D 33 281-303 (1988)

Norsk Hydro.
Three-phase flowmeter holds promise for subsea usage.
World Oil. July 1991 pp52-53

Oberbeck A.
Ueber die Warmeleitung der flussigkeiten bei berucksichtigung der stemungen infolge von temperaturdifferenzen.
Annalen der physic und Chemie. Neue Folge. 7 271 (1879)

Oddie G.M.; Lenn C.P.
Ultrasonic Scattering from Liquid Drops and the Consequences for Two Component Flowmetering.
Ultrasonics International 89. Madrid, Spain 3-7 July 1989
pp1051-1056. Butterworth Scientific.

Oddie G.M.; Lenn C.P.
Ultrasonic Characterisation of Two-Component Liquid-Liquid Systems.
International Conference on the Flow Measurement of Commercially Important Fluids. London, 28 Feb. - 1 March 1990. IBC Technical Services.

Oddie G.M.; Fernando L.M.
Experimental Results For BCR Project Water Flow.
DFEI Report No. LF/18/220E/105. August 1990.

Packard N.H.; Crutchfield J.P.; Farmer J.D.; Shaw R.S.
Geometry from a time series.
Phys. Rev. Letts. 45(9) Sept 1980, pp 712-716.

Perry, J.H.
Chemical Engineers Handbook.
McGraw-Hill, 1973.

Pierce A.D.
Acoustics: An Introduction To Its Physical Principles And Applications.
McGraw-Hill 1981

Piotrowska A.
Propagation Of Ultrasonic Waves In Suspensions And Emulsions. Part 1: Investigation Of Emulsions And Pigment Suspensions By An Acoustic Method.
Ultrasonics 1971,Jan. pp14-20

Piotrowska A.
Propagation Of Ultrasonic Waves In Suspensions And Emulsions. Part 2: Relation Between Ultrasonic Properties And Certain Characteristics Of The Medium.
Ultrasonics 1971,Oct. pp235-239

Pippard A.B.
Response and stability: an introduction to the physical theory.
Cambridge (1985)

Pogaridis D.
Ultrasonic Range Gated Flow Measurement Using a Microprocessor Controlled Digital Correlator.
PhD Thesis. Dept. Electronic and Electrical Engineering, University of Salford. May 1988.

Poincaré H.
Les méthods nouvelles de la méchanique céleste.
3 vols Gauthier-villars, Paris (1899)

Price T.J.; Mullin T.
An experimental observation of chaos arising from the interaction of steady and time dependent flows.
Nature 340 294-296 July (1989)

Pyragas K.; Sepys A.
A high speed method for determining the number of active degrees of freedom of dynamic systems with chaotic behaviour.
Lit. Fiz. Sbornic. 27(4) 437-447 (1987)

Rayleigh J.W.S. See Strutt J.W.

Rizwan-Uddin; Dorning J.J.
A chaotic attractor in a periodically forced two phase flow system.
Nucl. Sci. Engng. 100 393-404 (1988)

Ruelle D.
Deterministic chaos: The science and the fiction.
Proc. R. Soc. Lond. A. 427 pp241-248 (1990).

Rybcznski A.
Bull. Intern. Acad. Pol. Sci. Lett. (Cracovie), Cl. Sci. Math. Nat., Ser. (A) pp40-46 (1911)

Sakaguchi T.; Akagawa K.; Hamaguchi H.; Imoto M.; Ishida S.
Flow regime maps for developing steady air-water two phase flow in horizontal tubes.
Mem. Fac. Eng. Kobe Univ. 25 191-202 (1979)

Saltzman B.
Finite amplitude free convection as an initial value problem. 1.
J. Atmos. Sci. 19 329-341 (1960)

Scott D.S.
Properties of cocurrent gas-liquid flow.
Advances in Chemical Engng. 4 199-277 Academic (1963)

Seybert A.F.; Casey D.K.
An Integral Equation Method For Coupled Fluid/Fluid Scattering In Three Dimensions.
J. Acoust. Soc. Am. 1988,84(1) pp379-384

Shaw R.S.
The Dripping Faucet as a Model Chaotic System.
Aerial Press, Santa Cruz, CA. 1984.

Sheng J.; Hay A.E.
An Examination Of The Spherical Scatterer Approximation In Aqueous Suspensions Of Sand.
J. Acoust. Soc. Am. 1988,83(2) pp598-610

Shiokawa S.; Unno Y.; Moriizumi T.; Iehisa N.
Ultrasonic Measurement On Water Suspension Of Small Particle Flowing Through A Tube As A Model Of Biological Substance.
Jap. J. Appl. Phys. 1986,25(Supp25-1) pp121-123

Sirok B.; Grabec I.
Chaotic properties of a pulsating solid particles/gas flow.
Stroj Vest, vol 34 n 10-12 Oct-Dec 1988, pp162-165.

Sparrow C.
The lorenz equations; bifurcations, chaos and strange attractors.
Applied mathematical Sciences. 41 Springer (1980)

Spedding P.L.; Nguyen P.T.
Regime maps for air-water two-phase flow.
Chem. Engng. Sci. 35 779-793 (1980)

Stakutis V.J.; Morse R.W.; Dill M.; Beyer R.T.
Attenuation Of Ultrasound In Aqueous Suspensions.
J. Acoust. Soc. Am. 1955,27(3) pp539-546

Stenzel H.
On The Perturbation Of The Sound Field Caused By A Rigid Sphere.
Elektrische Nachrichten-Technik. 1938,15 pp71-78

Stepanishen P.R.
Pulsed Transmit/receive Response of Ultrasonic Piezoelectric Transducers.
J. Acoust. Soc. Am. 1981,69(6) pp1815-1827

Stokes G.G.
Motion of Solid Spheres in Fluids of Infinite Extent.
Trans. Cambridge Philos. Soc. 9 pp8-27 (1851).
Also in; Maths. Phys. Pap. 3 p1.

Strutt J.W. (Later Baron Rayleigh)
The Theory Of Sound. Vols I+II
Macmillan 1944.

Swinney H.L.
Observations of order and chaos in nonlinear systems.
Physica 7D 3-15 (1983)

Taitel Y.; Dukler A.E.
A model for predicting flow regime transitions in horizontal and near horizontal gas-liquid flows.
AIChE J. 22(1) 47-55 (1976)

Takens F.
Detecting strange attractors in turbulence.
Dynamical systems and turbulence. Eds. Rand D.A.; Young L.S. Lecture notes in mathematics vol898 366-381 Springer (1981)

Taylor G.I. (after Couette)
Stability of a viscous liquid contained between two rotating cylinders.
Phil. trans. R. Soc. Lond. A. 223 289-243 (1923)

Taylor G.I.; Görtler H.
See Görtler H.

Tozeren H.
Drag On Eccentrically Positioned Spheres Translating And Rotating In Tubes.
J. Fluid Mech. 1983,129 pp77-90

Tsang L.; Kong J.A.; Habashi T.
Multiple Scattering Of Acoustic Waves By Random Distribution Of Discrete Spherical Scatterers With The Quasicrystalline And Percus-Yevick Approximation.
J. Acoust. Soc. Am. 1982,71(3) pp552-558

Twersky V.
Low-Frequency Scattering By Mixtures Of Correlated Nonspherical Particles.
J. Acoust. Soc. Am. 1988,84(1) pp409-415

Urick, R.J.
Principles Of Underwater Sound For Engineers.
McGraw Hill, 1965

Weight J.P.
Ultrasonic Beam Structures In Fluid Media.
J. Acoust. Soc. Am. 1984,76(4) pp1184-1191

Weisman J.
Flow pattern identification in concurrent vapour-liquid flow.
Proc. Jap-US seminar in two phase flow dynamics. Inter-university seminar house, Kansai, Japan (1979)

Williams G.
J. Atmos. Sci. 35 1399-1426 (1978)
In: Beatty J.K.; O'Leary B.; Chaikin A. The new Solar system.
Cambridge (1981)

Wimmer M.
Experiments on the stability of viscous flow between two concentric rotating spheres.
J. Fluid Mechanics 103 117-131 (1981)

Wohl P.R.; Rubinow S.I.
The Transverse Force on a Drop in an Unbounded Parabolic Flow.
J. Fluid Mech. 62(1) pp185-207 (1974)

Wood A.
Acoustics.
Blackie 1946

Xiaomao Wu; Tekle E.; Schelley Z.A.
Dripping Faucet Apparatus with Temperature and High-Resolution Timing and Flow Rate Controls.
Rev. Sci. Instrum. (USA) 60(12) pp3779-3782 (1989)

Yang Y.S.
The design, development and field testing of a water-cut meter based on a microwave technique.
SPE paper 20697 September 1990.

Zemanek J.
Beam Behaviour Within The Near Field Of A Vibrating Piston.
J. Acoust. Soc. Am. 1971,49(1.2) pp181-191

Appendix A. Single Droplet Experiments.

A.1 Introduction.

This appendix describes the experimental techniques developed to allow the experimental investigation of the scattering of an ultrasonic wave from a single liquid droplet. During the course of this development, several interesting phenomena were observed concerning the motion of a droplet in a pipe flow. The results are described and investigated in the latter sections of the appendix.

A.2 Apparatus.

In order to study more closely the scattering of ultrasound from single liquid droplets in another immiscible liquid; an experimental design must be found that satisfies the following criteria;

(a) The acoustic observation section must have as small an effect on the sound wave as possible, so as not to interfere significantly with the wave scattered from the droplet. This precludes any sort of physical support, which would necessarily be a solid. A solid would strongly scatter any acoustic wave as well as deform the shape of the droplet. The only way around this is to produce a purely hydrodynamic support.

(b) The flow must be laminar, otherwise the droplet would not be stationary in the acoustic field. A turbulent flow could also deform the droplet.

(c) The flow rate has to be able to be controlled accurately enough to bring a single droplet to rest anywhere in the acoustic field, with the buoyancy forces exactly cancelling the hydrodynamic forces.

(d) This flow rate must remain stable over long periods of time ($\simeq$hours) in order to carry out adequate ultrasonic experiments.

(e) The apparatus must be easily dismantled and cleaned, so that repairs can be effected and contaminants removed.

(f) The design must be capable of being modified such that the flow in the observation section can be either (i) upwards or (ii) downwards, depending on whether the droplet is (i) more or (ii) less dense than the surrounding fluid.

The final design for $\rho_e<\rho_l$ appears in figure A.2a, with details of the ultrasonic observation section in figure A.2b, the droplet injector in figure A.2c and the final design for $\rho_e>\rho_l$ appears in figure A.2d.

An optical observation section was built in order to take stereo photographs of each droplet in the pipe, and the design appears in figure A.2e. Due to the complexities of the optics and the interpretations of the images, the design was not fully utilised or analysed. Most of the photographs of the following sections were taken directly through the pipe wall.

A.3 The motion of a single particle in another fluid.

The first approximation to the above title, is the classic Stokes' law of 1845, where a solid particle moves through an infinite fluid medium. The equation of motion being;

$$m\frac{d^2x}{dt^2} = 6\pi\mu a\frac{dx}{dt} + m^*g \qquad (A.3.1)$$

Where all of the terms have their usual meanings (see figure A.3a).

When the acceleration of the particle is zero, then the particle has reached its terminal velocity v_T, given by;

$$v_T = \frac{2(\rho-\rho')ga^2}{9\mu} \qquad (A.3.2)$$

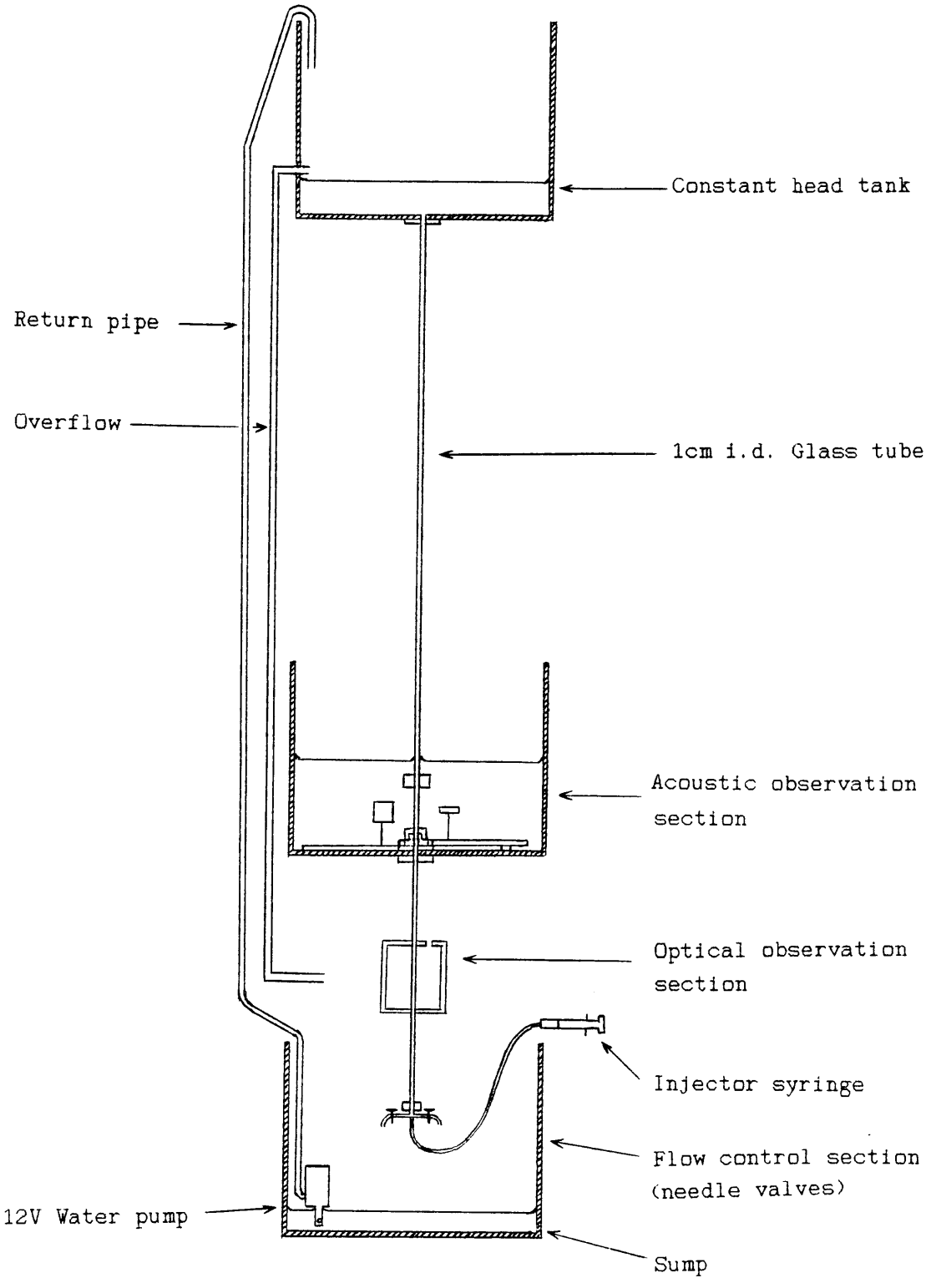

Figure A.2a Downflow Apparatus (≈1/10th scale).

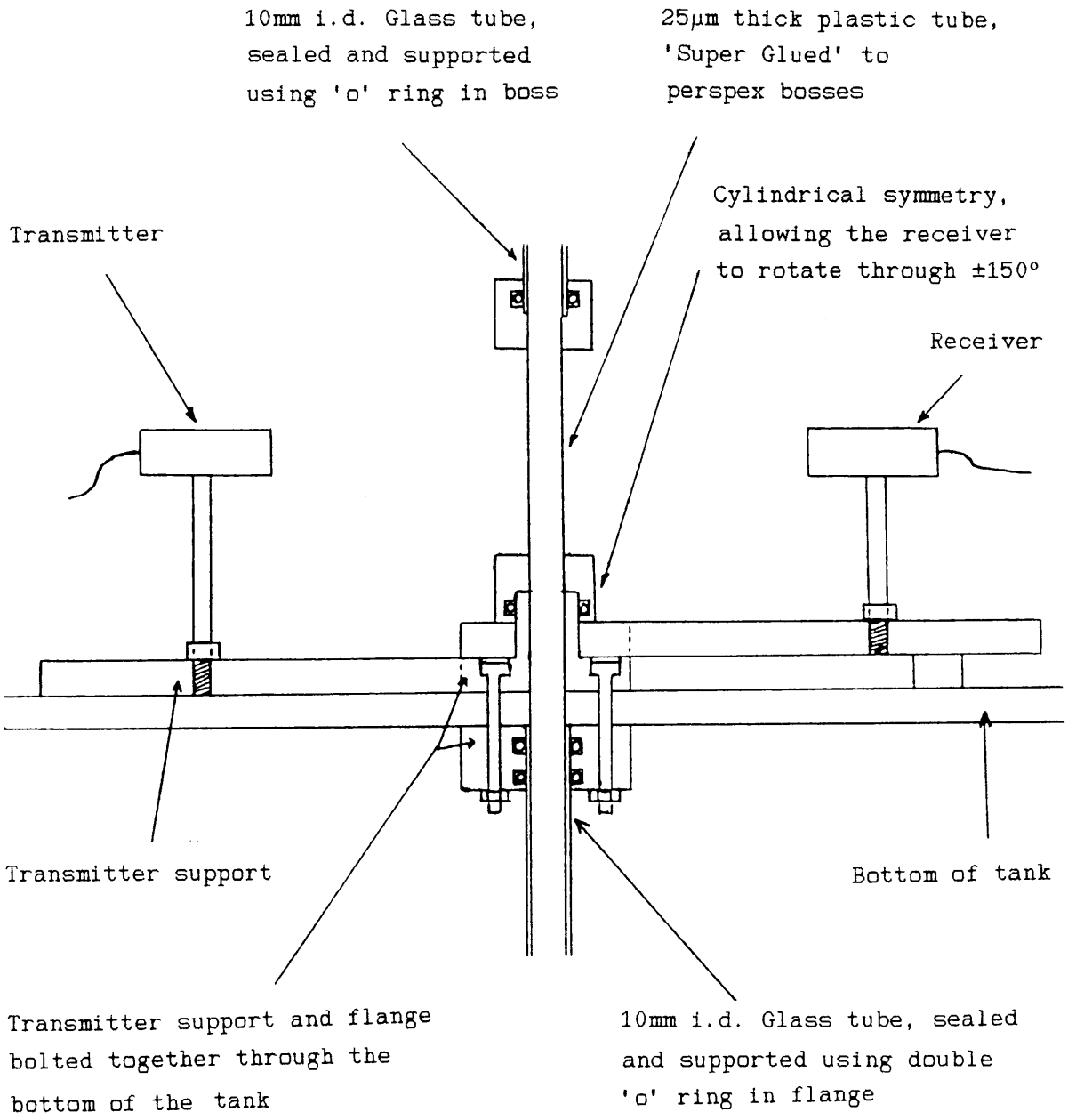

Figure A.2b The Acoustic Observation Section (not to scale)

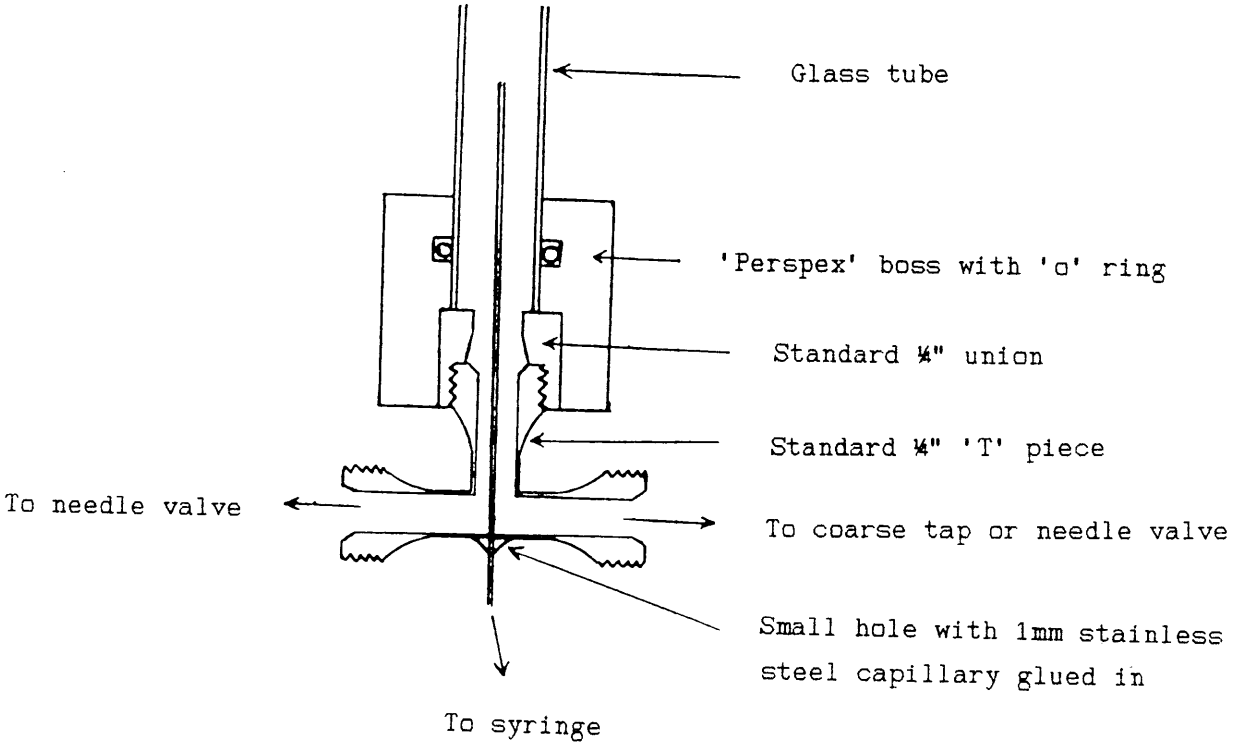

Figure A.2c Droplet Injector Section (not to scale).

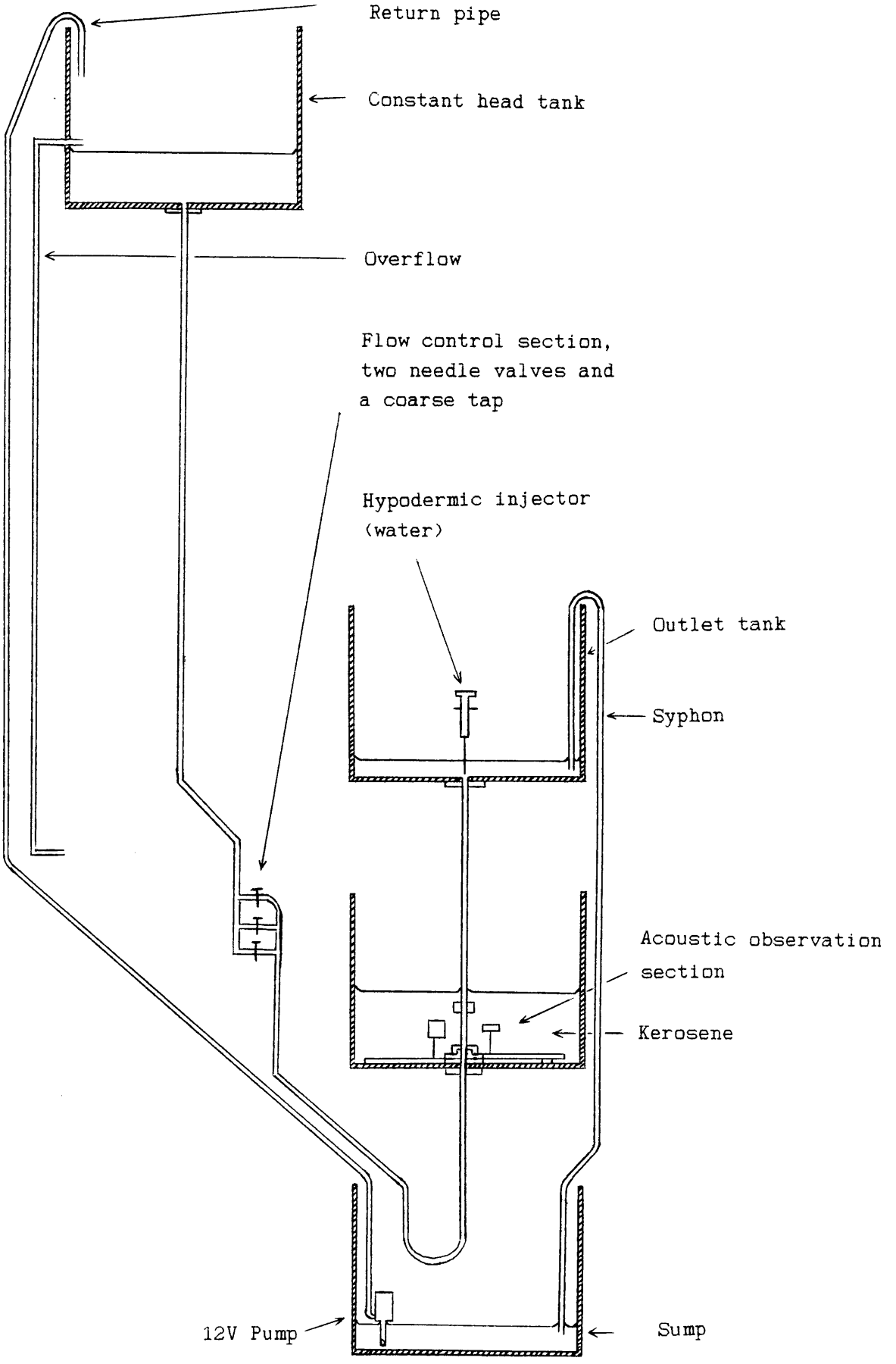

Figure A.2d Upflow Apparatus (≈1/10th scale).

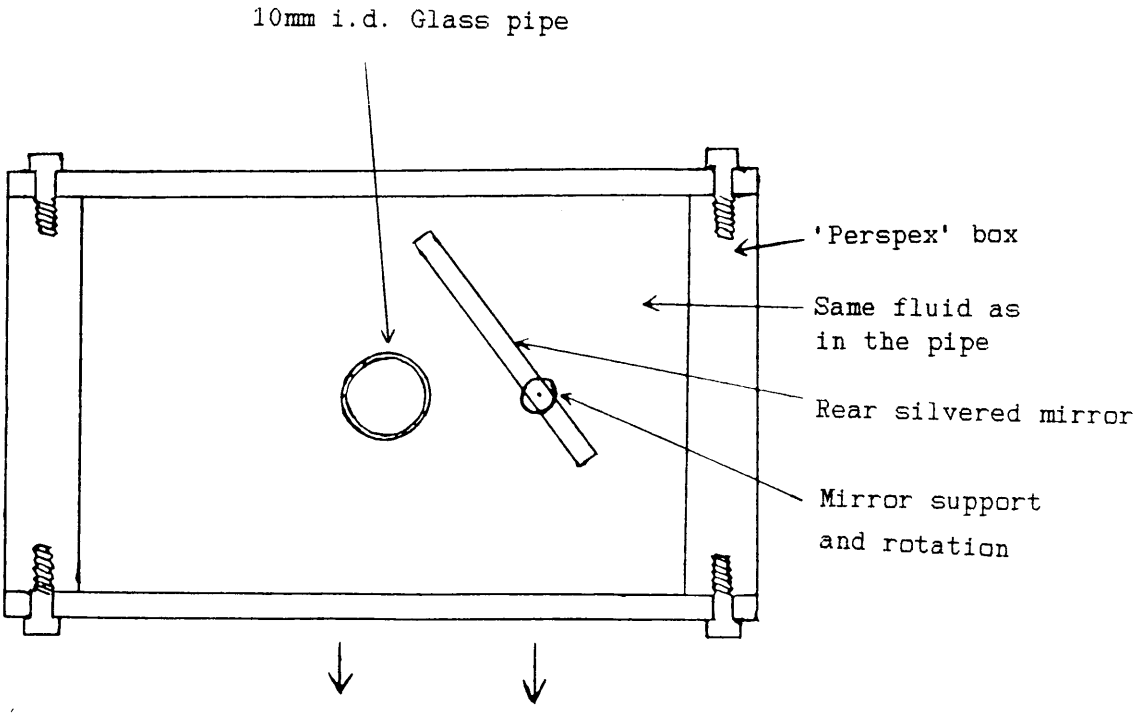

Figure A.2e Optical Observation Section

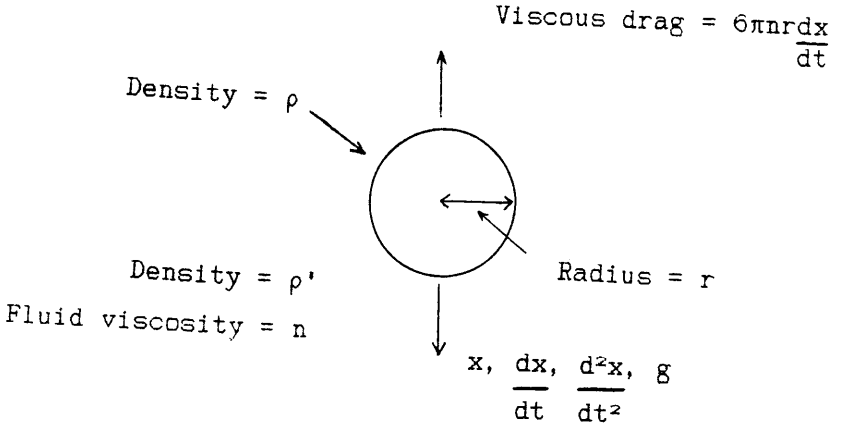

$$\text{Effective mass} = m^* = \frac{4\pi r^3(\rho-\rho')}{3}$$

Figure A.3a Basic coordinates for the motion of a single particle.

A basic calculation for the previous design criteria (b) and (f), is to consider a typical case, say, trying to suspend a droplet of kerosene (assumed solid, $\rho'=0.81 gcm^{-3}$, $r=0.5mm$) in a flow of water (Newtonian, $\mu=1x10^{-3}Nsm^{-2}$, $\rho=1gcm^{-3}$).

This gives a terminal velocity of $0.103ms^{-1}$ and a Reynolds Number ($Re=\rho va/\mu$) of 103 around the droplet. Thus a downwards flow of water of $\simeq 0.103ms^{-1}$ should exactly cancel the buoyancy force of the drop.

A preliminary test of the apparatus containing a drop of kerosene ($a\simeq 1mm$) required a flow rate of about $50cm^3$ in 15 seconds to hold the drop stationary. This gave the mean flow velocity in the pipe as $0.042ms^{-1}$ and a droplet Re of 42. Stopping the flow and measuring the time for the particle to rise 80cm in the pipe ($\simeq 13s$) at its terminal velocity, gave $v_T=0.0615ms^{-1}$ and a drop Re of 61.5.

Thus the hydrodynamic criteria (b) to (e) have been satisfied.

A few simple timing experiments revealed that the particle reached its terminal velocity very quickly, always within the first few cm of its motion. This can be checked mathematically as follows.

Equation A.3.1 is of the form;

$$\frac{d^2x}{dt^2} + A\frac{dx}{dt} = B \qquad \text{(A.3.3)}$$

A complementary function to this can be found of the form $x=\alpha_1 e^{Ct}+\alpha_2$, thus;

$$C^2\alpha_1 e^{ct} + AC\alpha_1 e^{ct} = 0 \qquad \text{(A.3.4)}$$

$$\therefore C = 0 \text{ or } -A \text{ and } x = \alpha_1 e^{-At}+\alpha_2 \qquad \text{(A.3.5)}$$

The other part of the general solution can be found via the particular integral, which, by inspection has the form; $x = \alpha_3 t$,

$$\therefore 0 + A\alpha_3 = B \qquad \text{(A.3.6)}$$

$$\therefore \alpha_3 = B/A \qquad (A.3.7)$$

Thus the general solution to equation A.3.1 has the form;

$$x = \alpha_1 e^{-At} + \frac{Bt}{A} + \alpha_2 \qquad (A.3.8)$$

Where A and B are given by;

$$A = \frac{9\mu}{2a^2\rho'} \qquad (A.3.9)$$

$$B = \frac{(\rho-\rho')g}{\rho'} \qquad (A.3.10)$$

In order to determine the coefficients α_1 and α_2 it is necessary to apply the boundary conditions that at the beginning of the motion, the position and velocity are zero. This leads to;

$$\alpha_1 = -\alpha_2 = B/A^2 \qquad (A.3.11)$$

Differentiating equation A.3.8 with respect to time gives the velocity of the particle at any time. Letting $t \to \infty$ then reveals the terminal velocity.

Clearly, it will require an infinite time, and infinite distance, for the particle to reach its terminal velocity, however the distance traversed in reaching say 90% of the terminal velocity should give an idea as to the lengths involved.

Substituting 90% of the value of the terminal velocity into the differential of equation A.3.8, solving for time and placing this in A.3.8 gives the required length as follows;

$$x_{90\%} = \frac{B}{A^2}\left[\log_e(10) - 0.9\right] \qquad (A.3.11)$$

Substituting the material properties into A.3.9 and A.3.10 and then into A.3.11, for the above droplet gives $x_{90\%} = -0.0065m$, thus confirming the experimental results.

A few other points, worthy of note, which became apparent during thee early tests, are listed below. They will be returned to, as and when necessary.

When the droplet is held statinary by the flow, it moves to an off axis position approximately 1/2 of the pipe radius from the axis. Initially, this was thought to be due to the pipe not being exactly vertical, however, careful alignment of the pipe produced a stable position for the droplet that could be anywhere on the circle of this radius. This would account for the discrepancy between the terminal velocity and the pipe flow velocity (both experimentally determined), as shown in figure A.3b

The terminal velocity for a kerosene droplet (assumed solid, $a \simeq 1mm$) from Stokes' law is $0.414ms^{-1}$, almost 7 times greater than the experimental value. Other effects such as the boundary conditions set by the pipe walls, the particle position within the pipe and the fluid properties of the particle, must be having a considerable effect on the motion of the particle.

When the kerosene particle is allowed to rise through the stationary pipe liquid, it always moves to the off axis position at about R/2, independent of its initial position.

To return the kerosene droplet back down the pipe requires the flow velocity within the pipe to be greater than the terminal velocity of the droplet. Under these conditions, the droplet moves to the axial position. This is consistent with previously reported experimental results (Wohl 1974).

Thus, in summary, the motion of the droplet in the pipe, during a timing experiment, appears as is shown in figure A.3c.

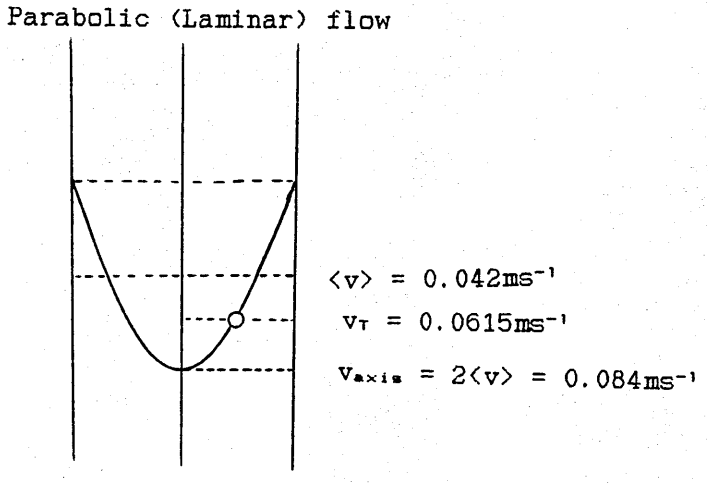

Figure A.3b Velocities Within The Pipe

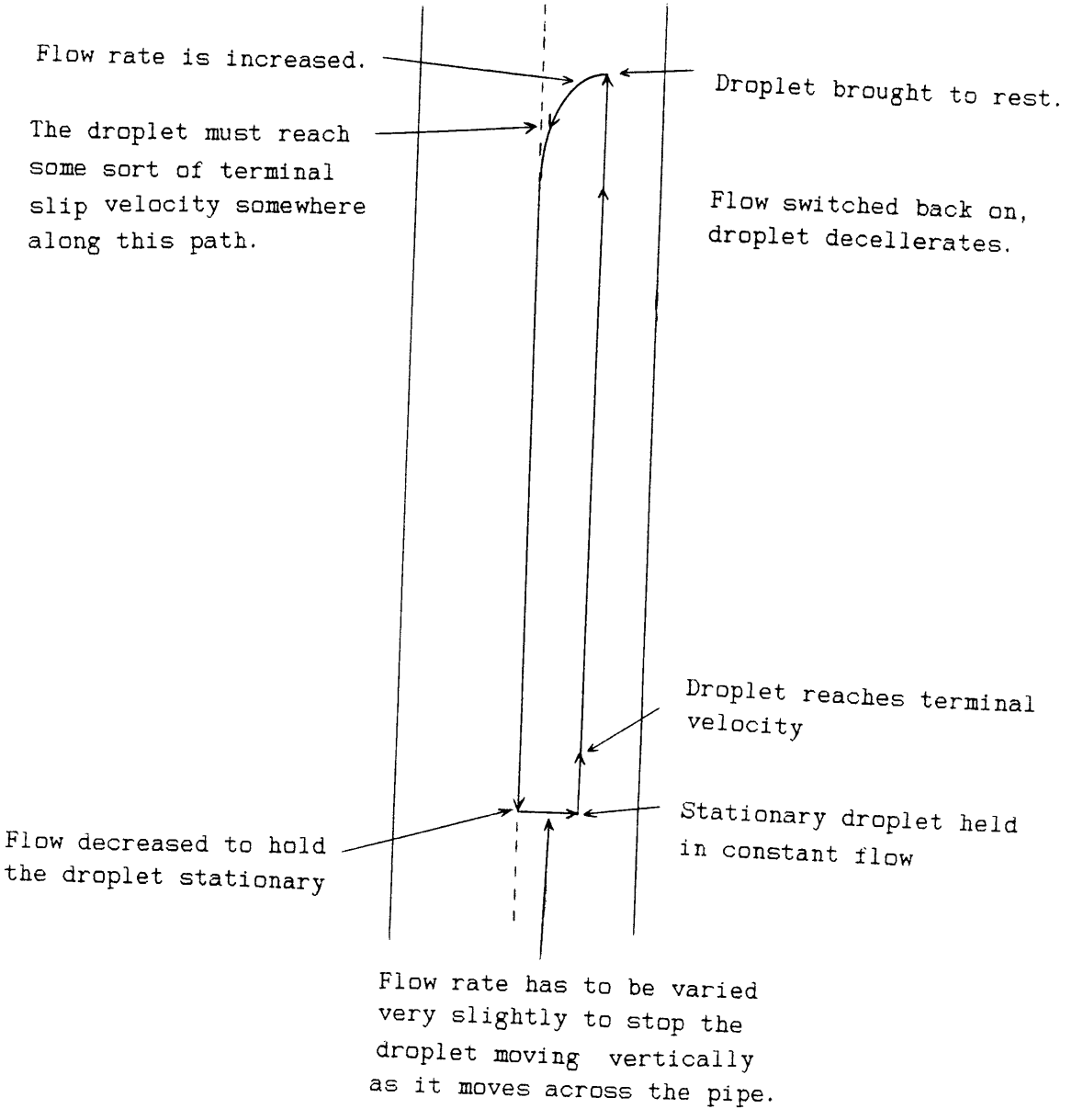

Figure A.3c Particle Motion Within The Pipe.

The discrepancies and possible causes mentioned above require further investigation, since a simple method to determine droplet size would be to measure the terminal velocity and compare this with some sort of calibration curve.

The terminal velocities of several more kerosene droplets have been measured and are compared with Stokes' law for a solid particle of the same size in figure A.3d.

The size of the droplet is determined photographically, and the motion of the particle is timed by hand (±0.01s on the clock and ±0.1s on the hand). The largest error is in the interpretation of the photographs (≃5%), with the spread in the value of v_T due to timing errors amounting to ≤1%.

The internal fluid motion of the droplet, due to the motion of their centre of gravity relative to the surrounding medium, has been studied extensively, due to its importance in process/chemical engineering applications. For example; fuel atomisation at fuel injectors, emulsions and mixing/interfacial chemistry.

The laminar equations were first solved independantly by Rybczynski (1911) and Hadamard (1911) and the method is described below.

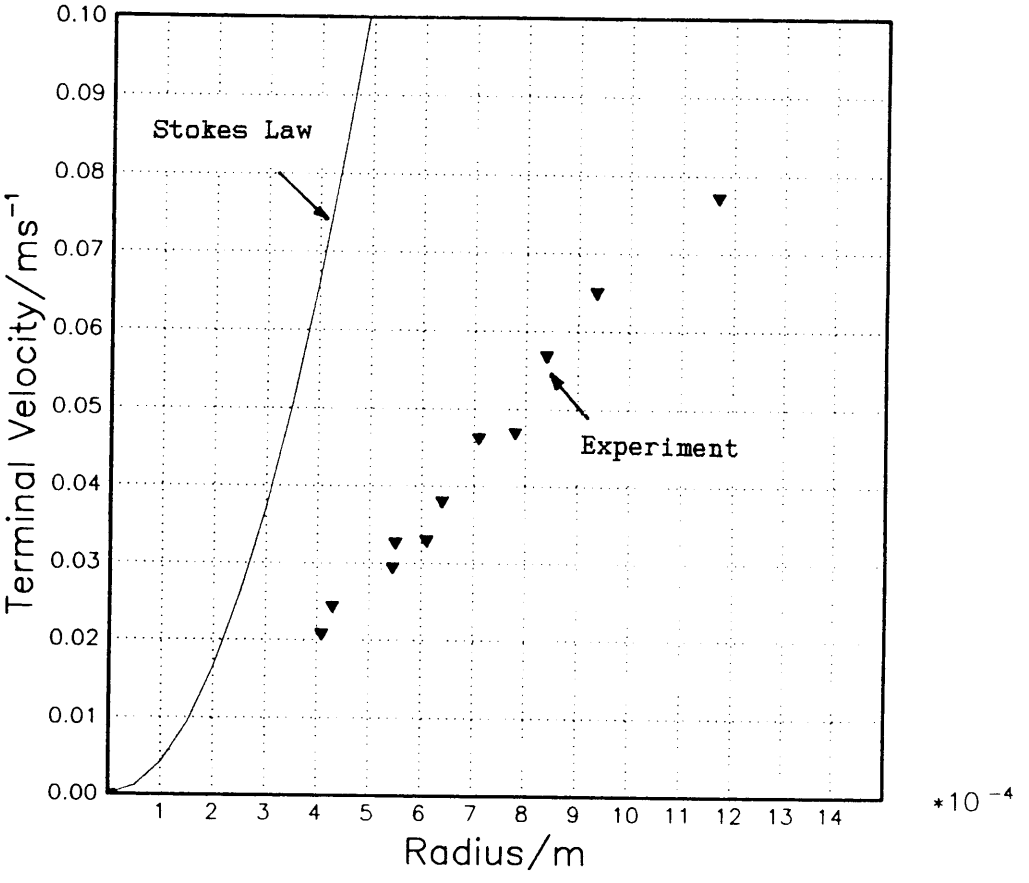

Figure A.3d. Comparing terminal velocities for kerosene droplets in water in a 1cm pipe, with Stokes Law for a solid particle of the same size and material properties.

A.4 Derivation of the Rybcznski-Hadamard Equation.

This work follows the method of Levich (1960), and as well as being a useful exercise, provides insight into where the various terms appear from.

The general equations for an infinite outer liquid in spherical polar coordinates, having noted the symmetry about φ (figure A.4a);

The pressure is given by the Navier Stokes equations, thus;

$$\frac{\delta p}{\delta r} = \mu\left[\frac{\delta^2 V_r}{\delta r^2} + \frac{1}{r^2}\frac{\delta^2 V_r}{\delta\theta^2} + \frac{2\delta V_r}{r\delta r} + \frac{\cot\theta\,\delta V_r}{r^2\,\delta\theta} - \frac{2\delta V_\theta}{r^2\delta\theta} - \frac{2V_r}{r^2} + \frac{2\cot\theta V_\theta}{r^2}\right] \qquad (A.4.1)$$

$$\frac{1}{r}\frac{\delta p}{\delta\theta} = \mu\left[\frac{\delta^2 V_\theta}{\delta r^2} + \frac{1}{r^2}\frac{\delta^2 V_\theta}{\delta\theta^2} + \frac{2\delta V_\theta}{r\delta r} + \frac{\mathrm{ctg}\theta\,\delta V_\theta}{r^2\,\delta\theta} - \frac{2\delta V_r}{r^2\delta\theta} - \frac{V_\theta}{r^2\sin^2\theta}\right] \qquad (A.4.2)$$

And the continuity equation is;

$$\frac{\delta V_r}{\delta r} + \frac{1}{r}\frac{\delta V_\theta}{\delta\theta} + \frac{2V_r}{r} + \frac{V_\theta\cot\theta}{r} = 0 \qquad (A.4.3)$$

For the inner liquid the equations have exactly the same form with $V(r,\theta)$ and p replaced by $V(r,\theta)'$ and p' respectively.

The easiest way of setting the boundary conditions is to make the centre of gravity of the droplet the origin of the coordinate system, by moving the rest of the system, infinite pipe and liquid, upwards with a velocity U.

The equation of the pipe wall is thus;

$$r\sin\theta = R \qquad (A.4.4)$$

$\therefore$ as $r \to \infty$, at the pipe wall, the effect of the droplet must be zero;

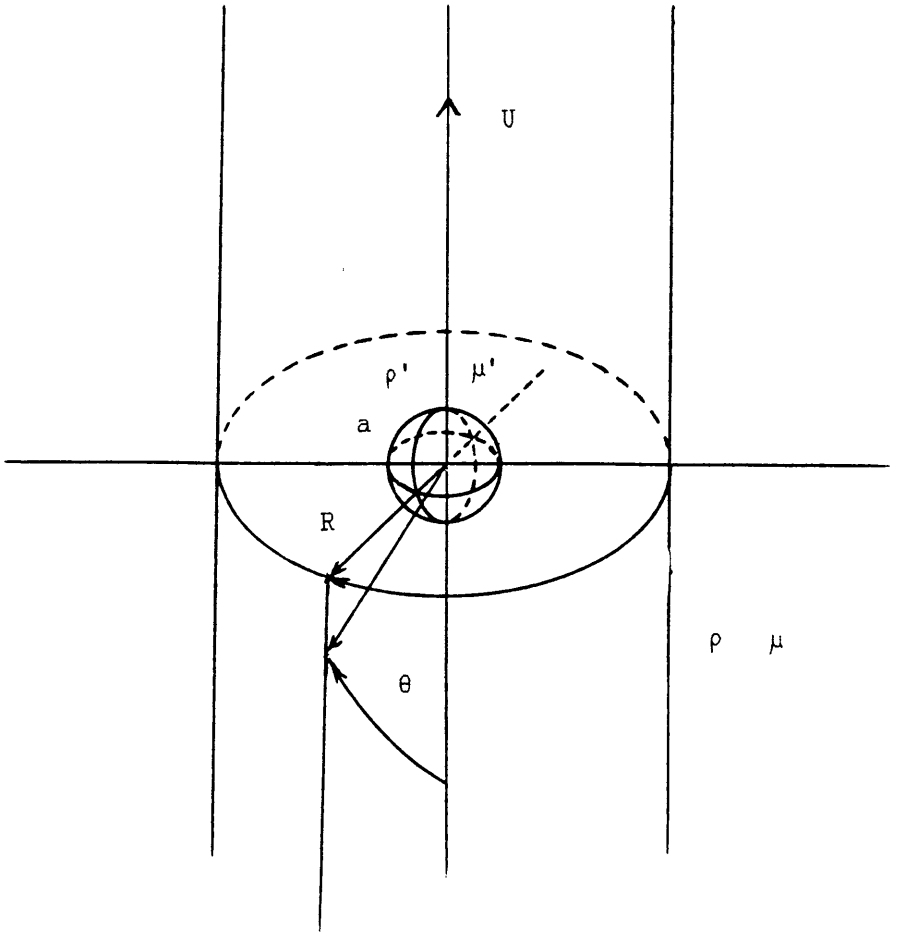

Figure A.4a Co-ordinate system for a liquid sphere on the axis of a cylindrical pipe.

$$V_r = -U\cos\theta \qquad (A.4.5)$$

$$V_\theta = +U\sin\theta \qquad (A.4.6)$$

The stress tensor at the surface of the droplet reduces to;

the normal component;

$$P_{rr} = -p + 2\mu\frac{\delta V_r}{\delta r} \qquad (A.4.7)$$

and the tangential component;

$$P_{r\theta} = \mu\left[\frac{1}{r}\frac{\delta V_r}{\delta\theta} + \frac{\delta V_\theta}{\delta r} - \frac{V_\theta}{r}\right] \qquad (A.4.8)$$

The pressure in the outer liquid is $p-\pi$ where p is the hydrostatic pressure determined by the coordinate system and π is the buoyancy pressure or effective pressure due to the inner liquid.

Thus at the surface of the droplet (r=a);

$$-(p-\pi) + 2\mu\frac{\delta V_r}{\delta r} = -p' + 2\mu'\frac{\delta V_r'}{\delta r} \qquad (A.4.9)$$

$$\mu\left[\frac{1}{r}\frac{\delta V_r}{\delta\theta} + \frac{\delta V_\theta}{\delta r} - \frac{V_\theta}{r}\right] = \mu'\left[\frac{1}{r}\frac{\delta V_r'}{\delta\theta} + \frac{\delta V_\theta'}{\delta r} - \frac{V_\theta'}{r}\right] \qquad (A.4.10)$$

Also for the droplet to remain spherical, with no slip at the interface requires, respectively;

$$V_r = V_r' = 0 \qquad (A.4.11)$$

$$V_\theta = V_\theta' \qquad (A.4.12)$$

This completes the mathematical description of the system, and now all that is required is to solve the above equations with the boundary conditions.

Sensible solutions for each of the parameters would have the following forms;

$$V_r = f(r)\cos\theta,\ V_\theta = \varphi(r)\sin\theta \text{ and } p = \mu\psi(r)\cos\theta \qquad \text{(A.4.13)}$$

$$V_r' = f'(r)\cos\theta,\ V_\theta' = \varphi'(r)\sin\theta \text{ and } p' = \mu'\psi'\cos\theta \qquad \text{(A.4.14)}$$

Substitutuing (A.4.13) into (A.4.1) gives;

$$\mu\frac{\delta\psi}{\delta r}\cos\theta = \mu\frac{\delta^2 f}{\delta r^2}\cos\theta + \frac{1(-f)}{r^2}\cos\theta + \frac{2\delta f}{r\delta r}\cos\theta + \frac{\cot\theta f(-\sin\theta)}{r^2}$$

$$- \frac{2\varphi}{r^2}\cos\theta - \frac{2f}{r^2}\cos\theta - \frac{2\cot\theta\varphi}{r^2}\sin\theta \qquad \text{(A.4.15)}$$

$$\therefore \quad \frac{\delta\psi}{\delta r} = \frac{\delta^2 f}{\delta r^2} - \frac{f}{r^2} + \frac{2\delta f}{r\delta r} - \frac{f}{r^2} - \frac{2\varphi}{r^2} - \frac{2f}{r^2} - \frac{2\varphi}{r^2}$$

$$\therefore \quad \frac{\delta\psi}{\delta r} = \frac{\delta^2 f}{\delta r^2} + \frac{2\delta f}{r\delta r} - \frac{4(f+\varphi)}{r^2} \qquad \text{(A.4.16)}$$

$$\frac{\delta^2 f}{\delta r^2} + \frac{2\delta f}{r\delta r} - \frac{4(f+\varphi)}{r^2} = \frac{\delta\psi}{\delta r} \qquad \text{(A.4.17)}$$

Similarly, (A.4.2) gives;

$$\frac{\delta^2\varphi}{\delta r^2} + \frac{2\delta\varphi}{r\delta r} - \frac{2(f+\varphi)}{r^2} = \frac{-\psi}{r} \qquad \text{(A.4.18)}$$

and (A.4.3);

$$\frac{\delta f}{\delta r} + \frac{2(f+\varphi)}{r} = 0 \qquad \text{(A.4.19)}$$

Now f, φ and ψ need reducing to functions of r only;

(A.4.19) gives;

$$\varphi = \frac{-r\delta f}{2\delta r} - f \qquad \text{(A.4.20)}$$

∴ (A.4.18) gives;

$$\frac{\psi}{r} = \frac{\delta^2}{\delta r^2}\left[\frac{r\delta f}{2\delta r} + f\right] + \frac{2\delta}{r\delta r}\left[\frac{r\delta f}{2\delta r} + f\right] - \frac{1\delta f}{r\delta r} \qquad \text{(A.4.21)}$$

$$\therefore \quad \psi = \frac{r^2\delta^3 f}{2\ \delta r^3} + \frac{3r\delta^2 f}{\delta r^2} + \frac{2\delta f}{\delta r} \qquad \text{(A.4.22)}$$

∴ (A.4.17) gives;

$$\frac{r^3\delta^4 f}{\delta r^4} + \frac{8r^2\delta^3 f}{\delta r^3} + \frac{8r\delta^2 f}{\delta r^2} - \frac{8\delta f}{\delta r} = 0 \qquad \text{(A.4.23)}$$

Letting $f = r^n$ reduces (A.4.23) to;

$$n(n-1)(n-2)(n-3) + 8n(n-1)(n-2) + 8n(n-1) + 8n = 0$$

$$\therefore \quad n(n-2)(n+1)(n+3) = 0$$

Leaving n=0, +2, -1 or -3

$$\therefore \quad f = \frac{b_1}{r^3} + \frac{b_2}{r} + b_3 + a_1 r^2 \qquad \text{(A.4.24)}$$

and;

$$\varphi = \frac{b_1}{2r^3} - \frac{b_2}{2r} - b_3 - 2a_1 \qquad \text{(A.4.25)}$$

$$\psi = \frac{b_2}{r^2} + \frac{10a_1}{r} \qquad \text{(A.4.26)}$$

Outside the drop, the general equations are;

$$V_r = \left[\frac{b_1}{r^3} + \frac{b_2}{r} + b_3 + a_1 r^2\right] \cos\theta \qquad \text{(A.4.27)}$$

$$V_\theta = \left[\frac{b_1}{2r^3} - \frac{b_2}{2r} - b_3 - 2a_1 r^2\right] \sin\theta \qquad \text{(A.4.28)}$$

$$p = \mu\left[\frac{b_2}{r^2} + 10a_1 r\right] \cos\theta \qquad \text{(A.4.29)}$$

The equations for the motion inside the drop are found using a similar method, with b_3 replaced by another constant a_2. Because this constant is not a coefficient of r, it will be a function of material properties only, and does not need to balance across the interface.

$$V_r' = \left[\frac{b_1}{r^3} + \frac{b_2}{r} + a_2 + a_1 r^2\right] \cos\theta \qquad \text{(A.4.30)}$$

$$V_\theta' = \left[\frac{b_1}{2r^3} - \frac{b_2}{2r} - a_2 - 2a_1 r^2\right] \sin\theta \qquad \text{(A.4.31)}$$

$$p' = \mu'\left[\frac{b_2 + 10a_1 r}{r^2}\right] \cos\theta \qquad \text{(A.4.32)}$$

And the hydrostatic pressure at any point on the surface of the drop is given by;

$$\pi = (\rho' - \rho) g a \cos\theta \qquad \text{(A.4.33)}$$

Inputting the boundary conditions (A.4.9) to (A.4.12) leaves:

$$V_r = \left[\frac{b_2}{r} + \frac{b_1}{r^3} + b_3\right] \cos\theta \qquad \text{(A.4.34)}$$

$$V_\theta = \left[\frac{b_1}{2r^3} - \frac{b_2}{2r} - b_3\right] \sin\theta \qquad \text{(A.4.35)}$$

$$p = \frac{\mu b_2 \cos\theta}{r^2} \qquad \text{(A.4.36)}$$

And Inside The Drop;

$$V_r' = (a_1 r^2 + a_2)\cos\theta \qquad \text{(A.4.37)}$$

$$V_\theta' = -(2a_1 r^2 + a_2)\sin\theta \qquad \text{(A.4.38)}$$

$$p' = 10\mu' a_1 r \cos\theta \qquad \text{(A.4.39)}$$

Thus as $r \to \infty$,

$$-U\cos\theta = \left[\frac{b_2}{r} + \frac{b_1}{r^3} + b_3\right]\cos\theta \qquad \text{(A.4.40)}$$

And at r=a, for all θ

$$0 = \left[\frac{b_2}{r} + \frac{b_1}{r^3} + b_3\right]\cos\theta \qquad \text{(A.4.41)}$$

$$0 = (a_1 r^2 + a_2)\cos\theta \qquad \text{(A.4.42)}$$

$$\left[\frac{b_1}{2r^3} - \frac{b_2}{2r} - b_3\right]\sin\theta = -(2a_1 r^2 + a_2)\sin\theta \qquad \text{(A.4.43)}$$

(A.4.40) gives

$$b_2 = -U \qquad \text{(A.4.44)}$$

(A.4.41) gives

$$U = \frac{b_2}{a} + \frac{b_1}{a^3} \qquad \text{(A.4.45)}$$

(A.4.42) gives

$$a_1 a^2 + a_2 = 0 \qquad \text{(A.4.46)}$$

(A.4.43) gives

$$\frac{b_1}{2a^3} - \frac{b_2}{2a} + U = -2a_1a^2 - a_2 \qquad \text{(A.4.47)}$$

Substituting (A.4.34) and (A.4.37) into (A.4.9) gives

$$-(p - \pi) + 2\mu\left[\frac{-b_2}{a^2} - \frac{3b_1}{a^4}\right]\cos\theta = -p' + 2\mu' 2a_1 r\cos\theta \qquad \text{(A.4.48)}$$

$$\therefore \quad -\frac{\mu b_2}{a^2}\cos\theta + \pi + 2\mu\left[\frac{-b_2}{a^2} - \frac{3b_1}{a^4}\right]\cos\theta = -10\mu' a_1 r\cos\theta + 2\mu' 2a_1 r\cos\theta \qquad \text{(A.4.49)}$$

$$\therefore \quad -\frac{3\mu b_2}{a^2} - \frac{6\mu b_1}{a^4} + \pi\sec\theta = -6\mu' a_1 a \qquad \text{(A.4.50)}$$

Substituting (A.4.34), (A.4.35), (A.4.37) and (A.4.38) into (A.4.10);

$$\mu\left[\frac{1}{a}\left[\frac{b_2}{a} + \frac{b_1}{a^3} + b_3\right](-\sin\theta) + \left[\frac{3b_1}{2a^4} + \frac{b_2}{2a^2}\right]\sin\theta - \frac{1}{a}\left[\frac{b_1}{2a^3} - \frac{b_2}{2a} - b_3\right]\sin\theta\right] =$$

$$\mu'\left[\frac{1}{a}(a_1a^2 + a_2)(-\sin\theta) + (-4a_1a)\sin\theta - \frac{1}{a}(-(2a_1a^2 + a_2)\sin\theta)\right] \qquad \text{(A.4.51)}$$

$$\therefore \quad \mu\left[\frac{-b_2}{a^2} - \frac{b_1}{a^4} - \frac{b_3}{a} - \frac{3b_1}{2a^4} + \frac{b_2}{2a^2} - \frac{b_1}{2a^4} + \frac{b_2}{2a^2} + \frac{b_3}{a}\right] =$$

$$\mu'\left[-a_1a - \frac{a_2}{a} - 4a_1a + 2a_1a + \frac{a_2}{a}\right] \qquad \text{(A.4.52)}$$

$$\therefore \quad \mu\left[\frac{-3b_1}{a^4}\right] = \mu'(-3a_1a) \qquad \text{(A.4.53)}$$

$$\therefore \quad \frac{\mu b_1}{a^4} = \mu' a_1 a \qquad \text{(A.4.54)}$$

$$\therefore \quad \mu b_1 = \mu' a_1 a^5 \qquad \text{(A.4.55)}$$

Thus in summary so far;

$$u = \frac{b_2}{a} + \frac{b_1}{a^3} \qquad \text{(A.4.56)}$$

$$a_1 a^2 + a_2 = 0 \qquad \text{(A.4.57)}$$

$$\frac{b_1}{2a^3} - \frac{b_2}{2a} + U = -2a_1 a^2 - a_2 \qquad \text{(A.4.58)}$$

$$\frac{-3\mu b_2}{a^2} - \frac{6\mu b_1}{a^4} + \pi \sec\theta = -6\mu' a_1 a \qquad \text{(A.4.59)}$$

$$\mu b_1 = \mu' a_1 a^5 \qquad \text{(A.4.60)}$$

Eliminating b_1/a^3 using (A.4.56) leaves;

$$\frac{b_1}{a^3} = U - \frac{b_2}{a} \qquad \text{(A.4.61)}$$

$$a_1 a^2 + a_2 = 0 \qquad \text{(A.4.62)}$$

$$\frac{U}{2} - \frac{b_2}{2a} - \frac{b_2}{2a} + U = -2a_1 a^2 - a_2 \qquad \text{(A.4.63)}$$

$$\frac{-3\mu b_2}{a^2} - \frac{6\mu}{a}\left[U - \frac{b_2}{a}\right] + \pi \sec\theta = -6\mu' a_1 a \qquad \text{(A.4.64)}$$

$$\mu\left[U - \frac{b_2}{a}\right] = \mu' a_1 a^2 \qquad \text{(A.4.65)}$$

Which reduce to;

$$a_1 a^2 + a_2 = 0 \qquad \text{(A.4.66)}$$

$$\frac{3U}{2} - \frac{b_2}{a} = -2a_1a^2 - a_2 \qquad \text{(A.4.67)}$$

$$\frac{-6\mu U}{a} + \frac{3\mu b_2}{a^2} + \pi\sec\theta = -6\mu' a_1 a \qquad \text{(A.4.68)}$$

$$\mu U - \frac{\mu b_2}{a} = \mu' a_1 a^2 \qquad \text{(A.4.69)}$$

Eliminating a_2 using (A.4.66) leaves;

$$a_2 = -a_1a^2 \qquad \text{(A.4.70)}$$

$$\frac{3U}{2} - \frac{b_2}{a} = -a_1a^2 \qquad \text{(A.4.71)}$$

$$\frac{-6\mu U}{a} + \frac{3\mu b_2}{a^2} + \pi\sec\theta = -6\mu' a_1 a \qquad \text{(A.4.72)}$$

$$\mu U - \frac{\mu b_2}{a} = \mu' a_1 a^2 \qquad \text{(A.4.73)}$$

Eliminating a_1 using (A.4.73) produces;

$$a_1 = \frac{\mu U}{\mu' a^2} - \frac{\mu b_2}{\mu' a^3} \qquad \text{(A.4.74)}$$

$$\frac{-6\mu U}{a} + \frac{3\mu b_2}{a^2} + \pi\sec\theta = -6\mu' a\left[\frac{\mu U}{\mu' a^2} - \frac{\mu b_2}{\mu' a^3}\right] \qquad \text{(A.4.75)}$$

$$\frac{3U}{2} - \frac{b_2}{a} = -a^2\left[\frac{\mu U}{\mu' a^2} - \frac{\mu b_2}{\mu' a^3}\right] \qquad \text{(A.4.76)}$$

Expanding the last two terms leaves;

$$\frac{-6\mu U}{a} + \frac{3\mu b_2}{a^2} + \pi\sec\theta = \frac{-6\mu U}{a} + \frac{6\mu b_2}{a^2} \qquad \text{(A.4.77)}$$

$$\frac{3U}{2} - \frac{b_2}{a} = \frac{-\mu U}{\mu'} + \frac{\mu b_2}{\mu' a} \qquad (A.4.78)$$

Reducing these gives;

$$\pi \sec\theta = \frac{3\mu b_2}{a^2} \qquad (A.4.79)$$

$$U\left[\frac{3}{2} + \frac{\mu}{\mu'}\right] = \left[\frac{b_2}{a}\left[1 + \frac{\mu}{\mu'}\right]\right] \qquad (A.4.80)$$

Eliminating b_2 finally gives;

$$U = \frac{2a\pi\sec\theta}{3\mu} \cdot \frac{(1 + \mu/\mu')}{(3/2 + \mu/\mu')} \qquad (A.4.81)$$

Substituting for π from (A.4.9) leaves;

$$U = \frac{2(\rho - \rho')ga^2}{3\mu}\left[\frac{\mu + \mu'}{2\mu + 3\mu'}\right] \qquad (A.4.82)$$

This is the Rybcznski-Hadamard formula, which reduces to the familiar Stokes' Law when μ' tends to ∞, thus;

$$U = \frac{2(\rho - \rho')ga^2}{9\mu} \qquad (A.4.83)$$

Thus it can be seen that Stokes' Law has been modified by a factor of

$$3\left[\frac{\mu + \mu'}{2\mu + 3\mu'}\right] \qquad (A.4.84)$$

For a kerosene droplet in water, $\mu \simeq 0.001 Nsm^{-2}$ and $\mu' \simeq 0.00115 Nsm^{-2}$, this amounts to 1.18, which means that the particles are travelling more quickly than given by Stokes. This is to be expected since a mobile surface produces less drag.

A further modification (Boussinesq 1913), allows the interface, between the droplet and the surrounding medium, to have a different viscosity to either of the media. He defined a surface viscosity coefficient 'e' which expresses the relationship between the surface tension and the rate at which the surface is changing. The end result is a modification to Stokes' Law of the form;

$$3\left[\frac{\mu + \mu' + 2e/3a}{2\mu + 3\mu' + 2e/a}\right] \qquad \text{(A.4.85)}$$

The exact value of e at any instant is determined by the effects of soluble or insoluble contaminants on the interface. The effect of the value of e can only make the terminal velocity tend towards that given by Stokes' Law, since with total contamination, the surface will be effectively rigid, and internal circulation will not occur. Another way of looking at this modification, is that since $0<e<\infty$, then;

$$3\left[\frac{\mu + \mu'}{2\mu + 3\mu'}\right] \geqslant 3\left[\frac{\mu + \mu' + 2e/3a}{2\mu + 3\mu' + 2e/a}\right] \geqslant 1 \qquad \text{(A.4.86)}$$

A.5 Discussion and Conclusions

Thus even after the analysis of the last section, and the results presented therein, other phenomenae must be considered.

A more plausible explanation for the discrepancies shown in the Figure A.3d will be the effects of the pipe wall on the motion of the droplet. A first order correction to Stokes' Law was found by Ladenberg (1890), with a more recent form being the 5th order correction of Gerrard (1960);

$$\frac{V_T}{V_{Stokes}} = 1 - \frac{2.104a}{R} + \frac{2.09a^3}{R^3} - \frac{0.95a^5}{R^5} \qquad \text{(A.5.1)}$$

Other approximations allow for a rotation of the particles as they fall through the fluid (Ambari 1985, Tozeren 1983). This rotation produces lateral forces analagous to the Magnus/Robins effect (Barkla

1971). Small dust particles trapped on the interface of a few of the droplets while they were held stationary by the flow, revealed that the droplets do not rotate. No data on particle rotation during free fall could be taken with this apparatus. The previous authors have evaluated the modifications and for the range of sizes involved here, the effects do not amount to more than 10% of Stokes' Law.

The effect of particle spatial eccentricity in the pipe was first studied by Harmathy (1960) and more recently by Ambari (1984). His findings (figure A.5a) are that the Stokes velocity must be modified (reduced) by a factor of not less than 3.8 for a=0.43mm and R=1cm, and has this minimun value at c/R=0.4, where c is the eccentricity. However for a/R≈0.1, this effect would be considerably reduced. The sensitivity of the correction factor with particle position eccentricity also sets very strict limits on the vertical alignment of the pipe as mentionad in section A.3. Clearly, the larger droplets will get closer to the pipe wall than the smaller droplets and so will produce greater shear forces and drag than the basic Stokes' Law, thus reducing the functional dependence on r from r^2 to somewhere closer to r^1 for large r, though retaining the quadratic terms for small r (Harmathy 1960).

The experimental results, as well as Stokes' Law, the Rybczynski-Hadamard modification, Gerrard's modificaion and Ambari's work are summarised in figures A.5b, A.5c and A.5d.

Till these discrepancies can be explained and quantified more accurately, the timing method will not be used as the main means of determining drop size. The photographic method, is slightly more accurate but takes considerably longer.

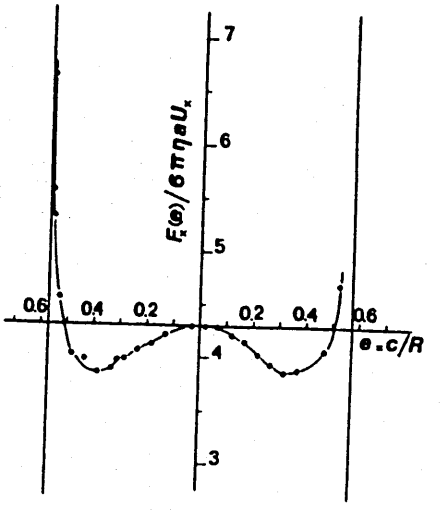

Figure A.5a Effect of particle eccentricity on drag force, compared with Stokes' Law (Ambari 1985).

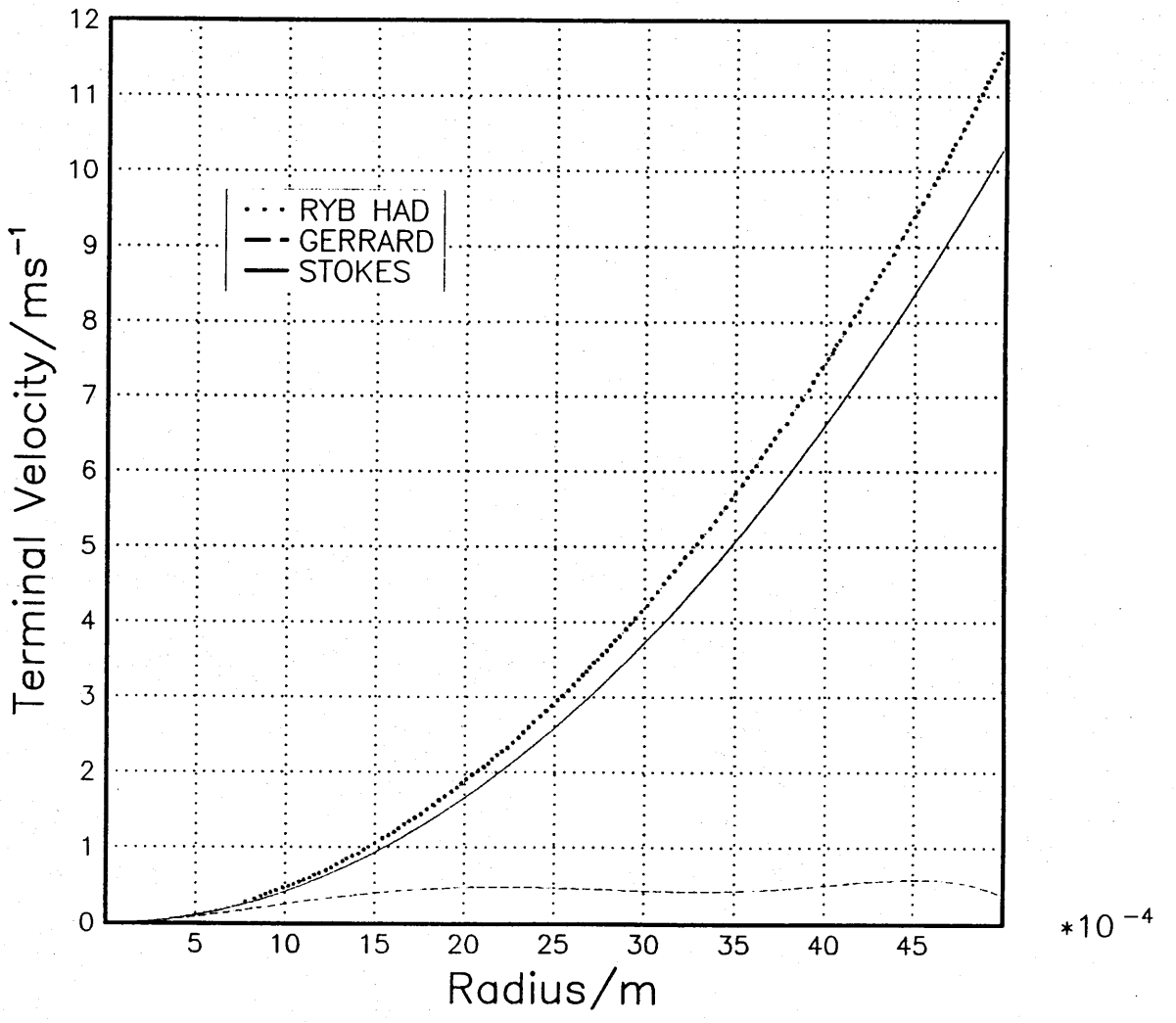

Figure A.5b Terminal velocities in a 1cm pipe for large kerosene droplets in water according to Stokes, Gerrard and Rybcznski-Hadamard

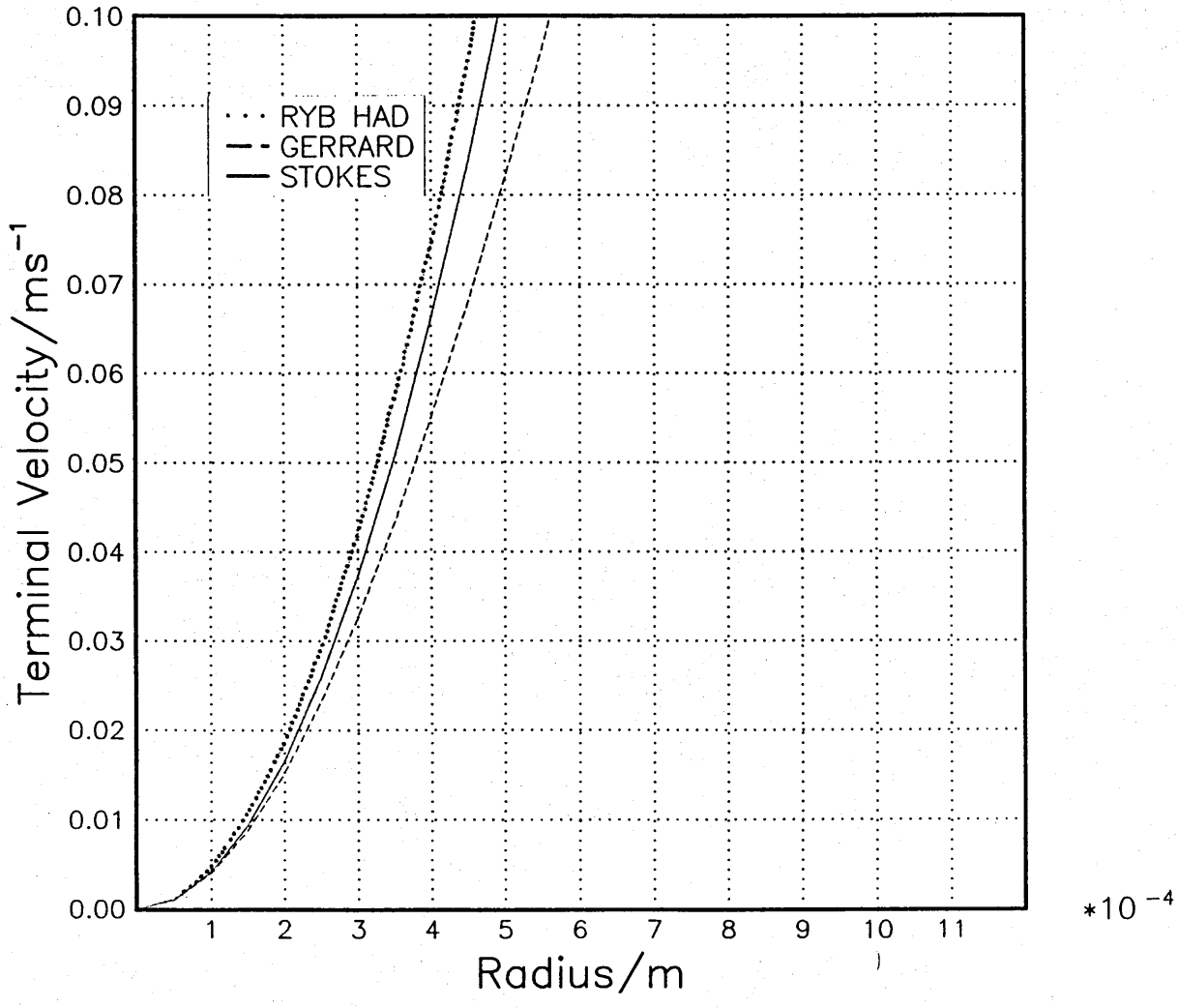

Figure A.5c Terminal velocities in a 1cm pipe for small kerosene droplets in water according to Stokes, Gerrard and Rybcznski-Hadamard

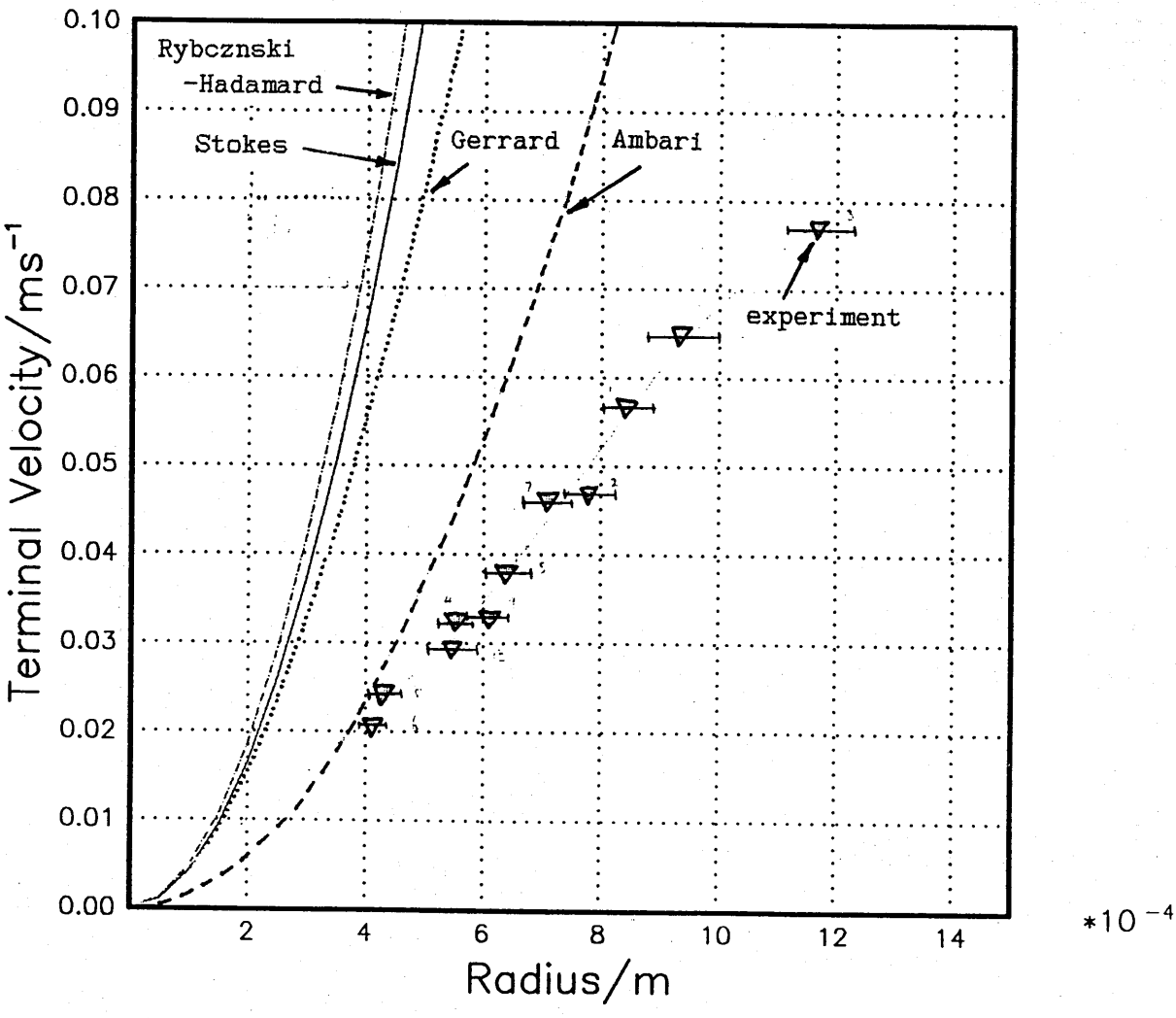

Figure A.5d Comparing theories with experiment. Stokes , Gerrard , Rybcznski-Hadamard , Ambari and the experimental data . All for kerosene in water , cylinder diameter = 1cm.

Appendix B: Larger Scale Experiments.

B.1 Introduction.

In order to carry out larger scale experiments an apparatus had to be designed that could create oil/water flows that were comparable with those encountered in the oil processing industry (see chapter 1). To make the flow phenomena repeatable, a detailed understanding of the behaviour of the apparatus and the fluid properties is required. A test section in the form of a spool piece was also constructed that would allow the ultrasonic interrogation (angular scattering, Döppler scattering etc) of the flow. This appendix describes the design, construction and testing of a custom built flow loop.

B.2 Apparatus Design.

The principal aim of this part of the work was the characterisation of the droplet flow regime of an oil/water flow. Four distinct possibilities existed for generating this flow regime.

(i) Both fluids could be drawn into a single pump, and then mixed by the pump, before being sent down the pipe.
(ii) Both fluids could be pumped separately, and then forced through some sort of mixing device before entering the pipe.
(iii) Both fluids could be pumped separately, with the natural turbulence in the pipe providing the mixing.
(iv) Both fluids could be pumped separately, and then some sort of externally controllable mixing device used to generate the droplets.

Methods (i) and (ii) provide very little control over the nature of the flow regime generated, above and beyond velocity and void fraction. Similarly, the third method is limited in that droplet size is only a function of the mean pipe velocity if all the other physical properties are constant, and so is not controllable externally. The final method provides the greatest experimental control over the behaviour of the flow. The mixer that was finally developed was a single nozzle jet

mixer, which has advantages over other methods of dynamical mixing (eg stirrers) in that it is easier to clean and maintain, has no moving parts and does not impede the flow when it is not activated. This is the simplest type of mixer and its behaviour has been analysed in detail elsewhere (Fernando 1990). This will be covered in section B.8 and chapter 5.2.

No specification had been made as to which fluid was to be continuous, and so the apparatus needed to be flexible enough to allow for either the water or oil to be the continuous phase to similar superficial velocities ($\simeq 5ms^{-1}$). For most multiphase systems, it is usually stated that a minimum of 100 diameters should be allowed for a horizontal flow to develop, and slightly less for a vertical flow. Thus for pipes of 2" diameter, test lengths of around 5m are required. Allowing for a few bends and return pipes, a pressure drop of $\simeq$30psi and a flow rate of $\simeq 0.01 m^3 s^{-1}$ are required (Miller 1978). These criteria are satisfied by a Worthington Simpson pump 65WJE160 for both fluids, though one pump required modified seals to be useable in oil.

The separation method also had to be considered carefully, if emulsification and complete mixing were to be avoided. The simplest method is by gravitation in settling tanks. If the flow loop were to be operated at the highest flow rates for about 5 minutes in a single shot mode, then the storage volume needed to be at least $3m^3$.

A schematic diagram of the final flow loop is shown in figure B.2a, and a photograph of the constructed loop in figure B.2b.

B.3 Fluid Properties.

The next problem was the liquids that were to be used in the flow. The experiments described in chapter 3 involved tap water and kerosene, for reasons described in that chapter, essentially mimicking some North Sea crude oils, both physically and acoustically. On the larger scale of the proposed rig, kerosene has several serious disadvantages.

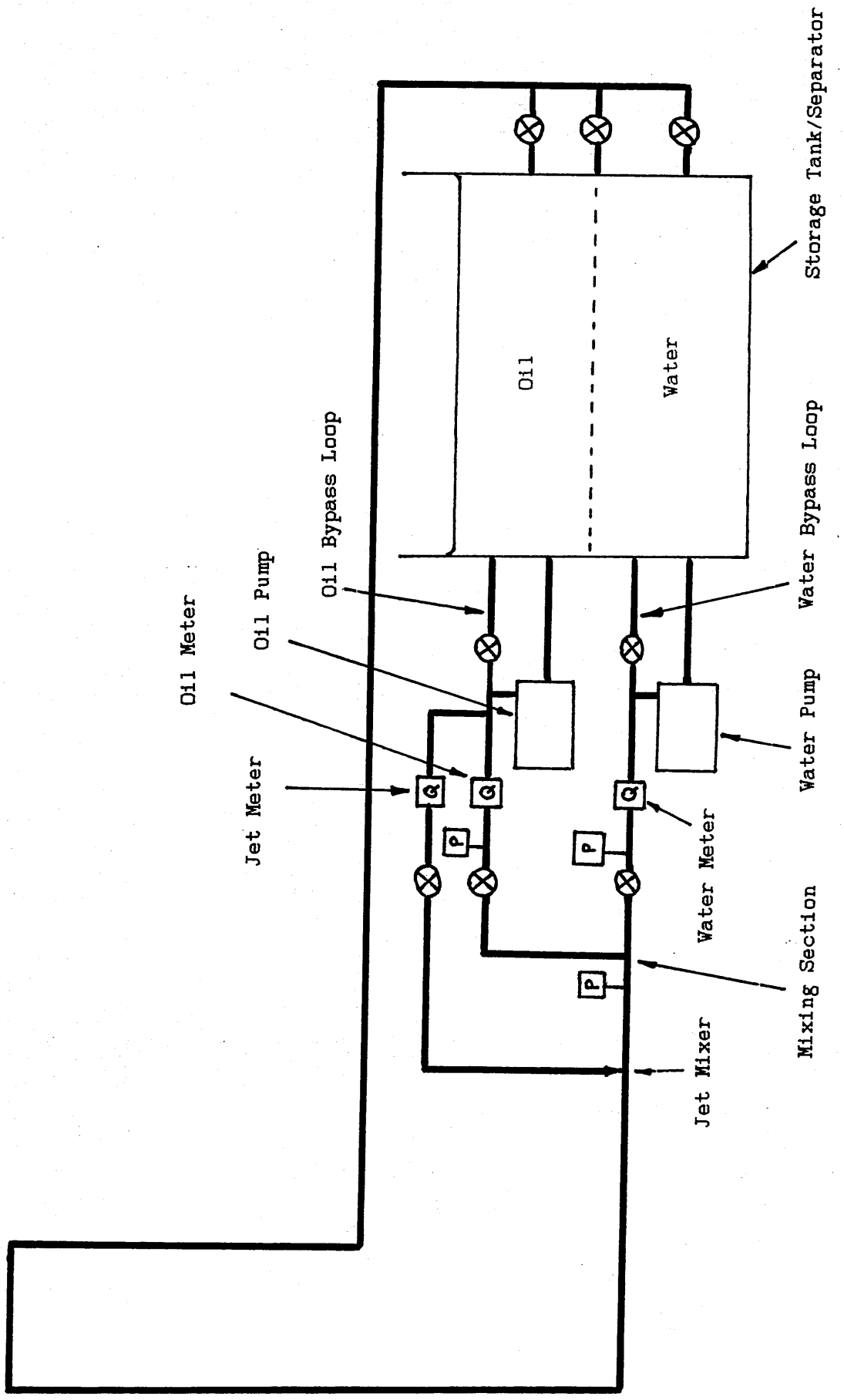

Figure B.2a Schematic of the two component flow loop.

Figure B.2b Photograph of the flow loop

(i) The flash point of kerosene is 39°C, and so cannot be stored indoors in any quantity in an open container.
(ii) The liquid is not pure, containing aromatic hydrocarbons to several % by volume and so producing strong odours.
(iii) The liquid is a pale yellow colour, and several of its components are broken down by light, leading to a gradual darkening of the liquid.

The last two make the physical and chemical properties of the kerosene vary with time, and all three made the fluid unacceptable for the proposed experiment. A substitute had to be found that did not suffer these problems.

For physical and chemical stability, and similarity with kerosene, it is easiest to consider a pure oil or at least a very narrow fraction. It must have a very high flash point, that could never be reached in the laboratory, a low volatility, and ideally be transparent. Several oils satisfy these criteria, and are commercially available in quantity. The one that was finally chosen was BP Dielectric 180, and was kindly donated by BP Exploration.

The physical properties of both the tap water and the D180 were found using standard techniques and the results are summarised in the table below (figure B.3a). All measurements were taken at 18±0.5°C

	Method	Tap water	D180
Density	Density bottle	998.0±0.4 kgm^{-3}	748.6±0.3 kgm^{-3}
Speed of sound	Acoustic Interferometer	1480.2±0.6 ms^{-1}	1295.5±1.3 ms^{-1}
Viscosity (Kinematic)	Ubbelohde Tube	1.0574E-6 m^2s^{-1}	1.9930E-6 m^2s^{-1}
Viscosity	Calculation	1.055E-3 Nsm^{-2}	1.492E-3 Nsm^{-2}
Surface tension with air	wire	0.06306 Nm^{-1}	0.02895 Nm^{-1} (t=0) 0.02535 Nm^{-1} (t=∞)
Interfacial Tension	wire	0.02950 Nm^{-1} (t=0) 0.03670 Nm^{-1} (t=∞)	

Figure 6.3a Table of the experimentally determined physical properties of the fluids.

B.4 Flowmeter Calibration.

As can be seen from figure B.2a, there were three turbine meters on the flow loop: one for the main water flow (FEU048), one for the main oil flow (FEU052) and one for the jet mixer (FEU043F). All of the meters were supplied with water calibrations, though out of date. It is clear that turbine meters are sensitive to variations in density and viscosity (Hayward 1984) and that calibrations can drift with time. Thus it was decided to recalibrate all of the meters in their appropriate fluids.

Both FEU048 and FEU052 had their water calibrations checked against a recently calibrated turbine meter supplied by the EEC for another project (Community Bureau of Reference Intercomparisons Project, Oddie 1990). Each meter agreed with this test meter to within 1.2% over the ranges shown in figure B.4a. Thus it could be concluded that both meters were working correctly. These meters were then installed in the test loop, to be checked on the experimental fluids. A gravimetric calibration of FEU052 would have been the ideal method, however it is impractical at the higher flow rates due to the quantity of oil involved. An alternative method is to use Laser Döppler Anemometry to measure the fluid velocity downstream of the meter. Two possibilities exist for this method of calibration:

(i) Find the flow profile in the pipe using the LDA, and then integrate to find the total flow rate and the calibration point.
(ii) Measure only the centreline velocity, assume the form of the flow profile and hence calculate the flow rate.

Method (i) had been investigated extensively as a part of the above mentioned EEC project and errors of the order 1% had been found for fully developed straight pipe flow. This error arises mainly from the accuracy of the velocities measured near the wall (Oddie 1990). The second method is considerably quicker ($\simeq$1:100), and the errors in assuming a profile, for example the Prandtl 1/7th power law, are also of the order 1% again due to wall effects. Hence the second method was used. Prandtl's law gives the velocity of any point in the pipe as a function of it position (y), the radius of the pipe (r) and the centre line velocity (U_{CL}), as follows:

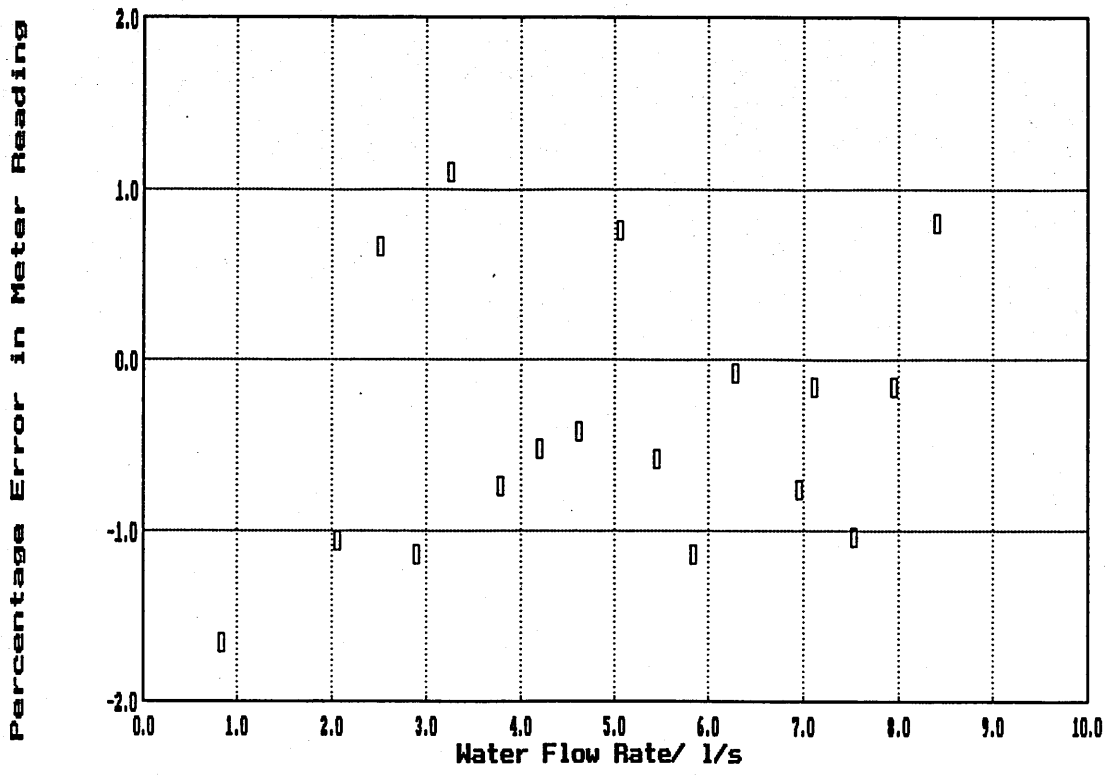

Figure B.4a Example of flowmeter comparison between FEU052 and the BCR meter

$$U(y) = U_{CL}(r-y)(y/r)^{1/7}$$

Thus, integrating the point profile across the pipe, will give the total flow rate:

$$\pi r^2\langle U\rangle = 2\pi U_{CL}\int_0^r (r-y)(y/r)^{1/7}\,dy$$ where $\langle U\rangle$ is the mean velocity.

$$= \frac{49\pi r^2 U_{CL}}{60}$$

$$\therefore U_{CL} = 1.224\ \langle U\rangle$$

The oil meter was calibrated in this way, and to provide a check on the method, the water meter was also recalibrated.

As for the jet mixing meter, the flow rates required to produce suitable mixing were quite small, and so velocities in large pipes (for accurate LDA) would also be quite small. This meter was gravimetrically recalibrated for the oil, as small turbine meters are very sensitive to changes in viscosity. It was found that the meter was being used below its linear region for some of the jet flow rates. To make the later experiments easier, look-up graphs were produced, to give an idea of the various flow parameters within the pipe. These are reproduced in figures B.4b, c and d, where other relevant fluid parameters are also included.

B.5 Single Phase Testing of the Flow Loop.

As can be seen in figure B.2b, much of the test loop is constructed from Perspex (polymethylmethacrylate) tubing. This is of the extruded type, as opposed to the cast variety, and so is rated to between 30 and 50psi, depending on the construction of the joints. The pumps are rated to 50psi, and so a quick investigation was carried out to find the maximum pressures in the system as a function of fluid flow rate for both the oil and the water. The results appear in figures B.5a and B.5b.

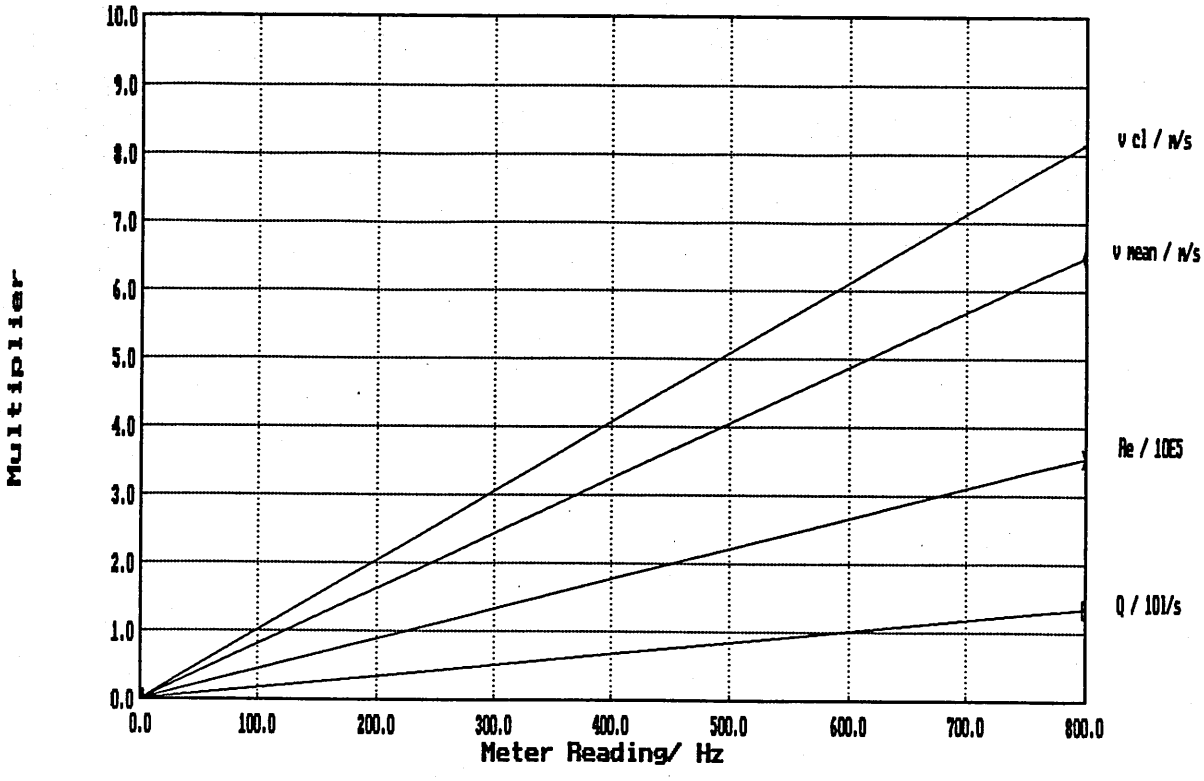

Figure B.4b Water flow parameters in the 2" pipe

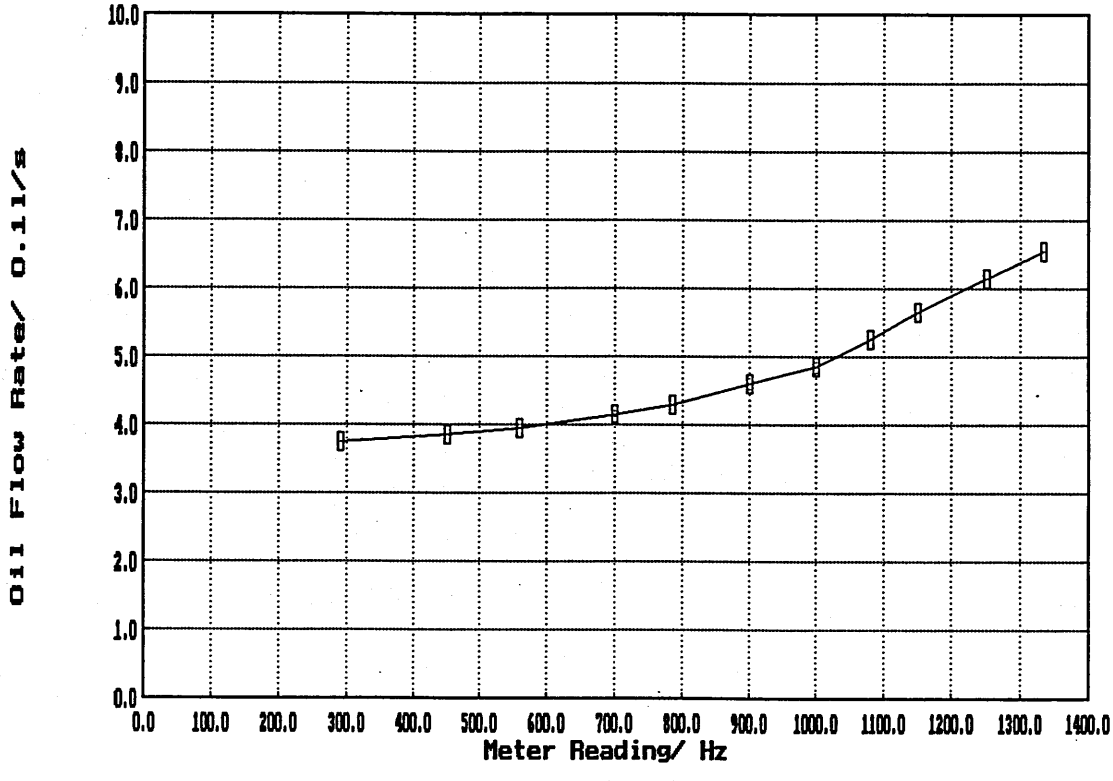

Figure B.4c Oil flow through the jet mixer

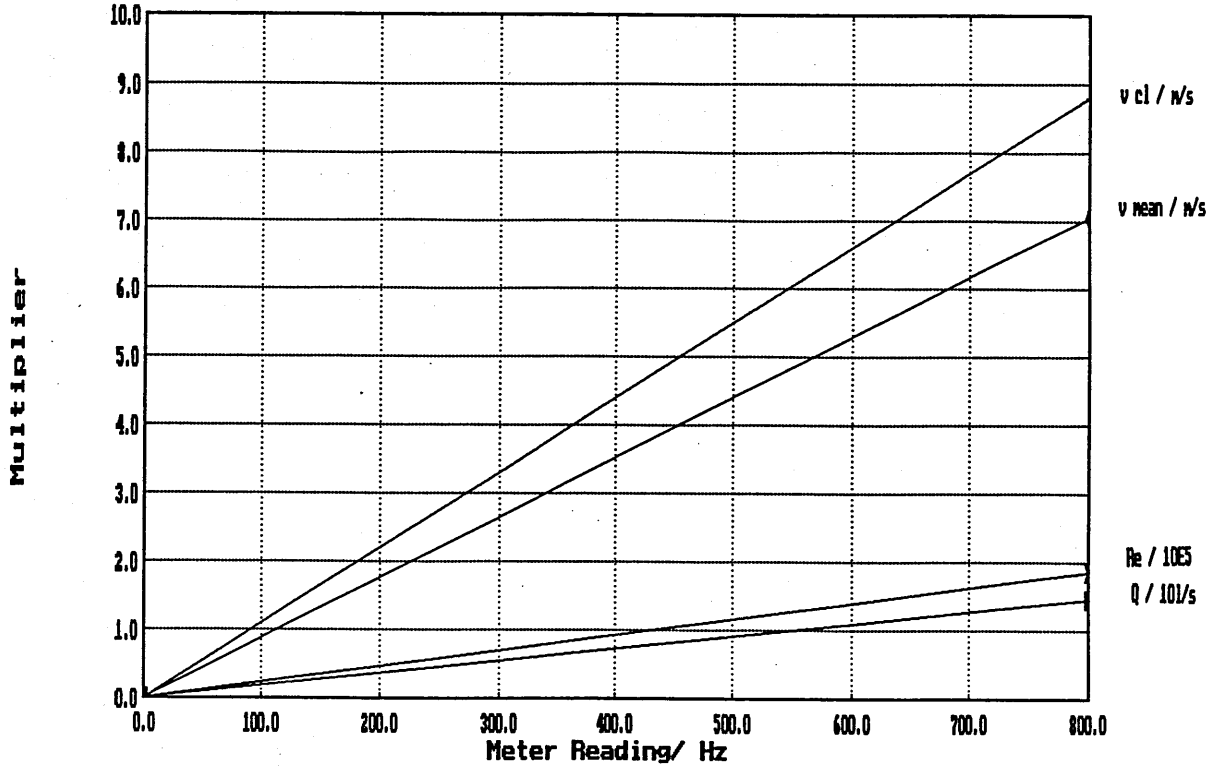

Figure B.4d Oil flow parameters in the 2" pipe

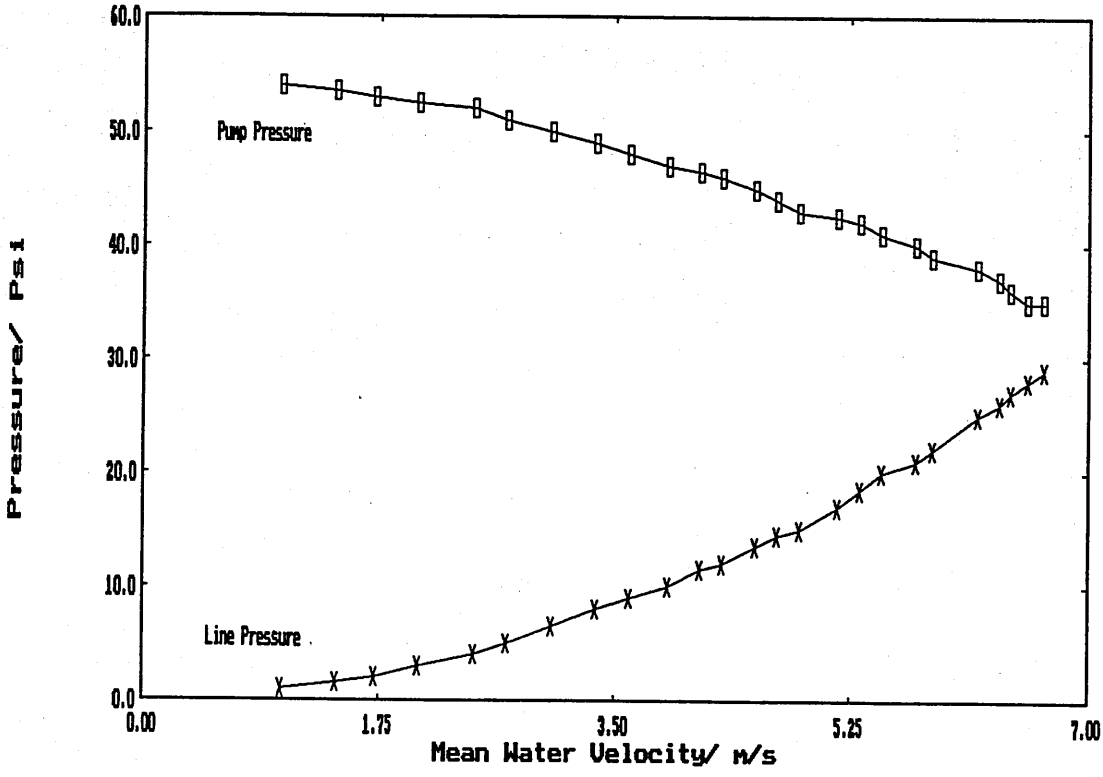

Figure B.5a Flow characteristic of the water pump

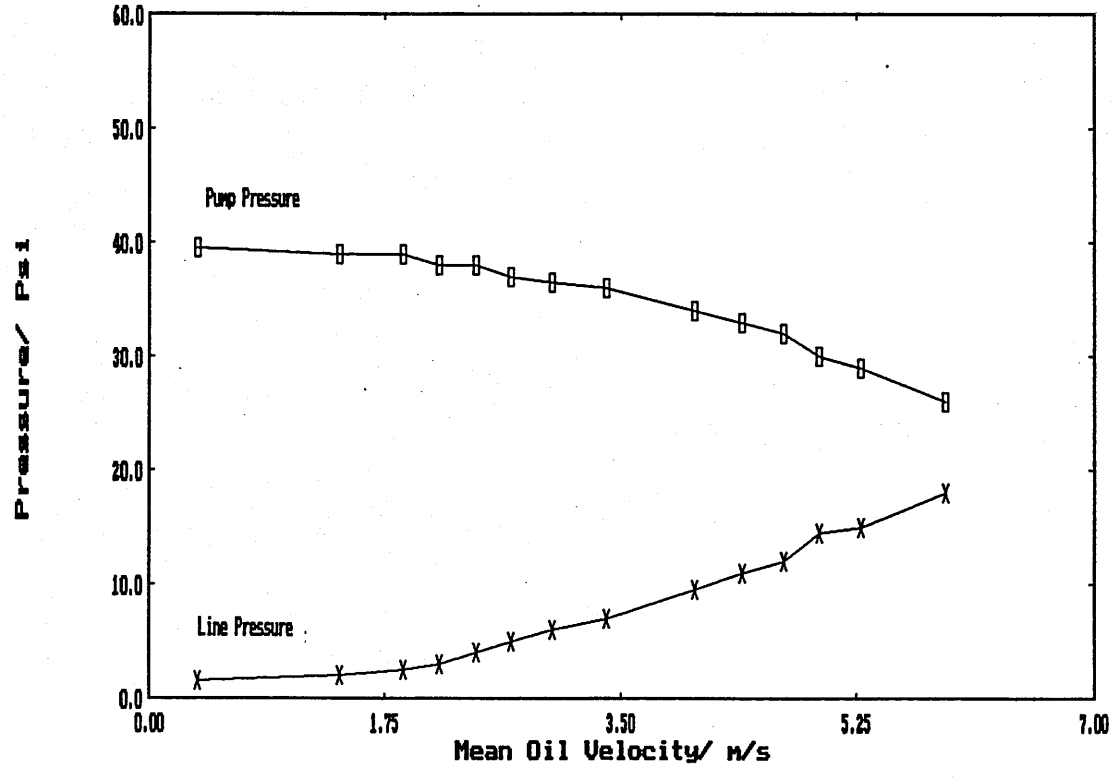

Figure B.5b Flow characteristic of the oil pump

As was mentioned in section B.3, the physical properties of the fluids are a function of temperature. The temperature rise of the appropriate liquid in the main tank was noted whilst the above experiments were being carried out. For both liquids, the rate of change of temperature was around 0.02°C/minute for the highest flow rates, though it is fairly independent of flow rate. Viscosity is the most sensitive parameter, and noting that it varies by 3%/°C (Perry 1973) for water, and that the viscosity is measured to ±2%, then the apparatus should have been capable of being run continuously for about 30 minutes before temperature variations in this and the other physical parameters became significant.

There is also a problem with gases dissolved in the liquids. This must be addressed carefully at this stage if it not to interfere with future experiments. Small quantities of dissolved gas tend to come out of solution whenever the carrying liquid is subjected to a severe pressure drop such as occurs in flow rate controlling valves when only a small percentage of the available flow is required. In this apparatus, the phenomenon could be clearly seen and heard in the pipe. The presence of any gas scatterers will interfere with any ultrasonic experiments carried out in the pipe. The bubbles could be eliminated by increasing the pressure within the whole apparatus.

B.6 Multiphase Testing Of The Loop.

As a basic test of the behaviour within the loop under multiphase conditions, a systematic survey was carried out of the appearance of the flow as a function of the oil and water flow rates. Both horizontal and vertical phenomena were observed and are sketched in figures B.6a and B.6b, which take the form of simple flow regime maps. The ideas behind flow regime maps will be greatly expanded in appendix C and chapter 6.

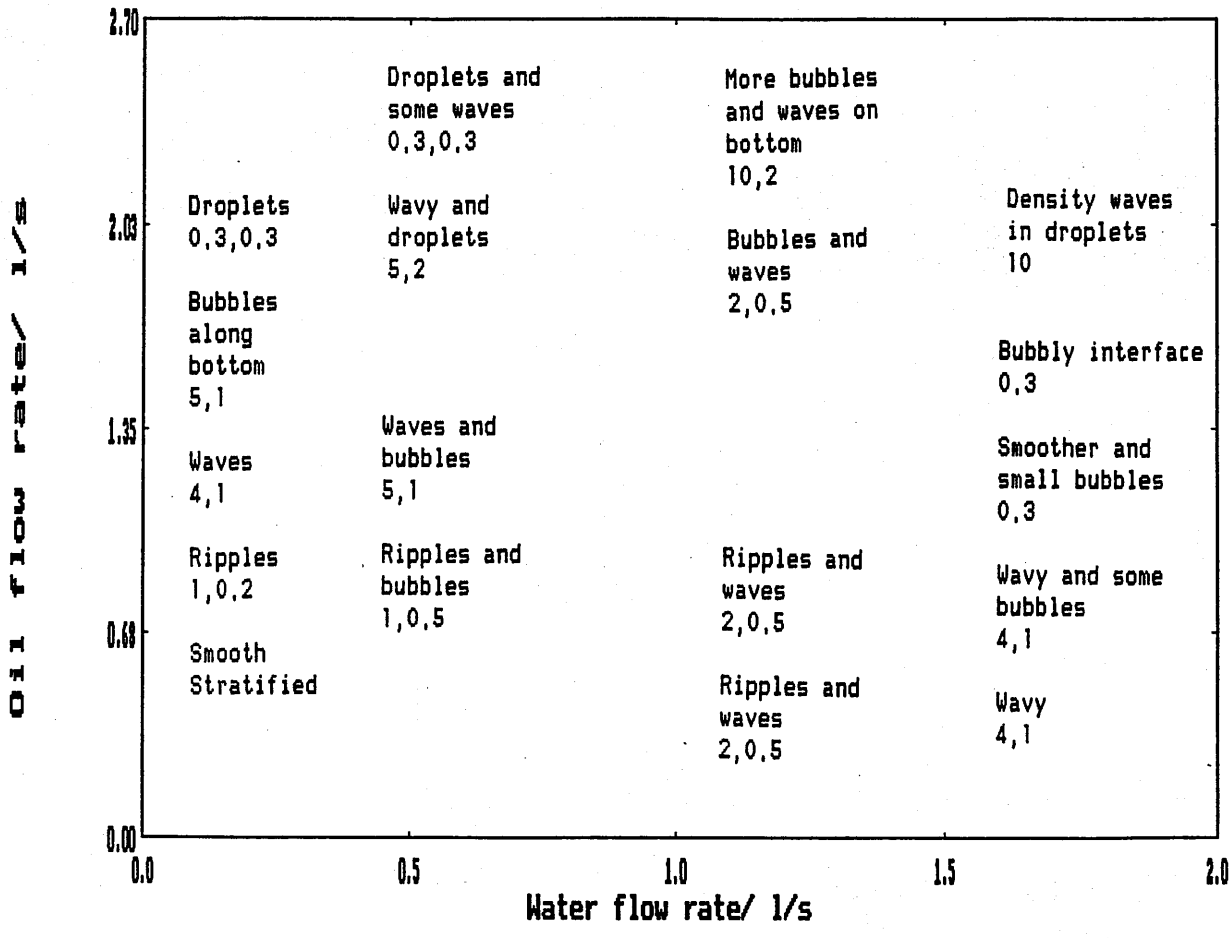

Figure B.6a Flow regime map for horizontal oil/water flow in the 2" pipe. The numbers appended to the descriptions refer to characteristic axial and transverse lengths (in cm), determined visually.

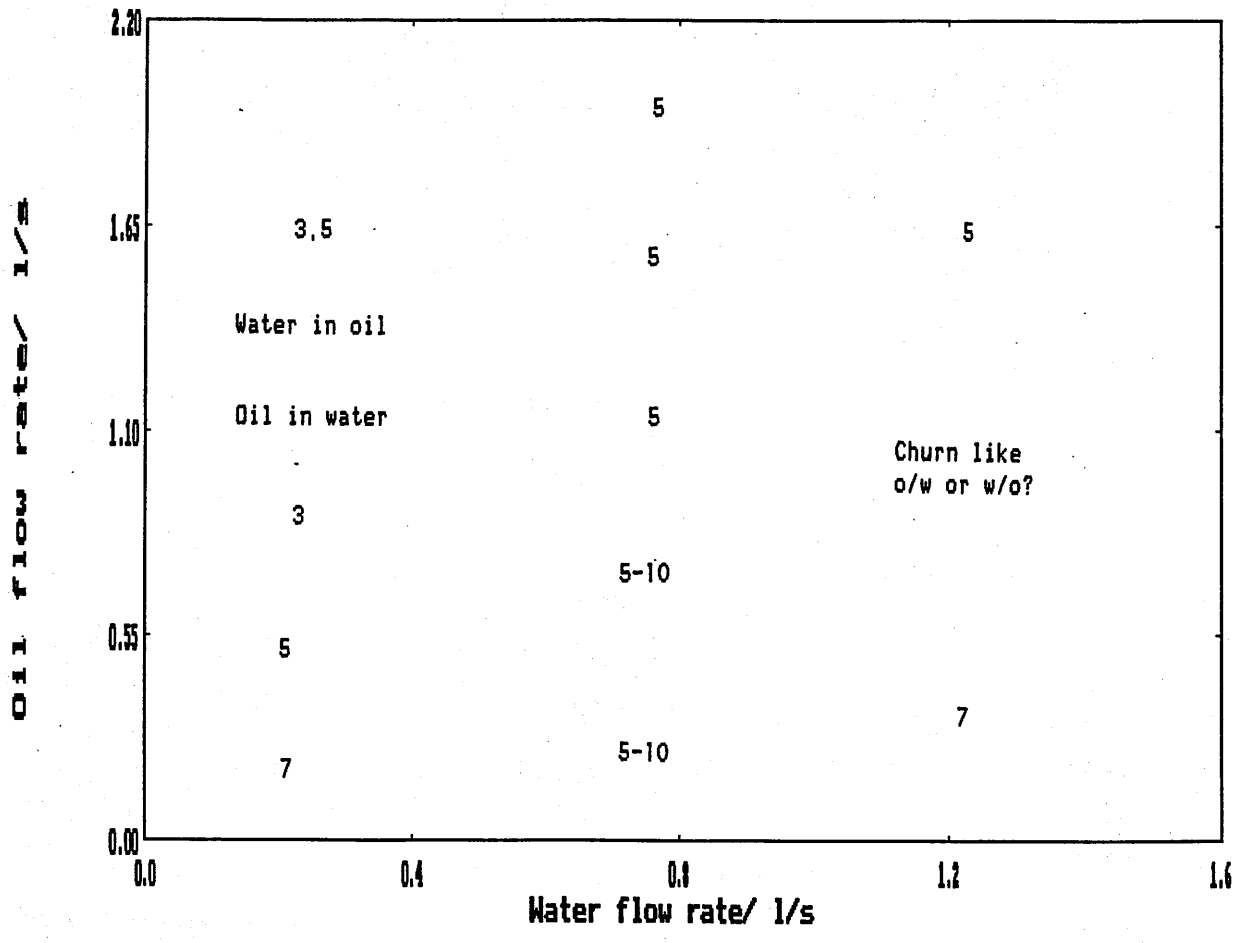

Figure B.6b Flow regime map for vertical oil/water flow in the 2" pipe. The flows are very difficult to describe, and again, the numbers refer to characteristic axial lengths (in cm).

B.7 Construction of the Test Section.

The design of the test section needed to be flexible enough to allow several different ultrasonic experiments to be carried out with minimum disruption to the apparatus. The following techniques had to be attainable within a single spool piece:

(i) Angular scattering
(ii) Döppler scattering
(iii) Long wavelength attenuation and speed of sound
(iv) Spatial filtering

The most difficult problem was the measurement of the angular scattering at as many angles as possible. It was found to be impossible to design a mechanism that would allow the angle between the transmitter and receiver to be varied continuously. The next best solution was to have several transmitter and receiver positions, various combinations of which would allow scattering through different angles to be studied. The final design is sketched in figure B.7a and a photograph appears in figure B.7b.

The spool piece was constructed from a cast perspex block. This allowed the positioning of the transducers on the 'o' rings to be checked before the loop was run and also allowed any air bubbles that might be trapped on the transducer faces to be seen and then bled off, by relaxing the retaining bolts on the rear of the transducers. The original design allowed for circlips to hold in the large, low frequency transducers, however misalignment of spring steel circlips would have seriously damaged the perspex, and so retaining bolts were used instead.

To prevent rust on the blanking plugs, and to allow easy insertion of the transducers, engine oil was smeared on all surfaces during each reassembly. Details of the ultrasonic transducers, along with their electronics can be found in chapter 5.3 where the ultrasonic experiments are carried out.

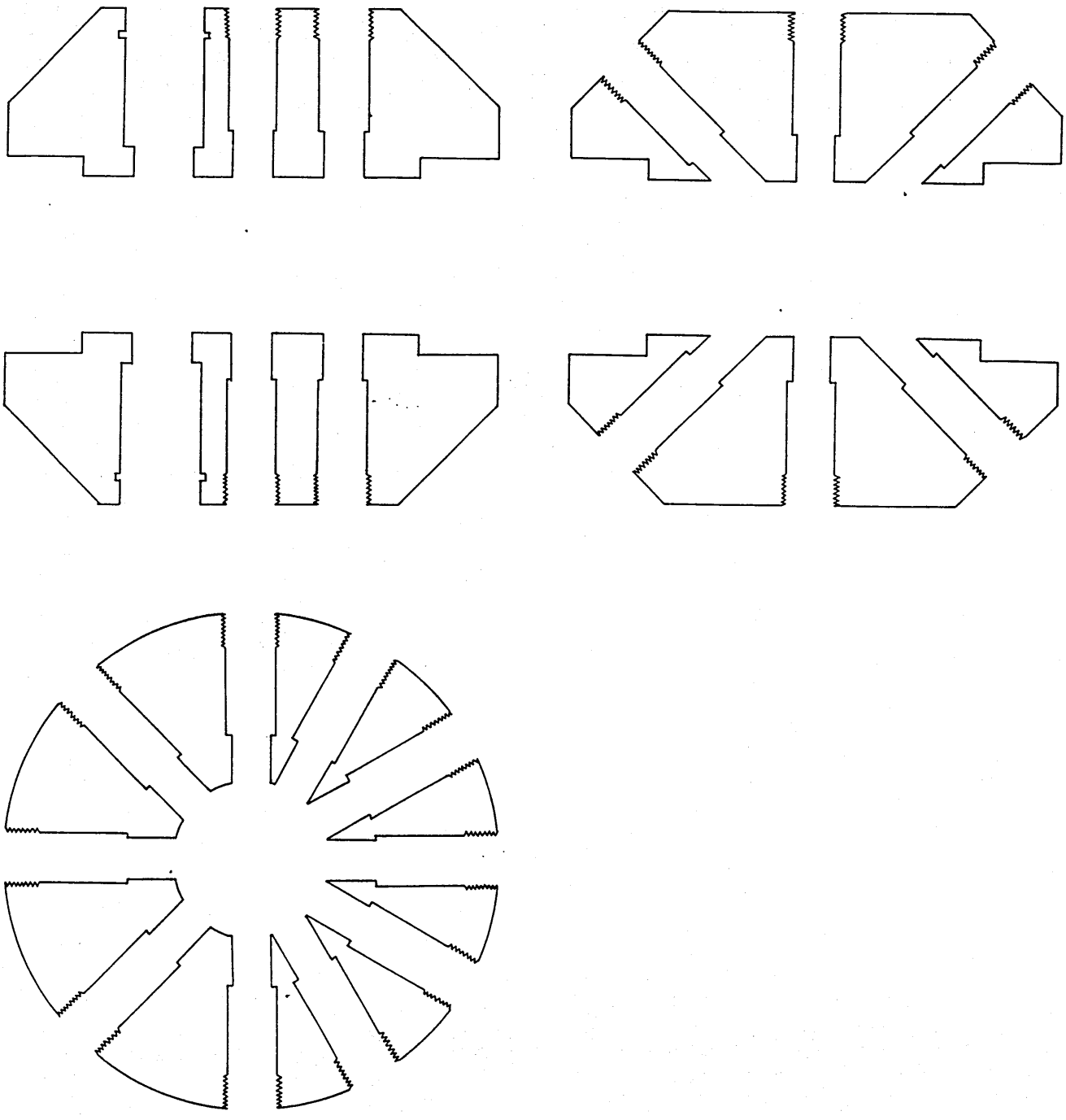

Figure B.7a Sectional drawings of the spool piece

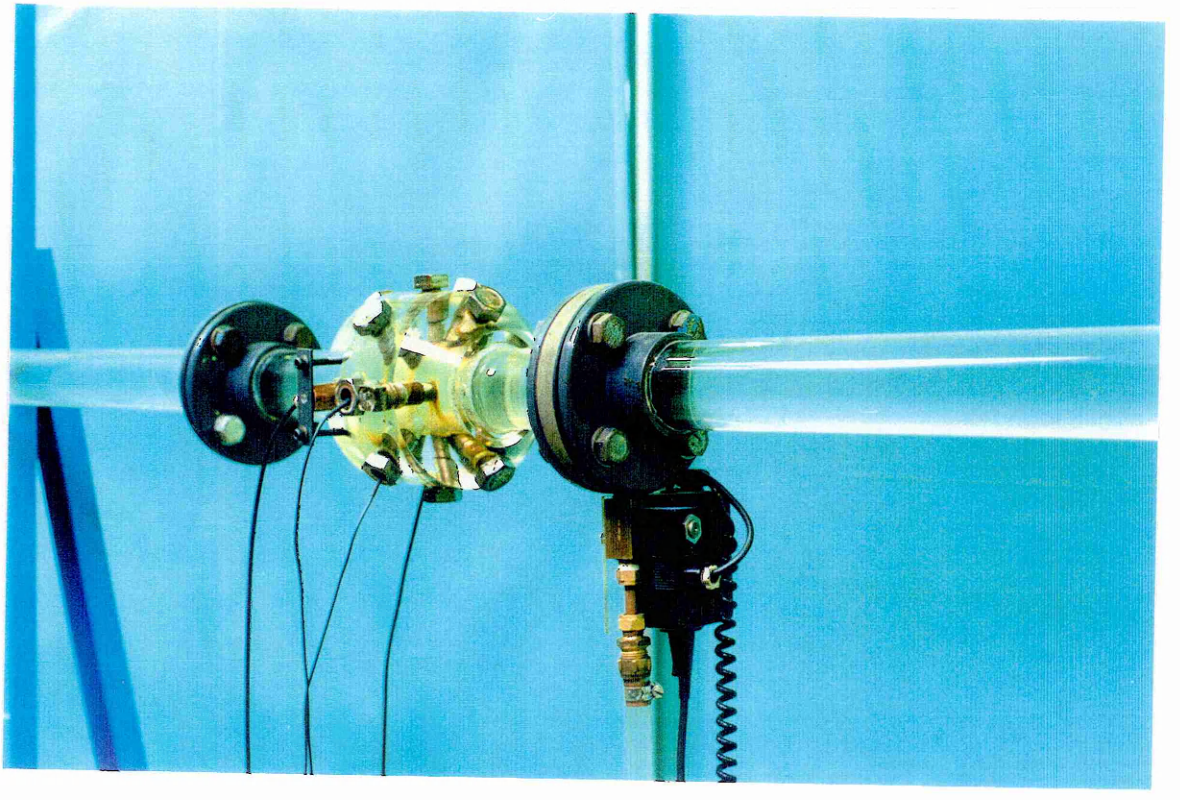

Figure B.7b Photograph of the finished spool piece in use. Note also the jet mixer and solenoid valve/actuator (Section B.8)

B.8 Construction of the Jet Mixer.

The jet mixer consisted of a small diameter pipe taken directly from one of the main pump outlets, through the meter FEU043F, then a solenoid valve, and finally the injector nozzle. The nozzle consisted of a straight piece of copper pipe, whose outlet was flush with the inner surface of and directed towards the center of the main pipe and its axis was normal to that of the main flow. The flow rate was controlled by the valve upstream of the flowmeter, and the droplet size was varied by changing the flow rate and the inner diameter of the nozzle (see chapter 5.2 for more details). A photograph of the injector section and solenoid valve appears in figure B.7b.

B.9 Cleaning the Apparatus and General Maintenance.

The use of both oil and water in the same apparatus pose several problems above those encountered in single phase flow loops. These are summarised below.

(i) As can be seen from figure B.3a, the interfacial tension varies with time, implying some sort of chemical reaction between the oil and water, probably due to the migration of ionic impurities within the water, as the phenomenon has not been observed with distilled water (Hayes 1988). For a small droplet, the migration would be complete after a few seconds, however with a tank containing three tonnes of fluid, the reaction took about three weeks if the tank was stirred continuously. The reaction product was a soap like scum which resided on the interface between the two fluids, and had to be removed before each run to stop it contaminating the pipework and, more importantly, the meters. Despite this cleaning procedure, the reaction took place independently within the pipe, leaving slimy deposits.

(ii) As the water in the tank was totally covered by the oil, the tank had to be continuously aerated to avoid anaerobic bacteria thriving in the water. These bacteria still appeared in the water droplets that stuck to the side of the tank and were surrounded by the oil, producing

a foul smell and discolouring the water. The discolouring appeared after about three days and became very serious after two weeks.

(iii) On disposing of the water, care must be taken to minimise oil losses to the drain, in order to avoid infringing the local pollution regulations.

(iv) The apparatus could not be cleaned with any substances that might act as surfactants to the oil/water reaction (for example, detergents and alkalis) and, as the oil was to be used repeatedly, any cleaning agents could not be soluble in the oil. Observing these precautions meant that the interfacial properties remained constant throughout the experiments.

With these conditions in mind, the following cleaning procedure was adopted every three weeks.

(i) The system was allowed to stand with the pipes full of water for one day after the last experiment. This allowed total separation of the oil and water components.

(ii) The oil was siphonedoff the surface of the water in the tank. The last few litres, including any scum, water etc were placed in a waste barrel to allow further separation.

(iii) The water was drained from the tank, and the sides of the tank were regularly washed with clean water to remove any residual scum.

(iv) The residual water was vacuumed out and the tank allowed to dry.

(v) The tank was partially refilled with water and a sterilising fluid such as sodium hydroxide (Milton Fluid) was added, and the tank was thoroughly cleaned.

(vi) The tank was drained, rinsed and dried again.

(vii) The pipework was drained and then disconnected at the bends. The pipes were then pigged using a bristle brush and cloth soaked in the sterilising fluid.

(viii) The pipe was thoroughly rinsed and reassembled.

(ix) The tank was partially refilled with water. The whole system was then rinsed and then drained.

(x) The tank was then refilled with water and oil ready for use.

This whole procedure could be carried out in 12 hours..

B.10 Discussion and Conclusions.

This appendix has described the design and testing of a large scale two-component flow loop. As this was a new test facility, each element of the loop had to be investigated in turn in order to find the limits and usefulness of the loop. Though some of the procedures appeared lengthy, they were considered the minimum necessary to provide good repeatable experimental conditions.

Appendix C: Select Literature Review: Multiphase and Multicomponent Flows.

C.1 Introduction.

Thus far the terms multiphase and multicomponent have been used quite vaguely as the experiments have centred around a very special case, the spherical discontinuity and disperse flows. The aim of this appendix is to briefly review the state of the art in multiphase and multicomponent flows, and to see how the current understanding and terminology has been arrived at. The review will cover the work of various authors in the areas between semi-empirical and purely experimental multiphase and multicomponent flows. Flow regimes and the transitions between them will be covered as well as attempts to produce coherent classifications in the form of flow regime maps

The term multiphase implies a combination of phases (ie solid, liquid or gas), where each phase can be made of the same or different materials. The term multicomponent implies a single phase (usually liquid), but different materials. The terminology has been used indiscriminately in the past, and ideally it should be qualified, so that there can be no doubt as to the specifications of the problem. For example, the most complex flows occurring in the oil industry comprise sand/oil/water/gas mixtures and so are multiphase/multicomponent systems, and can be ambiguously described.

Most of the work in this area has centred around gas/liquid, liquid/liquid and liquid/vapour flows, ie fluid/fluid flows, and this review will be limited to fluid/fluid flows within cylindrical pipes.

C.2 Flow Transitions

Consider two fluids flowing in a pipe, with the entrance criteria to the system being constant. As the interface between the two fluids is compliant (ie can be stretched and otherwise deformed), the two fluids

can be distributed across the conduit in a variety of ways, depending on the following system parameters;

Superficial velocity of fluid 1	U_{1s}
Superficial velocity of fluid 2	U_{2s}
Pipe diameter	D
Density of fluid 1	ρ_1
Density of fluid 2	ρ_2
Viscosity of fluid 1	μ_1
Viscosity of fluid 2	μ_2
Interfacial tension between fluids	σ_{12}
Acceleration due to gravity	g
Pipe roughness	ε
Pipe inclination angle	β

Other parameters that enter under more specialised circumstances are heat flux, various heat capacities, thermal conductivities, boiling points, temperatures, pressures, reactions between the fluids and pipe walls (wetting and surface tension) and the compressibility of any gaseous phase.

As the 11 parameters in the list above are dimensioned in terms of [M], [L] and [T], the Buckingham Pi theorem can be invoked to reduce them to the following 8 dimensionless parameters;

$$\frac{U_{1s}+U_{2s}}{(gD)^{\frac{1}{2}}},\ \frac{U_{1s}}{U_{2s}},\ \frac{g\rho_1 D^3}{\mu_1^2},\ \frac{\varepsilon}{D},\ \frac{\rho_1}{\rho_2},\ \frac{\mu_1}{\mu_2},\ \frac{\sigma\rho_1 D}{\mu_1^2},\ \beta$$

The primary method of determining what is happening within the pipe is visual observation, or for faster phenomenae, high speed photography. Other methods will be described later in this section which provide secondary information about the flow. Clearly, every combination of experimental parameters will produce a unique flow pattern within the pipe and this would require an infinite number of descriptive terms or an accurate measurement of every dependent parameter. This is not practical, and since many of the flow patterns show similar qualitative characteristics when subjectively observed, they are

grouped together under broad flow regime titles. In horizontal pipes, these regimes go under the following titles;

Stratified: smooth
wavy
laminar
roll-wave
inertia
Wave
Plug: elongated bubble
Slug: proto slug
slug 3
Annular: flow through
wavy
mist
semi annular
Pulsating froth
Spray
Bubble: dispersed bubble
Homogeneous: disperse

and in vertical tubes;

Bubble
Slug: annular
frothy
quiet
dispersed
Plug: piston
Annular: pulsating
mist
wispy
Churn
Dispersed bubble
Homogeneous
Froth

Several of the basic flow regimes are sketched in figures C.2a and C.2b for horizontal and vertical flows respectively.

Many of these flow regimes do not have distinct boundaries and are very sensitive to the experimental parameters. Thus to map a fluid fluid flow would require at least an 8-Dimensional map to incorporate the important variables described above. Clearly a 2-D map would be the most practical to use, but in choosing two parameters for the axes, the others are lost, and so the maps are very experimentally specific and cannot be extended to other situations. See appendix B.6 for a typical example derived for the main experimental loop.

C.3 Generalised Flow Maps.

Of the 7500 papers and theses published this subject between 1954 and 1984, almost all were restricted to finding the boundaries of a particular flow regime, whilst varying a few of the relevant variables. Only a few attempts have been made to collate this information.

The earliest flow regime map was produced by Baker (1954), and is reproduced in figure C.3a. On the axes w_l and w_g are the mass flow rates in lb mass/hr, the densities are in lb/ft^3, the liquid viscosity is in cp and the interfacial tension in dyn/cm. The use of a dimensional axis limits the applicability of this map to parameters that are close to those of the original experiments. Inspite of this, the simplicity of the map means it is still used extensively, sometimes with the minor modifications to be described below.

In the Baker map, the parameters λ and ψ were invoked to take into account the possible variations in material properties from system to system, and were defined as follows;

$$\lambda = \left[\frac{\rho_g}{\rho_a}\cdot\frac{\rho_l}{\rho_w}\right]^{\frac{1}{2}} \qquad (C.3.1)$$

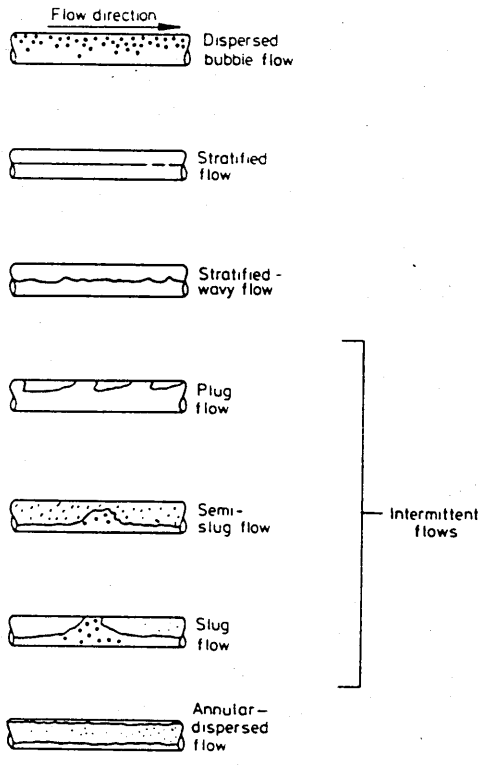

Figure C.2a Flow regimes for gas/liquid flow in a horizontal pipe.

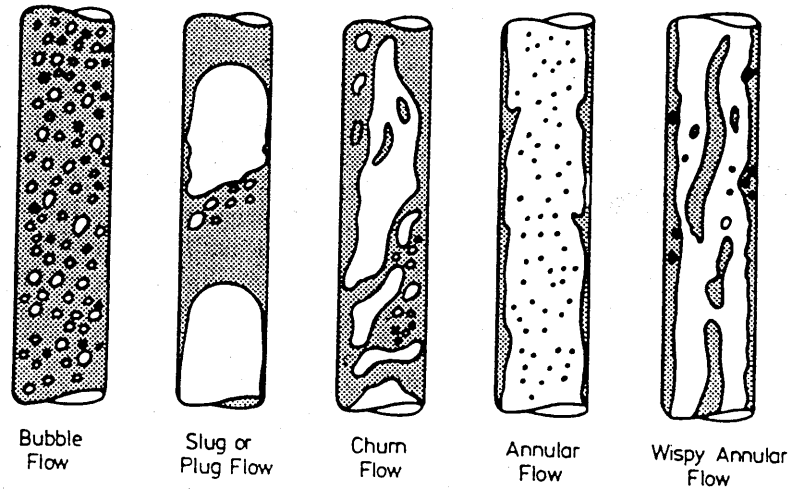

Figure C.2b Flow regimes for gas/liquid flow in a vertical pipe.

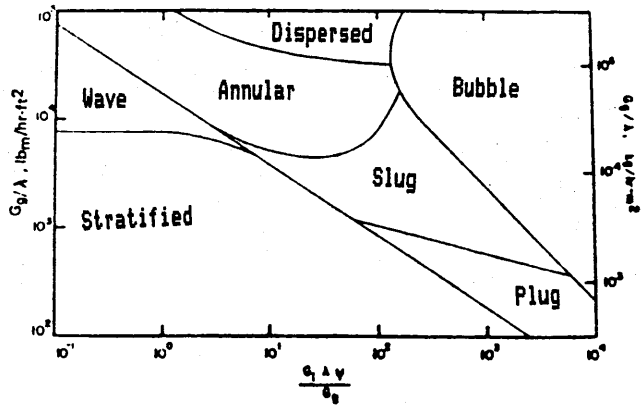

Figure C.3a Baker flow pattern map (1954).

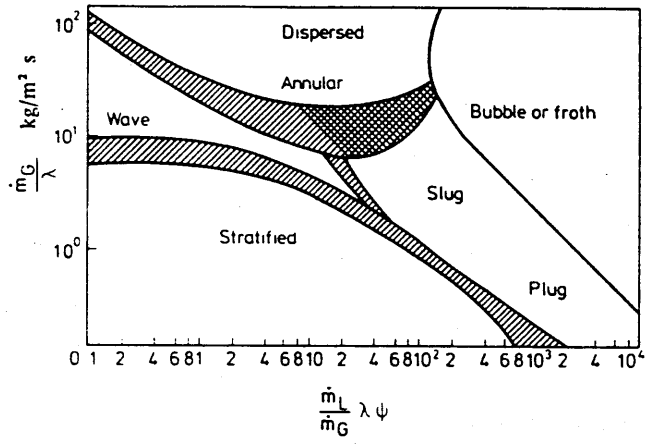

Figure C.3b Scott's modification to the Baker flow map (1963).

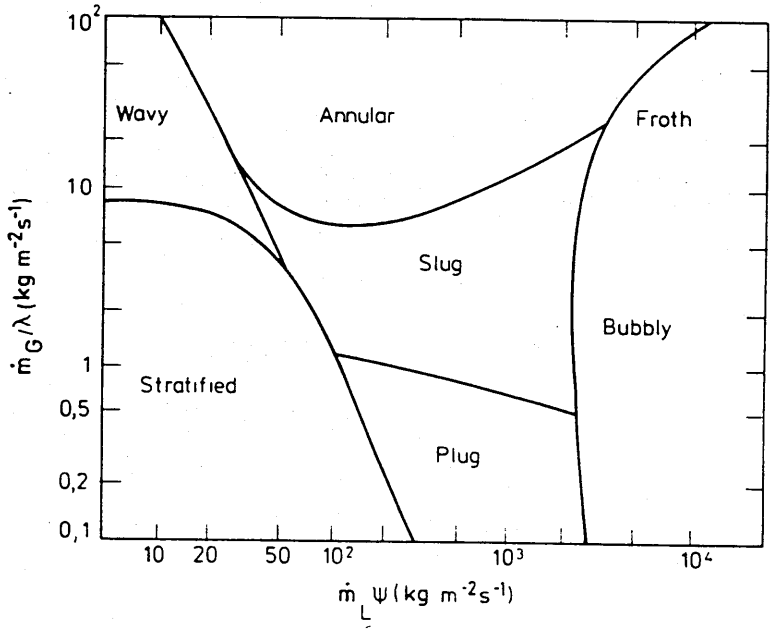

Figure C.3c Bell's modification to the Baker flow map (1969).

$$\psi = \frac{\sigma_w}{\sigma}\left[\frac{\mu_l}{\mu_w}\left(\frac{\rho_w}{\rho_l}\right)^2\right]^{1/3} \qquad (C.3.2)$$

where the subscripts g,a,w and l refer to gas, air, water and liquid respectively. Thus for a water/air system, $\lambda=\psi=1$.

This work was extended by Scott (1963), to include the transition regions between the regimes, and the transition from annular to dispersed was omitted due to the fact that it is almost impossible to observe (figure C.3b). The axes were later simplified by Bell (1969), though they are still dimensional (figure C.3c).

A different approach, proposed by Eaton (1967) and shown in figure C.3d, involves a definition of a two phase Reynolds number and Weber number as follow;

$$Re = 1488\,\frac{M_m E_l^2}{D\mu_m} \qquad (C.3.3)$$

$$We = 453D\left[\frac{\rho_l V_l^2 E_l^{1/3}}{\sigma} + \frac{\rho_g S^2 (1-E_l)^{1/3}}{\sigma}\right] \qquad (C.3.4)$$

where the subscript m refers to the mixture, M is the mass flow rate, S is the average slip velocity in ft/s and E_l is the in situ volume fraction of the liquid. This last factor means that a holdup correlation has to be used, which considerably reduces its accuracy and ease of use. The slug to froth transition was originally known as slug three flow. The use of an effective Weber number, We, made from an arithmetic rather than a geometric mean, is a most unusual approach, and has not been explored anywhere else.

The most directly usable axes for the flow maps are the material superficial velocities, U_{ls} and U_{gs}, since these are the most easily varied and measured experimental parameters. These axes were first used by Mandhane (1974), and the results are compared with the works of Govier and Aziz (1972) in figure C.3e and Taitel and Dukler (1976) in figures C.3f, g and h. All of these maps show similar shapes, but

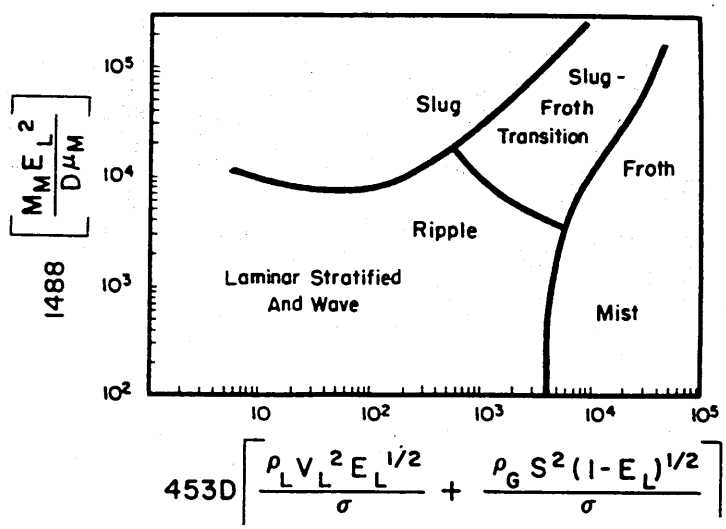

Figure C.3d Eaton's flow map (1967).

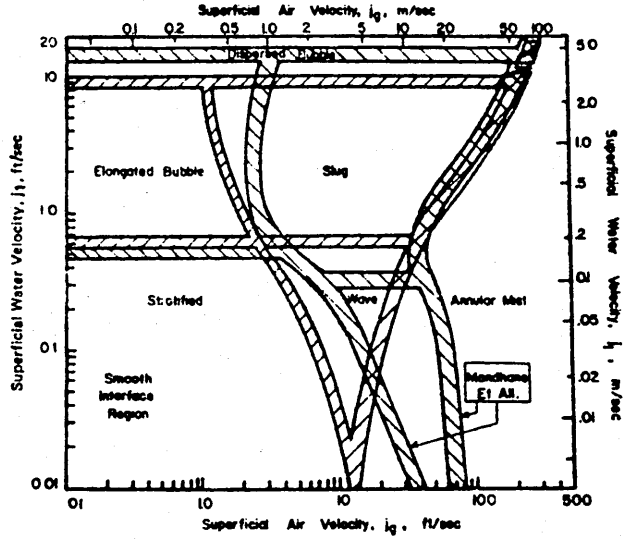

Figure C.3e Comparison between Mandhane's flow map (1974), with the work of Govierand Aziz.

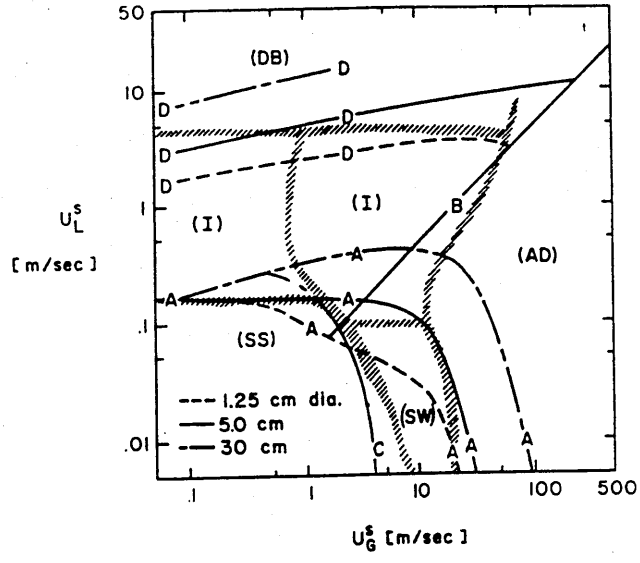

Figure C.3f Comparison between Mandhane's flow map (shaded), the experimental results of Taitel, showing variations with pipe diameter (1976).

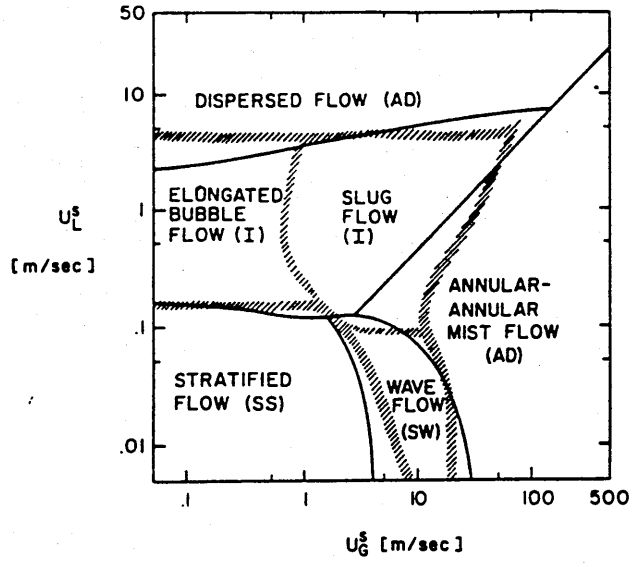

Figure C.3g Comparison between Mandhane's flow map (shaded), and the experimental results of Taitel (1976).

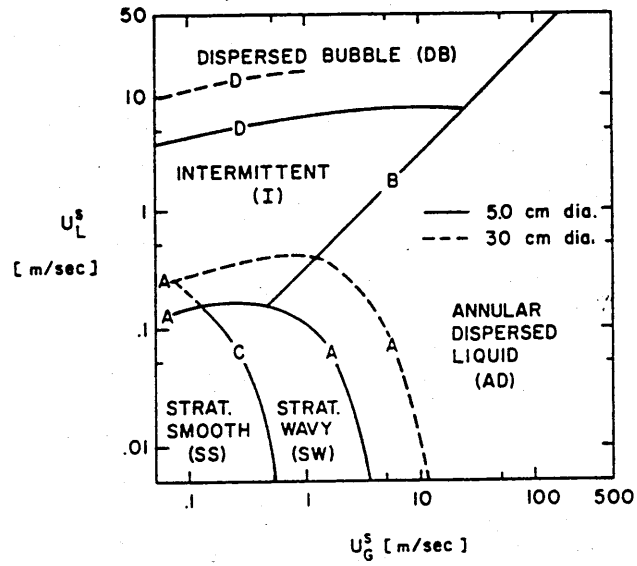

Figure C.3h Variation of transition boundaries with fluid properties (Taitel 1976).

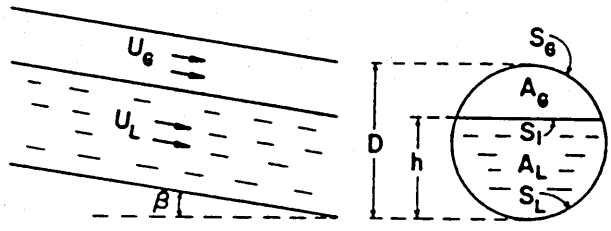

Figure C.3i Definition of some system parameters for gas/liquid flow in a pipe.

with large distortions due to variations in unmapped experimental criteria.

Taitel and Dukler continued with their work (Dukler 1986, and the references therein), and were the first to publish a theoretical analysis of some of the more obvious transitions and compare them with experimental results. This was in contrast to the vast number of empirical correlations published previously, and the analysis below, follows their description of the following transitions;

A: Stratified wavy - Intermittent
B: Annular - Dispersed
C: Stratified smooth - Wavy
D: Intermittent - Dispersed

The most basic flow in a horizontal pipe containing two fluids is smooth stratified. All other flow regimes must be considered as a more stable equilibrium that has been arrived at after the smooth stratified flow has been perturbed. For a given piping system, the flow regime at a point is independent of the past history of the flow through that system, for a given set of flow parameters. See figure C.3i for some of the terms used below.

A momentum equation for each phase can be written as;

$$-A_l\left[\frac{dP}{dx}\right]_l - \tau_l S_l + \tau_i S_i + \rho_l A_l g \sin\beta = 0 \qquad (C.3.5)$$

$$-A_g\left[\frac{dP}{dx}\right]_g - \tau_g S_g - \tau_i S_i + \rho_g A_g g \sin\beta = 0 \qquad (C.3.6)$$

Noting that, for an equilibrium flow;

$$\left[\frac{dP}{dx}\right]_l = \left[\frac{dP}{dx}\right]_g \qquad (C.3.7)$$

then;

$$\frac{\tau_g S_g}{A_g} - \frac{\tau_l S_l}{A_l} + \tau_i S_i \left[\frac{1}{A_l} + \frac{1}{A_g}\right] + (\rho_l - \rho_g) g \sin\beta = 0 \qquad \text{(C.3.8)}$$

The shear stresses can be found from;

$$\tau_l = \frac{f_l \rho_l U_l^2}{2}, \quad \tau_g = \frac{f_g \rho_g U_g^2}{2} \quad \text{and} \quad \tau_i = \frac{f_i \rho_g (U_g - U_i)^2}{2} \qquad \text{(C.3.9)}$$

and the friction factors;

$$f_l = C_l \left[\frac{D_l U_l}{\mu_l}\right]^{-n} \quad \text{and} \quad f_g = C_g \left[\frac{D_g U_g}{\mu_g}\right]^{-m} \qquad \text{(C.3.10)}$$

The above equations require the definition of an equivalent hydraulic diameter, as follows (Agrawal 1973, Miller 1978);

$$D_l = \frac{4A_l}{S_l} \quad \text{and} \quad D_g = \frac{4A_g}{S_g + S_i} \qquad \text{(C.3.11)}$$

Provided the flow is fairly smooth, the above diameters arise because the liquid is behaving as in open channel flow and the gas as in closed duct flow. Thus $f_i = f_g$ and $f_i \ll f_l$.

For laminar flow, Taitel and Dukler take, $C_g = C_l = 16$, $n = m = 1$ and for turbulent flow, $C_g = C_l = 0.046$ and $n = m = 0.2$.

Reducing these equations to a dimensionless form in D, D^2, U_{ls} and U_{gs}, and denoting these with a tilde, leaves;

$$X^2 \left[\frac{(\tilde{U}_l \tilde{D}_l)^{-n} \tilde{U}_l^2 \tilde{S}_l}{A_l}\right] - \left[(\tilde{U}_g \tilde{D}_g)^{-m} \tilde{U}_g^2 \left(\frac{\tilde{S}_g}{A_g} + \frac{\tilde{S}_i}{A_l} + \frac{\tilde{S}_i}{A_g}\right)\right] - 4Y = 0 \qquad \text{(C.3.12)}$$

Where;

$$X^2 = \frac{4C_l}{D}\left[\frac{U_{ls} D}{\mu_l}\right]^{-n} \frac{\rho_l U_{ls}^2}{2} = \frac{|(dP/dx)_{ls}|}{|(dP/dx)_{gs}|} \qquad \text{(C.3.13)}$$

$$Y = \frac{(\rho_l - \rho_g)g\sin\beta}{\frac{4C_g}{D}\left[\frac{U_{gs}D}{\mu_g}\right]^{-n}\frac{\rho_g U_{gs}^2}{2}} = \frac{(\rho_l - \rho_g)g\sin\beta}{|(dP/dx)_{gs}|} \qquad (C.3.14)$$

Thus X is the familiar Lockhart-Martinelli parameter, proposed in 1949 for steam/water flow, and used with varying degrees of success for all other types of multiphase flows since then. Y is a measure of the relative sizes of the gravitational forces and the axial pressure drop.

A geometrical analysis reveals that all of the dimensionless variables can be rewritten in terms of $\tilde{h} = h/D$, thus;

$$\tilde{A}_l = 0.25\{\pi - \cos^{-1}(2\tilde{h}-1) + (2\tilde{h}-1)(1-(2\tilde{h}-1)^2)^{1/2}\} \qquad (C.3.15)$$
$$\tilde{A}_g = 0.25(\cos^{-1}(2\tilde{h}-1) - (2\tilde{h}-1)(1-(2\tilde{h}-1)^2)^{1/2})$$
$$\tilde{S}_l = \pi - \cos^{-1}(2\tilde{h}-1)$$
$$\tilde{S}_g = -\cos^{-1}(2\tilde{h}-1)$$
$$\tilde{S}_i = (1-(2\tilde{h}-1)^2)^{1/2}$$
$$\tilde{U}_l = \tilde{A}/\tilde{A}_l$$
$$\tilde{U}_g = \tilde{A}/\tilde{A}_g$$

Thus the coefficients in equation C.3.12 can be calculated in terms of h/D, and thus for a given pair of X and Y, determined by the external system parameters, the equilibrium liquid level (h/D) can be found. This requires a Reynolds number to be calculated for each phase, using the real velocity and the hydraulic diameter (rather than superficial velocity and pipe diameter), to determine whether each flow is laminar or turbulent, and hence the values of n,m and C.

Now that the equilibrium liquid level is known, the next problem is to find what happens when this surface is perturbed, producing some deviation in the liquid level. Several possibilities have been proposed, and are summarised below;

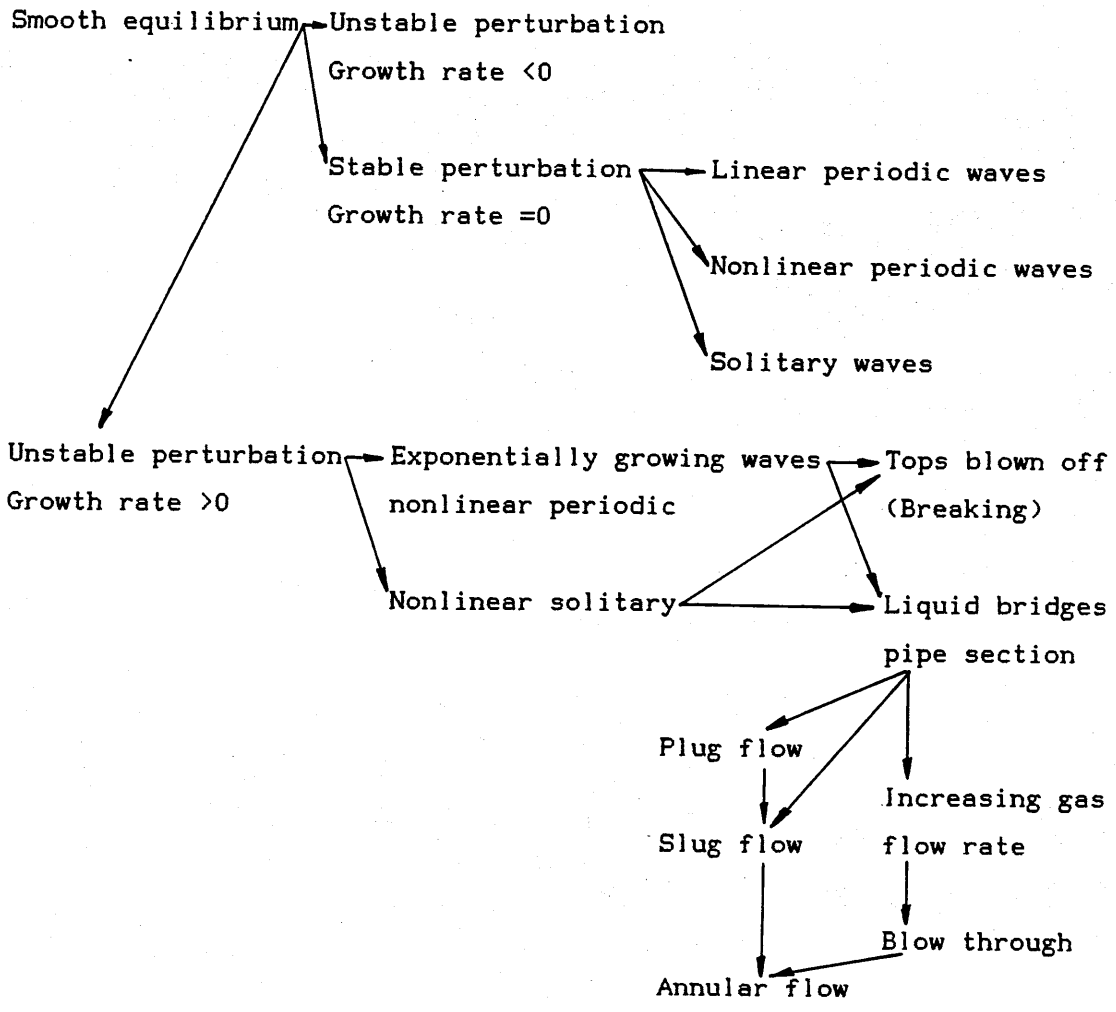

The general approach towards the behaviour of a finite disturbance is via the Kelvin-Helmholtz instability (Chandrasekhar 1961). Here, the wave will grow if;

$$U_g > \left[\frac{g(\rho_l-\rho_g)h_g}{\rho_g}\right]^{1/2} \qquad \text{(C.3.16)}$$

This was originally proposed for large rectangular ducts, where the liquid level is much smaller than the depth of the duct. This has been extended to flows in round pipes (Taitel and Dukler 1976), and leads to;

$$U_g > C_2\left[\frac{(\rho_l-\rho_g)g\cos\beta A_g}{\rho_g(dA_l/dh)}\right]^{1/2} \qquad \text{(C.3.17)}$$

Where;

$$C_2^2 = \frac{(A_g'/A_g)^2}{1+A_g'/A_g} \simeq 1-h/D \qquad (C.3.18)$$

The latter approximation being valid for finite waves when $h/D \geqslant 0.5$, and the primes indicate the values at the disturbance. Reducing these to a dimensionless form leaves the criterion as;

$$F^2\left[\frac{1}{C_2^2}\frac{U_g'^2 dA_1/dh}{A_g}\right] \geqslant 1 \qquad (C.3.19)$$

Where F is the Froude number, modified by the density ratio, thus;

$$F = \left[\frac{\rho_g}{\rho_1-\rho_g}\right]^{1/2} \cdot \frac{U_{gs}}{(Dg\cos\beta)^{1/2}} \qquad (C.3.20)$$

Thus this is the criterion for waves growing out of control, and producing, plug, slug, annular and other intermittent flows. These transitions can be mapped in terms of F versus X or Y, as in line A in figure C.3j, where X has been rewritten in terms of h/D.

It has been observed that for $h/D \leqslant 0.35$, the transition from stratified wavy goes directly to annular mist, and for $h/D \geqslant 0.5$, intermittent flows occur. This criterion is dependent solely on the concepts of conservation of fluid, and so is independent of the other experimental parameters, and leads to the vertical lines shown as b in figure C.3j.

The above two criteria have considered the behaviour of finite disturbances, however, the transition from smooth stratified to a finite disturbance requires the analysis of the behaviour of an infinitessimal disturbance. This transition is not yet understood due to the non-obvious method by which energy is transferred from the gas to the liquid. The following equation was proposed by Jeffries (1925);

$$(U_g-C)^2 C \geqslant \frac{4n_1 g(\rho_1-\rho_g)}{s\rho_g} \qquad (C.3.21)$$

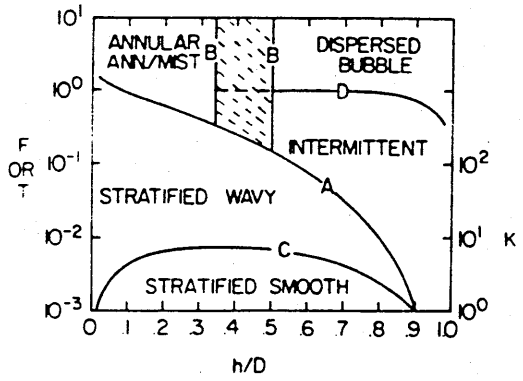

Figure C.3j Theoretical flow map from Taitel and Dukler (1976).

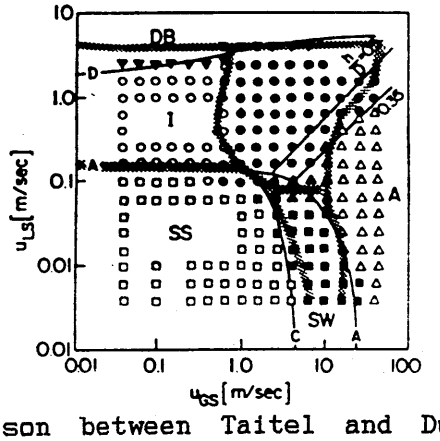

Figure C.3k Comparison between Taitel and Dukler (experiment and theory) and Mandhane (shaded), for a 2.5cm air/water flow (Dukler 1986).

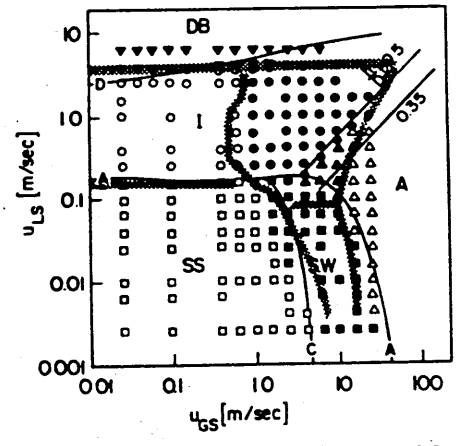

Figure C.3l As above, but for a 5.1cm tube (Dukler 1986).

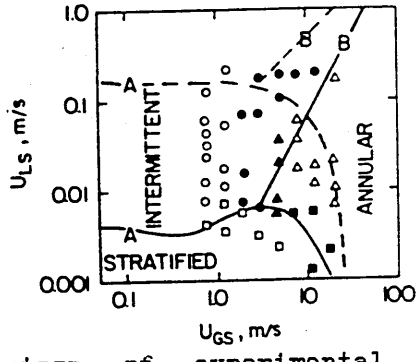

Figure C.3m Comparison of experimental results (3.8cm, 165Cp Glycerine/air) with theory for 165Cp and theory for 1.0Cp liquid (Dukler 1986).

Where C is the wave speed on the interface and s is a sheltering coefficient in the lee of the wave (≈0.01-0.03). Noting that, at the transition, $U_g \gg C$ and $U_l \approx C$, leaves;

$$U_g \geq \left[\frac{4n_l(\rho_l-\rho_g)g\cos\beta}{s\rho_g U_l}\right]^{1/2} \qquad (C.3.22)$$

In dimensionless form, this criterion reduces to;

$$K \geq \frac{2}{\tilde{U}_g \tilde{U}_l^{1/2} s^{1/2}} \qquad (C.3.23)$$

where;

$$K^2 = F^2 Re_{ls} = \frac{\rho_g U_{gs}^2}{(\rho_l-\rho_g)Dg\cos\beta} \cdot \frac{DU_{ls}}{n_l} \qquad (C.3.24)$$

Again, as with the last two transitional criteria, the terms in brackets can be rewritten in terms of h/D. Hence the criterion for the transition fron smooth stratified to stratified wavy is plotted as line C in figure C.3j.

A recent investigation (Jurman 1989), into the transition from smooth stratified to stratified wavy, and the types of waves involved, in a rectangular duct, has shown that the Orr-Sommerfeld wave equation for the surface of the thin film has two singular solutions. These solutions are characteristic of smooth stratified and shock waves. A Hopf bifurcation occurrs in the smooth stratified solution, leading to stable periodic waves (the eigenvalues are purely imaginary), as the lowest linear solution. Other waveforms such as solitary waves also appear as solutions.

An alternative perspective, which has yet to be considered, is to consider the gas forcing its way downwards and displacing the liquid, rather than lifting the liquid. This would lead to an analysis identical with the Rayleigh-Taylor instability, where a denser liquid lies above a less dense liquid and so is inherently unstable.

The final, and probably the most important transition, is where the flow becomes homogeneous. At this point, the turbulent fluctuations in one of the fluids is enough to overcome the buoyancy or gravitational forces in the other. Consider a turbulent liquid entraining a gas. The buoyancy force per unit length of the gas is;

$$F_b = g\cos\beta(\rho_l-\rho_g)A_g \qquad \text{(C.3.25)}$$

The force due to turbulent fluctuations is (Levich 1962);

$$F_t = \tfrac{1}{2}\rho_l\overline{V'^2}s_i \qquad \text{(C.3.26)}$$

Where V' is the radial velocity fluctuation whose rms value is taken to be the friction velocity, thus;

$$\left(\overline{V'^2}\right)^{1/2} = U^* = U_l(f_l/2)^{1/2} \qquad \text{(C.3.27)}$$

Therefore, for $F_t \geqslant F_b$ the criterion becomes;

$$U_l \geqslant \left[\frac{4A_g}{s_i}\,\frac{g\cos\beta}{f_l}\left(1-\frac{\rho_g}{\rho_l}\right)\right]^{1/2} \qquad \text{(C.3.28)}$$

And in dimensionless form, this becomes;

$$T^2 \geqslant \frac{8\tilde{A}_g}{\tilde{s}_i\tilde{U}_l^2(\tilde{U}_l\tilde{D}_l)^{-n}} \qquad \text{(C.3.29)}$$

Where;

$$T = \left[\frac{(4C_l/D)(U_{ls}D/n_l)^{-n}(\rho_l(U_{ls})^2/2)}{(\rho_l-\rho_g)g\cos\beta}\right]^{1/2} = \left[\frac{|(dp/dx)_{ls}|}{(\rho_l-\rho_g)g\cos\beta}\right]^{1/2} \qquad \text{(C.3.30)}$$

Again, this can be rewritten in terms of h/D, and is plotted as line D in figure C.3j. Figures C.3k, l and m show comparisons between the experimental results of Taitel and Dukler (1976), their theory,

outlined above, and the first two also show the results of Mandhane (1974), all with axes of superficial velocity.

Figures C.3n to C.3u show the results of several other authors, Hoogendoorn (1959), Govier et al (1977), Choe (1978) and Weisman (1979), culminating in the very detailed works of Sakaguchi (1979) and Spedding et al (1980). These last two are the most recently published flow regime maps, and give details of intermediate transitions, as well as the basic four described above. It is worthy of note, that these maps contain several boundaries which bifurcate into areas surrounded by quadratic-like curves.

Figure C.3v reproduces the only published flow regime map for oil/water flow in a horizontal pipe. This is from Charles et al. (1961) who used oils with viscosities of 6.29 and 16.8cp and a specific density of 0.988. Experimental data pertaining to liquid/liquid flows is almost non existent. This is surprising, since by varying the density ratio, the effect of gravity can be varied considerably, allowing transitions to occur at lower flow rates.

Vertical fluid/fluid flow has been studied almost as extensively as the horizontal situation, due to its importance in reactor core cooling, and chemical transfer processes. These are usually modelled using unreactive gas/liquid flows, which leads to results that are easier to test experimentally. Flow transitions have been observed in numerical models of periodically forced heat exchanger tubes (Rizwan-Uddin 1988), but this is beyond the unreactive and simple flows under review here. Figure C.3w shows the Hewitt-Roberts map (1969) for vertically upwards two phase flow. Figures C.3x and y show Spedding and Nguyens' data (1980) for verically upwards and vertically downwards flow.

All of these maps consider cocurrent flow, ie the liquid and gas going in the same direction. However, there is the possibility of countercurrent flows. In the horizontal case, this is fairly trivial, since only smooth stratified and stable waveforms can exist within the pipe. Any liquid bridges lead to a violation of the countercurrent definition and catastrophic pressure surges. In a vertical pipe, where

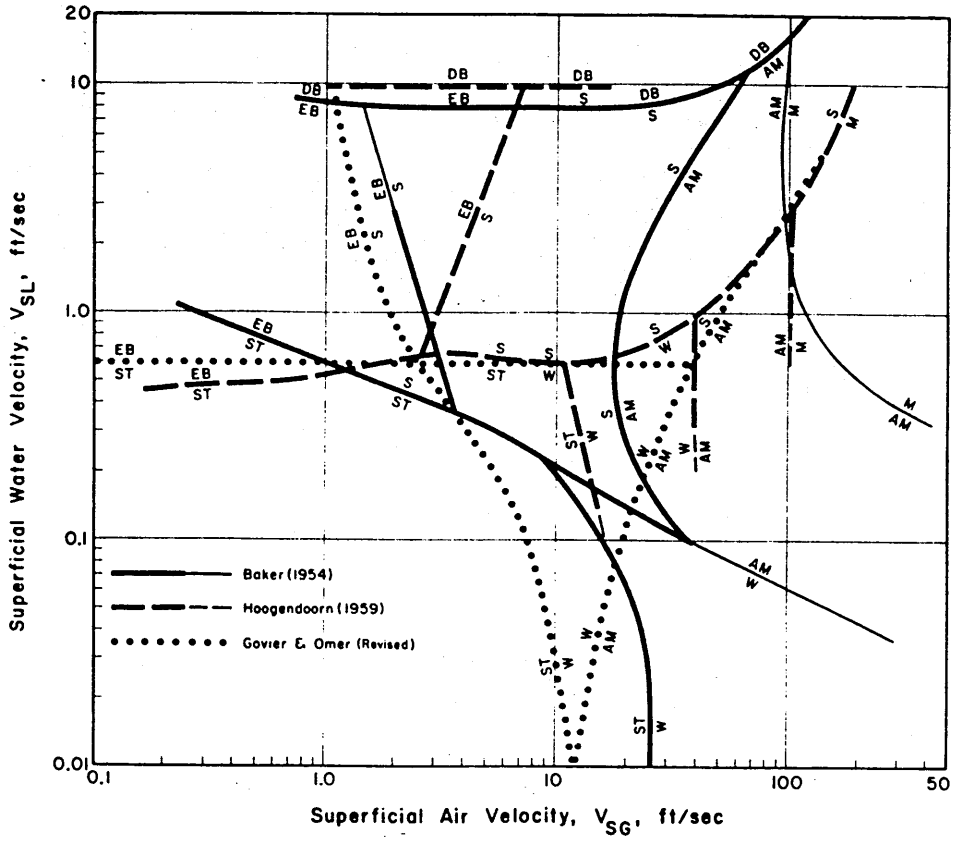

Figure C.3n Flow map comparisons between Baker (1954), Hoogendoorn (1959) and Govier and Omer (revised by Govier and Aziz 1977).

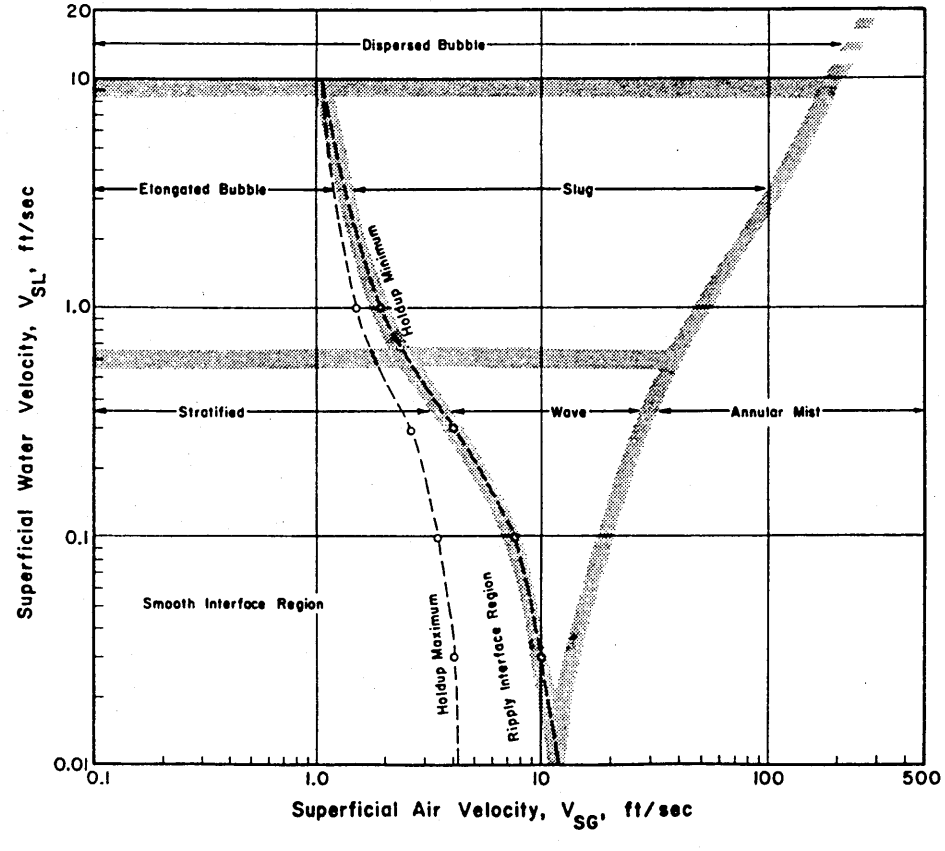

Figure C.3o The revised Govier Omer map (1977).

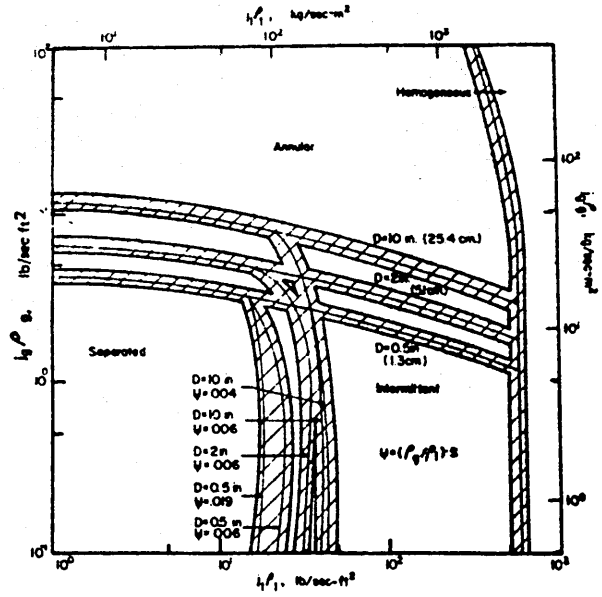

Figure C.3p A superposition of experimental transitions by Choe (1978), limited to 1" pipes, but good for most combinations of fluids.

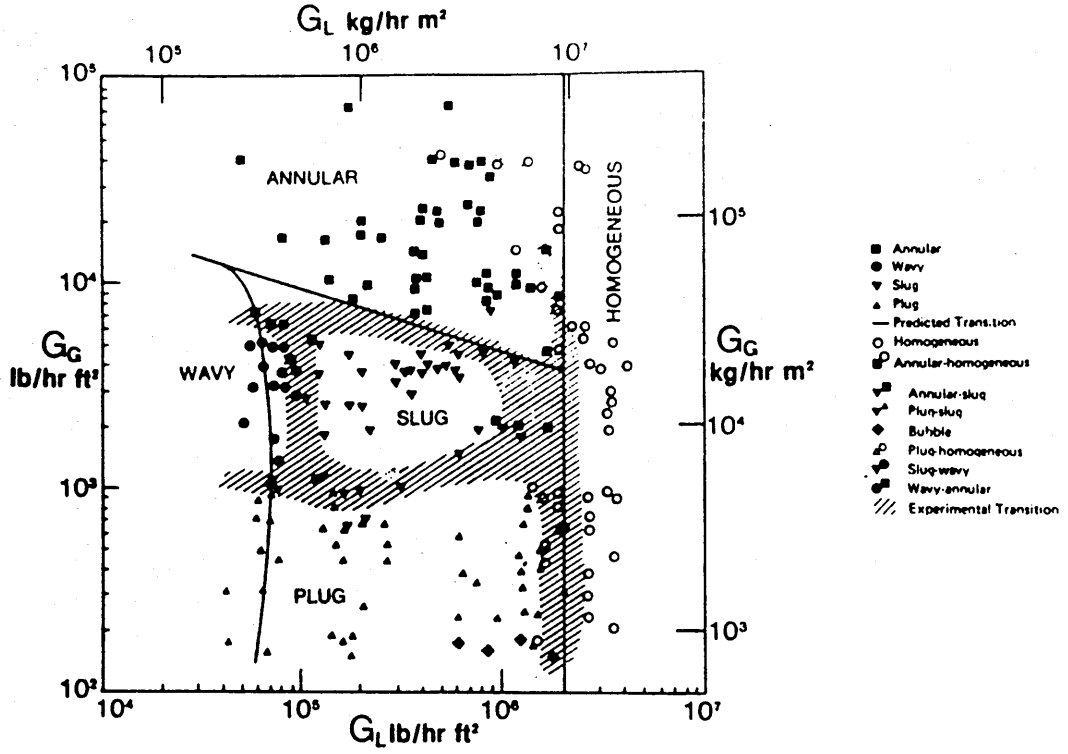

Figure C.3q Flow patterns observed at the end of a 1.2cm diameter tube by Weisman (1979).

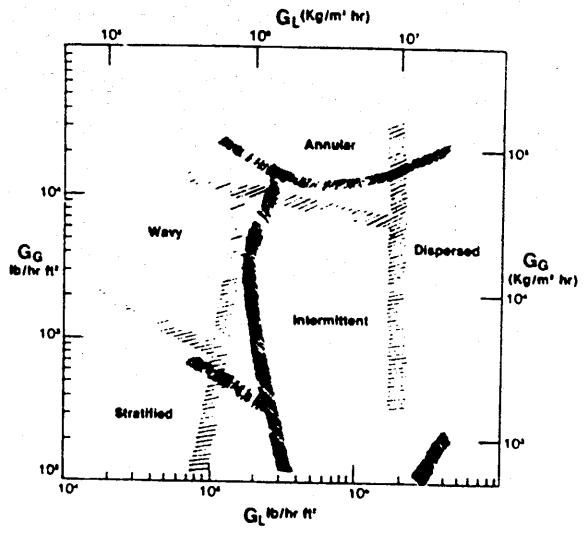

Figure C.3r Comparison of transitions in 2.54cm and 12.7cm air/water flows from Weisman (1979).

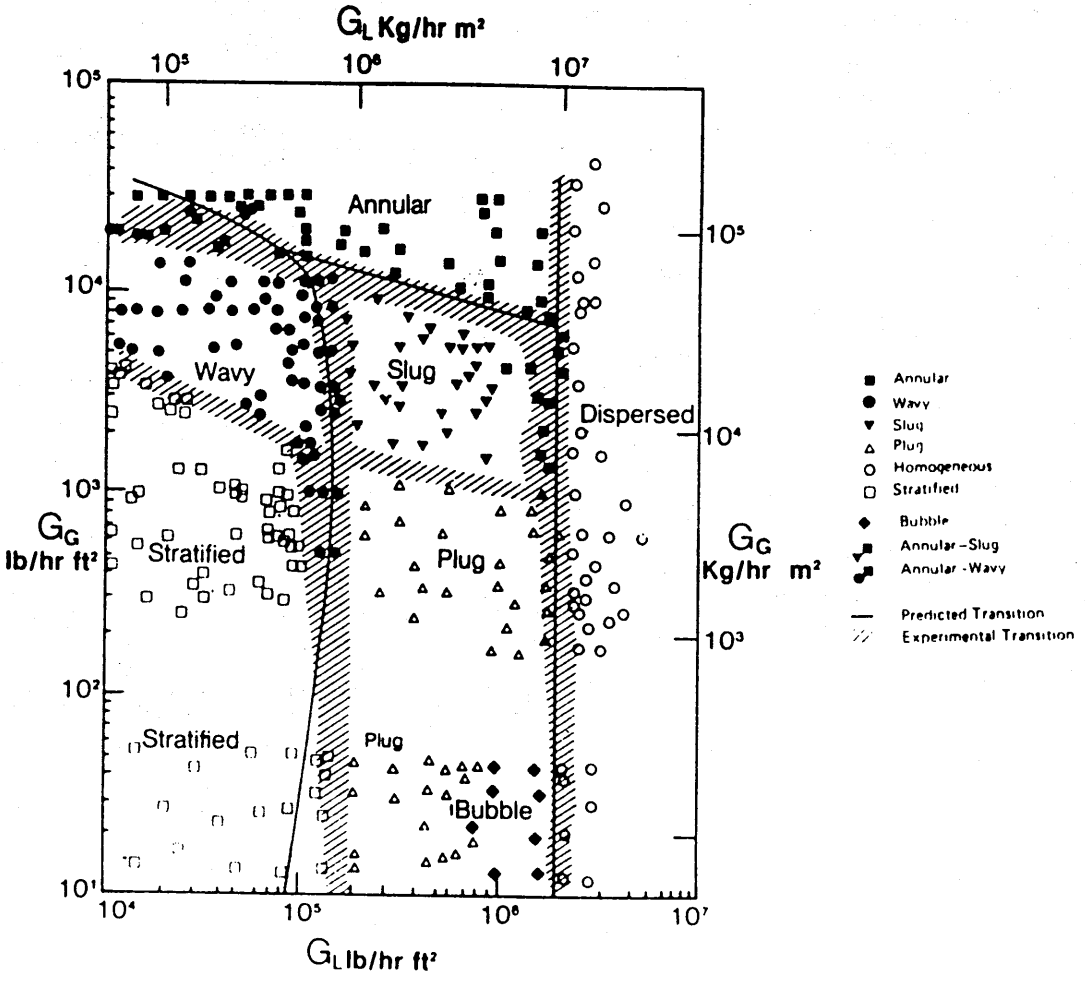

Figure C.3s Comparison of experiment and theory at the end of a 5.1cm air/water pipe from Weisman (1979).

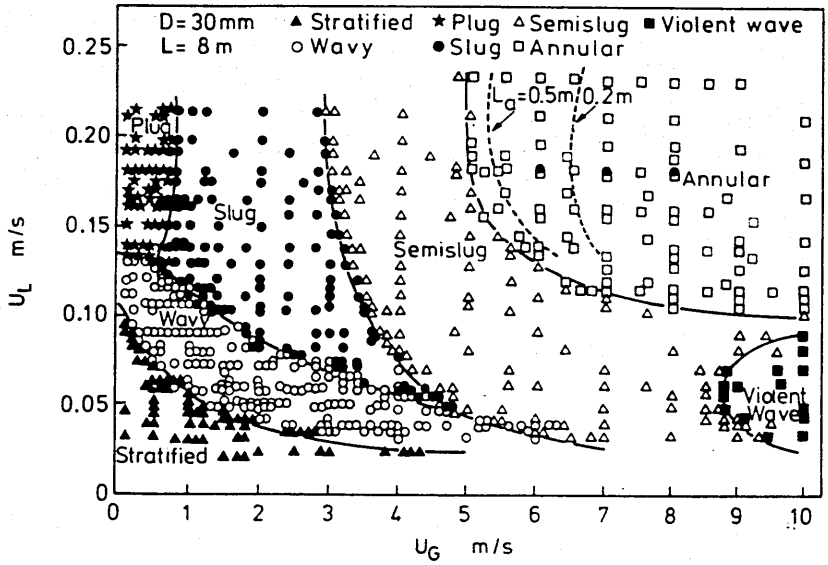

Figure C.3t Flow regime map by Sakaguchi (1979) for 30mm air/water flows. Note the unusual orientation of the axes, and La is the pipe length required for fully developed annular flow.

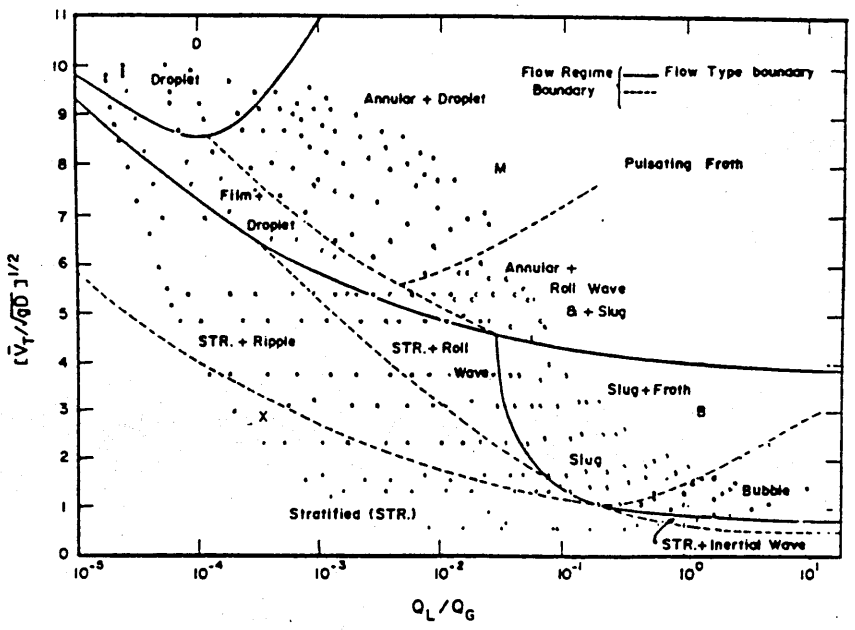

Figure C.3u Flow regime map by Spedding and Nguyen for 4.55cm air/water flows (1980).

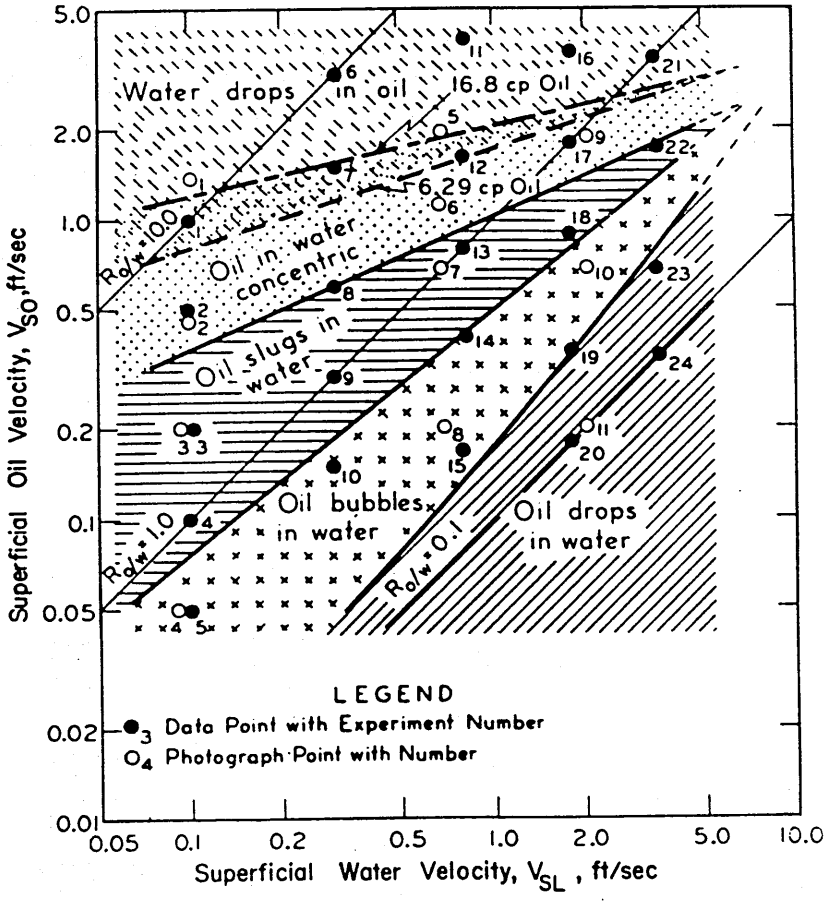

Figure C.3v Flow regime map for oil/water flow in a horizontal pipe (Charles et al. 1961)

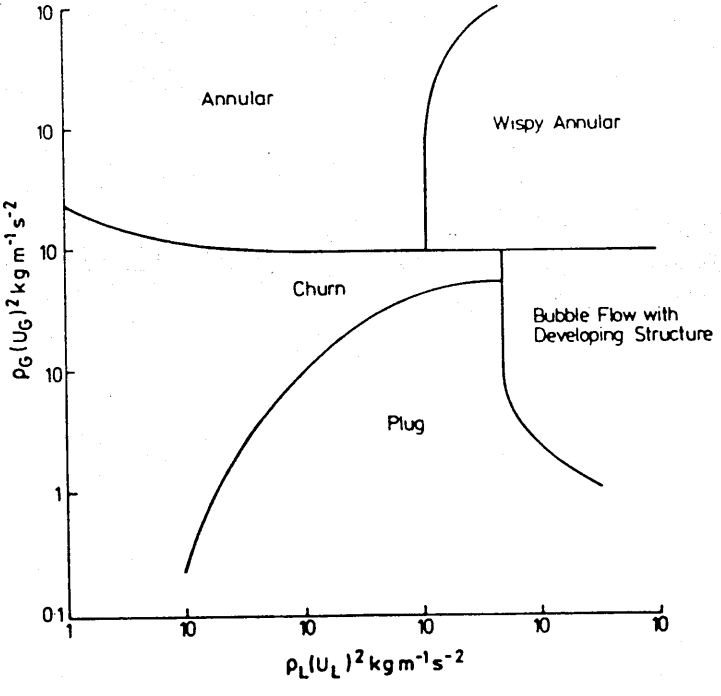

Figure C.3w The Hewitt-Roberts map for vertically upwards gas liquid flow (1969).

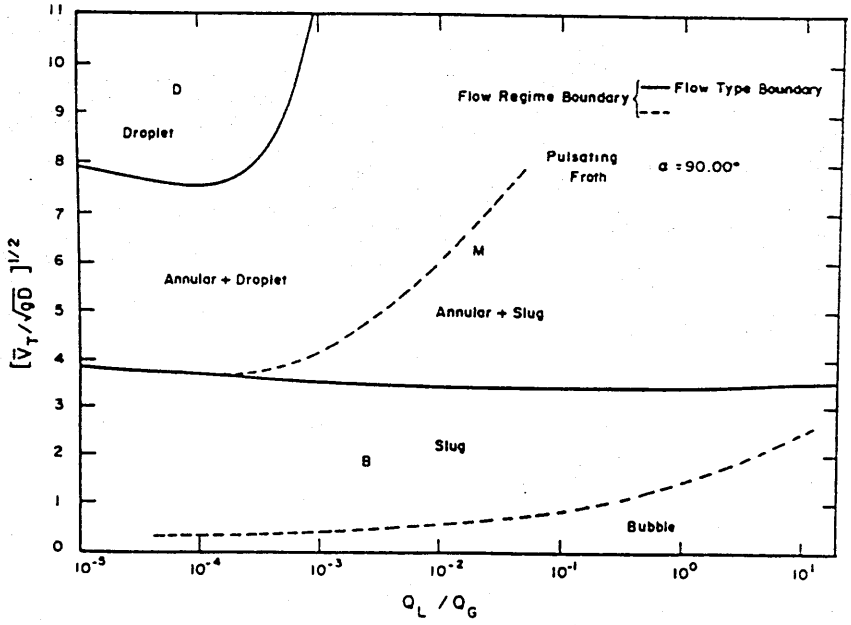

Figure C.3x Spedding and Nguyen's map for vertically upwards gas/liquid flow (1980).

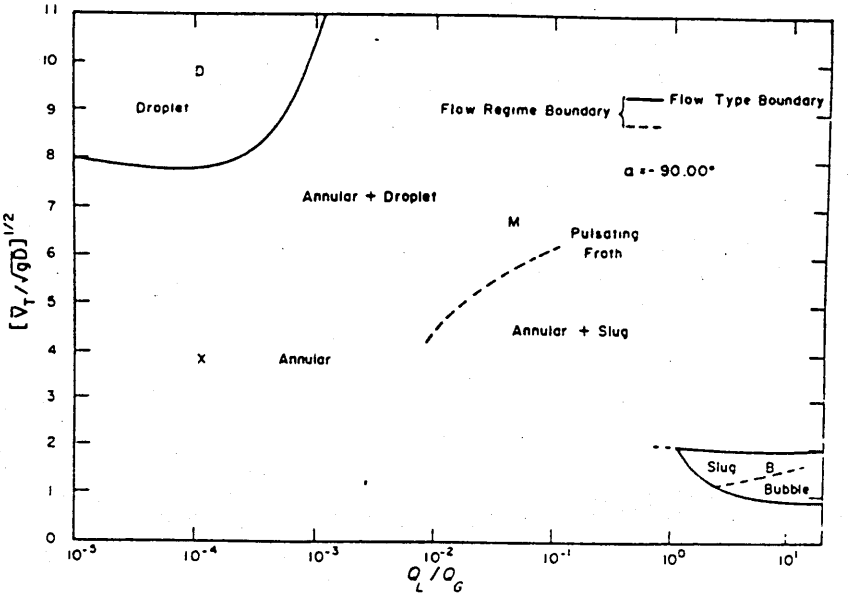

Figure C.3y Spedding and Nguyen's map for vertically downwards gas/liquid flow (1980).

gravity doesn't provide a symmetry to be broken, flow regimes such as droplet, annular, mist etc, can exist in the counter current system.

For example the transition between countercurrent and cocurrent, known as flooding, the liquid flow rate must be zero, and the liquid is suspended in the pipe against gravity, by the friction forces of the gas. This provides a very well defined transition which will reappear in appendix D.

All of the above flow regime maps have been determined primarily by visual observation. Several of the transitions can be picked up using experimental techniques which determine some structural parameter which is characteristic of the distribution of the materials in the flow.

These include;

- Visual observation
- Photography - high speed phenomenae
- X-ray photography - opaque liquids/tubes
- Optical methods - refraction, scattering, absorption
- Photon attenuation - Single or multibeam X-ray and γ-ray
- Hot film anemometry
- Electrical conductance
- Electrical capacitance
- Pressure or pressure drop fluctuations
- Wall shear stress fluctuations

The results of these experiments could be analysed using either a non-parametric approach or a parametric approach. The first involves the usual statistical analysis in the amplitude, time and frequency domains, leading to characteristic distribution and correlation functions. Stochastic discriminants (such as moments of different orders) or shape comparisons could then be used. The parametric approach requires a semi-empirical model to be generated in terms of power series, based on the time series. The implementation of these techniques has been reviewed by Drahos (1989).

C.4 Discussion and Conclusions.

As yet, there is no method of solving the Navier-Stokes equations for an arbitrary fluid flow (including fluid/fluid flows), and no unified approach to predicting, even semi-empirically, the transition boundaries within these flows. "There is a need for objective and reliable diagnostic criteria, since confidence in the flow pattern maps, used in design and operation, is limited" (Drahos 1989).

Returning to the flow maps, consider a flow map in X_1-X_2 parameter space, and let the inlet conditions be known to be x_1,x_2. These coordinates will define a point on the map, however, at a given point in the pipe, the parameters may not be x_1,x_2 and this point is merely the geometric center of the mean of all the trajectories of all the points within the pipe. At any instant, the system will be at a point somewhere else in the parameter space. The idea of parameter or phase space will be expanded in appendix D.

This appendix has reviewed a fairly representative sample of the published literature in the fields of multiphase and multicomponent flows. It is clear that there is a need for an improved understanding of this field, starting at a more fundamental level, rather than extending the semi-empirical results published to date.

Appendix D: Chaos In Fluid Flows.

D.1 Introduction

The following sections constitute an introduction to chaotic phenomenae, with the final aim of developing a new model for the flow of multiphase and multicomponent mixtures in pipelines. Because of the universality and diversity of chaotic phenomenae, the number of publications in this area has been increasing exponentially over the last few years, under many varied subject titles. It is not the aim of this work to cover the subject as a whole, space will not permit an undertaking of that magnitude, but to take a very specific line through the literature, drawing only on those works which appear necessary for the argument. This enables the work to remain of a readable length, but also means that some important concepts may have been overlooked. Where this becomes apparent, the reader will be referred to the appropriate literature.

The work begins in section D.2 with the logistic equation for population growth, and other phenomena, and a simple modification to the equation, which produces several interesting results. This leads to very explicit definitions of what will be understood by the terms deterministic, chaotic and random, in the ensuing sections.

Section D.3 begins with a description of 2-Dimensional free (Bénard) convection and the extensively studied Lorenz equations. These differential equations are studied numerically using a simple difference method, and the basic principles for extending this method in order to study other systems of more general differential equations are described. This leads to the concept of attractors.

Section D.4 studies attractors in more depth, with a rigorous definition of dimensionality, embedding dimensions, Hausdorff (fractal) dimensions, Poincaré sections, Hénon mapping, and the physical meaning of Liapunov exponents. Methods for determining these factors are described in section D.5, with especial reference to the

Grassberger-Procaccia method. The effects of numerical, digital, random and systematic noise are also outlined.

Section D.6 brings all of this information together and shows how the basic principles can been seen to be applicable to fluid flows and flow transitions. Outlines of possible experimental procedures that can be used to verify these conclusions are given and compared with current trends in experimental and theoretical work. Applications include the primary transition to turbulence in single phase flows, in (i) cylindrical Taylor-Couette flow, (ii) spherical Taylor-Couette flow, (iii) flow in curved ducts and (iv) flow in straight pipes.

Section D.7 extends the concepts to multiphase and multicomponent flows. The few pulished applications of chaos in multiphase flows are reviewed including core/annular flow instabilities, the flooding transition (air/water), horizontal gas/solids flows and coolant (periodic forced) flow in reactor cores. This leads to the conclusion that a given flow situation will have a characteristic Hausdorff dimension, which will remain finite for all experimentally realisable situations, the accuracy being limited by the resolution of the measuring technique and the scale of the smallest significant event in the system.

Section D.8 then brings all of the preceding sections together, providing a suitable starting point for the material appearing in chapter 6.

D.2 The Logistic Difference Equation.

As yet there are no satisfactory approaches to the problem of the transition between laminar flow and turbulence in hydrodynamical systems. The usual technique is to ensure that the system is either laminar or fully developed turbulent. The first is accurately modelled using simple potential theory and the second succumbs to statistical methods. In order to model the transition between laminar and turbulent, it is necessary to study other systems which show this type of transition, investigate the transition region, generalise the

methods (if possible) and then apply them to the hydrodynamical systems. the simplest system displaying such a transition is the logistic difference equation, which has been used by biologists to model population dynamics for over 50 years, though the full structure and significance of the equations has only been realised in the last two decades.

Consider the nth generation of a colony of animals, with a population x_n. The next generation will have a population that is a simple function of x_n, in general the equation will have the form;

$$x_{n+1} = R(x_n) \qquad (D.2.1)$$

If there are no controlling factors, for example rabbits in Australia in the 19th century, the equation takes the form;

$$x_{n+1} = rx_n \qquad (D.2.2)$$

This implies, unrealistically, that each generation breeds once and then dies. Thus for $r>1$, the population grows exponentially, and if $r<1$, the population dies out, and the population is only stable for $r=1$.

However, real populations are governed by more than the single reproductivity parameter, r. Other factors such as food supply, overcrowding or predator-prey interactions are of importance. For the single generation problem, the other factors can only enter in the following form;

$$x_{n+1} = rx_n - \sum_{m=2}^{\infty} s_m x_n^m \qquad (D.2.3)$$

Truncating thes feedback factors down to the first term, and with appropriate scaling, this reduces to the logistic difference equation;

$$x_{n+1} = rx_n(1-x_n) \qquad (D.2.4)$$

This equation has been extensively studied (Kadanoff 1985, Doherty 1988), and the results can be summarised as follows (figures D.2a and a'). For $0<r<1$, the population is unstable and $x_\omega \to 0$ for all x_0. For $1<r<3$, the population has two stable values, the trivial extinction, and the value $1-1/r=X_0$, the latter case occurring for all $x_0 \neq 0$. For $3<r<3.44$, x_n oscillates between two fixed values, X_1 and X_2, with X_0 being an unstable fixed point. When $r=3.44$, each of these stable fixed points period doubles to produce a stable 4-cycle, with stable points X_3-X_6, with X_0,X_1 and X_2 behaving as unstable fixed points between these. As r is increased further, the period doubling cascade continues, tending to the geometric series in r;

$r_0(=1) \to 2^0$,

$r_1(=3) \to 2^1$,

$r_2(=3.44) \to 2^2$,

$r_3(=3.545) \to 2^3$,

$r_4(=3.565) \to 2^4$,

$r_n \to 2^n$

$r_{n+1} \to 2^{n+1}$

$r_\omega(=3.5699) \to 2^\omega$

Where the higher order terms tend to the geometric series as follows;

$$\frac{r_n - r_{n-1}}{r_{n+1} - r_n} \to \delta_n = 4.6692016..... \qquad (D.2.5)$$

The constant δ_n is known as the Fiegenbaum universal constant (Fiegenbaum 1978), as it has been found (and shown) to be a characteristic of every iterative system containing a quadratic term. It should be noted that each successive iteration (generation) lies on opposite sides of the X_0 line. Thus a high order 2^n-cycle has a large scale structure, though the individual steps may appear random, depending on how many generations are observed.

At $r_\omega(=3.5699)$, the period of the cycle is infinite, thus making the motion appear totally chaotic. For $3.5699<r<4$, the totally chaotic

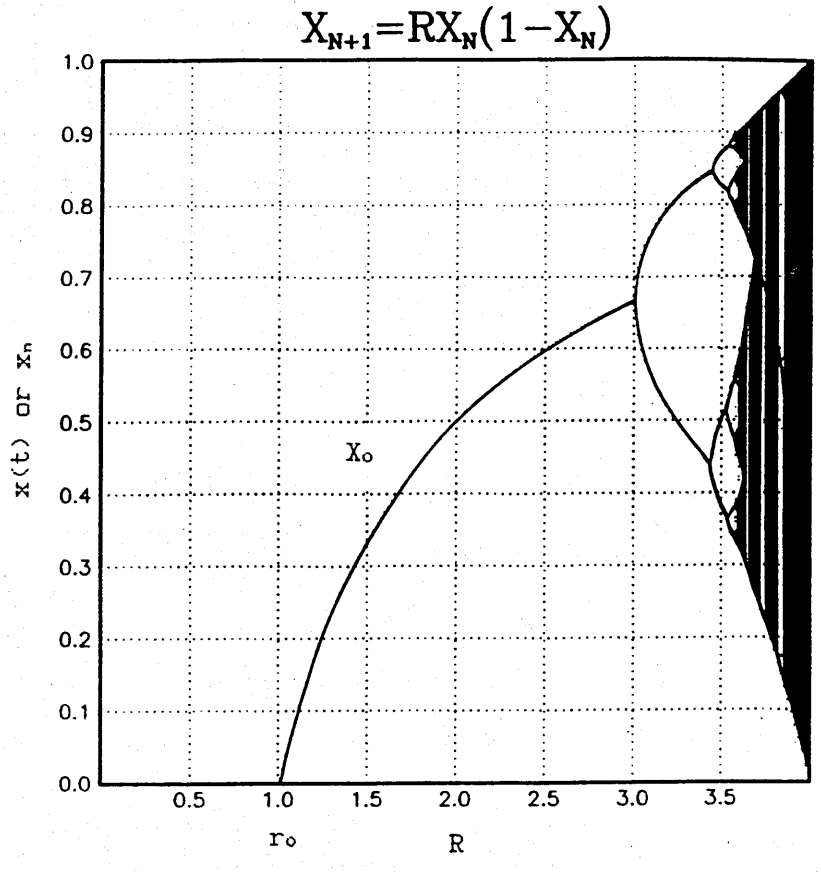

Figure D.2a Population dynamics in the normalised logistic equation.

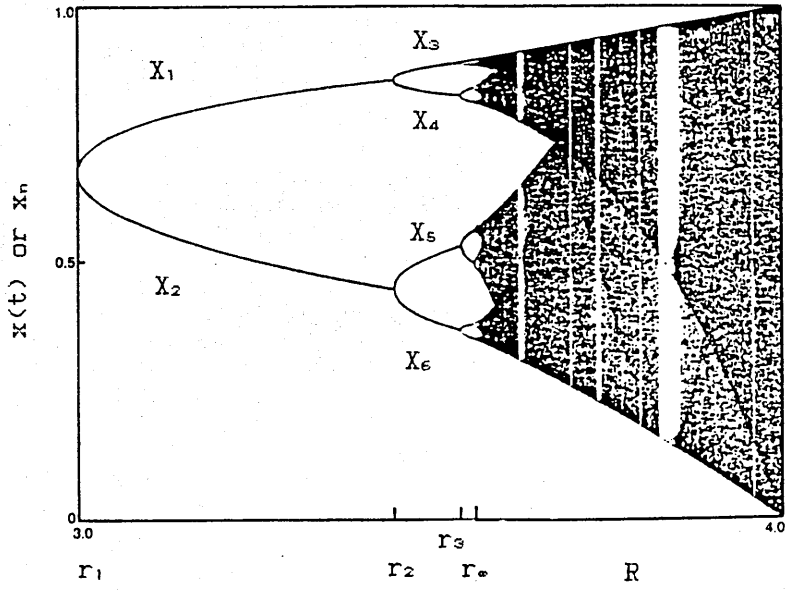

Figure D.2a' An enlarged version of the chaotic region showing some of the fine structure.

behaviour is interrupted for bands of r, within which, a period $k2^n$ cascade appears, where k is any positive integer. Within these windows there are also random outbreaks of chaotic motion, and thus the time series never repeats itself. Thus for $r<3.5699$, the system is totally deterministic, since x_{n+1} can be found to an infinite number of decimal places, even from a less than perfect value of x_0, provided the transients caused by the error in x_n are allowed to die down. For $r>3.5699$, if x_0 has a truncation error ε, the nth iteration has an error of $2^n\varepsilon$, and so when, $x_n + 2^n\varepsilon > x_0$, all correlation between x_n and x_0 is lost, and so the system can be considered random. A correlation function can be defined as;

$$c(\tau) = \lim_{\tau\to\infty} 1/\tau \int_0^{\tau} x'(t)x'(t+\tau)dt \qquad (D.2.6)$$

where;

$$x'(t) = x(t) - \lim_{\tau\to\infty} \int_0^{\tau} x(t)dt \qquad (D.2.7)$$

The system is considered to be chaotic if $c(\tau)\to 0$ as $\tau\to\infty$. The above derivation was originally carried out for r=4. At this point, an exact solution for x_n has been found (Kadanoff 1983), and the error analysis is a direct result of binary number theory and is also known as the Bernoulli shift. The analysis is applicable (in principle) to any chaotic system, and leads to the conclusion, that a chaotic system has a sensitive dependance on the initial conditions.

An alternative method of analysing the behaviour of the system is to consider the power spectrum of x. The discrete Fourier transform is defined as;

$$x(\omega_k) = \frac{1}{N^{1/2}} \sum_{n=1}^{N} (x_n - \langle x\rangle) e^{i\omega_k n} \qquad \text{where;} \qquad \omega_k = \frac{2\pi k}{N} \qquad (D.2.8)$$

and the power spectrum is a plot of $|x(\omega_k)|^2$ versus ω_k. If the population is known to be normalised ($0<x<1$), then this can be simplified to;

$$P(\omega) = \frac{1}{N}\left|\sum_{n=1}^{N} x_n e^{2\pi i \omega}\right|^2 \qquad (D.2.9)$$

For time independent signals, the power spectrum is a spike at zero frequency. In time-periodic signals, spikes appear at the frequency of oscillation and its harmonics. The harmonics are integer multiples of the fundamental frequency and appear due to the finite period of the observations or due to the discrete nature of the data. With the period doubling cascades, more spikes appear in the gaps, and eventually form a continuous background, which then swamps the primary signals (see figure D.2b).

It has been recently proposed (Morimoto 1989) that equation D.2.3 may be further modified to include other iterations (generations), of the following general form;

$$x_{n+1} = rx_n - \sum_{m=2}^{\infty} s_m x_n^m - x_n \sum_{l=1}^{\infty} p_l x_{n-l} \qquad (D.2.10)$$

Truncating each series to the first term and scaling appropriately, leaves;

$$x_{n+1} = Ax_n (1 - x_n - Bx_{n-1}) \qquad (D.2.11)$$

This equation was originally proposed as a possible model for the behaviour of a biological nervous circuit, where the chemical feedback controlling the impulses, takes longer than a single refractory (iterative) period to become ineffective. However it can be seen to be equally applicable to population dynamics where there are multiple generation interactions. In the biological sense, the value of B must be limited to, $0 \leqslant B \leqslant 1$, and clearly when $B=0$ equation D.2.11 reduces to D.2.4. Mathematically a finite solution can be obtained for $-1 \leqslant B \leqslant 4.26$.

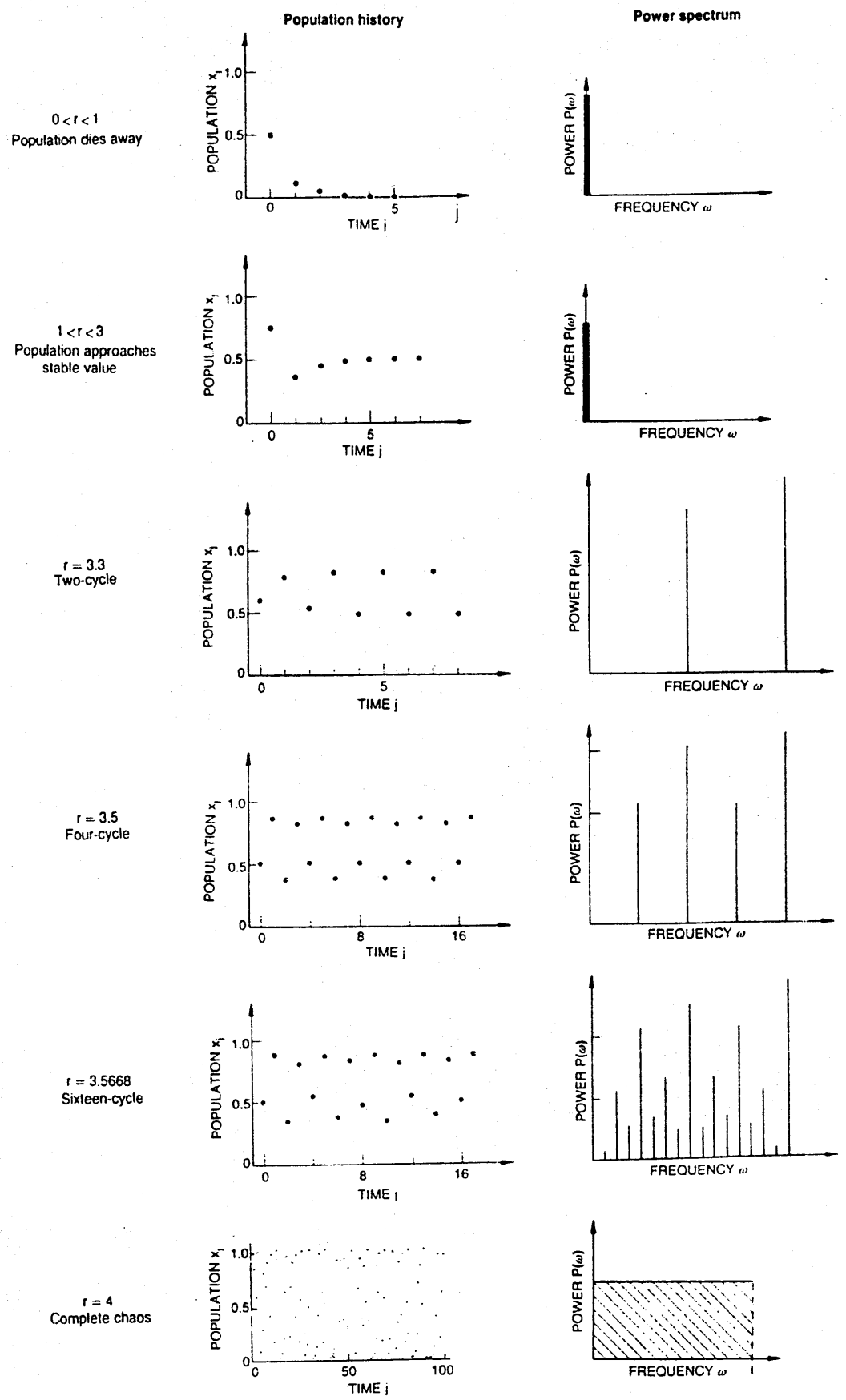

Figure D.2b Population histories and power spectra for various values of r discussed in the text (Kadanoff 1983).

Figure D.2c shows the variations of the bifurcation diagram (in A,x(t) space) as the value of B is varied. Note that the axes have been aligned such that the scales are uniform. When B changes slightly from 0, a pattern similar to the logistic (B=0) model is maintained, with some of the complex bifurcation pattern being suppressed. For B>0.1 only a periodic 2^1 or 2^2 pattern is left. In the region 0.15<B<0.21, a 3-cycle point suddenly appears. This 3-cycle point continues for 0.21<B<0.52 but also includes large areas of instability. This then jumps to a 4-cycle point at B=0.52, and shortly afterwards, an oscillatory section (following a Hopf bifurcation (Hopf 1949)) appears. These patterns are summarised in the form of a phase diagram in the A,B plane in figure D.2d.

D.3 The Lorenz Equations.

Before going into the details of the Rayleigh-Bénard problem and the Lorenz equations, it will prove useful to briefly introduce the idea of 'degrees of freedom' in a dynamical system. For a simple dynamical system that can be described by a single ordinary differential equation, there is only one possible solution to each possible set of initial criteria, ie the system is determinate and has one degree of freedom. If there are two possible solutions, this means two degrees of freedom and two ordinary differential equations are required to fully describe the system.

For a system whose number of degrees of freedom can be increased by changing an external parameter, a knowledge of the number of degrees of freedom of the system will be a useful parameter in characterising that system.

Clearly, if a hydrodynamic system is considered to be a continuum (Swinney 1983), each infinitessimal piece of space could have at least 6 degrees of freedom (3 position, 3 velocity, angular momentum vectors, potential etc), leading to an infinite number of degrees of freedom. Laminar flow can be considered to be a basic single body problem and thus be one dimensional. A simple derivation for the

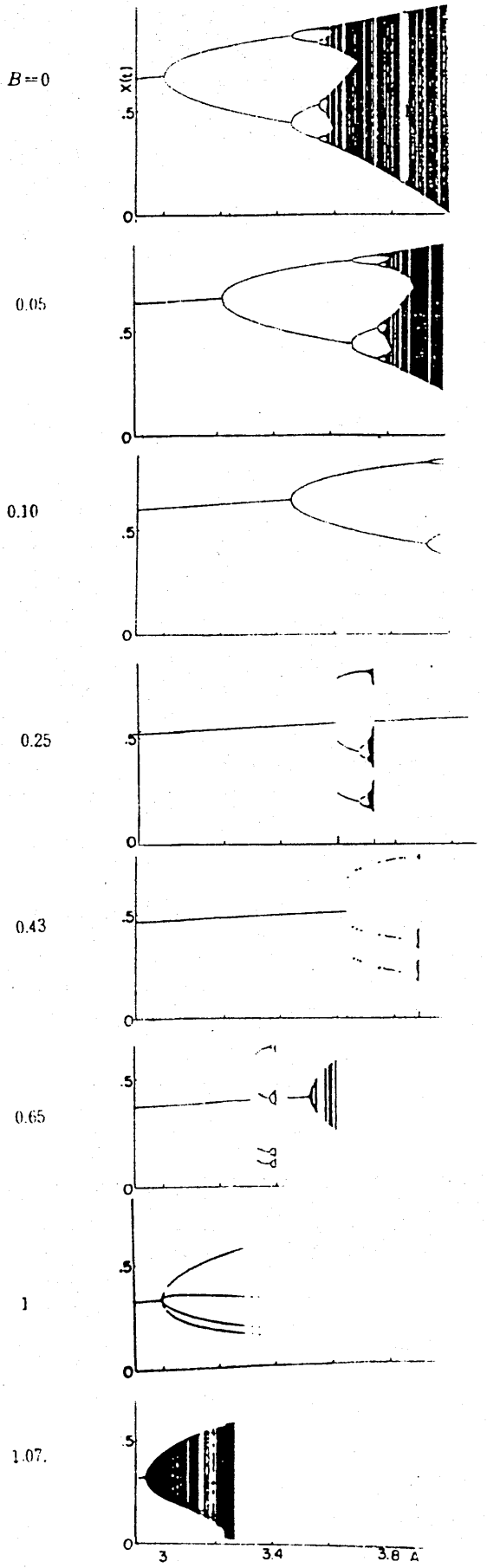

Figure D.2c Variations of the population dynamics for various values of the feedback factor B, in the modified logistic equation (Morimoto 1989).

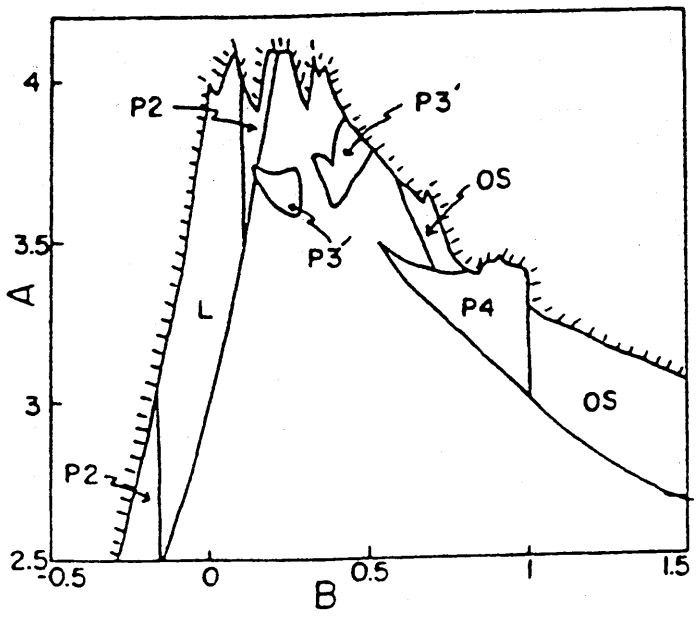

Figure D.2d Phase diagram in A,B space describing the type of population behaviour (Morimoto 1989).

Key; Shaded area - no convergent solution
Unmarked - fixed point only
L - logistic type behaviour
P2 - 2^1 or 2^2 limit cycles
P3 - 3-cycle
P3' - 3-cycle with instabilities
P4 - 4-cycle
OS - oscillating

number of degrees of freedom of a hydrodynamic flow (Landau 1959) gives;

$$N \simeq (R/R_c)^{9/4} \qquad (D.3.1)$$

Where R (= ρvl/n) is the Reynolds number, and v and l are taken to be those values which are characteristic of the 'whole' system. R_c is the critical Reynolds number, at which the first deviation from the classic laminar solution becomes a stable feature of the flow. Thus, just beyond the onset of this new type of flow, the number of degrees of freedom remains small, and hence the current interest in the structure of turbulent flows. Some authors (Newell 1988) have taken $N \simeq R^{9/4}$, which means that even laminar flows have a high dimensionality. A full derivation of D.3.1, along with a description of the classical view of turbulence, will be given in section D.6.

In a Raleigh-Bénard system, a fluid is contained between parallel plates, which is heated from below. The behaviour is usually studied (Swinney 1983) as a function of the Rayleigh number;

$$Ra = \frac{g\alpha d^3.\Delta T}{kn} \qquad (D.3.2)$$

Where g is the gravitational acceleration, α the thermal expansion coefficient (assumed positive), d the separation between the plates,, k the thermal diffusivity and n the kinematic viscosity. Other control variables are the Prandtl number, P = n/k, the aspect ratios $\Gamma_1 = l_1/d$ and $\Gamma_2 = l_2/d$ and the boundary conditions at the sidewalls.

A primary example of a Rayleigh-Bénard (Bénard 1900) system is the motion of the atmosphere, which is generally caused by convective forces, derived from solar heating. For low heating rates, the thermal conductivity of the atmosphere can maintain a stable equilibrium. However, as the heating rate is increased, above a certain critical value of Ra, convection sets in at various scales, depending on the other experimental criteria. The convective transport of heat and momentum are the cause of the essentially non-linear behaviour of the atmosphere.

Before considering such a complicated real system it will be useful to consider the pioneering work in this area (Saltzman 1960 and Lorenz 1961). The equations that are commonly referred to as the Lorenz equations can be derived as follows, using the same notation as the original papers, where;

x,y = horizontal coordinates
z = vertical coordinate
t = time
$u = dx/dt$
$v = dy/dt$
$w = dz/dt$
ρ = density
p = pressure
T = temperature
μ = kinematic viscosity
k = coefficient of thermal diffusivity
g = acceleration due to gravity
ε = coefficient of volume expansion
H = height of fluid
$\langle f \rangle$ = average of f over a horizontal plane
$f' = f - \langle f \rangle$
$(f)_{av}$ = average of f over the entire field
$f_1 = f - (f)_{av}$
f_0 = initial value of f
$p_{h0} = g(\rho)_{av}(z-H)$
$P = (p - p_{h0})/(\rho)_{av}$

The full equations of motion (Navier-Stokes, continuity etc) governing the motion of the convection can be reduced (Oberbeck 1879 and Boussinesq 1903) to the following;

$$\frac{du}{dt} + \frac{\delta P}{\delta x} - \mu \nabla^2 u = 0 \qquad \text{(D.3.4)}$$

$$\frac{dv}{dt} + \frac{\delta P}{\delta y} - \mu \nabla^2 u = 0 \qquad \text{(D.3.5)}$$

$$\frac{dw}{dt} + \frac{\delta P}{\delta z} - g\varepsilon T_1 - \mu \nabla^2 w = 0 \qquad \text{(D.3.6)}$$

$$\frac{dT_1}{dt} - k \nabla^2 T_1 = 0 \qquad \text{(D.3.7)}$$

$$\frac{\delta u}{\delta x} + \frac{\delta v}{\delta y} + \frac{\delta w}{\delta z} = 0 \qquad \text{(D.3.8)}$$

Also it is taken that;

$$\rho = (\rho)_{av}/(1 + \varepsilon T_1) \qquad \text{(D.3.9)}$$

The temperature gradient $\Delta T_0 = \langle T_0(0) \rangle - \langle T_0(H) \rangle$ is kept constant and both the upper and lower boundaries are considered to be rigid. If the motion is restrained to be in the x-z plane only, ie v=0, $\delta/\delta y$=0, then the governing equations are further reduced;

$$\frac{\delta u}{\delta t} + u\frac{\delta u}{\delta x} + w\frac{\delta u}{\delta z} + \frac{\delta P}{\delta x} - \mu \nabla^2 u = 0 \qquad \text{(D.3.10)}$$

$$\frac{\delta w}{\delta t} + u\frac{\delta w}{\delta x} + w\frac{\delta w}{\delta z} + \frac{\delta P}{\delta z} - g\varepsilon T_1 - \mu \nabla^2 w = 0 \qquad \text{(D.3.11)}$$

$$\frac{\delta T_1}{\delta t} + u\frac{\delta T_1}{\delta x} + w\frac{\delta T_1}{\delta z} - k \nabla^2 T_1 = 0 \qquad \text{(D.3.12)}$$

$$\frac{\delta u}{\delta x} + \frac{\delta w}{\delta z} = 0 \qquad \text{(D.3.13)}$$

Using (D.3.10) a stream function ψ can be defined as follows;

$$u = -\frac{\delta \psi}{\delta z}, \quad w = \frac{\delta \psi}{\delta x} \qquad \text{(D.3.14)}$$

$T_1'(x,z,t)$ and $\langle T_1''(x,z,t) \rangle$ are defined as follows;

$$T_1(x,z,t) = \langle T_1(z,t) \rangle + T_1'(x,z,t) \qquad \text{(D.3.15)}$$

$$\langle T_1(z,t)\rangle = \langle T_1(0,t)\rangle - \Delta T_0 z/H + \langle T_1''(z,t)\rangle \qquad \text{(D.3.16)}$$

The first equation gives the temperature with respect to the average in that plane and the second gives the average value of T_1 with respect to a hypothetical linear variation in temperature between the upper and lower boundary layers.

Substituting (D.3.16) into (D.3.15) leaves;

$$T_1(x,z,t) = \langle T_1(0,t)\rangle - \Delta T_0 z/H + \theta \qquad \text{(D.3.17)}$$

Where;

$$\theta = \langle T_1''(z,t)\rangle + T_1'(x,z,t) \qquad \text{(D.3.18)}$$

Eliminating P from (D.3.11) and (D.3.10) by reducing them to terms in $del^2\psi$ ($= \delta u/\delta z - \delta w/\delta x$) and introducing (D.3.14) and (D.3.18) produces the equations that govern the model;

$$\frac{\delta}{\delta t}\nabla^2\psi - \frac{\delta\psi\delta}{\delta z\delta x}\nabla^2\psi + \frac{\delta\psi\delta}{\delta x\delta z}\nabla^2\psi - g\varepsilon\frac{\delta\theta}{\delta x} - \mu\nabla^4\psi = 0 \qquad \text{(D.3.19)}$$

$$\frac{\delta\theta}{\delta t} - \frac{\delta\psi\delta\theta}{\delta z\delta x} + \frac{\delta\psi\delta\theta}{\delta x\delta z} - \frac{\Delta T_0\delta\psi}{H\,\delta x} - k\nabla^2\theta = 0 \qquad \text{(D.3.20)}$$

These can be further simplified by resorting to Jacobian operator notation, as follows;

$$\frac{\delta}{\delta t}\nabla^2\psi + \frac{\delta(\psi,\nabla^2\psi)}{\delta(x,z)} - g\varepsilon\frac{\delta\theta}{\delta x} - \mu\nabla^4\psi = 0 \qquad \text{(D.3.21)}$$

$$\frac{\delta\theta}{\delta t} + \frac{\delta(\psi,\theta)}{\delta(x,z)} - \frac{\Delta T_0\delta\psi}{H\,\delta x} - k\nabla^2\theta = 0 \qquad \text{(D.3.22)}$$

Rayleigh found that fields of motion of the form;

$$\psi = \psi_0\sin(\pi ax/H)\sin(\pi z/H) \qquad \text{(D.3.23)}$$

$$\theta = \theta_0 \cos(\pi a x/H)\sin(\pi z/H) \qquad \text{(D.3.24)}$$

would develop if;

$$\frac{g\alpha H^3 \Delta T}{\mu k} > \frac{\pi^4(1+a^2)^3}{a^2} \qquad \text{(D.3.25)}$$

which defines what is now known as the critical Rayleigh number and in this case occurs when $a^2=½$ and thus $R_c=27\pi^4/4$.

Saltzman (1960) derived a set of ordinary differential equations by expanding ψ and θ in double Fourier series in x and z, with functions of t alone for coefficients, and substituting these series into (D.3.21) and (D.3.22). The resulting infinite set of ordinary differential equations were then reduced to a set of seven equations, in seven variables and time, by omitting all but a very narrow range of functions of time. Upon numerical integration, four of these variables tended to zero and the other three would neither converge nor diverge, but underwent irregular, apparently non-periodic fluctuations.

Alternatively these three terms can be found by using the following equations rather than (D.3.23) and (D.3.24),(Lorenz 1961);

$$\frac{a\psi}{(1+a^2)k} = X2^{½}\sin(\pi a x/H)\sin(\pi z/H) \qquad \text{(D.3.26)}$$

$$\frac{\pi R_a \theta}{R_c \Delta T} = Y2^{½}\cos(\pi a x/H)\sin(\pi z/H) - Z\sin(2\pi z/H) \qquad \text{(D.3.27)}$$

And after some rearrangement, the resulting equations are;

$$\frac{dX}{d\tau} = -\sigma X + \sigma Y \qquad \text{(D.3.28)}$$

$$\frac{dY}{d\tau} = -XZ + rX - Y \qquad \text{(D.3.29)}$$

$$\frac{dZ}{d\tau} = XY - bZ \qquad \text{(D.3.30)}$$

Where dimensionless time, $\tau=\pi^2(1+a^2)kt/H^2$, $n/k=Pr$ the Prandtl number, $r=R_a/R_c$ and $b=4/(1+a^2)$. These three equations are dimensionless versions of Saltzman's equations A, D and G, and are now known as the Lorenz equations. The variable X is proportional to the intensity of the convective motion, Y is proportional to the temperature difference between the ascending and descending currents, and Z is a measure of the distortion of the vertical temperature profile from linearity.

It is also possible to derive the Lorenz equations for a leaky waterwheel (Sparrow 1980, Malkus 1979)! This does not extend the theoretical understanding of the equations, but provides a simple experimental demonstration of the transition to chaos.

Because of the severe truncation of the series, these equations can only be expected to bear any resemblence to real convection when the system is just supercritical.

As an aside, it can be noted that the variables Y and Z can be eliminated from the Lorenz equations above, leaving X(t);

$$\frac{d^3x}{dt^3} + (\sigma-b)\frac{d^2x}{dt^2} - (b+r+b\sigma+1+x^2)\frac{dx}{dt} + (r-\sigma-\sigma b+rb-\sigma x^2)x = 0 \qquad \text{(D.3.31)}$$

This equation has a very similar structure to the equations governing the van der Pol or Duffing oscillator (Miles 1989, Awrejcewicz 1989), which can be written as follows;

$$A_1\frac{d^2x}{dt^2} + (A_2x^2+A_3)\frac{dx}{dt} + (A_4+A_5x^2)x = f(t) \qquad \text{(D.3.32)}$$

This equation has been used to describe many systems which are forced and suffer non-linear damping, for example electrical circuits and mechanical oscillators (Pippard 1985).

In order to investigate the temporal behaviour of the Lorenz equations, they must be integrated, and the simplest method is by iteration. Noting that the differential of the nth iteration can be defined as follows;

$$\frac{dx_n}{dt} = \frac{x_{n+1} - x_n}{dt} \qquad \text{(D.3.33)}$$

and similarly for the differentials of y and z, leading to;

$$x_{n+1} = x_n + \sigma(y_n-x_n)\tau \qquad \text{(D.3.34)}$$

$$y_{n+1} = y_n + (rx_n-y_n-x_nz_n)\tau \qquad \text{(D.3.35)}$$

$$z_{n+1} = z_n + (x_ny_n-bz_n)\tau \qquad \text{(D.3.36)}$$

where τ is the time increment between the steps. If $r<1$, the equations converge to a stable point for all values of b and σ, as expected there is no fluid motion, and the heat is transferred through the liquid by conduction only. However for $r>1$, the evolution of the system in x,y,z space becomes more complicated. The possibilities are described below and full derivations and examples can be found elsewhere (Sparrow 1980, Doherty 1988).

(i) Stable singular points.

(ii) Attraction to and then entrapment onto a simple closed curve

(iii) Attraction to and then entrapment onto a curve that lies on the surface of a torus. If the solution is periodic, then the curve is closed and produces a one dimensional line on the surface. Quasi-periodic solutions are not closed, and eventually cover the whole surface.

(iv) Other closed, but unbounded, surfaces exist onto which the path can be attracted, however these do not enter the three dimensional case.

(v) Under certain cicumstances (chaos), the trajectory is attracted to an object, within which it wanders haphazardly. The path never settles onto a surface or repeats itself. This object is known as a strange attractor.

Figures D.3a and D.3b show the first 2000 points of the integration of the Lorenz equations, projected onto the x-z plane, for parameters given in the figures. As the integration time is increased, the space appears to be slowly filled with the line. Since, in reality, the line has zero width, the volume can never be filled, and the conditions in (v) above apply.

Having integrated the Lorenz equations by converting them into iterative equations, using (D.3.33), it would be interesting to find the form of the differential equations that produce the iterative equations that were studied in section D.2; namely the logistic equations. The following approximations will be employed;

$$\frac{dx_n}{dt} = \frac{x_{n+1} - x_n}{\tau} \qquad \text{(D.3.37)}$$

$$\frac{d^2x_n}{dt^2} = \frac{x_{n+2} - 2x_{n+1} + x_n}{\tau^2} \qquad \text{(D.3.38)}$$

$$\frac{d^3x_n}{dt^3} = \frac{x_{n+3} - 3x_{n+2} + 3x_{n+1} - x_n}{\tau^3} \qquad \text{(D.3.39)}$$

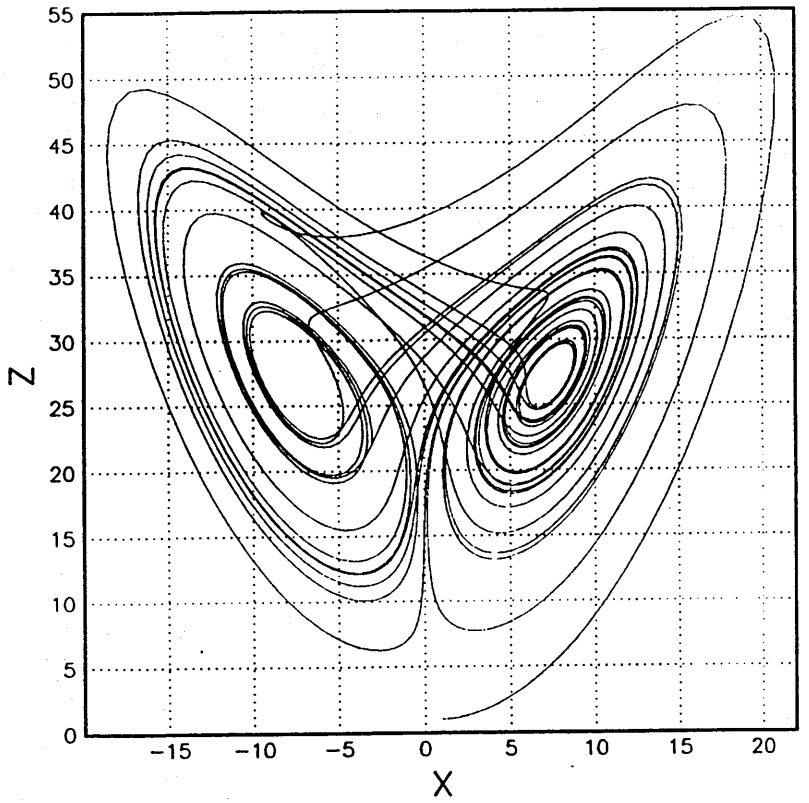

Figure D.3a. The first 2000 iterations of the Lorenz equations for; X_o=1, Y_o=1, Z_o=1, δt=0.01, σ=10, b=8/3 and r=28, projected onto the X-Z plane.

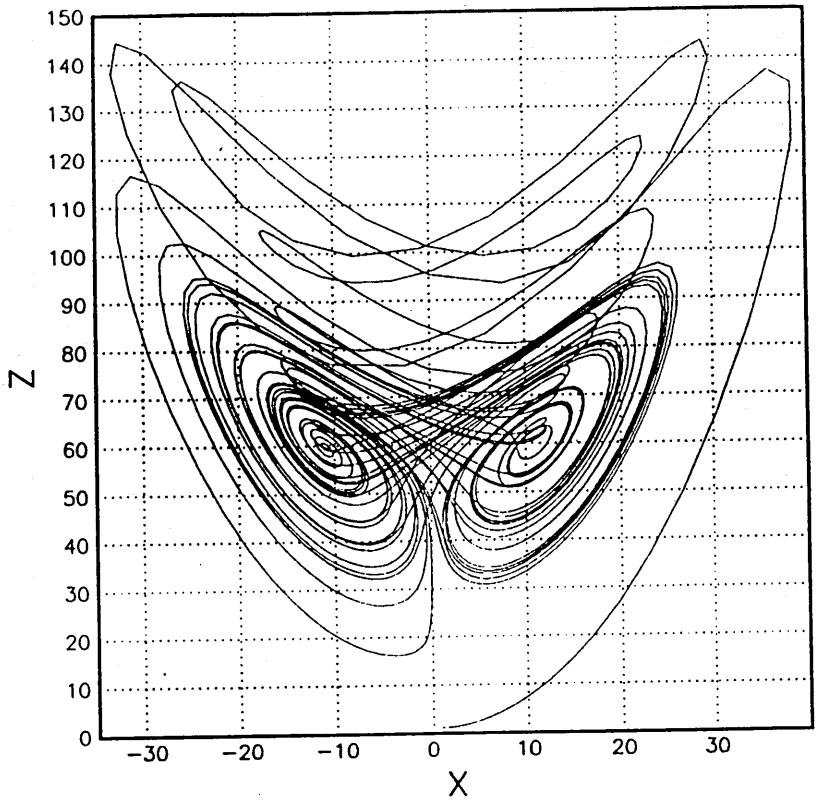

Figure D.3b. The first 2000 iterations of the Lorenz equations for; X_o=1, Y_o=1, Z_o=1, δt=0.01, σ=10, b=8/3 and r=60.5, projected onto the X-Z plane.

It can be seen that the basic logistic equation (D.2.4) contains only two generations, and so the differential equation will be first order, and of the form of (D.3.37), and can be reduced to;

$$\tau\frac{dx}{dt} + Rx^2 - x(1+R) = 0 \qquad \text{(D.3.40)}$$

The modified logistic equation, (D.2.11), with three generations reduces to;

$$\tau^2\frac{d^2x}{dt^2} + \tau^2R\left[\frac{dx}{dt}\right]^2 + \tau\frac{dx}{dt}(2\tau-R\tau+2Rx+RBx) + x^2R(1+B)+x(1-R)=0 \qquad \text{(D.3.41)}$$

Thus it should be expected that a system which can be described by either of these equations, with the appropriate scaling parameters τ, R and B will display any of the types of behaviour patterns described in (i) to (v) above.

D.4 Attractors, Theory and Experiment.

In the last section, the concept of phase portraits was introduced, in figures D.3a and D.3b. In projecting the three dimensional data onto a two dimensional plane, the information that was contained in the contracted dimension was lost. In a general experimental system, governed by parameters $P_1, P_2 \ldots P_N$, an N dimensional phase space will be required to cover all the possible variations in these parameters. For example, for two phase flow in a pipe, the basic parameters are, flow rate (2), density (2), viscosity (2), interfacial tension, pipe diameter, roughness, inclination and the acceleration due to gravity (appendix C). Compressibility, thermal and chemical effects could be included amongst these for completeness. The real parameters can usually be reduced to a smaller number N' of dimensionless parameters, using the Buckingham Pi theorem.

Thus when the system is switched on, the behaviour of any point within the system, or the system as a whole, will follow a trajectory in this N' dimensional phase space. Clearly, for all but the simplest cases, the experimental problems of determining all of the parameters are insurmountable. For real physical systems, the trajectory must be attracted to some shape, within the N' dimensional phase space, from any arbitrary starting point. The possible shapes were described in section D.2. Not all of the parameters that were originally defined for the system will have an influence on the trajectory, ie are constant or zero for the given experimental conditions. Thus the trajectory shape can have a dimensionality only less than or equal to N'. The minimum value of the dimensionality of the shape is known as the embedding dimension. Conversely, the embedding dimension is the minimum number of variables (O.D.E.'s and B.C.'s) required to define the system under those conditions.

For a system that is behaving in a chaotic manner, the trajectory in the phase space defines an object that has finite extent and infinite structure. Since the trajectory never crosses itself in the full embedding dimension, parts of this space are asymptotically filled with the line. Thus there is an infinitely long and infinitessimally thin line confined to a finite volume of this hyperspace.

The existence of structure in the object, even on the smallest scale, means that the object is a fractal, and the efficiency with which this fractal fills the space is known as the Hausdorff dimension (which is generally fractional) and must have a value less than or equal to the integer embedding dimension.

This can be summaraised as:

$$0 \leqslant \underset{\text{Real}}{\text{Hausdorff Dimension}} \leqslant \underset{\text{Integer}}{\text{Embedding Dimension (N')}} \leqslant \underset{\text{Integer}}{\text{All Parameters(N)}}$$

Measured data — O.D.E.'s — P.D.E.'s

Number of active degrees of freedom

The complexity of a system can be gauged by taking a Poincaré section (1879) of the attractor. This involves finding the patterns produced when the trajectory crosses a hypersurface that is at least one dimension smaller than the embedding dimension and can be as small as a 1-D line. The result is a series of dots where the intersection takes place.

For a non-chaotic system, the dots produce patterns that are either asymptotically discrete or merge to form a very simple shape. A chaotic system has a Poincaré section that has infinite structure, since the cross-section of a fractal is another fractal, and this is usually easier to recognise in a low dimensional section, rather than the whole attractor.

An example of this is the Hénon map (1976), in which the Lorenz equations (3-D) are reduced to a 2-D Poincaré section. The mapping of the discrete dots is governed by the equations;

$$x_{n+1} = -ax_n^2 + y_n + 1 \qquad \text{(D.4.1)}$$

$$y_{n+1} = bx_n \qquad \text{(D.4.2)}$$

Where $-1 \leqslant b \leqslant 1$, and the section has the structure shown in figure D.4a. The general shape is insensitive to the initial conditions (x_0, y_0),

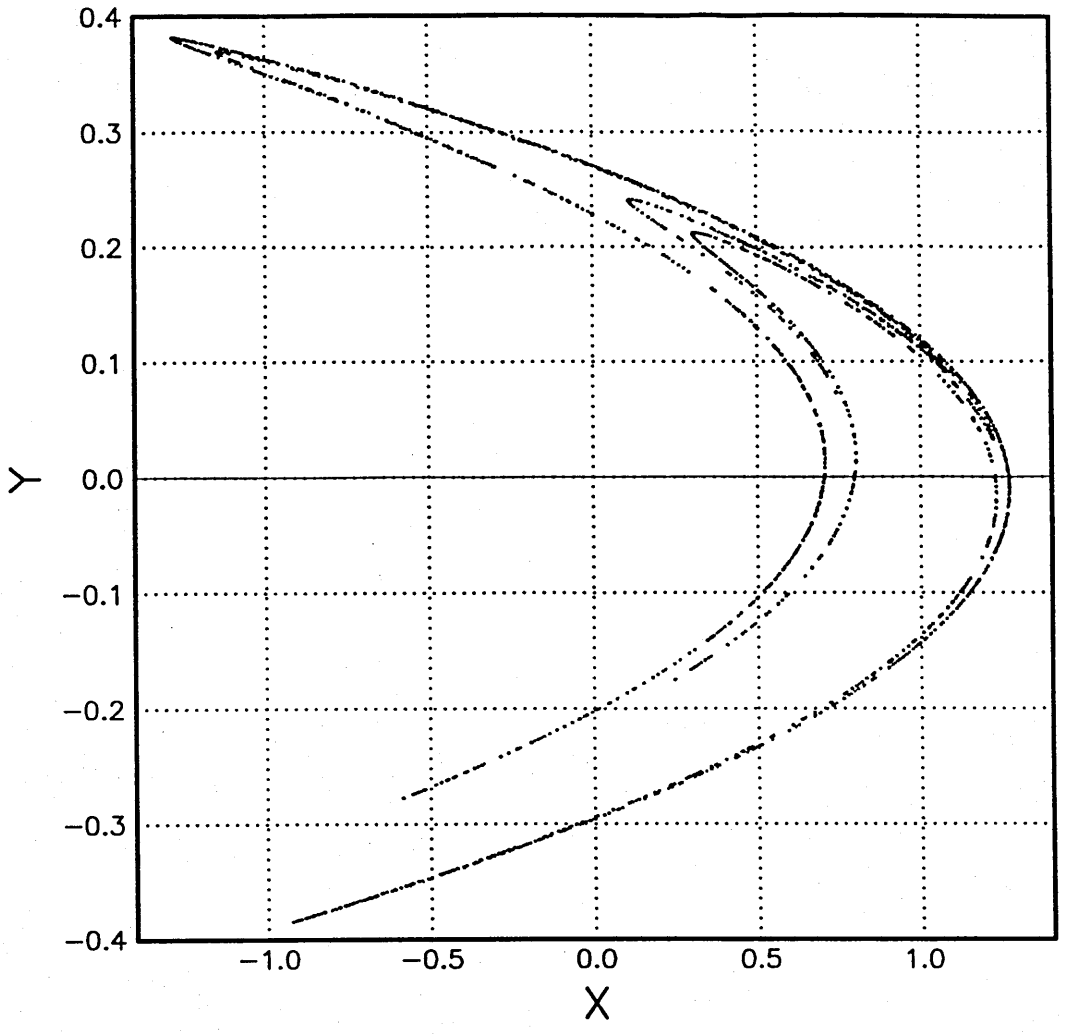

Figure D.4a. A Poincaré section of a Lorenz attractor, a Hénon map.

though the values of the nth iterations are very sensitive to the initial conditions. When b=0, the above equations reduce to the logistic equation (D.2.4), which suggests fundamental connections between the models for the Rayleigh-Bénard flows and very simple iterative equations, or that there may be alternative ways of attacking fluid flow problems than by approximating the Navier-Stokes equations.

Sensitivity to initial conditions has already been mentioned as a characteristic of chaotic systems. It is possible to quantify this attribute of an attractor as follows. Consider two points within the attractor (to save problems with initial transients), with coordinates $(P_1,P_2...P_N)$ and $(P_1+\Delta P_1,P_2+\Delta P_2...P_N+\Delta P_N)$, plotted in an N dimensional space that is greater than or equal to the embedding dimension. Allow both systems to run in the same coordinate system.

After a certain interval (iterations or time), the coordinates will be $(P_1',P_2'...P_N')$ and $(P_1'+\Delta P_1',P_2'+\Delta P_2'...P_N'+\Delta P_N')$, and the Liapunov exponent (also Lyapunov) is defined as;

$$\lambda_i = \exp(\sigma_i t) \qquad (D.4.3)$$

where,

$$\sigma_i = \frac{\Delta P_i - \Delta P_i'}{t} \qquad (D.4.4)$$

This is a measure of the rate at which two initially close points separate with time in each coordinate. Clearly for any $\lambda_i>0$, the points will separate along the P_i coordinate indefinitely, and all correlation between the two points will be lost in this direction. If all $\lambda_i<0$, the two points will asymptotically converge, and the system must repeat itself. Conversely, for any $\lambda_i>0$, any two points will diverge, no matter how close together they were in the beginning, and thus the system can never repeat itself, and the trajectory must be chaotic.

D.5 The Grassberger-Procaccia Algorithm.

It has been shown (Takens 1981, Packard 1980), that the attractor of a given system of N variables can be reconstructed by analysing the behaviour of a single variable. The dimensionality of this reconstructed attractor will be the same as that of the attractor drawn using the full set of variables, though the shape may be considerably distorted. The attractor can be constructed as follows.

Consider a single parameter x(t), measured at equal time intervals τ. The attractor is constructed by taking the consecutive readings as the independant variables. Thus in an m dimensional space, the first few points will be as follows;

$$x(t),\quad x(t+\tau),\quad x(t+2\tau),\ldots,x(t+(m-1)\tau)$$
$$x(t+\tau),\quad x(t+2\tau),\quad x(t+3\tau),\ldots,x(t+m\tau)$$
$$x(t+2\tau),\quad x(t+3\tau),\quad x(t+4\tau),\ldots,x(t+(m+1)\tau)$$

Figure D.5a shows such a plot in two dimensions (m=2), for the Lorenz equations for the given parameters. Figure D.5b shows a similar plot for the logistic equation, which, because of the discrete nature of the data (purely iterative, rather than differential), appears as a series of dots, and has a striking resemblence to figure D.4a.

The dimension of the attractor calculated in this space (see later), increases with m until m equals the embedding dimension, and then the dimension of the attractor is the Hausdorff dimension. Further increases in m have no effect on the attractor, as discussed earlier.

The dimensionality of the attractor (fractional if strange and chaotic) can be determined using;

$$d = \lim_{\varepsilon \to 0} \frac{\mathrm{Log}_{10} N(\varepsilon)}{\mathrm{Log}_{10} 1/\varepsilon} \qquad (D.5.1)$$

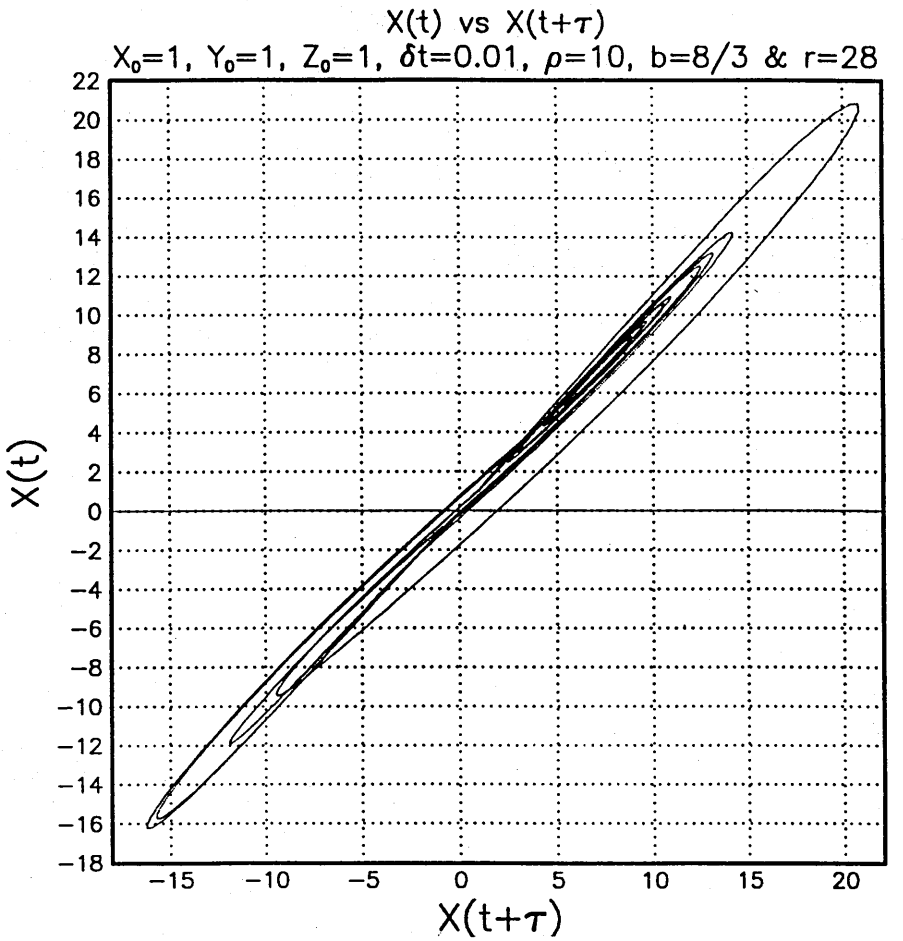

Figure D.5a. A reconstructed attractor from the X parameter of the Lorenz equations for the following parameters; X_o=1, Y_o=1, Z_o=1, δt=0.01, σ=10, b=8/3 and r=28.

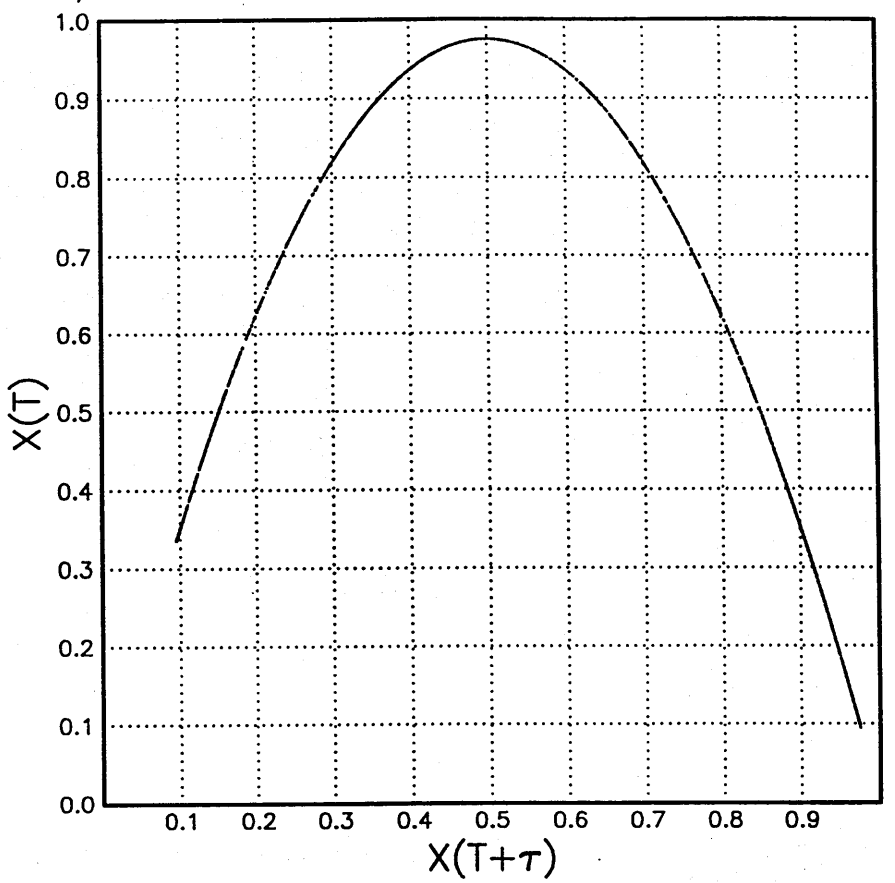

Figure D.5b. A reconstructed attractor for the logistic equation.

Where N is the number of m dimensional cubes of side ε required to cover the phase trajectory. This method is only easily carried out for $m\leq 2$, since the method requires considerable computer memory.

An alternative method for finding the embedding and Hausdorff dimensions, using more computational power, but less memory, has been proposed (Grassberger 1984).

A correlation integral is defined as follows;

$$C(\varepsilon) = \lim_{N\to\infty} \frac{1}{N^2} \sum_{i\neq j} \theta(\varepsilon - |R_i - R_j|) \qquad (D.5.2)$$

Where θ is the Heaviside step function that tests whether R_j is within a hypercube of side 2ε of R_i. The original work considered a hypersphere of radius ε, and produces the same correlations, but scaled by a linear factor $N^{1/m}$, where N is the total number of data points. This can be further simplified by noting that $|R_i - R_j| = |R_j - R_i|$, and for computational ease, the argument of the Heaviside function can be expanded, leaving;

$$C(\varepsilon) = \lim_{N\to\infty} \frac{2}{N^2} \sum_{j>i} \sum_{D=0}^{m-1} \theta(\varepsilon - |R_{i+D} - R_{j+D}|) \qquad (D.5.3)$$

As ε becomes small, this correlation is related to the Hausdorff dimension of the attractor, thus;

$$C(\varepsilon) \propto \varepsilon^d \qquad \text{or} \qquad d = \lim_{\varepsilon\to 0} \frac{\log_{10} C(\varepsilon)}{\log_{10} \varepsilon} \qquad (D.5.4)$$

The principles of the calculation are shown in figure D.5c. Thus if all the points after t_2 fit within the corresponding error bars (ε) of the template set up at t_1, the the m-dimensional point at t_2 has correlated with that template and $\theta=1$. If one or more of the points after t_2 lie outside ε, there is no correlation and $\theta=0$. A new template is set up for each t_1 and compared with all the other

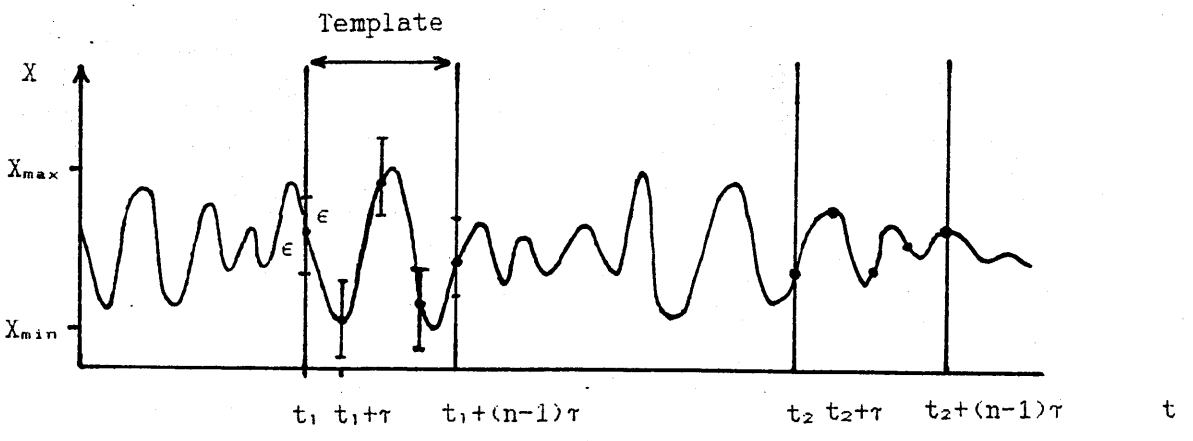

Figure D.5c. Setting up templates and error bars in order to calculate the correlation function.

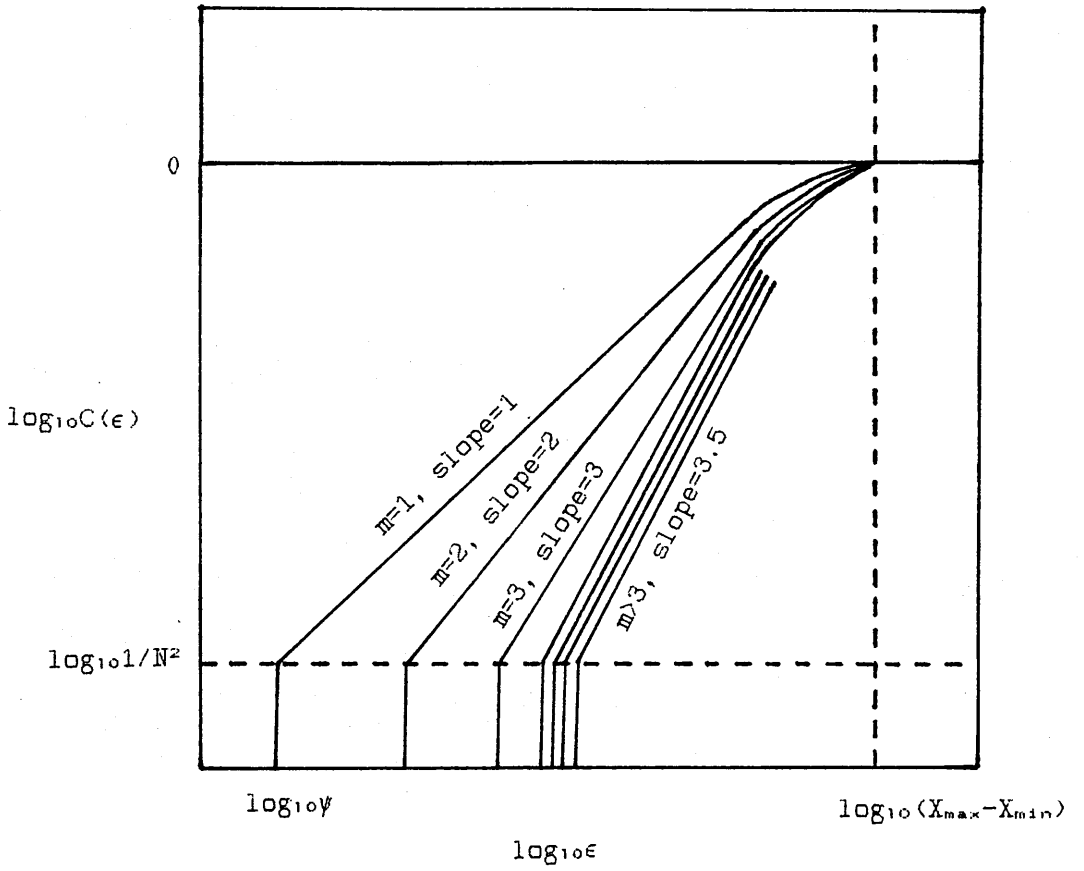

Figure D.5d. A sketch of the plot used to determine the Hausdorff dimension, showing the typical characteristics of limited data, where γ is the minimum distance between any two of the data points.

subsequent t's, and the whole process is repeated for various values of ε and m.

For m less than the embedding dimension, the correlation saturates and d=m. For m $\geq$ the embedding dimension, the correlation reveals the Hausdorff dimension via equation D.5.4. Thus systematically working through ε and m will eventually reveal the embedding dimension and the Hausdorff dimension.

For example, consider a phase trajectory that has a Hausdorff dimension of 3.5. A plot of $\log_{10}C(\varepsilon)$ versus $\log_{10}\varepsilon$ for increasing values of m would have the form shown in figure D.5d.

A computer program has been written to evaluate equation D.5.3 for an arbitrary data file. The correlation dimension and embedding dimension have been evaluated for several sets of numerical data, described in figures D.5e to D.5i.

Other routines have been devised (Landa 1990, Biage 1989), one involving matrix methods, which uses considerable memory space and array manipulation, and the second uses a statistical method, analogous to a random walk through the attractor (a Monte-Carlo method). Each has its advantages, but all involve calculating the correlation function (equation D.5.6) and then the Hausdorff and embedding dimensions (equation D.5.7). The methods described here have been used to find the complexity of several different experimental systems, from semiconductor oscillations, to electrodissolution in a spinning system, to the transition to flooding in a vertical gas/liquid flow (see section D.7 for more details). The general experimental criteria and the effects of noise will be discussed later in this section and in chapter 6.

A circuit has been proposed that will evaluate, in real time, the embedding dimension of a continuous experimental system (Pyragas 1987, Namjunas 1988 and Cenys 1988). The method is essentially an analogue/digital circuit that carries out the comparisons sketched in figure D.5c, except that the error bars are reversed, so that only

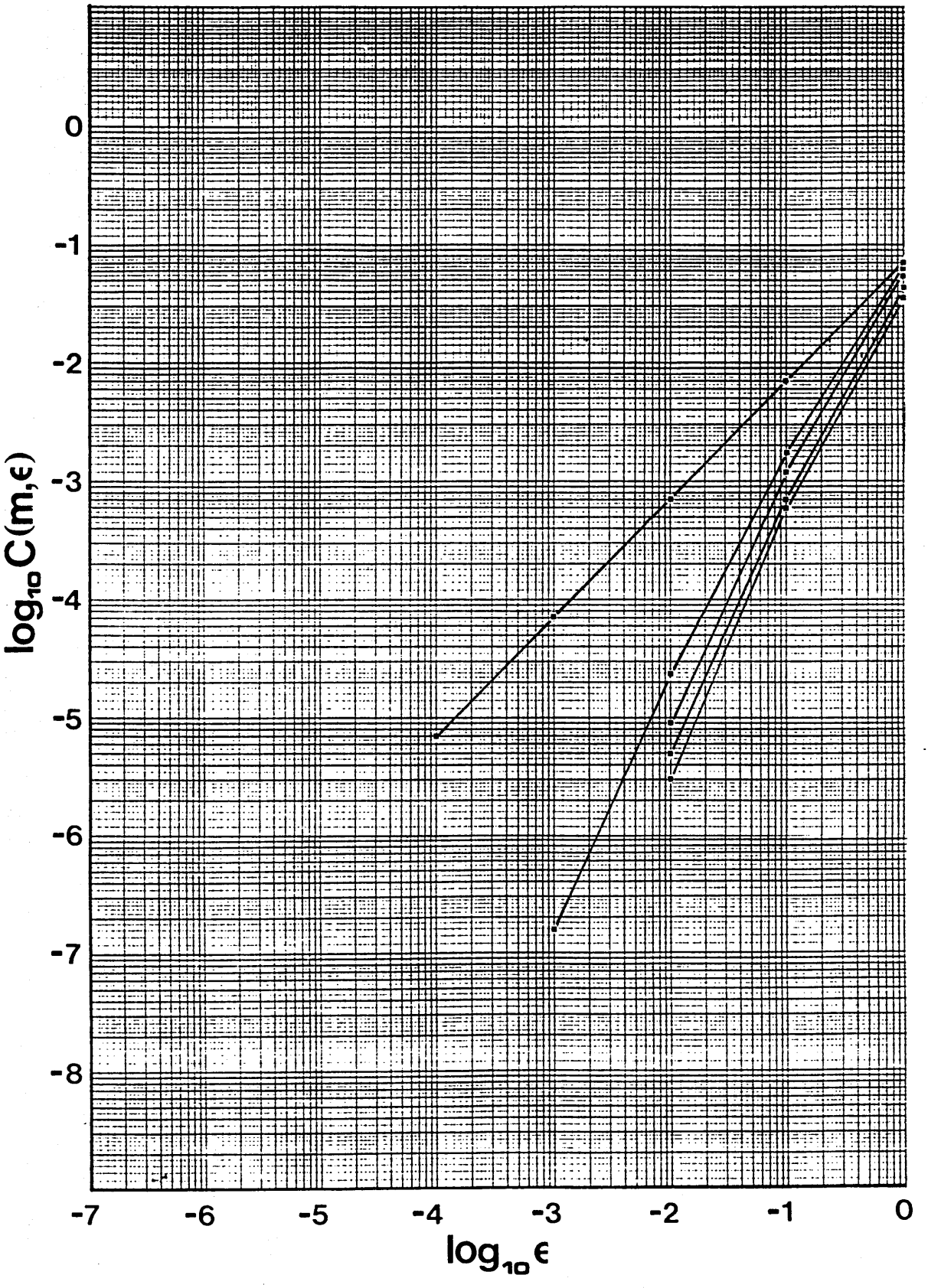

Figure D.5e. The Lorenz equations, using the same parameters as figure D.3a, are evaluated for 5000 iterations after ignoring the first 2000 iterations, to eliminate initial transients. The value of the slope of the graphs for increasing embedding dimension tends to a value of 2.30, and as expected for d=1 and 2, the slopes are 1 and 2 respectively. Thus the system is chaotic and governed by three variables.

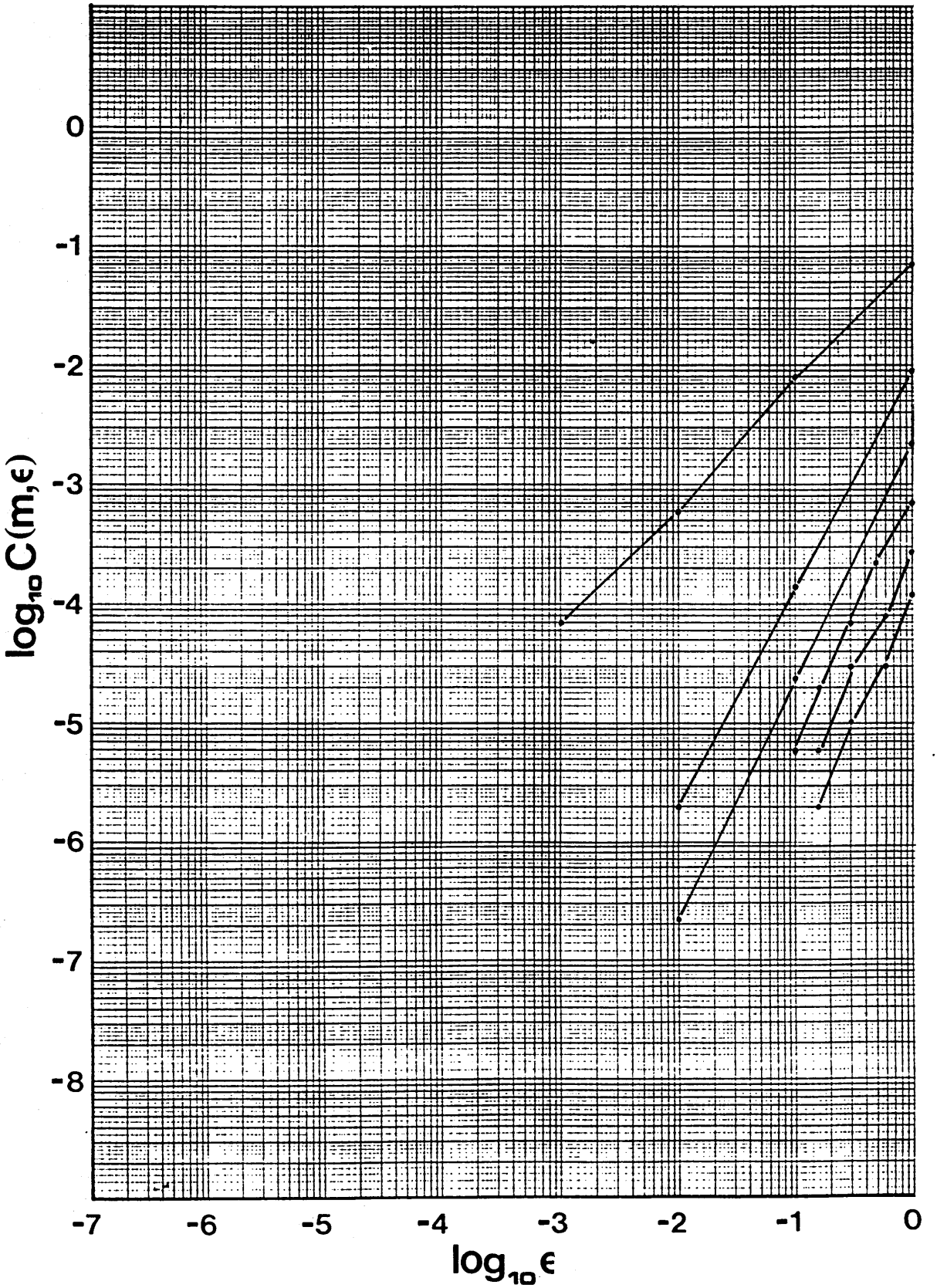

Figure D.5f. The Lorenz equations as above, but only every 100th point is taken from the time series. Thus, instead of mapping the whole attractor, only discrete points are taken. Again, the slope tends to a value of 2.30, and shows how insensitive the routine is, to the spacing of the data points.

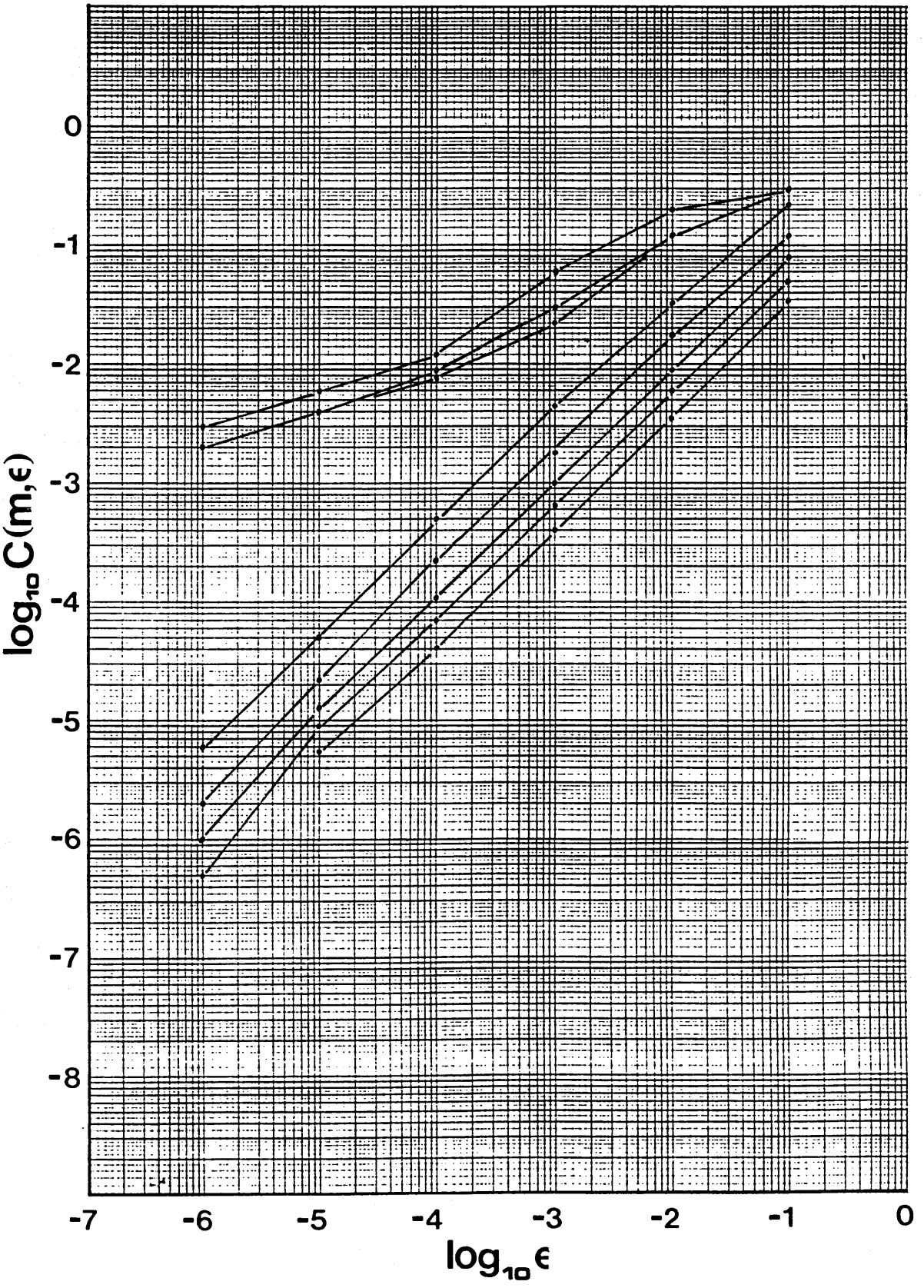

Figure D.5g. The unmodified logistic equation, with feedback factors (R) of 3.85 and 3.90. The slopes are 1/3 and 1 respectively represents the variation in the complexity of the behaviour as R is varied.

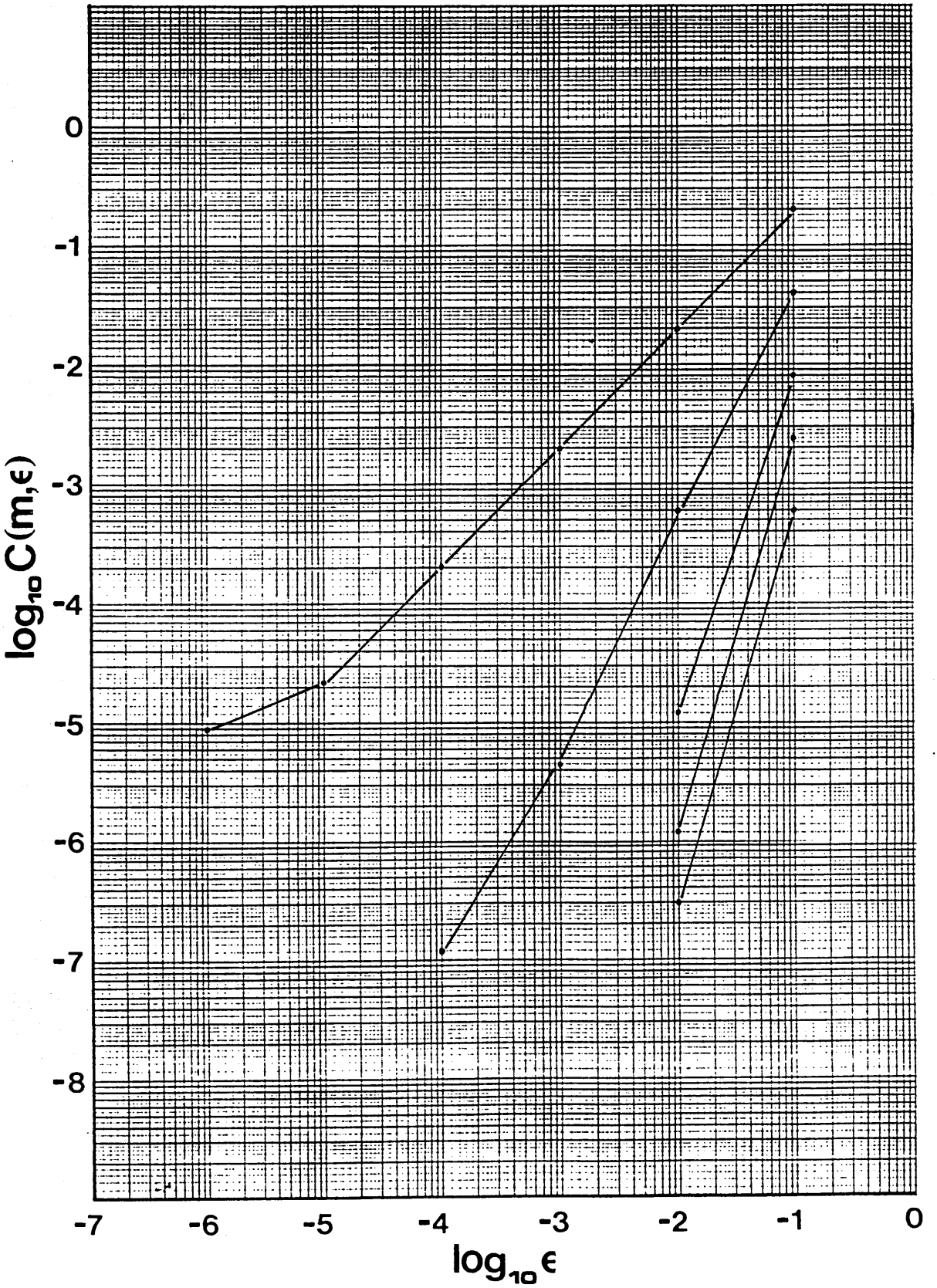

Figure D.5h. A pseudo-random number generator, given by the following equation; X(N)=100tan(N)-INT100tan(N), has an embedding dimension of at least 5. A purely random number series, would have an ∞ dimensionality, but would require an ∞ amount of data to be analysed.

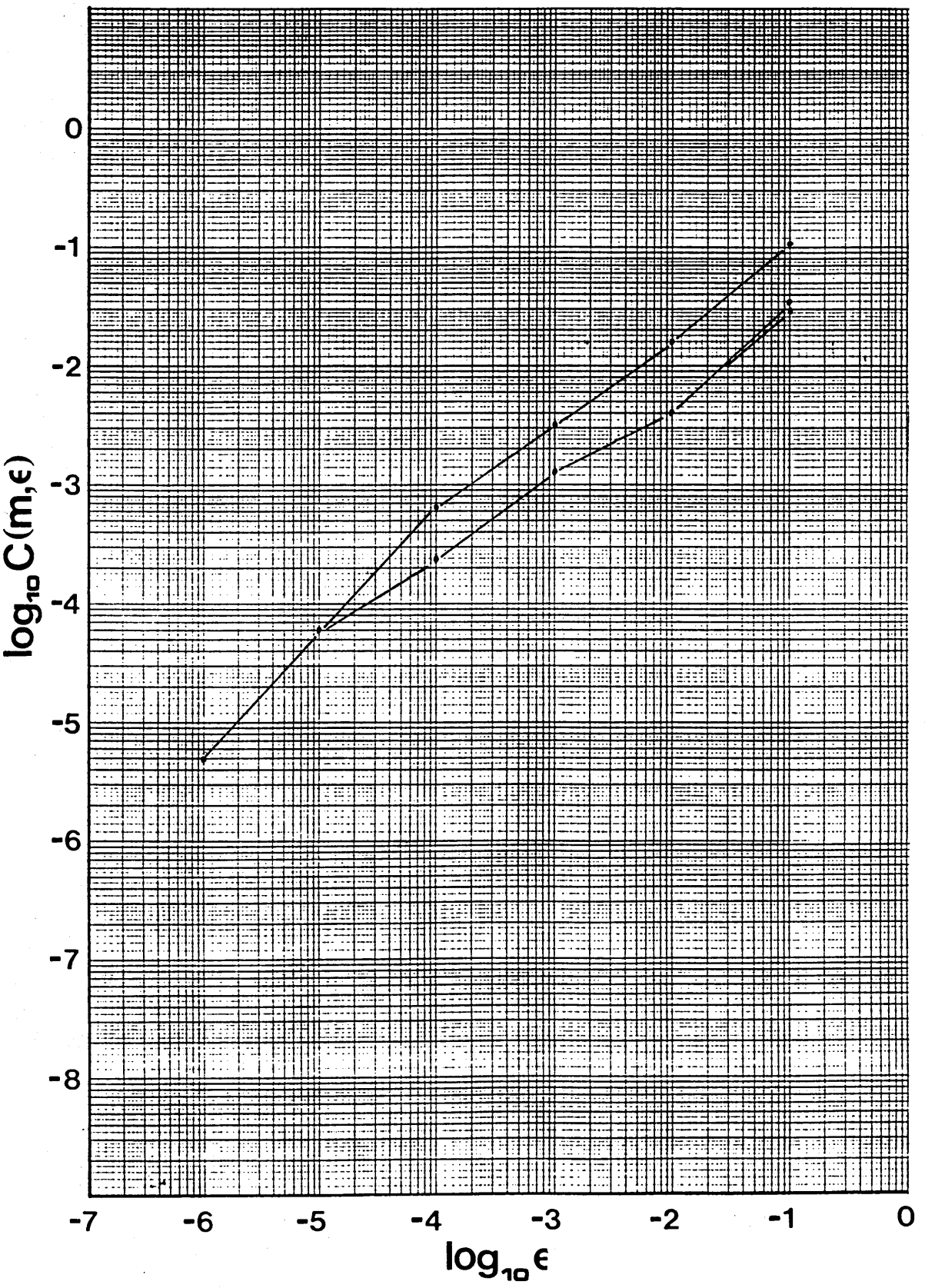

Figure D.5i. A simple series, given by the equation; X(N)=sin(N), has a slope of 1, as would be expected, since aplot of X(N) vs X(N+1) is a Lissajous figure, which is a one dimensional line.

points outside the error bars (above a certain limit), are considered. A block diagram of the circuit is given in figure D.5j.

The level detector generates short pulses when the signal crosses a certain predetermined level. The multivibrator generates a sequence of pulses at a chosen frequency. The frequency of the multivibrator is varied till it approximately equals the peak frequency of the P.S.D. of the input signal. The commutator then sets the number of multivibrator pulses to be used in the comparator, an integer that will be increased sequentially. When the intervals between the time at which the level detector pulses, is close enough to the interval between the multivibrator pulses, the comparator sends out a pulse (after a preset time delay), to increase the instantaneous brightness of the storage scope. A more detailed circuit diagram, showing how this can be realised, is given in figure D.5k. Typical traces from the storage scope are sketched in figure D.5l.

For m greater than or equal to the embedding dimension, the m period long template, set up by the multivibrator will totally define the trajectory, and so, the bright spot set up after the delay (constant) will always appear at a given point on the trajectory. If m is less than the embedding dimension, the trajectory will not be defined in the template, and the bright spot will appear at some random point on the trajectory. Thus as the length of the template is increased, the spread of the bright spots on the screen will decrease, reaching a minimum when the embedding dimension is reached.

The susceptibiliy of the above methods, of determining the dimensionality of an attractor, to experimental noise, is a function of several parameters; the embedding dimension itself, the length of the data file or time series analysed, the relative sizes of ε, the rounding errors in the data and the signal to noise ration of the data.

A real signal can be considered to be made up of a superposition of the following parts;

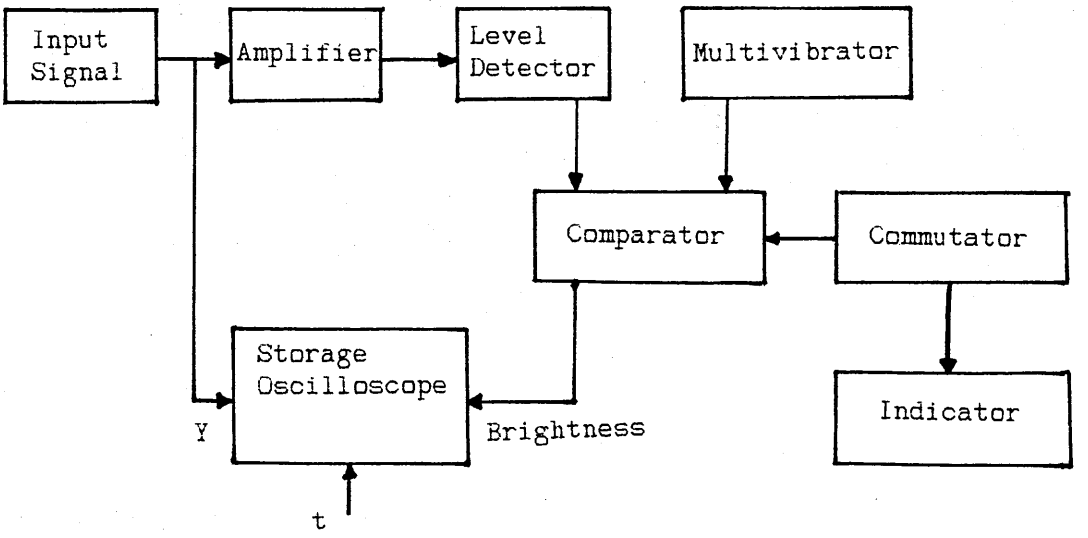

Figure D.5j. A block diagram of the circuit used to analyse experimental attractors.

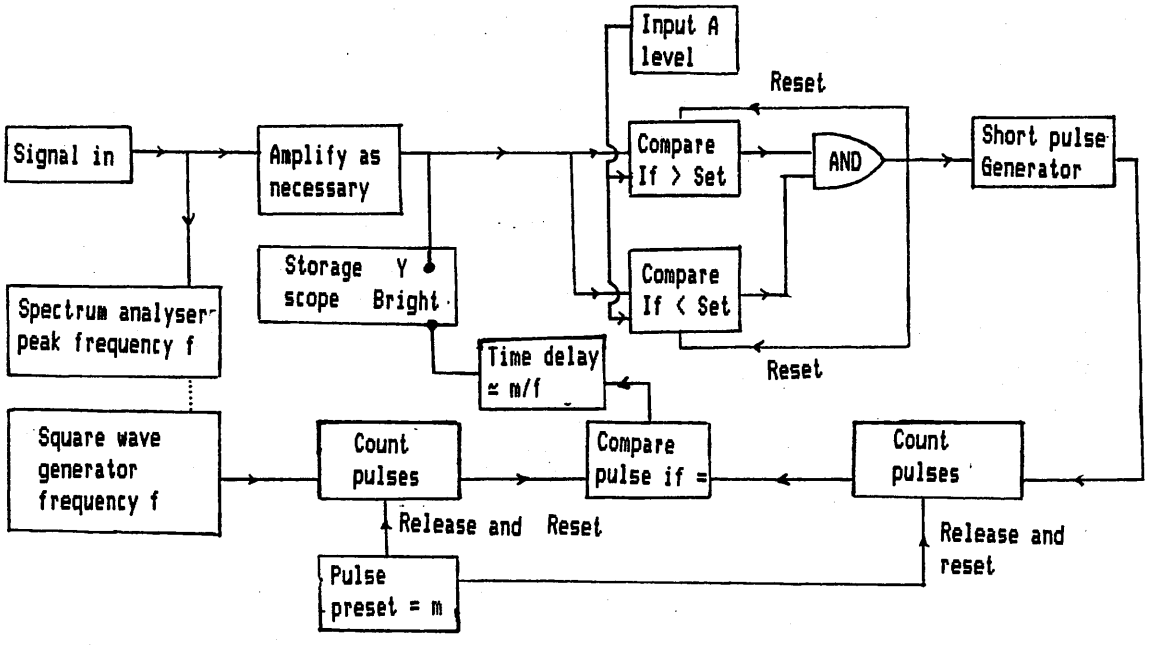

Figure D.5k. Circuit designed to realise the above block diagram.

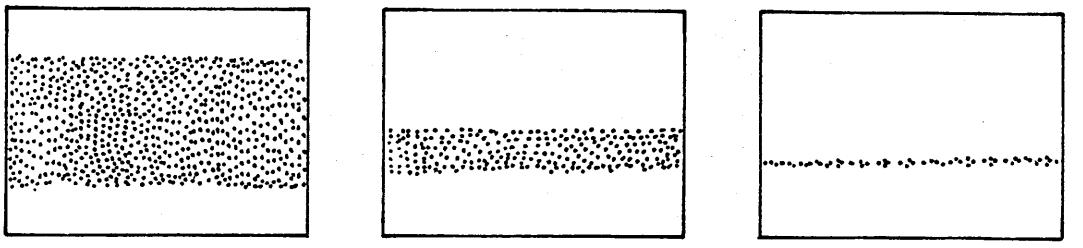

Figure D.51. Sketch of image seen on storage scope for various values of embedding dimension.

The absolute measurement, amplitude A_1

Systematic errors, amplitude A_2

Random errors/noise, amplitude A_3

Signal digitisation/quantisation errors/noise, amplitude A_4

Clearly, any method involving just the correlation integral (equation D.5.2) to determine the dimensionality of an attractor cannot differentiate between the various contributions to the signal, and will therefore find the attractor to the part making the largest contribution to the signal. Consequently, since random noise has an ∞ dimensionality (and will always be larger than the dimension of any experimental system), it should be minimised. Conversely, the amplitude of the noise sets lower limits on the size of ε, for which the correlation integral is considering tha absolute data only.

For the worst possible case; $A_3+A_4<\varepsilon<A_1$, and within this range of ε, A_1 must satisfy $C(\varepsilon)=\varepsilon^d$, for the correlation method to be valid. Where a system has two different mechanisms at work simultaneously, for example in many aspects of multiphase/multicomponent flow (see later, but briefly, there can be several different characteristic wavelengths in the flow, each producing a peak in the PSD, and produced by a different mechanisms), each mechanism can have its own Hausdorff dimension, to which the other signals can be considered as noise, and should be filtered out so that the signal to noise ratio is greater than unity over the range of frequencies to be studied.

D.6 Single Phase Fluid Flow Transitions.

Having now described several numerical systems which exhibit complicated transitions from order to chaos, the characteristics of the transition regions, and how they may be detected, studied and quantified, fluid flow transitions in simple systems will now be studied. This involves an introduction to stability theory (following Landau and Lifshitz 1959), to provide a basic and qualitative background to the rest of the section.

Consider an arbitrary fluid flow in a system that is governed by the full Navier-Stokes equations. These partial differential equations govern every aspect of the fluid flow, and cannot be solved exactly for anything but the simplest of flows. The solution of the equations usually involves linearisations and approximations (for example see section D.3), which lead to inaccuracies and loss of solutions. If several solutions to the equations of motion are found, then they are all possible, however, some are more likely to occur than others (consider stable and unstable points in figure D.2a), depending on the relative stability of each solution. A system will always tend towards the most stable solution, which can always be identified, since any perturbation, no matter how large, will not affect the asymptotic solution. All other solutions must be either inherently unstable, singular points or marginally stable, i.e. perturbations up to a certain size decay away and perturbations above this size allow the system to drop into a more stable solution.

The mathematical analysis of the stability of a flowing system tends to be very complicated, and has yet to be derived for the transition to turbulence in a straight pipe! A more complicated case, that can lead to a simple qualitative understanding of the transition to turbulence, is to consider the flow around a bluff body as the flow rate is increased.

For a low Reynolds number, the flow is simple and laminar, the streamlines being given by potential theory (the inviscid solution), and the velocity distribution takes the viscosity into account. Any perturbations to this flow, for example, Brownian motion fluctuations

(quantum mechanical), or irregularities in any of the solid boundaries, produces an effect which dies away more quickly than it can be amplified using the energy of the surrounding flow. Thus the flow is stable. Above a certain flow rate, the perturbation grows exponentially till it fills the system, drawing on the energy of the previously laminar flow.

At the transition between these two regimes, it is necessary to consider the nature of the perturbation. Clearly, it would be expected that the spectrum of a typical (natural) perturbation would be broad - almost noise-like. As the flow rate is increased, just through the critical Re transition, only one frequency of the arbitrary perturbation will initially be amplified and propagate through the medium, rather than decaying away. This one frequency will draw energy from the flow to the detriment of the other frequencies, thus delaying their appearance in the spectrum of the disturbed flow. This frequency selective amplification is utilised extensively in fluidic and vortex flowmeters and accounts for their large turndown ratios and linearity.

Once again, the previously stable solution becomes an unstable stationary point between the two branches of the oscillating bifurcation. Thus it is possible for the laminar state of flow to exist beyond the transition point, though it is very unlikely. The case for the transition to turbulence in a straight pipe provides problems in the defining of the perturbations, and the exact form (route) of the loss of stability. There are two possible sources for the perturbation, either from the wall (surface roughness or external vibrations) or from within the body of the fluid (Brownian fluctuations).

The primary transition from laminar flow around a bluff body appears in two stages, for $30<Re<100$, a stationary vortex pattern appears, and for $Re>140$ these vortices are periodically shed forming a wake. For pipe flow, the primary transition doesn't occur till $Re\approx2000$, and very careful experiments have maintained laminar flow upto $Re=140000$. At these high velocities, the finite length of the apparatus means that even if something is perturbing the flow, the expanding front of the perturbation may be swept from the pipe before it fills the cross-

sectional area of the pipe. For an infinite length of pipe, or an infinitely long experiment, the output of the pipe would always be turbulent for Re⩾2000. The transitions to turbulence in a straight pipe are a very special case of stability breakdown, because of the high symmetry perpendicular to the direction of the laminar streamlines.

Before going into more details of turbulence in straight pipes, a few examples, showing lower orders of symmetry (perpendicular to the laminar streamlines) will be considered.

The earliest investigations into flow stability were carried out in the system of flow that is generated between two concentric cylinders, when there is relative angular motion between the cylinders. The basic configuration of what is now known as a cylindrical Taylor-Couette cell (Taylor 1923) is shown in figures D.6a and a'. A simple analysis concerning the stability of a small element of the fluid to positional perturbations reveals that the flow will be stable (laminar Couette), provided that;

$$\Omega_o r_o^2 > \Omega_i r_i^2 \qquad \text{(D.6.1)}$$

where Ω is the angular velocity and r is the radius of the cylinders, subscripts o and i referring to the outer and inner cylinders respectively. This is known as the Rayleigh criterion.

A more advanced analysis, involving viscosity and its ability to suppress the onset of turbulence (Chandrasekhar 1961), is very mathematically involved, and in general, requires numerical solution.

Figure D.6b shows a flow map for the types of flow observed in a Taylor-Couette cell in terms of a Reynolds' number, defined for each cylinder as follows;

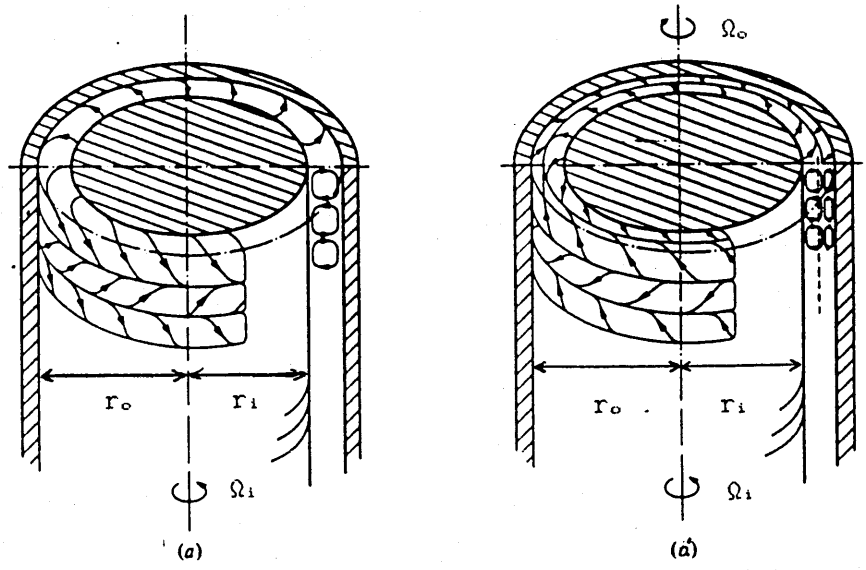

Figure D.6a. Cylindrical Taylor-Couette cell and basic vortex patterns for (a) inner cylinder rotating, outer cylinder at rest and (a') Counter rotating cylinders (Andereck 1986).

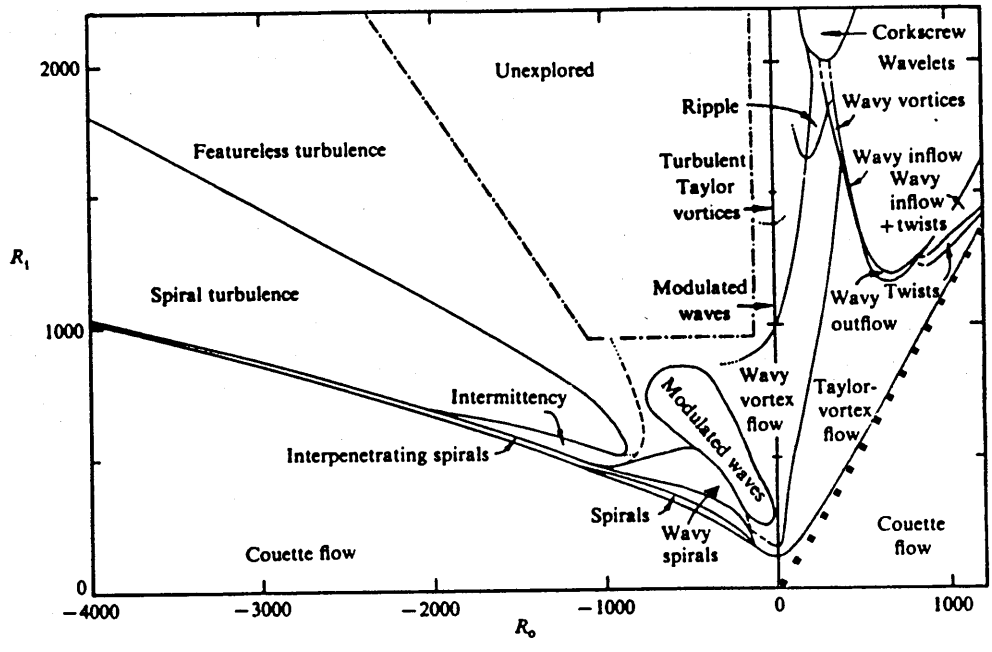

Figure D.6b. Flow pattern map for cylindrical Taylor-Couette flow in Reynolds' number space (Andereck 1986).

$$Re_i = \frac{r_i(r_o-r_i)\Omega_i}{n}$$

$$\text{and} \quad Re_o = \frac{r_o(r_o-r_i)\Omega_o}{n} \qquad \text{(D.6.2)}$$

The Rayleigh criterion appears as a straight row of dots from the origin, and the stabilising effect of viscosity is clearly visible around the origin, though for higher angular velocities, the experimentally determined transition from Couette flow asymptotically tends to the Rayleigh criterion.The primary transition from Couette flow is given very accurately by the numerical methods mentioned above.

It is clear from figure D.6b, that there are many different types of flows between the classical laminar Couette flow and the fully developed (featureless) turbulence which eventually occurs at high enough Re. The flow patterns are characterised by the various wavelengths and frequencies that appear in the vortices of the flow.

The shapes of the stability boundaries show considerable fine structure (Andereck 1986), and are very sensitive to the experimental criteria (Coles 1965). Many of them show approximately parabolic shapes and have other stability boundaries emanating from their lowest point, indicating some sort of bifurcation in this parameter space.

Experiments have been carried out using Laser Döppler Anemometry to analyse variations in the velocity at a point in the flow (Mullin 1983). Figures D.6c and c', show the time variation in the velocity at a point in the flow when the outer cylinder is at rest and the inner cylinder has a Re_i=129.47. The aspect ratio of the gap is varied by 0.15% between the two figures, showing the sensitivity of the flow to system parameters.

The attractors were reconstructed using methods described in the last section and are clearly less than 3-D, and the second example shows considerably more structure. The change in the structure of the attractor indicates that some sort of transition has occurred in the

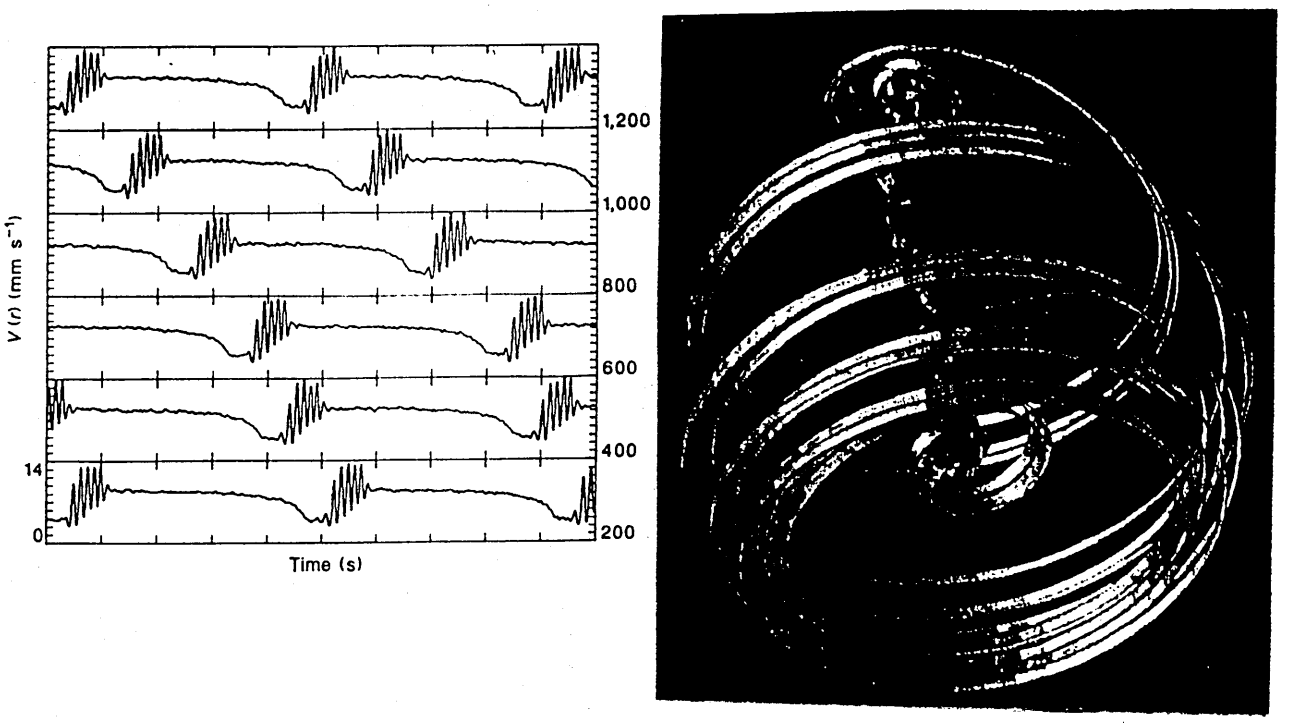

Figure D.6c. Radial velocity component at $(r_o+r_i)/2$, Re=129.47 with a fluid gap aspect ratio, Γ=4.278 as function of time, and the reconstructed attractor (Price 1989).

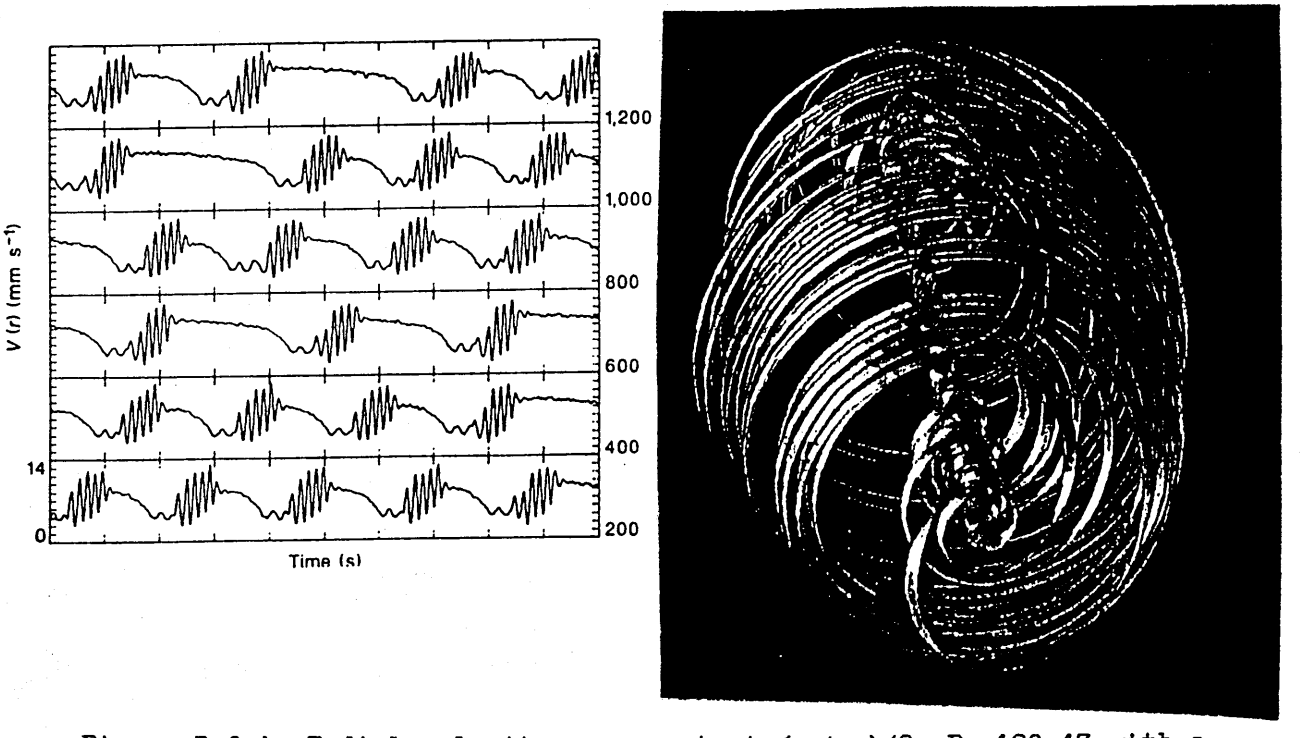

Figure D.6c'. Radial velocity component at $(r_o+r_i)/2$, Re=129.47 with a fluid gap aspect ratio, Γ=4.272 as function of time, and the reconstructed attractor (Price 1989).

flow, probably between Taylor vortex fow and wavy vortex flow (figure D.6b)

Similar experiments have been carried out in a spherical system (Wimmer 1981), and for a small fluid gap, the primary transition from Couette flow is given by exactly the same theory as for cylindrical flow. A comparison between the Rayleigh criterion, the theoretical primary transition for cylindrical Couette flow and the experimental results for spherical Couette flow are shown in figure D.6d. The types of vortices that are generated for various relative angular velocities are sketched in figure D.6e.

Thus it can be seen that when a fluid flows over a curved surface, the first deviation from a laminar flow situation, is in the form of simple vortices, whose axes are parallel to the mean flow and perpendicular to the normal from the surface. The general case between two solid surfaces with realtive motion is known as the Taylor vortex, and if only one surface is involved, or other surfaces are too far away to be considered relevant, then the vortices are known as Görtler vortices. Görtler vortices (Görtler 1944) occur in high shear boundary layers, and are very difficult to observe experimentally. The principle is sketched in figure D.6f.

On a much larger scale, these vortices have been used to explain the existence of large scale coherent structures observed in the wind on the surface of the earth, for example the trade winds. This was first proposed (Hadley 1735!) long before most of the southern hemisphere had been explored and before techniques existed to study high altitude wind speeds! The general circulations are skeched in figure D.6g, with a modern representation of the various flow (vortex) cells in figure D.6g'. These flows are not as simple as those sketched in figure D.6d since thermal forces also enter into the problem, but the large scale structure is qualitatively similar to laboratory experiments (see Lugt 1983 for a review).

A numerical model of a yet larger structure, the atmosphere of Jupiter, has been studied, in which the laminar flow is perturbed by a series of small scale eddies which develop into the obeserved zonal

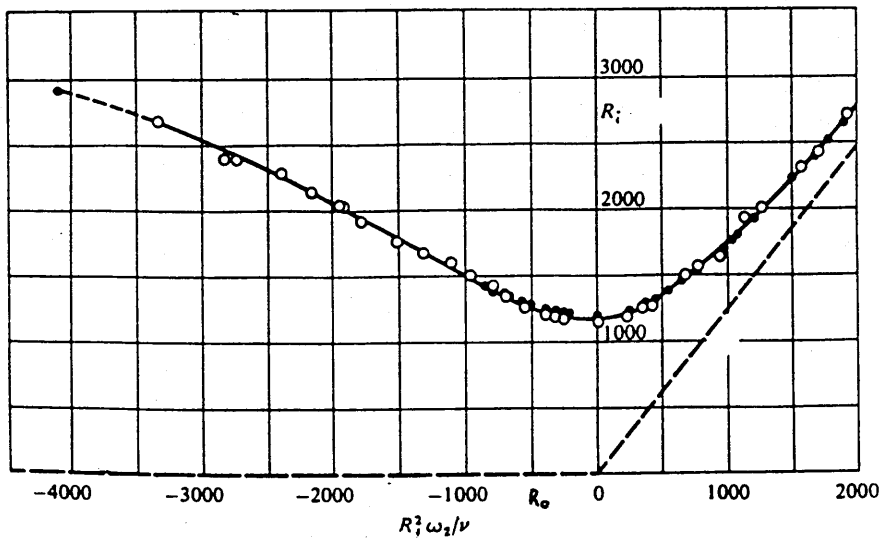

Figure D.6d. The transition from Couette flow, comparing the Rayleigh criterion (theory - dashed line), the cylindrical system (Theory - solid line) and the spherical system (experimental - points), (Wimmer 1981).

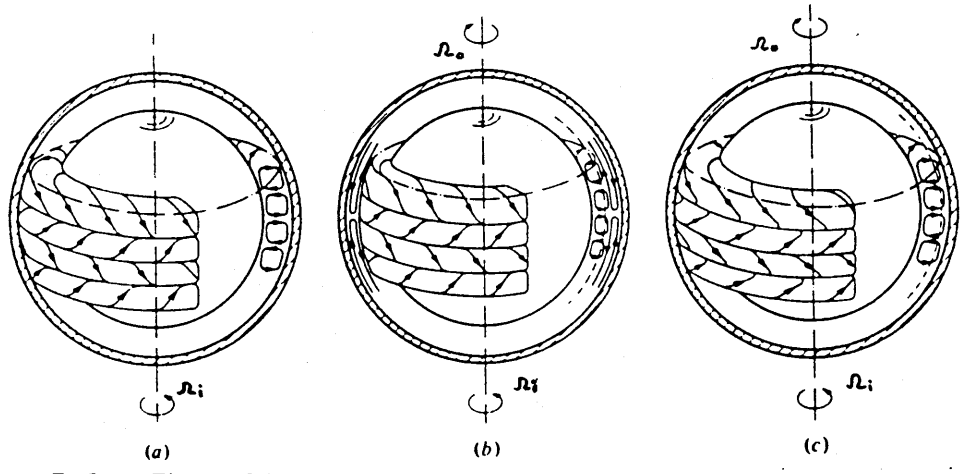

Figure D.6e. Streamlines of the vortices in spherical Couette flow for (a) inner sphere rotates, outer sphere at rest, (b) fast counter rotating spheres and (c) slightly counter rotating spheres (Wimmer 1981).

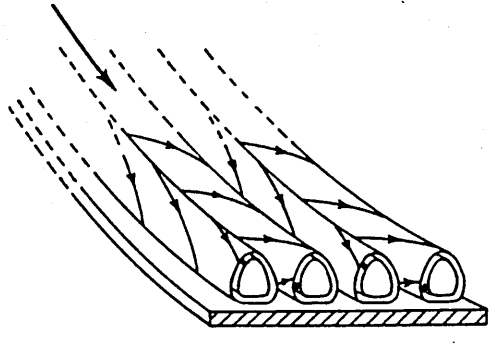

Figure D.6f. Görtler vortices on a concave wall.

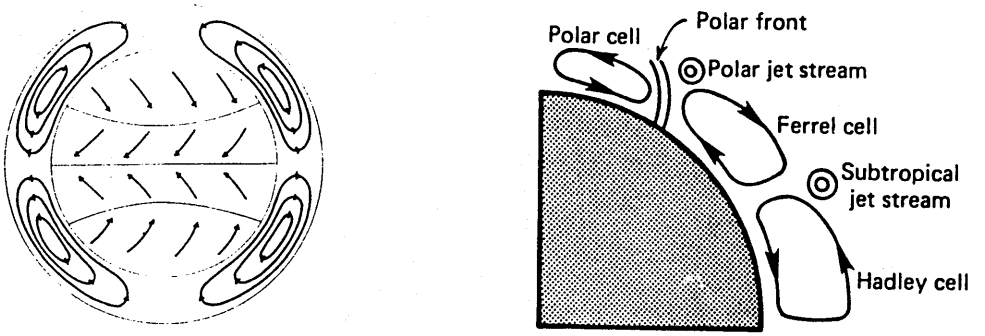

Figure D.6g. The motion of the earth's atmosphere according to Hadley and (g') a modern representation (Lugt 1983).

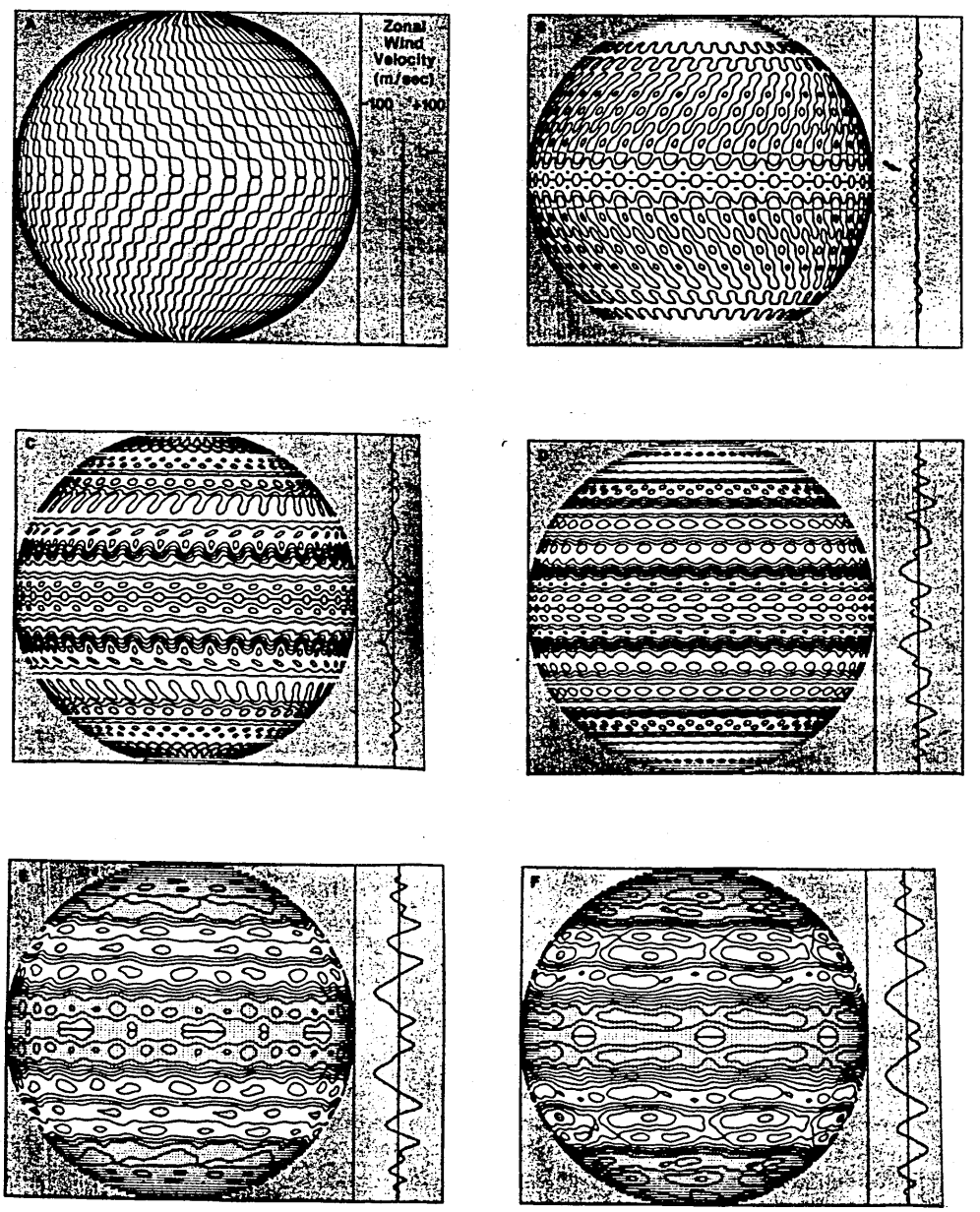

Figure D.6h. The development of zonal jets in the Jovian atmosphere after perturbing the laminar system (Williams 1978).

jets with a large scale structure (Williams 1978). The transitions from perturbation to large scale coherent structures are shown in figures D.6h, with the inset showing the mean zonal wind velocity. The cause and stability of the Red Spot amongst this level of coherence is still under active research, and has been modelled and experimentally verified for a 2-D circulating flow.

A more easily realisable experimental geometry is to consider the flow of a fluid around a bend in a pipe. It is usual to consider bends that go through 180°, and compare the output flow profile with the input flow profile. The primary perturbation is caused by unbalanced centrifugal forces acting in the plane of the bend (compare the Rayleigh criterion in Couette flow), again suppressed by viscous effects. Figures D.6i show flow visualisations at the exit of the bend as a function of mean Re and Dean number $K=Re(a/R)^{\frac{1}{2}}$. The figures on the left rely upon the natural centrifugal perturbation, whilst those on the right are also perturbed at the 90° point with a hyperdermic needle stuck through the pipe wall (see Cheng 1987 for more details).

The basic transition involves two counter-rotating (Dean 1927) vortices (vorticity is conserved, and is zero at the inlet), and the next higher perturbation produces two pairs of counter-rotating vortices. Another higher order perturbation to the flow can be caused by oscillations in the driving mechanism of the mean flow (i.e. the pump). Again, this generates extra pairs of vortices (Lugt 1983) and can be advantageous in heat exchangers, since this causes a greater circulation between the centre and walls of the pipe than a basic pair of Dean vortices.

As an aside, it should be noted that a straight horizontal pipe that is heated anisotropically produces (thermally driven) convection cells (Bénard), identical with the (momentum driven) Dean vortices of figure D.6i.

Combinations of 180° bends have been modelled numerically (Jones 1989), allowing for the bends to be in different planes. The coordinate system employed is shown in figure D.6j and the motion of a particle of fluid around a single 180° bend is given by;

Figure D.6i. Secondary flow patterns at the exit of a 180° bend (Cheng 1987).

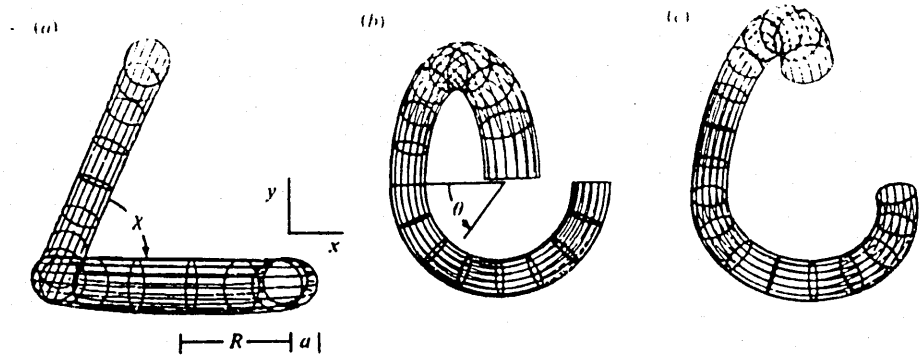

Figure D.6j. Perspective drawings and projections of the general coordinate system for two consecutive 180° bends, for various Re and Dean numbers (Jones 1989).

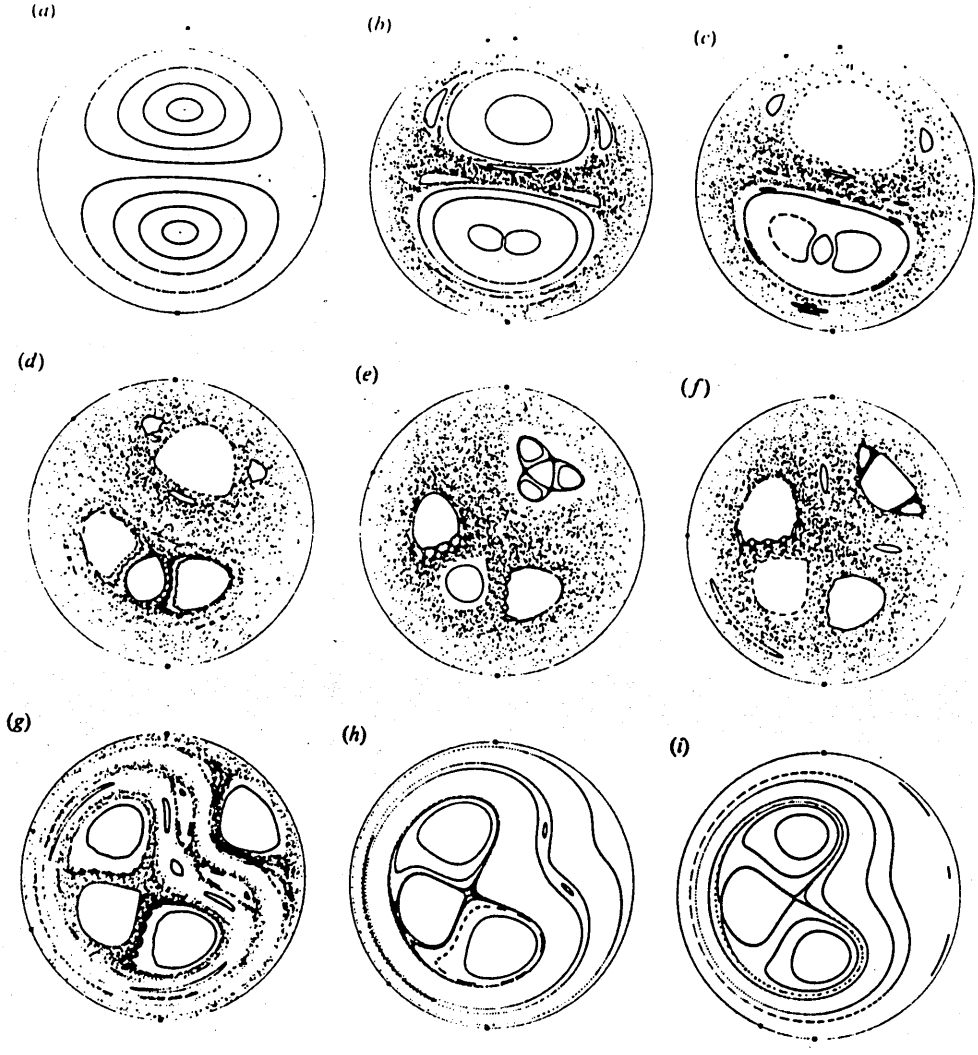

Tidy + clean

Figure D.6k. Poincaré sections for γ=100, and (a) χ=0, (b) χ=π/16, (c) χ=π/8, (d) χ=π/4, (e) χ=3π/8, (f) χ=π/2, (g) χ=5π/8, (h) χ=3π/4, (i) χ=7π/8 (Jones 1989).

$$\frac{dx}{d\theta} = \frac{\gamma}{1152}(4-5x^2-23y^2+x^4+8x^2y^2+7y^4) \qquad (D.6.3)$$

$$\frac{dy}{d\theta} = \frac{\gamma}{192}xy(3-x^2-y^2) \qquad (D.6.4)$$

Where;

$$\gamma = \frac{-a^2}{Ru^2}\frac{\delta p}{\delta \theta} \qquad (D.6.5)$$

And the end of the bend, the cross-sectional plane of the pipe is rotated through χ, and the particles path is integrated around the next bend. For combinations of two bends, the output of the second is used as an input for the first. Thus, starting from suitable points on the cross-section of the inlet, and iterating around the bend many times, produces a Poincaré section of the trajectory, projected onto the inlet or outlet plane. These Poincaré sections are plotted for several values of χ in figure D.6k. The fine structure in some of the plots indicates chaotic trajectories, and the large blank areas imply stable flow tubes through the chaos.

This behaviour provides two distinct areas of study, firstly, to find which combinations of pipework will produce the most effective mixing sections and secondly, to find how these flows will influence flowmeters that are downstream of the bends.

The transition to turbulence in a straight pipe was briefly mentioned at the beginning of this section, and although a cursory inspection reveals this to be a very simple problem to analyse and quantify, the absence of any universally accepted model covering the transition to turbulence and the behaviour of turbulent flows in straight pipes, shows this not to be the case.

This transition to turbulence shows none of the structures that heve been described in previous sections. In order to conceptualise the turbulence, the idea of eddies has been proposed and the following paragraphs will qualitatively describe their properties.

If a disturbed arbitrary flow is considered to be made up of eddies of size λ, then there will be a spectrum of λ, characteristic of the flow. Clearly, λ can be no larger than the size of the apparatus, l, and there will be a minimum size, known as the Kolmogorov length λ_o (Kolmogorov 1944), below which, the fluid dynamic forces are insufficient to maintain an eddy against the viscous forces. Thus below λ_o, the flow is laminar and the eddies of size λ_o are being continuously dissipated as heat. This implies a cascade of energy from the largest to the smallest scales.

If the energy dissipation per unit time per unit mass of fluid is ε, then the variation in velocity across an eddy is given by dimensional analysis as;

$$v_\lambda \simeq (\varepsilon\lambda)^{1/3} \qquad \text{(D.6.6)}$$

If the mean flow velocity is u and the fluctuations in u due to the combined effects of all of the eddies is Δu, and if the system is considered to be in a dynamic equilibrium, then conservation of energy means that;

$$\varepsilon \simeq \frac{v_\lambda}{\lambda^{1/3}} = \frac{\Delta u}{l^{1/3}} \qquad \text{(D.6.7)}$$

The Re of an eddy and the fluctuations in the whole flow respectively are given by;

$$Re_\lambda = \frac{v_\lambda \lambda}{\eta} \qquad Re = \frac{l\Delta u}{\eta} \qquad \text{(D.6.8)}$$

Therefore, combining (D.6.7) and the first part of (D.6.8) leaves;

$$Re_\lambda \simeq \frac{\Delta u}{\eta}\frac{\lambda^{4/3}}{l^{1/3}} \qquad \text{(D.6.9)}$$

Noting that $\Delta u/\eta l^{1/3}$ is a constant for the system, then it follows that;

$$\frac{Re_\lambda}{\lambda^{4/3}} \simeq \frac{Re}{l^{4/3}} \qquad (D.6.10)$$

whence;

$$\lambda_o \simeq l.\frac{Re_{\lambda o}^{3/4}}{Re^{3/4}} \qquad (D.6.11)$$

where $R_{\lambda o}$ is the Re below which the flow is laminar, i.e. Re_{crit}.

The number of degrees of freedom will be roughly equal to the number of Kolmogorov eddies, i.e.

$$N \simeq \frac{1}{\lambda_o^3} \simeq \frac{Re^{9/4}}{l^3 Re_{crit}^{9/4}} \qquad (D.6.12)$$

And the total number of degrees of freedom in the flow is given by;

$$N' \simeq (Re/Re_{crit})^{9/4} \qquad (D.6.13)$$

This is an important result and provides a way of characterising the flow provided Re_{crit} can be determined. For a pipe flow, Re_{crit} is found to be about 2000 experimentally. The following table gives some typical theoretical values for pipe flow.

Re/Re_{crit}	N'	Pipe Re	$\lambda_{o/m}$ for a 0.05m pipe
1	1	2000	0.05
1.36	2	2720	0.040
1.63	3	3260	0.035
1.85	4	3700	0.0315
2.04	5	4080	0.0293
2.78	10	5560	0.0232
7.74	100	15480	0.0108
21.5	1000	43000	0.0050
50	6648	100000	0.0027
100	31623	200000	0.0015
500	1200000	1000000	0.0005

Figure D.61 table of turbulent flow parameters.

It can be seen form these results that for Re<5000, the eddy sizes and the number of degrees of freedom are at odds with experimental results. For Re>50000, the eddy sizes are of the same order as is observed experimentally, and this area is known as fully developed turbulence. As only a small percentage of the eddies are in contact with the boundaries, the turbulence can be considered isotropic.

Clearly, the theory is incapable of modelling the flow transition. The similarities between this transition and the transition between simple and chaotic behaviour in a low order numerical system was first observed in Burgers' equations (Hopf 1949), but again, the number of degrees of freedom were introduced in the form described above.

The intractability of the straight pipe transition implies that the system is more complicated than the other systems described in this section. The only physical factor that could explain this difference is the symmetry of the system. The pipe flow has an infinite number of planes of symmetry in which the mean velocity vector can lie, whereas the other systems have just a single plane of symmetry. Symmetry arguments have been briefly touched upon in the literature, with reference to a Taylor-Couette system with a square outer container, and also with a fixed rod between the square box and the cylinder (Price 1989). The perturbation approach to the numerical modelling of the transition to turbulence has been successfully carried out for a straight rectangular duct (Lin 1955). Again this sytem has finite symmetries.

Thus it can be seen that flows with low order symmetries produce transitions and flow maps that have striking similarities with the maps produced by very simple differential equations and iterative routines. This implies that the flows themselves are governed by only a few parameters and so should be easily modelled. The flow in a straight circular pipe is another problem altogether.

D.7 Multiphase Flows and Transitions.

This section will cover in more detail than the previous sections, the few instances that have appeared in the literature where a multiphase flow has been shown to be chaotic. The first and a unique occurrence, involves the horizontal pneumatic transport of solid particles and the modulation of their number density by the flow. The second is a series of papers where various gas/liquid flows have been studied both numerically an experimentally, initially from the point of view of heat transfer efficiency of a two phase cooling system, though later for the fluid flow itself.

The horizontal flow of solid particles in a gas has been studied using the apparatus shown in figures D.7a and b (Sirok 1988). It is clear that the angular velocity of the feed mechanism will produce regular density waves in the concentration of the solids - determined photographically 14 diameters downstream of the mixing section. Indeed this is observed for certain gas flow rates as a mutually correlated signal with a sharp spectrum. The reconstructed attractor for this type of flow would be 1 dimensional, though is not given in the paper. However for other gas flow rates and at certain points in the cross-section of the pipe, the nature of the flow changes, leading to a correlation exponent, derived by the Grassberger-Procaccia algorithm, of 3.7. A version of the reconstructed attractor appears in figure D.7c and the graph used for determining the correlation exponent in figure D.7d.

Enhanced heat transfer caused by oscillating single phase flows in cooling systems has already been mentioned in section D.6. The effect of periodically driving the coolant of a boiling water reactor has been studied numerically (Rizwan-Uddin 1988). As was pointed out in section D.4, a numerical model has all of the variables at hand for analysis and variation. It was observed that for certain transients and periodic driving frequencies, the attractor drawn in the full phase space could be made to go through several transitions before settling on an attractor that was either a stable point, limit cycle, toroid or a strange (chaotic) attractor. The dimension of the strange attractor was found to be 2.048 in an embedding dimension of 6. Low

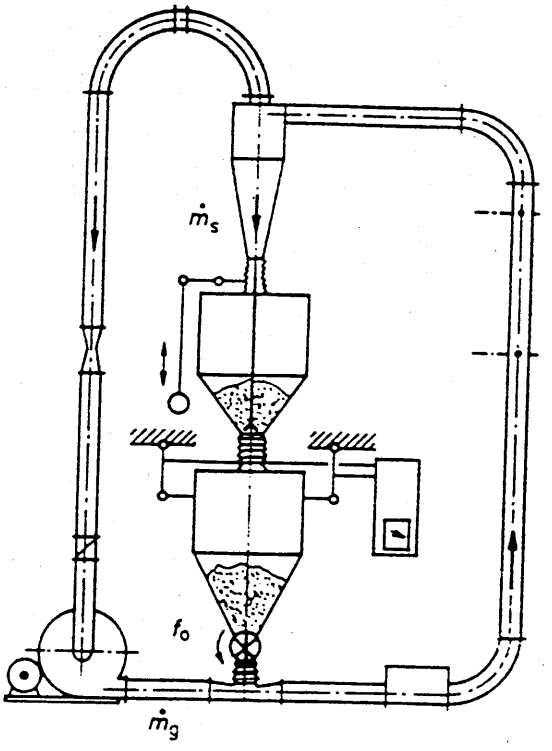

Figure D.7a Apparatus for pneumatic transport of solids (Sirok 1988).

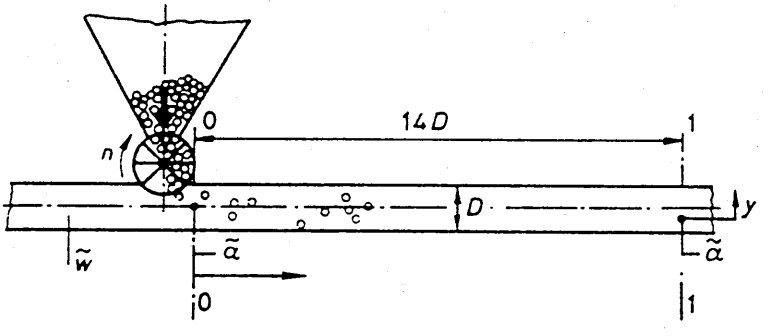

Figure D.7b Details of solids feed mechanism(Sirok 1988).

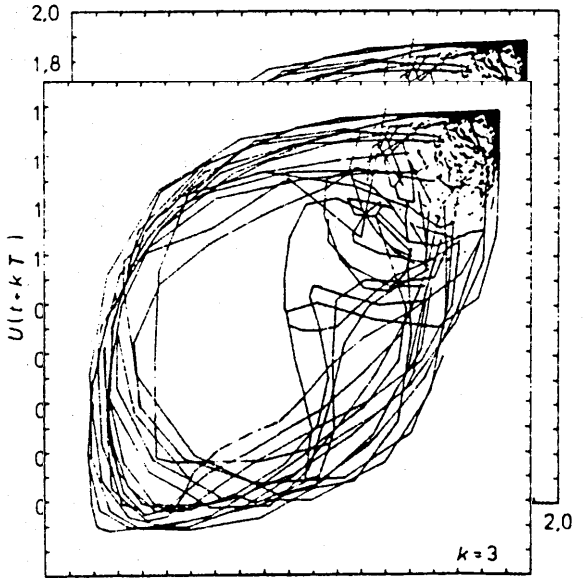

Figure D.7c Reconstructed attractor (Sirok 1988).

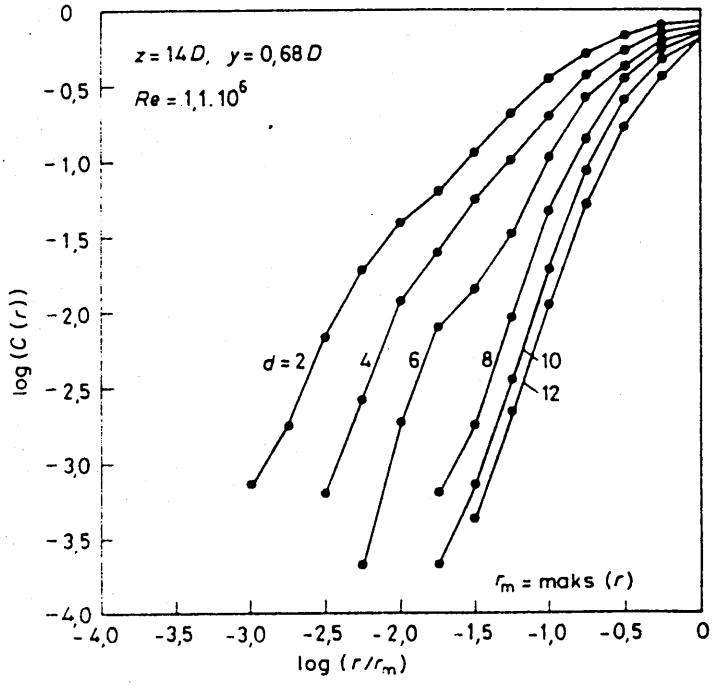

Figure D.7d Determination of the correlation integral for various embedding dimensions (Sirok 1988).

dimensional attractors would be expected from numerical models because of the simplifying approximations used to derive the model itself.

At about the same time upwards, downwards and horizontal annular flows were being studied experimentally (Hagiwara 1988). Hot wires were used to study the wall shear stress, and conductance methods used to measure the wall film thickness. Rather than using these signals as the basic time series, curiously, the intervals between consecutive peaks were chosen to produce another series which were then plotted on a discrete Lorenz plot. This is analagous to the Poincaré and Hénon sections appearing in sections D.2 and D.3, but with Δt_{n+1} plotted against Δt_n. The precedent for this approach appears elsewhere (Shaw 1984, Xiaomao 1989) where the intervals between drips from a tap are studied. In both cases, chaos is concluded, but not quantified.

Following directly on from this work, an experimental study of the flooding transition was carried out (Biage 1989). The flooding trasition is very well defined experimentally as the transition between countercurrent and cocurrent flows of a liquid film and a gas layer. At the transition, the water flow rate is on average identically zero, though tends to be very agitated. Conductance and capacitance techniques were used to determine the wall film thickness and a time series obtained and then analysed using the Grassberger-Procaccia algorithm. the attractor dimension was found to converge (section D.5, $M>2n+1$) on a value dependent on the flow regime and the position in the pipe. For countercurrent flows the correlation dimension was about 12 and for cocurrent flows the dimension was about 7. It was also suggested that the low value of this number and the implied number of variables and order of the governing equations may make the transition amenable to analysis. No attempt at the analysis was made.

Another numerical experiment in a boiling water reactor cooling system looked at density wave instabilities (Lahey 1989) as a function of Froude number. Again, bifurcations, limit cycles and chaotic attractors were observed in the behaviour of several of the variables.

The most advanced papar to date, has recently come to light (Franca 1991) and involves the use of fractal techniques (amongst others) to identify flow regimes in air/water systems. It also appears that the apparatus is also capable of air/oil/water flows - but results are not presented. The measurand was differential pressure at the pipe wall and a time series of the signal was analysed in the usual manner to find the coorrelation dimension. This dimension was found to be a function of flow regime as follows.

Flow Regime	Correlation Dimension
Wavy	1.03/6.21
Plug	7.17
Slug	5.07
Annular	0.97/5.93

Figure D.7e Table of correlation dimensions for various flow regimes (Franca 1991).

The wavy and annular flows showed two separate dimensions over different length scales, which were interpreted as two different deterministic phenomena occurring in the pipe at the same time, such as roll waves and surface waves, with the more intermittent flow producing the higher dimensions.

D.8 Discussions and Conclusions.

Starting from first principles, this appendix has covered those areas of chaos theory that seem most applicable to fluid flow problems, such as transitions between flows with different levels of complexity.

As mentioned in appendix C.4, there is no method of solving the Navier-Stokes equations for an arbitrary fluid flow (including

fluid/fluid flows), and no unified approach to predicting, even semi-empirically, the transition boundaries within these flows. "There is a need for objective and reliable diagnostic criteria, since confidence in the flow pattern maps, used in design and operation, is limited" (Drahos 1989).

The work of Biage has indicated that an approach involving the fractal dimension of some characteristic measureable parameter of the flow, can discriminate between flow regimes. It is proposed that every flow in a confined system (of low order finite symmetry) has a characteristic Hausdorff dimension, which is continuously variable around the parameter space of a given flow regime, and jumps in value (possibly by an integer), when a regime boundary is crossed. This can thus be used to determine flow regime boundaries.

As the embedding dimension also gives a measure of the complexity of the behaviour, a flow regime map, plotted in Hausdorff dimension contours, should also aid the modelling of the various flow types.

From an experimental point of view, the variation in results found using different types of measurements (point, path or area) needs to be investigated, to check that the readings are characteristic of the flow as a whole. There should be no problem detecting the Hopf bifurcation from smooth stratified flow, which shoud have a Hausdorff dimension of 1 for periodic waves, and between 1 and 2 for solitary waves. The droplet flow regime will probably have a Hausdorff dimension well in excess of 10, and may even be comparable with the number of droplets in the measurement region! The developement of the circuit described in section D.3 should enable this determination to be very speedy, and give a starting point for the Grassberger-Procaccia routine, to determine the value more accurately.

The trajectory, be it strange or otherwise on the X_1-X_2 plane is a projection of the full trajectory in the full embedding dimension. Thus the experimentally determined dimension will always be less than or equal to the embedding dimension, as outlined in section D.4. The trajectory itself may also cross the classical flow regime boundaries.

It should be expected that all of the flow regime transitions defined by Hausdorff boundaries should be derivable from a simple set of equations, similar to those described in section D.3. Although this will be an easier task than deriving the boundaries from the full Navier-Stokes equations for the two fluids, it is a comparable task to trying to find the logistic equation from a study of the rabbit population in Australia!

On a less fundamental note, the ideas underlying deterministic chaos would seem to pose a possible route to the solution - although only qualitative at the moment - to all complex fluid flows, and maybe eventually the transition to turbulence in a straight pipe.